University of Southampton

Faculty of Physical Sciences and Engineering

Interfacial Physics of Field-Effect Biosensors

by

Benjamin Mark Lowe

Thesis for the degree of Doctor of Philosophy

December 2016

UNIVERSITY OF SOUTHAMPTON

ABSTRACT

FACULTY OF PHYSICAL SCIENCES AND ENGINEERING

School of Electronics and Computer Science

Doctor of Philosophy

INTERFACIAL PHYSICS OF FIELD-EFFECT BIOSENSORS

by Benjamin Mark Lowe

Field-Effect Transistor-sensors (FET-sensors) are a class of pH and biomolecule sensors that can be produced at a low cost and with high sensitivity, as a result having potential for commercialisation and widespread use. The response of a FET-sensor is generated when the electric field at the sensor surface changes, thereby inducing a measurable change in current through the device. The electric field can be modified by pH or by binding of an analyte to the surface. The solid state counterpart, the Metal Oxide Semiconductor FET, has been extensively studied as it is the basis of modern electronics. FET-sensors are less well understood, mainly due to the inherent complexity introduced by the aqueous media present at the sensor surface. The FET-sensor surface is usually an oxide such as silica and its interaction with aqueous solution introduces many complex effects, such as ion-dynamics and pH dependent ionisation, which make these systems non-trivial to understand and predict. To-date, most models of FET-sensor response have relied upon mean-field assumptions which neglect the multi-scale nature of the system and even qualitative predictions of FET-sensor response remain challenging.

In the work presented here, the interfacial physics of FET-sensors were modelled using a variety of simulation techniques at different time- and length-scales. Acid-base surface charging reactions at the oxide surface of the sensor are an important part of FET-sensor response. Density Functional Theory (DFT) simulations revealed a new mechanism of surface charging and also showed that these reactions have no well-defined transition state which can be used to model their kinetics. A Kinetic Monte Carlo (KMC) model was validated that can be used describe the dynamics of surface-charging reactions on a device scale.

As FET-sensors operate by detecting changes in the interfacial electric field, the mean net charge density of surface-bound biomolecules is an important parameter in most models of BioFET response. Semi-empirical calculations were performed to estimate the net charge of two different biomolecular systems relevant to biosensing studies. The ion dynamics in the electrical double layer at the silica-water-biomolecule interface were investigated using classical Molecular Dynamics (MD) simulations, which suggested that, in contrast to commonly used net-charge arguments for FET-sensor response, the importance of water polarisation for FET-sensor response has been hitherto underestimated.

A quantitative analysis of data extracted from the FET-sensor literature was performed, comparing experimental biosensing data with pH-sensing data. This revealed some frequent problems related to reproducibility and comparability of experimental data in this field, and highlighted that optimisation of surface chemistry is an underappreciated component of sensor optimisation. Despite these limitations, BioFET research is a rapidly advancing field in which novel device design and operation methodologies are constantly being developed which increase the viability of BioFET devices for commercial use.

Contents

Academic Thesis: Declaration Of Authorship

I, BENJAMIN MARK LOWE, declare that this thesis and the work presented in it are my own and has been generated by me as the result of my own original research.

Interfacial Physics of Field-Effect Biosensors

I confirm that:

1. This work was done wholly or mainly while in candidature for a research degree at this University;

2. Where any part of this thesis has previously been submitted for a degree or any other qualification at this University or any other institution, this has been clearly stated;

- An Independent Research Project Report is included as an Appendix which was originally submitted as part of the module COMP6055 as part of the MSc-level year of my 4-year integrated PhD programme. This is clearly stated again at the beginning of the relevant Appendix.

3. Where I have consulted the published work of others, this is always clearly attributed;

4. Where I have quoted from the work of others, the source is always given. With the exception of such quotations, this thesis is entirely my own work;

5. I have acknowledged all main sources of help;

6. Where the thesis is based on work done by myself jointly with others, I have made clear exactly what was done by others and what I have contributed myself;

7. Parts of this work have been published as:

- Lowe, B. M., Skylaris, C.-K. & Green, N. G. Acid-base dissociation mechanisms and energetics at the silica-water interface: An activationless process. *Journal of Colloid and Interface Science*. 451, 231–244 (2015).

- B. M. Lowe, Y. Maekawa, Y. Shibuta, T. Sakata, C.-K. Skylaris & N. G. Green, 'Dynamic Behaviour of the Silica-Water-Bio Electrical Double Layer in the Presence of a Divalent Electrolyte'. *Physical Chemistry Chemical Physics*, Accepted for Publication, (2016), doi: 10.1039/C6CP04101A

Signed: .....

Date .....

Acknowledgements

This work was supervised by Prof. Chris-Kriton Skylaris and Dr. Nicolas G. Green.

My foremost thanks goes to my primary supervisor, Dr Nicolas Green. I am privileged to have had him as a supervisor; his ability to combine intelligent out-of-the-box thinking whilst retaining a good sense of humour is surely the hallmark of an excellent academic.

I also offer deep-felt thanks to Prof. Chris Skylaris for his continued support, regular meetings and patient attitude, without whom this PhD would not have been possible.

Thank you to both my supervisors for their regular meetings, which were both enjoyable and useful.

Many thanks to Prof. Yasushi Shibuta and Prof. Toshiya Sakata for allowing me to combine two of my passions, both Science and Japan.

My thanks goes to Max Phipps, Valerio Vitale, Jolyon Aarons and Dr. Jacek Dziedzic for their tips on how to use the ONETEP software and for keeping my morale up.

I would also like to thank Dr. Peter Lowe for his invaluable comments on readability of the thesis and immense wisdom in the field of biochemistry.

Similarly, thanks to Christoph Riedel for his help in navigating the sometimes scary world of LaTeX documentation and also for his typography and grammar suggestions.

All simulations, unless otherwise attributed in the text of this thesis, were performed by the author.

Dr. Kai Sun, Dr. Ioannis Zeimpekis are acknowledged for their collaboration on the 'Quantitative Analysis of FET-Sensor Literature Data: From pH Sensing to Biosensing' chapter. Their experimental work and discussions with them inspired the subsequent literature review and meta-analysis performed by myself.

Prof. Chris-Kriton Skylaris and Dr. Nicolas G. Green are acknowledged for their collaboration on Section 4.4 containing the work 'Acid-Base Dissociation Mechanisms and Energetics at the Silica-Water Interface: An Activationless Process'. Both simulations and writing were performed by myself, their contributions included meetings to discuss the significance of the findings and proof-reading of the text.

Dr. Yuki Maekawa, Prof. Yasushi Shibuta, Prof. Toshiya Sakata, Prof. Chris-Kriton Skylaris and Dr. Nicolas G. Green. are acknowledged for their collaboration on Section 7.3 containing the work 'Dynamic Behaviour of the Silica-Water-Bio Electrical Double Layer in the Presence of a Divalent Electrolyte'. Both simulations and writing were performed by myself, their contribution included meetings to discuss the significance of the findings and proof-reading of the text. Prof. Yasushi Shibuta provided High Performance Computing resources for this work.

The author acknowledges the use of the IRIDIS High Performance Computing Facility, and associated High Performance Computing and linux support services at the University of Southampton, in the completion of this work. This work also made use of the ARCHER UK National Supercomputing Service (http://www.archer.ac.uk). This work was supported by an EPSRC Doctoral Training Centre grant (EP/G03690X/1) and the JSPS 2015 Summer Fellowship.

Supplementary Data supporting this thesis including input files, output data and the OnetepConv software code can be found online at: `http://doi.org/10.5258/SOTON/403915`

1. Introduction

A wide range of nanomaterials, including nanoparticles [1], nanowires [2], and nanofilms [3], have been developed over the last three decades. Such materials have facilitated a new generation of solid-state electronic devices that include nanowire transistors [4, 5], magnetoresistive random-access memory (MRAM) [3] and solar cells [6]. In recent years, there has been a new focus on the application of nanotechnology to biomedical diagnostics, in which the unique properties of nanomaterials can be applied to detect biological molecules through the creation of nanosensors. As an example, the utility of nanosensors has been demonstrated through wide-spread usage as biosensors, either detecting glucose in blood or in pregnancy tests [7]. Beyond biological analytes, nanosensor applications extend into environmental analysis [8], explosives detection [9] and food safety [10]. In general, a biosensor consists of a biochemical receptor which recognises an analyte and a transducer which converts the binding of the receptor to the analyte into a measurable response [11].

Nanosensor design and engineering focuses on optimising time-to-readout, cost, limit of detection and dynamic range. Ideally, the nanosensor would require the smallest sample volume, and be highly sensitive and specific to the relevant analyte(s). For commercialisation, broader considerations must also be considered such the extent of market demand, the nature of the analyte sample (e.g. blood, urine, swab etc.), the requirements for internal controls to provide reliable sensor response, and regulatory requirements. A promising type of nanosensor based on field-effect transistor (FET) technology, may be capable of meeting these extensive goals.

FET-sensor operation can be qualitatively explained by the following mechanism: introduction of analyte to the surface of the sensor results in a change in the electric field, which causes a change in concentration of charge carriers within the device and finally resulting in a measurable change in the device conductivity. FET-sensors offer a key advantages over many traditional methods in bioanalysis [12] in that labelling of biomolecules is not required, which would reduce the assay development time, the readout time and the level of expertise and equipment required. In comparison with many currently available biosensors which operate via mass-detection [13, 14], the electrical detection offered by FET-sensors provides additional information on, for example, conformational changes [15] or extracellular potentials [16]. FET-biosensors have been shown to be capable of high selectivity [17], high sensitivity [18], and rapid detection of picomolar concentrations of analyte [19, 20].

FET-sensors can be divided into two broad categories: ion-sensitive FETs (IS-FETs) and Biologically-sensitive FETs (BioFETs). Ion-sensitive FETs were first developed in the 1970s by Bergveld [21–24] and can detect changes in electrolyte ion concentration (e.g. pH or Na^+ concentration). BioFETs can be used to detect the presence of biomolecules, which gained significant recognition in 2001 with the work of Cui et al. [25, 26] and over the last two decades has received a rapid increase in interest. For pH-sensing ion-sensitive FETs, a changes in surface charge induced by acid-base reaction at the surface cause a change in electric field thereby producing a measurable response. Whilst for BioFETs, binding of charged molecules to receptors at the surface of the device causes a change in the electric field, thereby producing a measurable response.

FETs are relatively well understood as solid-state devices, as evidenced through the wide availability of textbooks on FET theory [27–30] and the ubiquitous application of FETs in the modern computing

industry (e.g. in smartphones and laptops). In contrast, FET-sensors are much less well understood due to the complexity introduced by the aqueous media and surface chemistry, including surface ionisation and ion dynamics. Even qualitative predictions of the response of FET-sensors to the interaction of analyte molecules remains challenging [31].

FET-sensors are usually nanostructured in order to optimise the analyte-exposed surface area-to-volume ratio (e.g. 'nanowire', 'nanoribbon' etc.), but it can be microscopic and planar. The surface of a FET-sensor typically consists of an oxide-layer exposed to aqueous solution containing the analyte. This oxide component is most commonly composed of silica. The silica-water interface exhibits several unusual acid-base properties, and understanding of its interfacial chemistry remains an active area of research [32].

A key challenge of modelling FET-sensors is that the time-scales of interest span far longer than their solid-state counterparts. For example, the time-scales involved range from approximately $10^{-3}$to 10^{3} seconds for biomolecule binding events compared to approximately 10^{-12} seconds for the changes in conductivity of the sensor. The field-effect mechanism of FET-sensors is inherently a multi-scale problem as the stimulus for the sensor, such as biomolecules, are of the length scale of nanometres, and the device itself can be on a scale up to micrometres; the field-effect occurs over the length of the electrical double layer in the sample and into the surface layer of the device, which can be up to micrometre length scales depending on the scale of the sensor. As FET-sensors are capable of detecting these molecular-scale changes in electrostatics, even low levels of background noise can interfere with interpreting the response [33, 34]. A reliable model of FET-sensor response therefore requires an accurate description of the electric field across these disparate time- and length-scales, a complex problem as yet unsolved.

2. Thesis Outline

The overall aim of the work presented within this thesis is to improve understanding of the interfacial physics of BioFETs in order to facilitate rational improvement of BioFET design.

BioFET response is determined by the interplay between the chemical environment and the electrostatic environment at the surface. Surface-charging is a key component of this environment, and understanding the dynamics of this process has relevance not only to understanding FET-sensor response, but also a range of other fields such as geochemistry, whereby it is relevant to dissolution processes. A model capable of describing the dynamics of surface charging could be used to investigate, for example, how the oxide-surface charge is affected by biomolecule binding. With this motivation, a Density Functional Theory study of the energetics and mechanisms of surface charging at the silica-water interface was performed (Chapter 4) which modelled relevant atomic-scale chemical reactions occurring over picosecond time-scales. However, the use of such as model revealed that these reactions have no well-defined transition state which can be used to model the kinetics. Hence, a Kinetic Monte Carlo model capable of modelling the dynamics of surface charging over macroscopic time- and length-scales was validated and the resulting model may be used as a component in multi-scale modelling efforts of BioFET response (Chapter 5).

As BioFETs operate by detecting changes in the interfacial electric field, the mean net charge density of biomolecules on the surface is an important parameter in most models of BioFET response. Therefore, semi-empirical calculations were performed to estimate the net charge of two different biomolecular systems relevant to biosensing studies (Chapter 6). Literature BioFET response models have almost exclusively treated the charge introduced by the biomolecule as smeared out in an infinitely thin surface charge [2, 35–45] and therefore cannot accurately describe the changes in electrical double layer structure (and therefore electric field and sensor response) induced by binding of charged macromolecules. Given these limitations of existing models, simulations of the electric field as a function of the distribution and dynamics of charges within the system were required. Classical Molecular Dynamics simulations were performed to investigate the electric field at the silica-water-biomolecule interface over nanosecond-time-scale and nanometre-length scales (Chapter 7). This study suggested that the importance of water polarisation in BioFET response has been hitherto underestimated.

Whilst IS-FETs have achieved commercial success as pH sensors [21], BioFETs are currently unsuitable for immediate commercialisation due to a lack of reliable detection capability and stable response. As a step towards a better understanding of how to address this and to design more informative and reliable metrics, a quantitative analysis of the FET-sensor literature data was performed (Chapter 8), comparing experimental biosensing data with pH-sensing data. This revealed some common problems in the field related to reproducibility and comparability of experimental data and highlighted that surface chemistry optimisation is an underappreciated component of sensor-optimisation.

3. General Background

3.1. The Field-Effect Transistor (FET)

The concept of FETs date back to 1925, when J.E. Lilienfeld filed a patent for a semiconducting device for which the electric current through the device could be varied upon exposure to an electrostatic influence [46]. This design represents one of the simplest forms of FET, and is now often referred to as the bipolar junction transistor. This type of device was largely superseded in the 1950s with the invention of the Metal Oxide Semiconductor FET (MOSFET). Advances in photolithography and other relevant processes meant that MOSFETs could be produced reliably at low-cost, and easily integrated into circuit boards. As a result, MOSFETs have become the standard (referred to as 'CMOS technology') in microelectronics [27] and can be found in a wide variety of electronic devices that exist today [47].

3.1.1. MOSFET Structure and Operation

A schematic representation of the structure of a MOSFET is shown in Figure 3.1. A potential difference is applied between the source and the drain electrodes (V_{ds}) which generates a current which flows between the source and drain electrodes through the semiconductor and depending on the electric field at the surface. This current is commonly referred to as the 'drain current' (I). The drain current can vary by many orders of magnitude as the device switches from being a poor conductor to a good conductor, hence why the device is called a transistor. The drain current is modulated by the field-effect (Section 3.1.2) based on the magnitude of the voltage, between the source and gate (referred to here as the gate voltage V_{g}). The minimum gate voltage required to pass a significant current through the semiconductor is termed the 'threshold voltage' (V_{T}), which can be controlled to some extent by varying the backgate-source voltage (V_{bg}).

The structure of the semiconductor is usually doped silicon and the gates can be metal; however, despite their name, MOSFETs need not actually contain metal because the gates can be composed of polysilicon. Polysilicon is a form of silicon composed of non-aligned, randomly oriented domains of silicon crystals. Polysilicon can act as a resistor or a conductor depending on doping concentration and grain boundary properties.

Due to their significant commercial applications, MOSFETs have been extensively studied and engineered ever since the 1950s and therefore it is no surprise that the principles behind MOSFETs operation are generally well understood. Highly predictive models for MOSFET operation have been developed based on conventional semiconductor physics. [30, 48]

3.1.2. The Field-Effect and MOSFET Theory

The term 'field-effect' refers to the phenomenon that drives a change in conductivity/drain current through a semiconducting layer with changes in the magnitude of an external, electrically isolated, electric field. It is almost exclusively used to describe transistors in which the current is controlled by

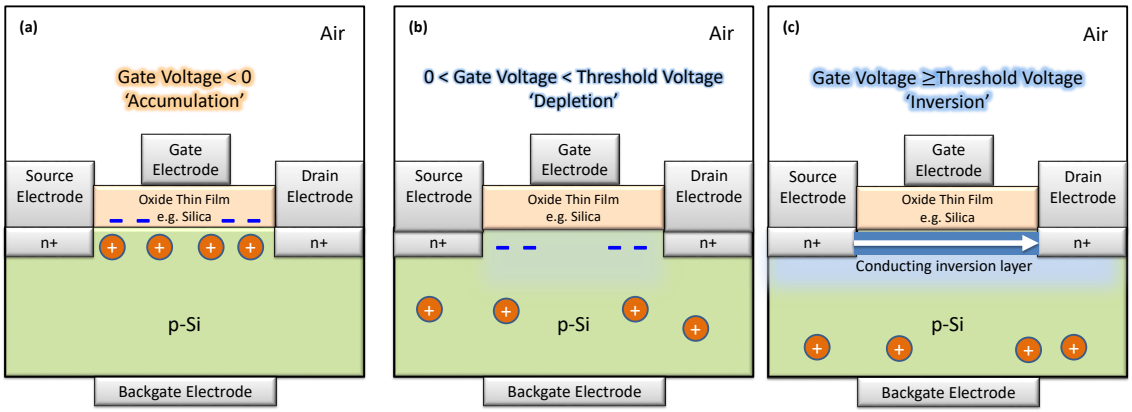

Figure 3.1.: A schematic representation of the operation of an ideal p-doped MOSFET. A potential difference is applied between the source and drain terminals. The source and drain terminals are heavily doped such that they have a high electron concentration, which is termed n+. (a) When the applied gate voltage is less than zero (negative) 'accumulation' of mobile positive majority carriers occurs but no significant current can flow between the n+ doped terminals. (b) As a positive gate voltage is applied, 'depletion' occurs in which the mobile positive carriers are depleted from the surface by the positive gate voltage and a negative charge is generated in the silicon substrate due the remaining presence of, significantly less mobile (i.e. immobile from the perspective of device operation), ionised acceptor ions. Again, no significant current can flow between the source and drain electrodes (c) As the gate voltage is increased beyond the threshold voltage, 'inversion' occurs, in which minority carriers are attracted to the highly positive gate voltage, resulting in a 'inversion layer', or 'n-channel', in which conduction can occur between the source and drain electrodes, resulting in a significant drain current. The transistor is sometimes said to be 'on' in this state.

an external electric field[1]. In MOSFETs, this external electric field originates from the gate electrode which is separated from the semiconductor by an insulating oxide layer (and thus is 'external'), but in principle it could arise from any source of charge at the surface such as biomolecule binding, as will be described later.

A qualitative explanation of the field-effect can be given by example. Before a voltage is applied to the gate, the device is 'off' and the semiconducting layer acts as an insulator. In an ideal p-type device, the main semiconductor region is p-doped (majority charge carriers are positive electron holes, and minority charge carriers are electrons) and situated between heavily doped source and drain regions which are electron rich terminals, referred to as n+ terminals. Normal operation of this device has a potential difference applied between the source and drain and a separate potential difference applied to the gate relative to the substrate. There are three situations that can be considered:

(a) If a negative bias (gate voltage < 0), the positive majority charge carriers (p-type, therefore holes) will accumulate at the semiconductor-oxide interface and 'accumulation' occurs. As the channel is still electron deficient, electrons cannot flow between the source and drain terminals and there is no significant drain current. (shown in Figure 3.1, a).

(b) If a weak positive bias is applied (0 $<$ gate voltage $<$ threshold voltage), 'depletion' occurs. The majority carriers (p-type: holes) move away from the surface leaving behind a channel which is free of majority carriers, and only the significantly less mobile (i.e. immobile from the perspective of device operation) negatively charged dopants/impurities remain. No significant drain current can flow between the source and drain as there are no mobile carriers (shown in Figure 3.1, b).

(c) If a strong positive bias is applied (gate voltage $\geq$ threshold voltage), 'inversion' occurs as the

[1]The field-effect is defined by Webster's New World College Dictionary as: 'designating or of an electronic component or device, especially a transistor, controlled by an external electric field' [49].

potential is strong enough to also induce the movement of negative minority charge carriers (electrons) to the surface and current can now readily flow from the source to the drain. This region of minority carriers is referred to as the 'inversion layer'. The onset of inversion occurs when the gate voltage is equal to the threshold voltage (as shown in Figure 3.1, c).

For an n-type MOSFET, p+ doped terminals are used instead of n+ terminals and the converse logic is applied to qualitatively describe the drain current-gate voltage characteristics. The backgate voltage affects the thickness of the inversion layer and also modulates the value of the threshold voltage [50].

Whilst in the example described in this section the device was initially 'off' before a gate voltage was applied (i.e. charge signs and biases are inverted), in practice the MOSFET threshold voltage can be modified to change the default state of the device. For instance, the device can be set to be 'on' prior to applying a gate voltage, either by usage of a back-gate voltage or changing the material properties of the device.

3.1.2.1. Parameter Regions of Operation

When the applied gate voltage is low, i.e. $V_{\mathrm{g}} < V_{\mathrm{T}}$, and the semiconductor is only weakly inverted, the drain current is known as the 'subthreshold current' and the device is operated in the 'subthreshold region'. In the subthreshold region the drain current is non-linearly related to the gate voltage. In this region,$I \sim \exp(q(V_{\mathrm{g}} - V_{\mathrm{T}})/(mk_{\mathrm{b}}T)$, where q is the elementary charge and m is an empirical constant related to the susceptibility of the device to changes in gate voltage. When a larger gate voltage is applied and a low drain-source voltage is used, i.e. when $V_{\mathrm{g}} > mV_{\mathrm{ds}} + V_{\mathrm{T}}$, then the device operates in what is termed the 'linear region'. In this region the drain current is linearly proportional to the gate voltage ($I \sim (V_{\mathrm{g}} - V_{\mathrm{T}})V_{\mathrm{ds}}$). With increasing drain-source voltage V_{ds}, a 'pinch-off' point (i.e. when $V_{\mathrm{g}} < mV_{\mathrm{ds}} + V_{\mathrm{T}}$), is reached at which the drain current approaches a constant value. This is termed the 'saturation region'. [30]

3.1.3. MOSFETs as Sensors

As MOSFETs can detect changes in the electric field at the oxide interface they have the capability of being used as sensors (FET-sensors), for example to detect changes in ion concentraton such as pH or Na^+ concentration. When the surface is functionalised (i.e. coated/derivatised) with a receptor which is specific to a (bio)chemical analyte then the FET-sensor is termed a BioFET [25]. This type of device measures electrical properties, in contrast to many conventional biosensors which operate on detection of the mass of the analyte [51, 52]. As a result, properties unmeasurable using conventional biosensors can be determined, such as extracellular electric potentials from physiological systems [16], conformational changes of the analyte [15]. An intriguing example applications are to directly couple the device to an insect antenna in order to measure its sense of 'odour' or detecting extracellular acidification due to cellular metabolism of single-cells [25]. In summary, FET-sensors have the potential to meet the requirements of a highly successful nanosensor such as low-cost, high sensitivity and fast readout [21].

A FET-sensor is essentially a MOSFET in which the gate electrode is replaced by a solution containing the analyte and binding of the analyte to the FET-sensor surface results in electrostatic 'gating' of the FET. Usually a 'reference electrode' is placed into the solution, which provides a stable bulk potential. Similarly to the gate electrode in conventional MOSFET devices, this voltage can be biased, and therefore the region of operation of the transistor can be controlled via the choice of the reference electrode voltage. This voltage is also referred to as the 'gate voltage', V_{g}, in analogy to the gate electrode of conventional MOSFET devices. Another key difference between FET-sensors and

MOSFETs is that there is often no p-n junction within the device, this means that the theory from the traditional MOSFET design (Figure 3.1) is not necessarily directly transferable to FET-sensors. For example, for silicon nanowires, the doping of the nanowire plays a minor role compared to the doping of the source/drain terminals in determining what species (i.e. holes or electrons) are primarily responsible for current transport [18]. FET-sensors must have a surface layer in contact with the aqueous solution which is specific to the analyte, and therefore for pH sensing a careful choice of oxide material is required, and for biosensing, the surface is usually chemically functionalised with 3-triethoxysilylpropylamine (APTES) in order to covalently bond a receptor such as, for example, biotin or an antibody.

A schematic of a typical FET-sensor setup is shown in Figure 3.2. When the semiconductor layer of FET-sensors has microscopic dimensions and is flat, it is termed a 'planar semiconductor' layer. Alternatively, it can have nanoscale dimensions, for example, a nanowire (nanometre depth and width, microscopic length) or a nanoribbon (nanoscopic depth, microscopic width and length). The principle of operation is that changes in the electric field at the oxide-electrolyte interface induce a change in the surface potential at this interface ($\Delta\psi_{\mathrm{s}}$), assuming no competition from other effects, and that electrostatic gating is the dominant mechanism [53], then the changes in the electric field results in a change in the semiconductor-oxide surface potential that is equal in magnitude. An equal magnitude shift in the threshold voltage (ΔV_{T}) occurs, which is proportional to the amount of bound analyte, and a field-effect-induced change in current occurs which is proportional to both ΔV_{T} and the ability of the transistor to amplify the signal.

There are two alternative ways of measuring the output response of FET-sensors, termed potentiometric and amperometric detection. In potentiometric detection, supporting circuitry is used to maintain a fixed drain current though the device from drain to source (I) and the change in surface potential or threshold voltage is obtained directly [54]. In amperometric detection, for a fixed liquid potential (V_{g}) set by a 'reference electrode' in the liquid, the change in drain current (ΔI) though the device is measured and, using knowledge of the device properties, it is possible to calculate the shift in threshold voltage using the measured change in drain current. It is common to perform amperometric measurements in which the gate voltage is swept across a range of values and the drain current is measured for each gate voltage resulting in a curve on a graph of gate voltage against current ('I-V_{g}' curve). This is performed before and after analyte addition resulting in two parallel curves and the shift in the threshold voltage can be extracted from the resulting graph. FET-sensors can therefore be used to directly quantify analyte binding, as the amount of bound analyte should be directly proportional to the shift in measured ΔV_{T}. Each of these methods for measuring the response of FET-sensors is shown in Figure 3.3. A detailed discussion of the relevant changes in potential within FET-sensor systems (as opposed to MOSFETs) can be found in Shinwari et al. [55].

It is worth noting that, in principle, the transistor component of the device is not needed for a working sensor, i.e. changes in surface potential due to analyte binding can be measured without the transistor simply by placing analyte upon an oxide surface and measuring the potential difference between the oxide to a reference electrode in solution (requiring a high impedance amplifier). This is similar to how conventional glass electrodes work for pH sensing. However, the transistor component facilitates miniaturisation of the device, thereby providing smaller sample volumes and faster response times [21]. Moreover, the transistor component amplifies the signal and, relative to high-impedance measurements, offers an improved signal-to-noise ratio [56] whilst removing the requirement for large and expensive measurement equipment.

The most common and commercially successful forms of FET-sensor are ion-sensitive FETs, which can operate as pH sensors [21]. The mechanism of ion-sensitive FETs is simply that changes in the concentration of ions, due to changes in the acidity of solution (H_3O^+ or OH^- concentration) in the

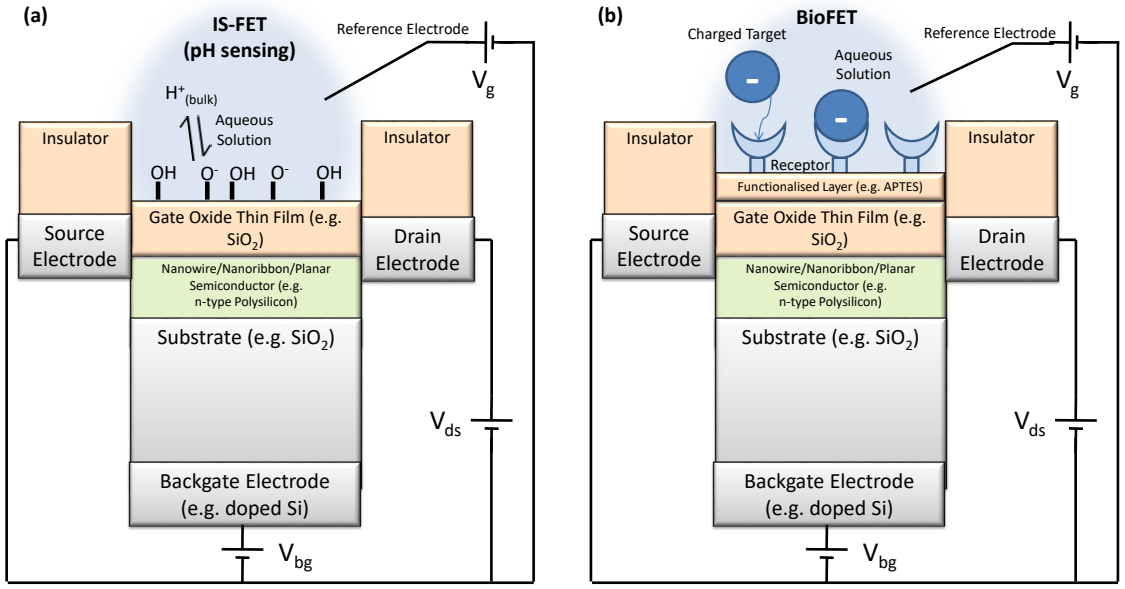

Figure 3.2.: Schematic representation of typical FET-sensor setups. (a) Ion-sensitive FET sensors have an oxide membrane which is selective to binding of a small ion, for example, H^+ in the case of a pH sensing IS-FET. For pH sensing IS-FETs, changes in pH alter the acid-base equilibria present at the oxide surface, resulting in a field-effect. An increase in pH results in an increase in deprotonation of the surface and an increasingly negatively charged surface. (b) Biologically-sensitive FET sensors can detect biomolecules in aqueous solution selectively due to their chemically functionalised surface which contains receptors which are specific to the analyte biomolecule. Functionalisation of the surface usually entails addition of a 3-triethoxysilylpropylamine (APTES) layer so as to covalently bond a receptor such as, for example, biotin or an antibody. For FET-sensors with an 'n-type' (or equivelently 'n-channel') semiconductor, an increasingly negatively charged surface (e.g. due to increased pH for an IS-FET or due to binding of a negatively charged protein for a BioFET), will result in increased positive electron hole carriers near the surface, and therefore switch the device off (no drain current). Positive charge will bring majority carriers (electrons) to the surface via accumulation, forming a conductive channel. For a 'p-type' (or equivalently 'p-channel') device, the response is expected to be opposite polarity. Dimensions of the semiconductor component vary: nano-dimension structures such as nanowires and nanoribbons (approximately nanometre thickness, micrometre surface area) are common, but some are 'planar' (~micrometre thickness, micrometre surface area).

case of pH-sensors, induces a change in the surface charge and thus a measurable field-effect response. BioFETs are another type of FET-sensor that can detect biomolecules selectively in solution. The principle behind BioFET operation is that the surface is functionalised with a receptor specific to the target molecule and providing the target molecule is charged, binding of the target biomolecule to the receptor will induce a field-effect response.

The first BioFET devices originated in the 1970s and were based on ion-sensitive FET technology, however their large size resulted in a poor signal-to-noise ratio [57]. Advances in nanofabrication and theory meant that, by 2001, BioFETs based on nanowires could be fabricated [26, 58]. The advantage of using nanoscale devices is generally held to be that the high surface-area-to-volume ratio means that small local changes at the surface can have a significant effect on the semiconductor carrier concentration, with a corresponding increase in the normalised change in drain current due to binding of molecules (i.e. the change in drain current divided by drain current prior to binding). Improved response with increased surface-area-to-volume ratios has been supported by experiments [18, 59–61], but the theoretical explanation is still an area of active debate [62, 63].

Nanowires have been shown to be capable of sub-picomolar detection of analyte [19, 26, 61]. Nanowires can be fabricated using low-cost chemical vapor deposition, but their orientation can be hard to control and therefore chemical vapor deposition was succeeded by electron-beam lithography on silicon-on insulator (SOI) technology, which has the advantage of being fully compatible with existing CMOS

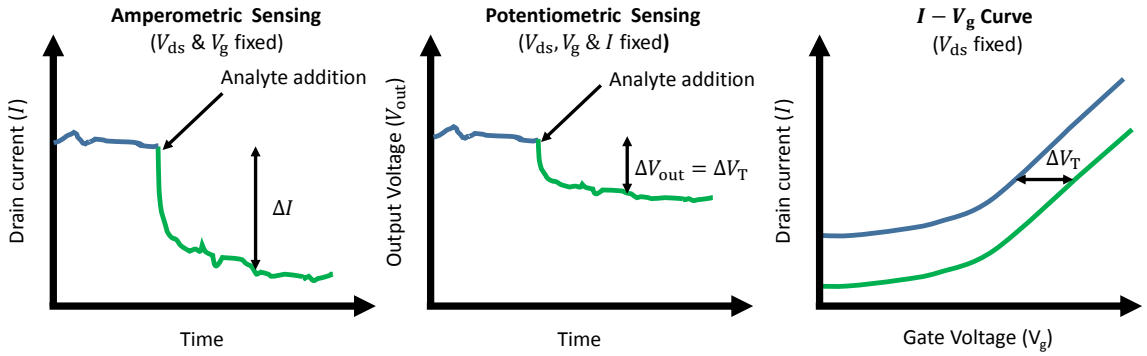

Figure 3.3.: Summary of different methods of measuring FET-sensor response. The blue line represents the response prior to analyte addition, and the green line after analyte addition. A change in surface potential ($\Delta\psi_s$) upon analyte binding induces an equal change in threshold voltage of the transistor (ΔV_T). This results in a change in drain current (ΔI) through the transistor. The change in current can be measured (amperometric sensing) or the change in threshold voltage (potentiometric sensing). Commonly, the drain current is measured as a function of gate voltage ('$I - V_g$ curve') both before and after analyte addition, resulting in two parallel curves from which the shift in threshold voltage can be extracted. The value of ΔV_T is proportional to the amount of bound analyte, whereas the value of ΔI is proportional to both ΔV_T and the ability of the transistor to amplify the signal.

technology and produces a high degree of control of the nanowire geometry. Despite these advantages, this technique can be expensive and slow, and therefore there has recently been increasing interest in nanoribbons. Nanoribbons are up to approximately a micrometre wide but remain nanoscopically thick. Nanoribbons have been shown to obtain comparable sensitivity to nanowires [18, 59]. Various other nanoscale geometries have been proposed, such as stacked arrays of nanowires [64] and 'nanobelts' [65] but the optimal geometry remains unclear.

3.1.3.1. Reference Electrode

An ideal reference electrode ensures that the potential at the electrode-electrolyte interface is insensitive to changes in the electrolyte solution [66]. If this is the case, then any measured change in the threshold voltage of the transistor (ΔV_T) can be assumed to be induced by changes in the electrolyte-insulator interface potential ($\Delta\psi_s$). In a 'conventional' reference electrode, the constant activity of the reference ion is maintained by placing the reference metal inside a reference electrode compartment connected to the sample by a liquid junction. Unfortunately, miniaturisation of this system is problematic and results in reference electrodes with reduced lifetimes [67] and therefore a common alternative in the field of FET-sensing is the use of a 'pseudo-reference electrode' in which a bare metal wire is used instead. Unlike conventional reference electrodes, the interfacial potential of a pseudo-reference electrode is not known *a priori*, but under controlled conditions it can still maintain a stable potential. The reference electrode can be biased or unbiased providing the gate voltage (V_g) in the bulk aqueous sample, and is sometimes referred to as a 'liquid-gate' voltage or 'top-gate' voltage in the literature.

The most commonly used pseudo-reference electrodes are Ag/AgCl which is consists of a silver electrode usually chemically or electrochemically chloridised [68]. Other noble metal pseudo-reference electrodes such as Gold (Au) and Platinum (Pt) are sometimes used, but can have issues with drain current instability and pH dependency [69]. Though Pt-pseudo-reference electrodes have been used in various biosensing experiments with the biomolecule streptavidin [70–72], many experimental groups have confirmed that Pt reference electrodes are unreliable and are therefore not recommended for use in FET-sensing. Ag/AgCl pseudo-reference electrodes have been investigated in detail by Rajan (2013) [73] and Rim et al. [69] through a comparison to a conventional reference electrode and it was concluded that they can be suitable for use in biosensing experiments.

It is often stated that a reference electrode (with corresponding liquid-gate potential, V_g) is required for a reproducible and stable signal of FET-sensors [67, 74–76]. Nonetheless, it is not uncommon for devices to be fabricated without any reference electrode in the liquid [59, 61, 65, 77, 78] which may be due to dielectric breakdown of the device when a voltage is applied to the reference electrode [61]. Such devices often utilise a back-gate voltage as a pseudo-reference electrode.

3.1.4. Modelling and Simulation of Field-Effect Transistors Sensors, a Complex System

The magnitude and polarity of the overall charge of biomolecules (referred to here as 'net-charge arguments') are often used to rationalise experimentally observed BioFET response [61, 79]. Unfortunately, such arguments are purely qualitative, and in some examples, presented later (Section 3.1.5), cannot even explain the experimentally observed polarity of the response.

Several attempts to improve on simple net-charge arguments have been made, but necessarily require a model in which the geometry of the device is incorporated. Elfström et al. have studied the size dependence of silicon nanowires both experimentally and using simulations. They used 2D semiconductor simulation software ('ISE-TCAD') to study the semiconductor-oxide interface charge density and concluded that, for nanowire FET sensors, the sensitivity increases with decreasing nanowire width [18].

BioFET modelling is inherently a multi-scale problem. The stimulus for the sensor, biomolecules, are of a length scale of a nanometre, and the device itself can be on a scale up to micrometres with the field-effect occurring over the electrical double layer and into the surface layer of the device which can be up to micrometre length scales. The device will respond to fluctuations in ions up to approximately 0.01 ps time-scales [80, 81] (e.g. to rearrangement of small-ions in the electrical double layer [82]) all the way up to microsecond to minute time-scale due to protein binding [83].

Several attempts at modelling BioFET response have been made which recognize the multi-scale nature of the problem [31, 39–41, 84]. Heitzinger et al. have developed a multi-scale model of the electrostatics at the surface of the sensor which can be coupled with any charge transport model in a self-consistent manner. Their method is based on homogenisation of the Poisson equation and represented the biomolecule binding layer as a boundary layer which has both charge from biomolecules and a dipole moment. In contrast to typical net-charge arguments, their model suggested that the dipole moment, which can be interpreted as the orientation of biomolecules, is more important than the net-charge of the biomolecules [39, 40].

Nair and Alam have utilised analytical solutions to the Poisson-Boltzmann equations and reaction-diffusion equations to explain the limiting behaviour of the devices [2, 36], and, in a similar vein, a Nature perspective article demonstrated a framework for nanosensor design based on using reaction-diffusion kinetics to interpret experimental data [83]. While such approaches are valuable, they neglect an explicit attempt to predict the electrostatics at the interface; a feature which would likely be necessary in a model capable of quantitative predictions of FET-sensor response.

Some attempts to explicitly model the charges on the sensor surface due to binding of biomolecules have been made. Baumgartner et al. [41] used a method based on homogenisation of Poisson's equation, and utilised the 'PROPKA' method for predicting the pH-dependent mean net-charge of biomolecules [85, 86]. The PROPKA method is an empirical model for residue pK_a prediction and is discussed in more detail in Section 6.1. The work of Baumgartner et al. shows good agreement with experimental results and although they claim not to have used fitting parameters, in selecting the best results from a set of device parameters and in choosing an arbitrary protein functionalisation density,

this claim seems limited at best. They concluded that the backgate voltage is an important influence on the sensitivity of the sensor, and remark that the number of interacting parameters present in BioFETs makes them significantly more difficult to model than traditional FETs.

Further attempts to model the direct coupling between surface electrostatics and device response have been made by De Vico et al. [31, 84], who have proposed a complete computational methodology for quantitative prediction of the response of nanowire BioFETs by combining the surface screening model of Sørensen [35] with the PROPKA method. They noted that such simulations can help with the interpretation of experimental results. However, they found that within the literature, key experimental parameters such as charge carrier density or the receptor density on the surface, are often not published. This lack of knowledge about the device can make accurate quantitative predictions difficult. The model of De Vico et al. has recently been further utilised in the work of Lloret et al. [87] to support their experimental work studying the effect of buffer composition on FETs. Other recent multi-scale models include that of Nozaki et al. on Schottky-barrier FET-sensors [88] and Moore et al. on nanopore FET sensors [81].

Despite the work described in this section, a detailed understanding of FET-sensors remains elusive. While much previous work has been done on attempting to model the device response, little has been done on explicitly modelling the electrostatics at the surface and attempting to model the dynamics of the processes involved on a molecular length scale, which is something that is addressed within the research presented within this thesis.

3.1.5. Anomalous FET-sensor Results

In this section, attention is drawn to various examples from the literature in which FET-response has provided results which are anomalous based on conventional electrostatic gating arguments, whereby the magnitude and polarity of the protein net charge is expected to correspond to the magnitude and polarity of FET-response. This is a key motivation for the research in this thesis, which aims to improve understanding of the interfacial physics of BioFETs.

3.1.5.1. Neutral Molecules

There have been various reports of detection of neutral molecules via induced changes in charge at the interface; for example, glucose-sensing has been achieved by modifying the equilibria of surface-functionalised phenylboronic acid such that it develops a negative charge by reaction with hydroxide ions in the water [89, 90]. Ah et al. functionalised the surface such that the presence of neutral analyte will result in detectable specific binding of negatively charged gold nanoparticles [91].

Cahen and Naaman have reported that no change in net charge at the surface is required for a change in the measured direct current (DC) device response, but rather only a change in dipole moment of the molecular layer at the surface is sufficient [15]. This throws into question some of the very basic assumptions often made about how BioFETs work. Cahen and Naaman functionalised the surface with a monolayer of a long-chain non-polar molecule (octodecyl tricholorosilane) and then added gaseous neutral absorbates such as $O_2/N_2/H_2O$ [15]. A n-type GaAs device was used for the FET, suggesting that a positive electric field at the surface should result in accumulation of majority carriers and increase in device drain current [92]. Their experiment showed that, relative to pure N_2 gas, a reduction in drain current was observed on the introduction of O_2 gas and an increase in drain current with the introduction of H_2O vapour. The authors attributed this response as due to changes in the surface-bound monolayer dipole moment induced by the gas/vapour.

Tarasov et al. functionalised their FET-sensor with a neutral organic molecule (octadecyldimethylmethoxysilane) and showed that as the functionalisation reaction proceeded there was a change in surface potential shift. The shift was explained via a Surface Complexation Model (Section 3.3.2.1) as due to the neutral molecule modifying the density of solvent-accessible titratable groups at the oxide surface of the sensor [93].

Kulkarni et al. have reported detection of neutral molecules using a 'heterodyne detection' methodology with FET-sensors [94]. Their methodology utilises the response generated due to mixing between analyte-induced conductance modulation and analyte-induced alternating current (AC) excitation; this signal is a function of the dipole moment of the molecule.

These results suggest that although it is commonly assumed that BioFETs operate on the principle that the net-charge of a biomolecule determines both the magnitude and polarity of the BioFET response, this result is an oversimplification. They suggest that the dynamics of electrolyte and surface charges might be affected in such a way as to generate a direct current (DC) response, even upon binding of a neutral molecules. Studies which involve neutral molecules have received surprisingly little attention despite their relevance to understanding the mechanism of BioFET operation.

3.1.5.2. Reversed Response

In some cases, BioFET response is opposite in polarity to that which would be expected based on conventional electrostatic gating arguments. As an example, streptavidin is a protein commonly used in biosensing experiments, and has a net negative charge in physiological buffer solution at pH 7.4 (Section 6.3). Therefore upon binding of streptavidin to a FET-sensor, the response is expected to be analogous to a 'negative gate voltage' from traditional MOSFET theory, and thereby cause a decrease in drain current for an n-type device. In practice, there are many examples whereby even the basic qualitative prediction of polarity of FET-sensor response has been incorrect, i.e. the response is 'reversed' relative to expectations.

Bradley et al. observed a decrease in drain current and a negative ΔV_{T} upon streptavidin binding; given that this device was a p-type device, this is opposite to that expected based on electrostatic gating net-charge arguments [95]. The device was based upon an unfunctionalised carbon nanotube as the channel material rather than a conventional semiconductor-oxide structure, and therefore there is no oxide layer and it is possible for the analyte to reach direct contact with the nanotube and bind non-specifically. For devices without oxide layers at the surface it might be possible to explain the 'reversed' response in terms of the gating mechanism not being due to the field-effect, but instead due to charge transfer. Bradley et al. used a charge-transfer mechanism to explain their results, suggesting positive amine groups of streptavidin might be binding directly to the surface of the nanotube resulting in effective positive gate voltage despite the net negative charge of streptavidin [95, 96]. It should be noted that some of the experiments of Bradley et al. were performed at high biomolecule concentration and low buffering capacity; in such cases, the bulk pH may be changed by the biomolecule, thus bringing into doubt their validity as later discussed in Section 8.5.3.

Ishikawa et al. observed a similar phenomenon for an In_2O_3 semiconductor with a phosphate oxide surface, neither of which are common choices in the field. The surface was linked to biotin via a succinimidyl linking molecule [97]. In contrast to that predicted from net-charge arguments, upon binding of streptavidin they observed an increase in drain current and negative shift of -14 mV for ΔV_{T}. Ishikawa observed a strong dependence of the device response to streptavidin upon changes in ionic strength, indicating that the mechanism was electrostatic gating via Coulombic interactions, as opposed to direct charge-transfer to the semiconductor [53]. In order to test the hypothesis that this is due to amine groups from streptavidin, on average, oriented closer to the nanowire than the

negative charges on the protein (a hypothesis originally proposed by Bradley et al. [95] with little justification), De Vico et al. utilised a multi-scale simulation which accounted for the position of charges on the protein [31]. Their simulations suggested that this explanation is not sufficient to explain the 'reversed' response. De Vico et al. proposed a possible explanation based on the similar length scale between the device used (approximately 5 nm) and streptavidin [98], suggesting that the small scale of the device might limit the extent to which it is exposed to streptavidin, stating that if only part of the tetrameric structure of structure was 'sensed' then the altered charge distribution could conceivable produce the reversed signal.

'Reversed' responses have been observed by Heller et al. using their carbon nanotube FETs [53]. The drain current was measured as a function of gate voltage (V_g) before and after treating the sensor-surface with 1 µM of horse heart cytochrome-c (HHCC) in PBS buffer and they observed that the resulting curves intersected, i.e. that depending on the choice of V_g for this system, the opposite response might be obtained. Heller et al. concluded that the 'reversed' response was due to Schottky barrier effects (i.e. work function modulation of the contact regions) [53] and therefore this effect can be avoided in devices that have been well-passivated to protect the contacts from the electrolyte.

Upahyay et al. utilised an InAs semiconductor device in their FET-sensor, in which the oxide surface had non-specifically bound, biotin-functionalised Bovine Serum Albumin as the receptor for the streptavidin. Addition of streptavidin showed the 'expected' signal polarity at low ionic strength, but showed 'reversed' signals at high ionic strengths. They did not provide an explanation for the 'reversed' response [99]. In their system, a plausible explanation for the reversed response is that varying ionic strength modified the concentration of negatively-charged biotin-functionalised Bovine Serum Albumin on the surface.

Most biosensing systems utilise a system in which there is a silica surface functionalised with a layer of (3-Aminopropyl)triethoxysilane (APTES) in order to link the receptor of the biomolecule to the surface. The above examples of 'reversed' signals from the streptavidin literature all originate in systems which contain distinctly different surface chemistry to this common setup but further research is needed to identify what properties of the above systems cause this unexpected behaviour.

3.2. Electrostatics of Electrochemical Systems

Given that the 'field-effect' is electrostatic in origin, an introduction to some relevant electrostatic (and electrodynamics) theory is presented in this section. For an in-depth discussion of electrostatic theory, the reader is referred to standard texts such as that of Duffin [100]. Whilst the idea of an 'electric potential'[2] is a general concept in physics, in the field of chemistry, some specific terms have arisen such as the 'electrostatic potential'. This section provides an introduction to relevant terminology in chemical systems (Section 3.2.1) followed by a description of the most common models of the electrostatics of liquid-surface systems (Section 3.2.2). Finally, as atomistic calculations are an important part of the research presented in this thesis, an introduction to how electrostatics are commonly evaluated in atomistic simulations is presented (Section 3.2.3).

3.2.1. Terminology

The basis of electrostatics can be seen as originating from both Coulomb's Law and the Superposition Principle. Coulomb's Law describes the forces exerted between two charges, and the Superposition Principle allows these interactions to be evaluated easily over large systems containing many charges.

[2] Often termed the 'electrical potential' in Engineering, and 'electric potential' in Physics

The electric field is a useful concept which can be defined as a measure of the force that *would be* exerted on a charge *if it* were placed at any particular point in the space of the system. A further useful quantity is the electric potential difference, which describes the work done in moving a unit charge from an initial position (A) to a final position (B) (V_{AB}). Strictly speaking, only potential differences can be measured, but if the potential of A is set to zero then the potential difference is sometimes simply referred to as 'the electric potential (at B)' (V_B).

The previous considerations represent well-established terminology from electrostatics [100]. It should be noted that in the field of chemistry, the term 'electrostatic potential' has become common to describe a specific kind of potential difference which is useful for systems which cannot be conveniently represented as spatially-discrete point charges. This is the case in chemical systems due to the delocalisation of the electron density. The 'electrostatic potential' is exactly equal to the Coulombic interaction energy between the unperturbed charge distribution of the system and a positive unit charge at a distance, $\mathbf{r}$ [101]. Thus the term 'electrostatic potential' used in chemistry is essentially an electric potential *energy* evaluated at the position of a charge for a system composed of molecules. The unfortunate similarity in the terms 'electrostatic potential' in chemistry and 'electric potential' in physics have resulted in some authors using these terms interchangeably (e.g. [15]). For a more detailed description of the 'electrostatic potential', see Appendix A.

3.2.2. The Electrical Double Layer

When any solid is exposed to aqueous solution, the water molecules reorientate and charges in solution, either from autoionised water (H_3O^+, OH^-) or from electrolyte (e.g. Na^+, Cl^-), change their arrangement in response to the surface. This phenomenon is fundamental to many fields of science such as, electrochemistry, colloids, tribology, solid-supported catalysis and bionanotechnology [102]. The structured arrangement of charges and oriented dipoles (e.g. oriented water molecules) which composes the interfacial region at the boundary of an electrolyte is termed the 'electrical double layer' [102]. Although the term 'electrical double layer' often used to describe solid-water interfaces, the phenomenon actually occurs at *all* phase boundaries [102]. The term 'double layer' comes from the historical models of electrified interfaces in contact with electrolyte, in which the structure was modelled as simply two 'sheets' of charge.

Various commonly used models for the Electrical Double Layer are presented here as such models are a key component of attempts to model BioFET device response. In addition, one of these models is compared to the novel results of atomistic simulations later presented in this thesis (Section 7.3). Many of the commonly used mathematical models for the double layers still used today were developed in the early 20th century [103]. A detailed discussion of electrical double layer modelling can be found in standard texts [104–107].

In spherical coordinates, the electric potential, $\phi(r)$ due to a point charge q_2, ('Coulomb Potential') can be written as:

$$\phi = \frac{q_2}{4\pi\epsilon_0 r}, \tag{3.1}$$

where ϵ_0 is the permittivity of free space. The Poisson equation is a generalisation of this equation to a volume distribution of charge density $\rho(r)$ where the dielectric need not be vacuum, and has a relative permittivity ϵ_r:

$$\nabla^2\phi(r) = -\frac{\rho(r)}{\epsilon_0\epsilon_r}. \tag{3.2}$$

The charge density $\rho(r)$ can be expressed as a sum over all i species of ion present with charge $z_i(= -1$ or $+1$ in a monovalent electrolyte), where $c_i(r)$ is the concentration of the ion in solutions at distance

r:

$$\rho(r) = q\sum_i z_i c_i(r). \tag{3.3}$$

The earliest model of the double layer was the Helmholtz model which modelled the surface as a parallel plate capacitor with the surface as one plate and the solution ions as the other. It can be divided into two planes, the inner Helmholtz plane passes through the centres of specifically bound ions (or adsorbed water), and the outer Helmholtz plane passes through the centres of solvated ions. Between both planes, the electric potential varies linearly with distance.

One of the limitations of the Helmholtz model is that it neglects the thermal 'smearing' of ions in solution. The Boltzmann distribution can be used to model how the concentration of ions will decay from high concentration of surface cations near the surface to the bulk concentration, $c_{i\infty}$, where the concentration of positive and negative ions in solutions is equal. The concentration of ions at a specific distance from the surface $c_i(r)$ can therefore be expressed as a function of the electric potential $\phi(r)$:

$$c_i(r) = c_{i\infty}\exp(\frac{-qz_i\phi(r)}{k_\mathrm{b}T}), \tag{3.4}$$

where k_b is the Boltzmann constant. By substituting Equation 3.4 into Equation 3.3, an expression is obtained for the charge density and inserting this charge density into the Poisson Equation (Equation 3.2), the resulting equation is the Poisson-Boltzmann Equation:

$$\nabla^2\phi(r) = -\frac{q}{\epsilon_0\epsilon_r}\sum_i z_i c_{i\infty}\exp(\frac{-qz_i\phi(r)}{k_\mathrm{b}T}). \tag{3.5}$$

This equation describes the electric potential at the interface between a charged object and the solution, taking into account the effect of screening by counter ions, e.g. around an ion or a surface. It can actually be thought of as a special case of a more general model which is used in many fields - the Poisson-Nernst-Planck (PNP) model. In the PNP model, the Poisson equation is used to describe the electrostatic potential, the gradient of which is used to drive ion motion. This is coupled with the Nernst-Planck equations which are used to describe electrodiffusion of ions in terms of ion concentration. The PNP equations are equivalent to the Poisson-Boltzmann equation in the case that the ionic flux from the electrodiffusion is zero [108], which is a common assumption in the case of equilibrated oxide-water interfaces with no convection.

Equation 3.5 cannot be solved analytically for spherical coordinates. However in the case of a charged plane, considering the dimension in the direction of the surface normal, x, assuming a symmetric $z:z$ electrolyte ($z_i = z_+ = -z_- = z$) then using the mathematical identity $\sinh(p) \equiv (\exp(p) - \exp(-p))/2$, Equation 3.5 the following expression is obtained:

$$\frac{\mathrm{d}^2\phi}{\mathrm{d}x^2} = \frac{2c_{i\infty}}{\epsilon_0\epsilon_r}\sinh\frac{ze\psi}{k_\mathrm{b}T}.$$

Integrating Equation 3.5 along the plane normal to the surface (x) yields $\frac{d\phi}{dx}$ (which is the electric field) and this resulting expression (not shown) can be solved analytically [104].

Debye-Hückel Approximation

Returning to polar coordinates, as the following expressions are valid for both radial (e.g. charges around an ion) coordinate systems and surface systems (considering only the dimension x). For the case of low surface potentials where $\phi(r)$ is small, i.e. $|\frac{qz_i\phi(r)}{k_\mathrm{b}T}| \ll 1$, the non-linear Poisson-Boltzmann equation can be linearised replacing the exponential term with a linear term. More specifically, from the series expansion of the form, $e^x = 1 + x + \frac{x^2}{2!}\cdots$, a substitution of $1+x$ can be used (where x is

$\frac{qz_i\phi(r)}{kT}$) resulting in the Debye-Hückel equation of 'linearised' Poisson-Boltzmann equation shown in Equation 3.6:

$$\nabla^2\phi(r) = -\frac{q}{\epsilon_0\epsilon_r}\sum_i z_i c_{i\infty}(1 - \frac{qz_i\phi(r)}{k_\mathrm{b}T}) = -\frac{1}{\epsilon_0\epsilon_r}\left[\sum_i qz_i c_{i\infty} - \sum_i \frac{q^2 z_i^2 c_{i\infty}\phi(r)}{k_\mathrm{b}T})\right]. \tag{3.6}$$

For a sufficiently large r, the boundary conditions of $\phi(r) = 0$ and $\frac{d\phi}{dr} = 0$ apply, which correspond to electroneutrality, such that the $\sum_i qz_i c_{i\infty}$ term in Equation 3.3 is equal to zero. Under these conditions the expression simplifies:

$$\nabla^2\phi(r) = \left[\frac{1}{\epsilon_0\epsilon_r}\sum_i \frac{q^2 z_i^2 c_{i\infty}}{k_\mathrm{b}T}\right]\phi(r) = \kappa^2\phi(r), \tag{3.7}$$

in which κ^{-1} is the Debye length. The approximation of assuming ψ is small is termed the Debye-Hückel approximation. Despite it not being strictly valid in most situations of interest in colloid science and electrochemistry [104], it is commonly used. One reason for this is its convenience, whereby screening by electrolyte can be described in a simple parameter - the Debye length, which is inversely proportional to the square root of the ionic strength.

The solution of Equation 3.7 is:

$$\phi = \phi_s e^{-\kappa r}, \tag{3.8}$$

where ϕ_s is the surface potential ($\phi_s = \phi(r = 0)$). From this expression, it can be seen that the potential decays exponentially as a function of distance from the surface. The electric field is the gradient of the potential, and therefore is simply $E = -\phi_s\kappa e^{-\kappa r}$.

Surface Charge

The surface charge (σ) can be related to the surface potential (ϕ_s) by applying the condition of electroneutrality, in which the surface charge plus the charge from the ions in the double layer must be zero. The resulting expression is referred to as the Grahame Equation:

$$\sigma = \sqrt{8\epsilon\epsilon_0 c_{i\infty} k_\mathrm{b}T}\sinh(\frac{q\phi_s}{2k_\mathrm{b}T})$$

The expression can be written equivalently in the form of hyperbolic cosine or exponential terms. It is also possible to linearise this expression using the Debye-Hückel approximation, to yield:

$$\sigma = \epsilon_0\epsilon_r\kappa\phi_s$$

Double Layer Models

In the Gouy-Chapman diffuse-charge model, the activity of ions in the double layer are treated as exponentially decaying as a function of distance from the interface, as shown in Equation 3.8 [102]. The Gouy-Chapman model is inaccurate for highly charged double layers, in part due to the lack of a finite-size description of the ions. In this model, at high surface potentials (high surface charges), the counter ion concentration at the surface becomes unphysically high. Stern proposed an alternative model which can describe systems at higher potentials, which combines the Helmholtz layer with the Gouy-Chapman diffuse layer known as the 'Gouy-Chapmann-Stern' model.

The majority of BioFET models incorporate a model of the electrical double layer based on either the Poisson-Boltzmann equation (Equation 3.5) [2, 36–45] or the linearised Poisson-Boltzmann equation [31, 35, 84, 87] (Equation 3.7).

3.2.3. Atomistic Simulation of Electrostatics

When performing atomistic simulations, it is often the case that a finite system is most conveniently approximated using a periodic system. Making this approximation facilitates an emulation of 'bulk'-like properties which would otherwise be unobtainable. For example, when studying a surface system, a surface 'slab' can be generated which is periodic in the plane of the surface, and a large vacuum gap is inserted between its periodic images to minimise the unphysical Coulombic interactions in the out-of-the plane direction.

Calculating Coulombic interactions in these periodic settings is a challenging problem. A coulomb sum would require an infinite number of calculations, and the long-range nature of Coulombic forces mean that truncation of the sum of to a finite number of atoms is still expensive. Various approaches have been developed to calculate periodic Coulombic interactions [109], but in this thesis the 3D periodic Ewald sum (EW3D) [110–112] was used in all periodic atomistic calculations unless otherwise specified [113, 114]. Detailed explanations of the Ewald algorithm is provided in Frenkel and Smit [111] and Hansen (1986) [112].

3.3. Silica-Water Processes, Structure and Dynamics

Silica and water represent two of the most abundant chemical systems on the planet, and therefore it is unsurprising that understanding the interface between them is relevant to a wide variety of systems such as drug-delivery [115], prebiotic chemistry [116], geochemical processes [117] and chemical engineering [118]. Of particular relevance to this thesis, most FET-sensors incorporate a silica-water interface and therefore understanding of this interface is important for understanding FET-sensor design. In this section, the structure of silica surfaces is described (Section 3.3.1), followed by a description of models of charging processes (Section 3.3.2), a summary of processes that occur at the silica-water interface (Section 3.3.3). The dynamics of charge transport in pure water can provide insight into the charging properties at the silica-water interface, and therefore charge transport in pure water is described (Section 3.3.4), followed by an overview of silica-water interfacial processes (Section 3.3.5).

3.3.1. Structure of Silica Surfaces

Due to its huge technological [119] and geological significance [120], gaining a better understanding of the macroscopic and nanoscale behaviour of silica is a significant area of active research. For a comprehensive review of the structure and features of silica surfaces, the reader is referred to the review of Rimola et al [32]. Silica is a solid up to temperatures of 1600^oC that consists of silicon and oxygen, with a chemical formula of SiO_2. In its crystalline form, silica is dense and periodic, such as in the cases of Quartz, Cristoballite or Edingtonite. Silica can exist in different physical forms such its well-known vitreous form ('glass') which is dense and contains short-, but not long-range-, ordering of the molecules. Other less dense forms of silica exist such as porous sponges, aerogels and zeolites. [32]

Amorphous silica, also known as fused glass or vitreous silica, is of particular relevance to FET-sensors as it is the structure of the interface when silica is thermally grown or hydrated for long period of time [121], both of which are common for FET-sensors. Amorphous silica is composed of a mixture of chemically inert hydrophobic siloxane groups ($\equiv$ Si-O-Si $\equiv$), reactive hydrophilic silanol groups and SiO_n ring structures. The silanol groups can be subdivided according to how many siloxane O bonds there are to each silicon atom (Q^n notation), as shown in Figure 3.4. Q^1 sites are not found at the silica surface [32], and hence are not shown in Figure 3.4. Silanol groups can also be classified

according to their chemical structure and degree of hydrogen bonding (Geminal, Isolated, Vicinal) as is also depicted in Figure 3.4.

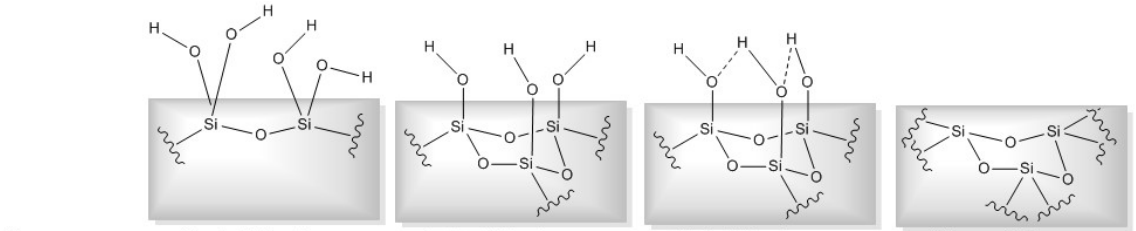

Type	Geminal Silanols	Isolated Silanols	Vicinal Silanols	Siloxane Bridges
Q Notation label	Q^2	Q^3	Q^3	Q^4
^{29}Si MAS NMR	-94 ppm	-100ppm	-100pm	
FTIR wavenumber	3743cm^{-1}	3743cm^{-1}	3660cm^{-1}	

Figure 3.4.: Summary of common silica nomenclature and some key features to distinguish silanol groups experimentally. Nuclear Magnetic Resonance (NMR) Chemical Shifts and Fourier-Transform Infrared (FTIR) Spectroscopy wavenumbers shown are from Vansant et al. [122].

On exposure to water, and over long time-scales (hours to days), surface dissolution occurs in which siloxane bridges are attacked by water molecules forming the more reactive and hydrophilic silanol groups (see Section 3.3.3.4). Defects at the surface can be produced thermochemically, photochemically or mechanically, but are rapidly eliminated by water [32]. Further defects include strained siloxanes rings such as the $(SiO)_2$ defect (often referred to as 'S2R'), three-coordinated silicon and non-bridging oxygen sites (R≡Si−O$^{\cdot}$ 'NBO'). Nonbridging oxygen sites are commonly observed in amorphous silica after light irradiation, as evidenced by Electron Spin Resonance measurements [123]. However the radical formed on irradiation readily accept an electron to complete their outer-shell forming silanolate groups, meaning that when modelling the silica-water interface, they are often simply treated as silanolate groups [123].

3.3.2. Surface Charge Modelling

When oxide surfaces are immersed in water, chemical reactions occur which result in the formation of a surface charge via reactions with hydroxide and hydronium ions. These are either (a), already present in water (pure water has a pH of approximately 7 at room temperature, and from the definition of pH this means that the concentration of hydronium ions and hydroxide ions of $1 \times 10^{-7}\,\mathrm{mol\,dm^{-3}}$ or (b), formed due to surface-induced breaking of neutral water molecules. Silanols can be neutral (Figure 3.4), protonated (Si-OH_2^+) or deprotonated (Si-O^-, 'silanolate') and it is these functional groups that determine this charge [124, 125]. The pH is the primary charge determining mechanism for oxide surfaces [126], with electrolyte effects having a measurable but less significant effect on the net charge of the oxide surface [127].

Deprotonation of silanol groups is thought to be the primary charge determining mechanism for silica [124, 125], and also governs dissolution rates (see Section 3.3.3.4) and has direct relevance to biosensing because the negative charges affect the binding of ions and molecules [128]. In order to model the charging process, the most common approach utilises pK_a values (Equation 3.9) to quantify the equilibrium acidity of functional groups at the silica surface. In order to describe the ion adsorption processes and acid-base properties of oxides 'surface complexation modelling' is often used. In these models, both theoretical models of the electrical double layer (similar or identical to those introduced in Section 3.2.2) and chemical equations to describe the reactions at the surface

are combined to describe empirical data such as proton-titration curves. These models have a large number of parameters which are often determined by constraining them to the values that provide the best fit to experimental data. Surface complexation models can be used to estimate the pK_a values at the surface.

$$pK_a = -\log(K_a) = \text{-log}\left(\frac{[A^-][H^+]}{[HA]}\right). \tag{3.9}$$

In Section 3.3.2.1 the surface complexation modelling is explained in more detail and, in Section 3.3.2.2, values of the acid-base dissociation constants at the silica surface are introduced in the context of their measured (and simulated) pK_a values; the assignment of these values has proved to be controversial area of research for silica, compared to other oxide surfaces.

3.3.2.1. Surface Complexation Modelling

Surface complexation models (SCMs), also called site binding models (SBMs) [129], are the traditional method used to simulate acid-base titration properties, or to model the degree of sorption of ions/solute as a function of pH, solute concentration and ionic strength. Work in this field began as far back as the 1950's using simple mass law arguments [130] and, subsequently, as the importance of surface charge in modelling titration processes became more apparent, incorporating these ideas into what are now known as surface complexation models.

A surface complexation model is a model of the electrical double layer which gives a molecular description of adsorption phenomena at equilibrium. An electrical double layer model, similar or identical to that already presented in Section 3.2.2, is coupled with a description of the acid-base reactions at the surface and ion-complexation reactions. In order to model the acid-base properties, two models of the chemical equilibria are often considered: the 1-pK (Equation 3.10) and the 2-pK models (Equation 3.11 & Equation 3.12). In the following chemical equations, the term 'S' is used to represent a metal (or metalloid) species from a metal oxide (e.g. Si in SiO_2, Al in Al_2O_3, Ti in TiO_2 etc.).

1-pK model:

$$SOH^{-1/2} + H^+ \rightleftarrows SOH_2^{+1/2} \tag{3.10}$$

The principle of this model is that only one ionisable site is represented explicitly, and that binding of a proton increases the charge of the system by one positive unit. Physical interpretation of this mechanism directly to atomic mechanisms are rare because these models are primarily used to predict macroscopic surface charge, however an example interpretation could be $SO^- + H^+ \rightleftarrows SOH$ or $(2SOH)^- + 2H^+ \rightleftarrows (2SOH_2)^+$.

2 pK model:

$$\text{Si-OH} + H^+ \rightleftarrows \text{Si-OH}_2^+ \tag{3.11}$$

$$\text{Si-OH} \rightleftarrows SiO^- + H^+ \tag{3.12}$$

Borkovec (1994) [131] highlighted how both these models are simply approximate solutions to the many-body problem of proton adsorption at the oxide/electrolyte interface. The 2-pK model should be interpreted as between a pair of neighbouring ionizable groups, as opposed to a single site being consecutively protonated, as had often been assumed [131]. There are arguments in favour of each of the 1-pK or 2-pK models respectively [132], however the mean field approximation inherent in the 1-pK model is often sufficient to fit the data for most ionisable water-solid systems [131].

Surface complexation models represent an extensive field, and the reader is referred to textbooks such as those by Goldberg [133] and Lutzenkirchin [134] for a more detailed review, however, a brief outline will be given here.

Initial models considered a Stern-like model of the surface, such as the constant capacitance model (CCM) [135], whereas later models incorporated the double layer in the form of the diffuse double layer model (DDLM) [136] or the triple layer model (TLM) [137]. All three of these models are sometimes referred to as 'classic 2-pK models' because two-step protonation of a singly coordinated surface site is utilised (See Equation 3.11 and Equation 3.12). Later models, such as the multisite complexation model (MUSIC) [138], and the subsequent charge-distribution multisite complexation model [139] take into account the coordination environment of the surface, which can utilise either the 1-pK or 2-pK scheme, depending upon the implementation.

The term 'inner-sphere complex' is used in this field to describe adsorbed species with no intermediate water. The constant capacitance model and diffuse double layer model both represent inner-sphere complexes as a single surface plane, but the diffuse double layer model includes a diffuse layer extending into solution. In the triple layer model, as in the constant capacitance model and diffuse double layer models, inner-sphere complexes are also modelled at the surface but there is an intermediate range between the surface and the bulk solution, whereby outer-sphere complexes can form. Multisite complexation models use bond valence-based arguments and surface structural information in order to incorporate preferential binding to certain chemical environments at the surface. It is based on electrostatic arguments related to Pauling bond strengths, but does not explicitly account for surface molecular geometry and structure. [133]

The surface site density (e.g. silanol density, in the case of silica) is a key parameter and can be determined experimentally by a range of techniques but the results can vary by an order of magnitude [32]. This variability can originate from differences in the surface chemistry between different oxide preparations, but also is a result of the difficulty of accurately measuring this property with currently available experimental techniques. This variability presents a major limitation in Surface Complexation modelling, because the results are highly sensitive to the surface site density. Proton titration data, in which a high-surface area of oxide is titrated with a known concentration of acid or base [140]., is most commonly used to estimate the other parameters of the model. The values of the parameters can differ depending on the choice of method used for their determination from experimental data [141].

Surface complexation models have been used to fit the experimental data for charge density of silica as a function of both pH and NaCl concentration [142]. When using bond valence techniques, such as the multisite complexation model model, there is an assumption that $Si-OH$ near SiO^- groups will be at a higher pK_a due to electrostatic repulsion from the SiO^- [143]. This may be an oversimplification of the underlying physics, as *ab initio* molecular dynamics studies suggest that deprotonated groups can migrate across the surface [144].

3.3.2.2. Acid-base (pK_a) Properties of Silica

The traditional method of studying the acid-base properties of an oxide is to perform a proton titration in which sequentially small quantities of acid/base are added to a colloidal sample of the oxide, and the change in pH is measured after each addition [140]. This technique can provide information on the net surface charge, but requires high sample surface areas (e.g. colloids) and cannot provide information on the individual chemical equilibria or structuring at the surface. Some of the most compelling experimental evidence towards silica surface acidity and the structure of the silica-water interface originated from sum frequency generation (SFG) and second harmonic generation (SHG) measurements. The technique can provide measurement of the polarisation and electric field at the

interface, and a discussion of the theory behind these measurements is presented in Appendix B. A key limitation of this technique is that the region defined as the 'interface' (non-centrosymmetric chemical environment) is not always clear, and so it not trivial to map response onto its chemical origin using this technique alone.

The work of Ong et al. provided an important result in the field of silica-water chemistry. In their work, they measured the second harmonic generation response of silica over a range of pH values. Their results are presented in Figure 3.5 [145] and shows an increase in the surface-harmonic electric field with increasing pH. The increasing pH increases both charging and water polarisation resulting in an increased second harmonic generation response [146].

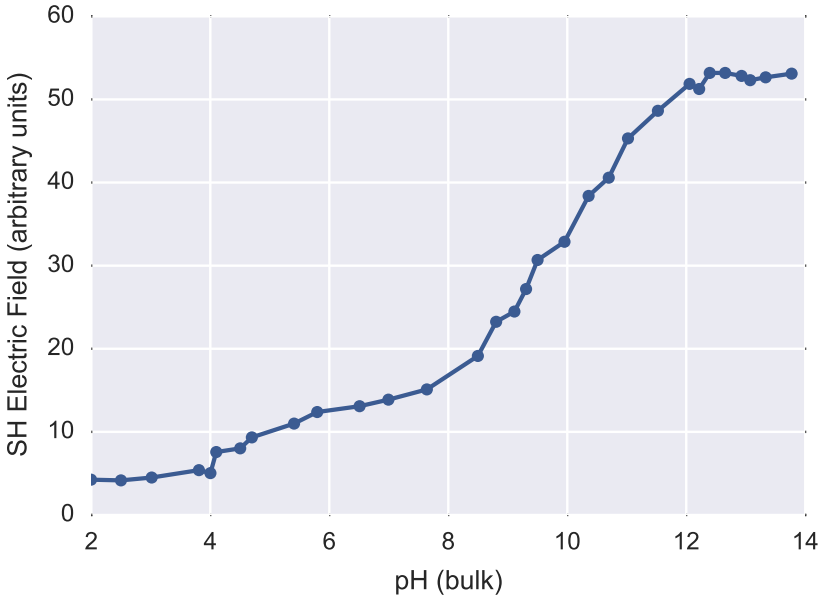

Figure 3.5.: Second harmonic generation electric field response on fused silica as a function of solution pH. The incoming beam was operated at 600 nm, 67° from the interface normal and the reflected SH beam is detected at 300 nm. Data points extracted from Ong et al. [145] and linear interpolation (solid lines) added as a visual guide.

By varying temperature and electrolyte concentration, Ong et al. showed that the observed signal showed a good theoretical fit to a model incorporating surface charge-induced polarisation effects. This therefore provides evidence for polarisation of water at the interface [145]. Ong et al. also argued that second harmonic generation can be used to directly measure the surface potential..

For silica-surfaces, the assignment of pK_a values has proved to be a highly controversial topic. Whilst historically it was thought that silica exhibited a single pK_a based on titration studies [32], the aforementioned paper by Ong et al. suggested that silica has two distinct pK_a values; 19% of silanols with a pK_{a1} of 4.5 and 81% with a pK_{a2} of 8.5 [145]. To obtain these values they fitted a constant capacitance model (Section 3.3.2.1) to their Surface Harmonic Generation data, and found that their data could best be accounted for by introducing two distinct pK_a values at the surface.

Further studies have suggested a pK_{a1} and pK_{a2} of 3 ± 1 and 7 ± 1 respectively [138, 147], and these are generally accepted. Cross-polarised magic angle spinning (CP-MAS) nuclear magnetic resonance spectroscopy [148], fluorescence microscopy [149] and evanescent wave cavity ring-down spectroscopy [150–152] have provided further evidence for the existence of two distinct pK_a values at the surface. It therefore seems likely that the historically reported single pK_a [153] may be a result of being performed at too low resolution to resolve both pK_a values.

The physical explanation for the two pK_a values remains an open question. An X-ray photoelectron

spectroscopy study by Duval et al. supported the existence of a two-stage protonation process (SiO^-, Si-OH and Si-OH_2^+) as in the 2-pK_a model [154]. However using a constant capacitance model (Section 3.3.2.1) they assigned pK_{a1} and pK_{a2} quite different to those generally reported with a pK_{a1} and pK_{a2} of -1 and 4 (note that, by comparison, a silica monomer pK_a is 9.8). Their key results are shown in Figure 3.6 [154]. The work of Duval et al. represents one of the few experimental techniques theoretically capable of quantifying the concentration of surface groups as a function of pH. The *ab initio* simulations of Leung et al. [144] and Rustad [155] have suggested that the silonium ion (Si-OH_2^+) is unlikely to have a pK_a greater than one. As a result of this pK_a, the silonium ion is expected to be in negligible concentrations at pH values relevant to biosensing (pH 6-9).

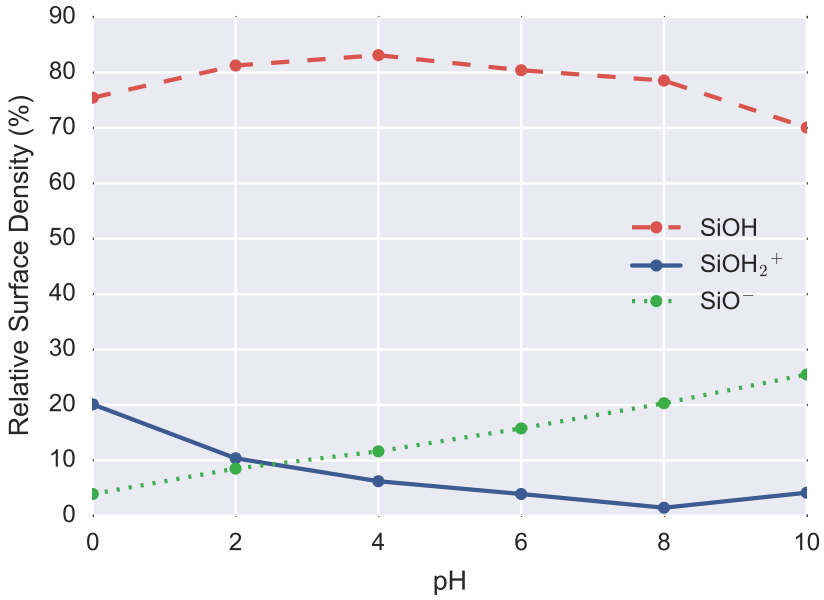

Figure 3.6.: Variation in relative density of different silica surface silanol species for Quartz, shown as a function of bulk pH. Calculated by deconvolution of measured X-ray photoelectron spectroscopy data. Data points extracted and replotted from [154].

The conflicting pK_a values determined by X-ray photoelectron spectroscopy and second harmonic generation serve to demonstrate the lack of understanding of this interface. In an attempt to explain the two different pK_a values observed in second harmonic generation measurements, some have suggested that it may a result of inter-silanol hydrogen bonding [156]. In opposition to this hypothesis, the *ab initio* simulations of Leung et al showed that both Q^2 and Q^3 (geminal/vicinal and isolated) silanols showed a pK_a greater than 7. They tentatively suggest that the highly acidic pK_a values (pK_a ~4.5) groups observed in experiment may be due to strained silica rings at the surface but they also note that such ring-systems are known to be highly unstable in water or moist air [144]. A further popular explanation for the existence of two unique pK_a values at the surface is that the more acidic sites have weakly hydrogen-bonded water associated with them, as presented schematically in Figure 3.7. This explanation is supported by the experiments of Ostroverkhov et al. [157] and the aforementioned simulations of Leung et al. which showed a pK_a which increased with the addition of more layers of water on the surface [144].

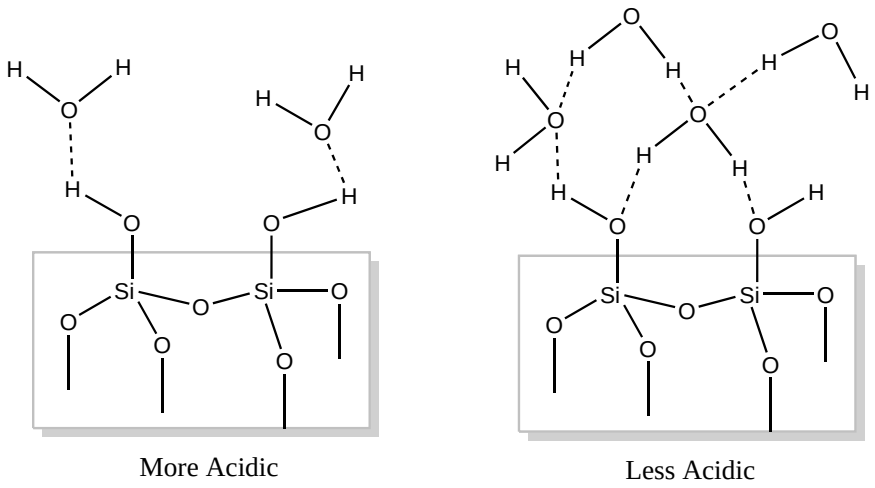

Figure 3.7.: A proposed explanation for the two unique pK_a values inferred from second harmonic generation response of Ong et al. [145, 146], in which silanols associated with weakly hydrogen-bonded waters are assigned a pK_a of ~4-5 and those with strongly associated hydrogen bonds a pK_a of ~9.

3.3.3. Processes at the Silica-Water Interface

The silica-water interface demonstrates a variety of complex chemical and physical processes, which span many time-scales. This thesis covers atomistic simulations of the silica-water interface and an appreciation of the relevant processes occurring at the surface is required for accurate set-up and interpretation of these simulations. For a detailed discussion of the molecular structure of the silica-water interface is in the extensive review by Rimola et al. [32]. In this section, a summary of many of the important processes at the silica water interface are outlined in Table 3.1, and these processes are described in detail in the following sections.

3.3.3.1. Protonation and Deprotonation

Protonation and deprotonation can be caused by interaction with an excess of protons (hydronium ions) and deficit of protons (hydroxide ions) respectively. For all oxides, this is the primary mechanism responsible for the experimentally observed changes in surface charge with varying pH [126]. A hydronium ion will readily donate its proton to a silanolate group to form a silanol because this produces a system with lower enthalpy, as shown in Table 3.1 reaction (1) from right hand side (RHS) to left hand side (LHS). In principle, a hydronium ion could also donate its proton to a silanol as shown in Table 3.1 equation (2), however experiments suggest (Section 3.3.2.2) that this reaction is not common for pH values $\gtrsim 1$ and therefore can be disregarded for this discussion. Similarly a hydroxide ion will readily deprotonate a silanol group to form a silanolate group as this produces a system with lower enthalpy, as shown in Table 3.1 reaction (3) RHS to LHS. These reactions can occur either as a direct collision between the reagents, or more likely via a hydrogen bonded network of water molecules. If the reactions occurs such that it involves H_3O^+ transport (protons transport) through a hydrogen-bonded network of water then it may be referred to as the Grotthuss mechanism [172]. If the reaction occurs such that it involves OH^- transport through a hydrogen bonded network of water then it has been described by Riccardi et al. as the 'Proton holes' mechanism [163]. Finally, the aforementioned reactions can proceed in the reverse direction whereby local fluctuations in the electric field combined with thermal motion can cause hydrolysis of water, thus reaching a system which is higher energy based on ground-state DFT calculations [144, 158–160, 162]. The rare-event nature of these 'reversed' reactions means that, due to computational expense, they cannot be simulated

Process	Types	Time-scales	Description	References
Protonation and Deprotonation	Due to collision of SiOH with H_3O^+, OH^- or water.	Time-scale to lower enthalpy state: Limited by rate of reorientation of water (picoseconds between $\lesssim$1 nm reagents) [158] time-scale to higher enthalpy state: open research question.	(1) $SiOH + H_2O \rightleftharpoons SiO^- + H_3O^+$ (2) $SiOH + H_3O^+ \rightleftharpoons SiOH_2{}^+ + H_2O$ (3) $SiO^{-+}H_2O \rightleftharpoons SiOH + OH^-$ The left hand side of each of these equations is the lower enthalpy state based on ground-state DFT cluster models [158–160]	Sim: [144, 158–163]
Intra-surface proton migration	-	Limited by rate of water reorientation (picoseconds between $\lesssim$1 nm groups)	Protons may be able to migrate across the surface, leading to the apparent motion of silanolate groups.	Expt:[164] Sim:[144]
Non-dissociative water adsorption, (Physisorption/interfacial water)	-	Picoseconds to surface equilibration	Second harmonic generation and vibrational sum frequency generation spectroscopy measurements indicate water is hydrogen bonded to the surface, and polarisation increases with pH.	Expt:[145, 157, 165, 166] Sim:[167]
Thermal dehydroxylation (condensation polymerisation)	-	Hours to days to surface equilibration	(4) $2\,Si{-}OH \longrightarrow Si{-}O{-}Si + H_2O$ Linear increase in dehydroxylation from treatment at 200°C with a turning point at 400°C at which the rate decreases. This is attributed to the removal of vicinal silanols. At 900°C the surface is fully dehydroxylated.	Expt:[121, 168] Sim:[169][170]
Dissociative water adsorption (chemisorption)	Aqueous re-hydroxylation and silica dissolution	Hours to days to surface equilibration.	Reverse of (4) $Si{-}O{-}Si + H_2O \longrightarrow 2\,Si{-}OH$ The surface siloxane bonds can be hydrolysed by water, resulting in dissolution of the surface and rehydroxylation.	Expt:[121] Sim:[171]

Table 3.1.: Summary of processes occurring at the Silica/Water interface. 'Sim'=Simulation, 'Expt.'=Experimental

using current *ab initio* techniques that proceed linearly with time and these reactions are poorly characterised.

In view of the similarities between the hydroxyl groups of silanols (Si−OH) and water (H−OH), silica-water chemistry has strong parallels with the chemistry of water, and the latter has received a lot more detailed attention. For example, the analogous 'reversed' (LHS to RHS) reaction for Table 3.1 (1) for water would be [173]:

$$H_2O + H_2O \underset{\text{recombination}}{\overset{\text{autoionisation}}{\rightleftharpoons}} OH^- + H_3O^+$$

This mechanism is discussed in more detail along with other features of water chemistry in Section 3.3.4.

3.3.3.2. Intrasurface Migration

The *ab initio* molecular dynamics simulations of Leung et al. [144] showed that protons can 'hop' from one silanol to nearby deprotonated groups either via direct proton transfer or through two to three mediating water molecules. As a result of proton 'hopping', the deprotonated groups effectively migrate across the surface. These simulations demonstrated migration of a deprotonated group over ~5 Å and the entire migration occurring process over ~2 ps. The variable-temperature NMR study of Kinney et al. proposed that a slight narrowing of the spectrum on cooling could be a result of a chemical exchange process amongst sites on the silica surface but stated that the results were inconclusive as they may instead be due to a reduction in motional broadening [164]. In the field of hydrogen fuel cell research, silica gels are under research as they have been shown to be capable of shuttling proton under an applied electric field [174–176].

3.3.3.3. Non-dissociative Water Adsorption (Physisorption)

It is well established that water can physisorb to the surface of amorphous silica. The hydrophilicity of some silica surfaces can be explained by *ab initio* studies which have shown that the adsorption energy of water can be greater than the heat of liquifaction [177]. Some silica surfaces exhibit a hydrophobic nature, in which case siloxane bridges are often invoked to explain this phenomenon because these functional groups are hydrophohic [122] .

As introduced in Section 3.3.2.2, second harmonic generation and vibrational sum frequency generation spectroscopy (VSFG) studies have shown that water is polarised at the silica-water interface [145, 157, 165, 166]. Sum frequency generation measurements show two distinct peaks in their spectrum, and therefore have demonstrated two types of physisorbed water at the silica/water interface which, in spectroscopy terminology, are termed 'liquid-like' or 'ice-like' based on the measured O−H bond vibration frequency. There is still some debate over the explanation for the origin of these peaks. One popular explanation is that the second harmonic generation/sum frequency generation spectra is due to water near the surface being oriented by a strong hydrogen bonding structure [157, 166],which is modulated with changes in pH. An alternative explanation is that the 'ice-like' peaks are due to water distant from the surface being oriented by the electric field [178].

Recent work in the field includes the work of Ostroverkhov et al. [157], who used phase-sensitive sum frequency generation to provide additional information on the orientation of the water at the surface. Their study supported the existence of multiple different surface sites with differing pK_a values and attribute the acidity of these values to the degree of ordering of water hydrogen bonds around each site. They also showed that with increasing pH, the orientation of water reverses from oxygen pointing towards the surface to hydrogen pointing towards the surface, which is consistent with increasing deprotonation leads to an increasingly negative surface charge [157]. The DFT-Molecular Dynamics study of Gaigeot et al. supports this interpretation of the vibrational spectra, demonstrating that the

orientation of the water hydrogen bonds to the surface can be used to explain the vibrational sum frequency generation spectroscopy results [167].

3.3.3.4. Dissolution

A large body of publications from the geochemical community has improved understanding of the mechanisms and rate of dissolution of silica. These findings have relevance to biosensing, as dissolution of the oxide surface of FET-sensors will result in surface properties changing over time, and therefore might contribute to drift in the sensor signal, or to transient responses.

The varied surface structure of silica, which is dependent upon its preparation, means that experimental measurements of the rate of dissolution can deviate significantly in their magnitudes. To illustrate this, Dove et al. [179, 180] have investigated the Quartz surface, and using data from 79 dissolution rate measurements from a range of scientists, they made a model to predict the rate of dissolution which is valid from a pH 2-13 and of NaCl concentration 0–0.2 $\mathrm{mol\,dm^{-3}}$. Their rate model utilised a surface complexation model to predict the surface-site species concentrations and used this in a simple chemical rate equation [179]. They predicted dissolution in a range of between $1 \times 10^{-13}\,\mathrm{molm^{-2}s^{-1}}$ to $1 \times 10^{-10}\,\mathrm{molm^{-2}s^{-1}}$, which equates to between 0.00021 $\mathrm{molecules\,nm^{-2}hr^{-1}}$ and 0.21 $\mathrm{molecules\,nm^{-2}hr^{-1}}$.

A combined sum-frequency generation and atomic-force microscopy study of Li and Bandara compared the effect of nanopure water with that of a pH 10 sodium hydroxide solution upon a quartz surface. Within 17 days they found that the surface dissolution had led to an amorphous surface. They found that the basic solution actually led to a smoother surface than the pure water system and hypothesised that hydroxide ions were creating either an electrostatic or chemical protective coating [181]. Perhaps of more relevance to biosensor design, a recent review of dissolution of elemental silicon (Si) exposed to aqueous electrolyte states that the silicon (Si) can be dissolved rapidly (nanometres per day) by an aqueous electrolyte solution [182].

The chemical mechanism of silica dissolution in water is generally accepted to be via hydrolysis of the siloxane bridges present at the surface, though the precise mechanism(s) and the role of hydroxide and hydronium ions remain unclear and an active area of research. Based on the observation that there is little change in dissolution rates as pH from pH 1.4 to pH 6, Knauss et al. infer that the role of hydroxide and hydronium ions is negligible in this region. Beyond pH 6 they observed increasing dissolution proportional to the reciprocal square root of the activity of protons.. The suggested that the different rate at higher pH may be the result of a different mechanism involving hydroxide and hydronium ions [183, 184].

Various *ab initio* studies have attempted to understand the mechanism of silica dissolution [184–187]. Nangia et al. [188] used DFT calculations to determine the transition state for dissolution via hydrolysis of siloxane bridges. They compared protonated, neutral and deprotonated model clusters and, using Transition State Theory [189], they produced a rate model which showed good agreement with the aforementioned model of Dove et al. [179].

3.3.4. Dynamics of Pure Water

As introduced in Section 3.3.2, proton transfer from silanol groups to bulk water is thought to be the primary charge determining mechanism for silica [124, 125]. In order to accurately model this phenomenon, an understanding of proton transport in bulk water is therefore also required, which will be addressed in this section. Not only this, but because water molecules possess similar chemical

functionality to the silica oxide surface silanol groups, it is likely that proton transfer dynamics are highly analogous.

3.3.4.1. Autoionisation

Water autoionises spontaneously, resulting in formation of hydronium (H_3O^+) and hydroxide ions (OH^-) [190]. Experimental studies still struggle to observe this process due to their extremely rapid occurrence. For example, in pure water exchange of protons with H^+or OH^- will occur over 1000 times per second for each water molecule [173], making simulation particularly useful in this field. To investigate the autoionisation process, Eigen and Maeyer used a pulsed applied electric field to perturb the equilibrium concentrations of H^+ and OH^- and based on these results, they inferred that a single water molecule has a mean apparent lifetime of about 11 hours before it will dissociate into OH^- and H_3O^+ [173] as a result of local fluctuations in the electric field due to thermal motion of the water.

The *ab initio* molecular dynamics simulations of Geissler et al. [190] suggest that many short-lived (~150 fs) charge-separated states may be present. The formation of a metastable charge-separated system requires a charge separation of at least 6 Å [191], from which it has been theorised that the pair of ions may diffuse away from each other with relative ease [173]. Geissler et al. used path-integral *ab initio* Car-Parrinello Molecular Dynamics (CPMD) and observed proton migration from H_3O^+ to an OH^- several molecules away on an approximately 100 fs time-scale, provided that there was a hydrogen-bonded chain of water present, termed a 'water wire' [190, 192]. If there was no water wire, they observed greater than 1 ps time-scales, consistent with the time-scale of water reorientation. [193].

3.3.4.2. Proton Migration Time-Scales

The lifetime of H_3O^+ in water has been investigated using a reactive force field by Lockwood and Garofalini [194]. They observed a small amount of autodissociation and recombination ('proton rattling') on a 100 fs time-scale, and excluded this from their calculations by excluding $OH^- + H_3O^+$ recombination reactions and considering only $H^+ + H_2O$ reactions. They showed that severing of water wires led to hydronium ions with a roughly picosecond lifetime, and demonstrated that proton migration over long time-scales (>100 ps) can be attributed to this process. Similar conclusions were found in the investigation of proton-transport performed by Lee et al. using a reactive force field [195].

3.3.4.3. Hydronium Transport

Protons are known to have an anomalously high mobility in bulk liquid water, explanations for which began even back in the 19th century with the theory proposed by Theodor Grotthuss [172]. Protons are now known to transport via a conduction mechanism, sometimes referred to within the literature as 'structural diffusion', but also known as the proton-hopping or the Grotthuss mechanism [172]. This mechanism is anomalously fast compared to classical diffusion (sometimes called 'vehicular diffusion' in this context) and involves the transfer of protons along water wires molecules like a 'bucket line'. The Grotthuss mechanism is about an order of magnitude faster than would be expected via diffusion for a particle the size of a proton, and is limited by the rate of reorientation of the water molecules [196]. Despite a huge amount of both experimental [197] and theoretical work [198], the precise mechanism of proton migration is still debated. It is generally thought that protons are arranged into either, or both, of the 'Eigen cation' $H_9O_4{}^+$ and the 'Zundel cation' $H_5O_2{}^+$, and that migration occurs by interconversion of protons between these clusters.

Marx et al. used *ab initio* simulations incorporating both thermal- and quantum- fluctuations to investigate proton diffusion in pure water [199]. They concluded that the rate of diffusion is determined by thermally-induced hydrogen-bond breaking in the second solvation shell, and that Transition State Theory does not apply because there is no well-defined transition state. They showed that the barrier to proton migration in pure water is vanishingly small at $\lesssim 0.15\,\mathrm{kcal\,mol^{-1}}$ ($k_\mathrm{b}T \approx 0.59\,\mathrm{kcal\,mol^{-1}}$ at 300 K) and that Zundel and Eigen cations are only limiting structures, with numerous structures in between. Finally, they showed that, at room temperature, the effect of quantum fluctuations is not qualitatively significant. Similar studies by Schmitt et al. have shown that, on average, a proton will 'hop' approximately once every two picoseconds [198] .

3.3.4.4. Hydroxide Transport

The mechanism of hydroxide transport is less well understood and characterised than hydronium transport. However, it is known that hydronium transport is approximately two times faster than hydroxide transport due to it occurring via a different mechanism [195, 200, 201]. The mechanism of hydroxide transport has been evidenced to occur via an intermediate cluster involving a hyper-coordinated hydroxide ion, with four water molecules hydrogen bonded to it. This involves a greater degree of reorientation than hydronium transport, which would explain the reduced transport rate of hydroxide ions. This has been supported by neutron diffraction data [202] and *ab initio* simulations [195, 200, 201], but the precise nature of the transport remains an active area of research.

Riccardi et al. suggested that hydroxyl-mediated proton-transfer mechanisms, which they termed 'proton hole' transport, are often overlooked [163]. They suggest that this may perhaps be due to the success of the Grotthuss mechanism at explaining proton-transfer without the need for hydroxyl ions. Using pK_a values they argued that, when the pK_a of both the donor and the acceptor are greater than 7, a hydroxide dominated 'proton hole' mechanism is in fact more energetically favourable than the Grotthuss mechanism. Tuckerman et al. suggest that the 'proton holes' mechanism has received far less attention than the Grotthuss mechanism as a result of the (erroneous) century-old assumption that the hydrated OH^- transport mechanism can be inferred from that of an excess proton by simply reversing the hydrogen-bonding polarities [200].

3.3.5. Summary of Silica-Water Interfacial Processes

Based on the previous sections on silica and water, a summary of the previously presented processes occurring at the silica-water interlace is presented here, with an emphasis on the surface charge, which is an important property for modelling FET-sensors.

The primary factor in determining the surface charge of silica in aqueous solution is its pH . Acid-base equilibria reactions of the silanol groups at the surface with H_3O^+ and OH^- result in protonation and deprotonation reactions, respectively. At very low pH (< 2), a small concentration of $\mathrm{Si{-}OH_2}^+$ is expected at the surface but at pH relevant to biosensing ($6 \lesssim \mathrm{pH} \lesssim 9$), the concentration of $\mathrm{Si{-}OH_2}^+$ is negligible. The Point of Zero Charge of silica is ~2. Above pH ~2 the surface is negative, as evidenced by zeta-potential measurements [154, 203]. Proton titration data shows a gradual increase in surface charge with increasing pH [204]. There exists compelling evidence (second harmonic generation, nuclear magnetic resonance spectrosopy, Florescence and X-ray photoelectron spectroscopy) for the existence of two distinct $\mathrm{pK_a}$ values for silanols at the surface [32]. Silica dissolves much more rapidly at high pH, which makes the surface structure increasingly complicated and difficult to predict at high pH.

The study of pH-dependent protonation-deprotonation has almost exclusively been in the context of equilibrium thermodynamic models such as surface complexation models. These have the advantage of

being easily compared and parameterised to readily available equilibrium experimental measurements such as pH, surface site density and surface charge. In contrast to equilibrium thermodynamic models, little experimental data exists showing non-equilibrium measurements of pH, surface site density and surface charge. Kinetic models which incorporate the microscopic details are rare.

A key challenge to commercialisation of current FET-sensors is due to undesirable drift and noise in the drain current response. The drift in drain current response has been associated with chemical modification of the oxide layer [205], and so an improved understanding of the kinetics of interfacial reactions is crucial, whilst noise in the response is partly due to dynamic fluctuations in the concentration of ions at the interface [33, 80].

3.4. Atomistic Simulation of Silica

As atomistic simulations of the silica-water interface are an important part of Chapter 4 and Chapter 7 in this thesis, in this section, relevant background to atomistic modelling of silica interfaces is introduced. A general consideration in any atomistic modelling is that the specific choice of model is a trade-off between accuracy and computational expense.

Many FET-sensors, such as those generated by Hakim et al. [58], have a surface which consists of silicon oxide grown by thermal oxidation of silicon. Thermal treatment of crystalline silica in air produces an amorphous silica structure, with some crystalline regions close to the substrate [206]. Exposure of crystalline silica (e.g. Quartz) to water has been shown to produce amorphous silica over time [181]. Given this evidence, an accurate model of silica for application in FET-sensors should capture important properties of amorphous silica.

An important experimental observable of silica is the density of hydroxyl groups on the surface because this quantifies the surface hydrophilicity and surface structure whilst also being strongly related to its charging behaviour due to protonation-deprotonation reactions. Despite the complicated surface structure of amorphous silica, it has been shown by Zhuravlev [121, 168] that the average number of Si-OH groups per square nanometre for a fully hydroxylated surface is a physiochemical constant of approximately 4.6 to 4.9 $\mathrm{OH\,nm^{-2}}$ which is independent of the procedure used to prepare the sample. The hydroxylation degree depends in a non-linear fashion upon the pre-treatment conditions and temperature. It has been reported by Zhuravlev that if thermal silica is pre-treated at 900^{o}C dehydroxylation occurs forming hydrophobic siloxanes down to roughly 3 terminal silanols [121]. When water is introduced to the surface then rehydroxylation occurs, though for pre-treatment temperatures above 400^{o}C this is a slow process [207]. Given these findings, an atomistic model of the amorphous silica-water interface should have a surface hydroxyl density in the region of approximately 5 $\mathrm{OH\,nm^{-2}}$.

Establishing molecular dynamics parameters suitable for the simulation of nanodevices [119] and silica interacting with biomolecules [208–210] are a current area of research. Multi-scale attempts to study the complex interface of water and silica have been attempted by Cheng et al. [211, 212], who have combined Density Functional Theory simulations, classical Molecular Dynamics simulations and continuum methods to model surface hydroxylation processes and bulk silica nanowire stress/strain dynamics.

Due to the range of surfaces possible and the many unknowns about the precise structure of silica surfaces, previous *ab initio* studies have either utilised highly idealised models based on small 'clusters' of silanol groups and water molecules [159, 160, 213–215] in isolation, or models based on 3D periodic systems containing 'slabs' of atoms which represent the surface. An example of a 'cluster' and a 'slab' model are illustrated in Figure 3.8.

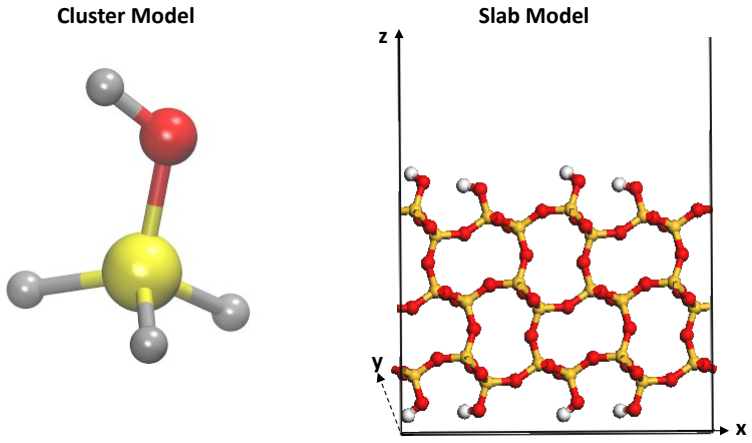

Figure 3.8.: Illustration of an example minimal 'cluster' atomistic model of the silica surface (SiH_3OH) and a 'slab' model of the silica surface (obtained by cutting through the (101) plane of α-cristobalite. Hydrogen is shown as grey or white, oxygen as red and silicon as yellow. Cluster models aim to emulate the surface using a molecule containing a small selection of the atoms. Slab models use periodic boundary conditions in the plane of the surface (x-y) to emulate the bulk-like properties of the surface. 3D periodic boundaries are often utilised, and therefore a 'vacuum' layer is inserted between periodic images in the z-direction.

Slab models can never be truly amorphous due to the periodic boundary conditions, but disorder can be represented using a large unit cell with disorder in the structure of the unit cell. Calculations on amorphous/disordered surface slabs require very large simulation cells and are very computationally expensive, and therefore with only a few exceptions [177, 216–218], have only been attempted using molecular mechanics [119, 219]. Past *ab initio* studies of silica tend to focus on slab models constructed via surface cleavage from highly ordered crystalline silica such as Cristobalite [169, 170, 220–222], Edingtonite [223–226] or Quartz [218, 227] and other silicates [228, 229]. The highly ordered surfaces facilitate smaller unit-cells and therefore lower computational expense, with the disadvantage of being less representative of the heterogeneity of amorphous surfaces.

When modelling silica using a slab model, after cutting/cleaving the crystal along a plane, the generated slabs often cut through chemical bonds and it is therefore common practice to 'passivate' the dangling bonds with hydrogen or hydroxyl groups. In reality, upon exposure to air, freshly cleaved silica is expected to react with moisture in the air to form hydroxyl groups, therefore the practice of passivating the surface is physically-motivated as well as practically-motivated for this system. As electrostatic interactions are typically evaluated using periodic boundary conditions such as the Ewald sum [110], the slab needs to be separated from its periodic image normal to the surface by a 'vacuum layer' to minimise unphysical periodic interactions in the out-of-plane direction, as shown in Figure 3.8. The thickness of this layer is chosen so as to be the minimal size required to produce negligible interactions between slabs.

4. Charging at the Silica-Water Interface

4.1. Chapter Introduction

In this chapter, *ab initio* calculations are presented which investigate surface-charging mechanisms and energetics at the oxide-water interface. Surface charge is a key factor in determining the response of FET-sensors because it generates a detectable change in the electric field at the interface. The importance of this phenomenon is evident from the prevalent use of FET-sensors to detect changes in pH, whereby acid-base reactions change the surface charge [21, 55]. Surface charging is also fundamental to a range of phenomena such as dissolution rates [179, 180, 230] and the surface adsorption of ions and molecules [128, 231]. Given that the silica-water interface is one of the most common interfaces on the planet and that silica is the most common oxide-surface of FET-sensors [232], silica was chosen as the chemical oxide to investigate for this work. The simulation approach of utilising DFT was chosen because it can accurately describe chemical-bond breaking and forming which is vital to describe the relevant chemistry in surface charging. DFT can be used to study dynamics over hundreds of atoms and time-scales of the order of hundreds of picoseconds, which is the time- and length-scale upon which individual protonation-deprotonation reactions occur.

The surface charge of silica in water is primarily determined by protonation and deprotonation reactions of the surface silanol groups with protons and hydroxide ions. Surface charging remains a poorly understood topic in the field of interfacial science and this is particularly the case for silica surfaces in which the acid-base properties of the surface are somewhat controversial (as discussed in Thesis Background Section 3.3.2). If understanding of the surface charging mechanisms and energetics can be improved, then predictive models of the dynamics of surface charging could be made which would provide insight into improved FET-sensor device engineering. For example, given the elementary charge sensitivity of FET-sensors [233], surface charging dynamics likely affect the measured noise. A key limitation to the commercialisation of FET-sensors is due to sundesirable drift in the current response and this has been associated with chemical modification of the oxide layer [205, 234]. With knowledge of the energetics of the transition-state(s) of the reaction, it is possible to use Transition State Theory [189] to predict the kinetics, which would be useful in describing FET-sensor noise. Therefore this was an initial aim of the work presented within this chapter.

In order to accurately model the surface at an atomistic resolution, a careful choice of atomistic model must be made. As discussed in the Background Section 3.4, the silica-water interface is thought to exist as an amorphous material with a density of hydroxyl groups of approximately $5\,\mathrm{nm}^{-2}$. However, for practical reasons, a periodic structure is often used to model the amorphous system. For this work, the chosen model was based upon the molecular structure of the (101) surface-plane generated from a cleavage of α-cristobalite, a polymorph of silica. This surface is attractive from the point of view of modelling an amorphous silica surface because it has a surface density of approximately $5\,\mathrm{OH\,nm}^{-2}$, similar to that in fully hydroxylated silica. Furthermore, α-cristobalite has a bulk density of $2.23\,\mathrm{g\,cm}^{-3}$ [235], close to that of amorphous silica ($2.20\,\mathrm{g\,cm}^{-3}$ [236]). Musso et al. have conducted a series of DFT studies on various silica polymorphs [221, 222, 237], including an investigation of the dynamics of water upon the surface used within this study; however their study did not address surface charging.

In this chapter, the theory of *ab initio* calculations is first outlined and an initial validation study is performed in order to ensure the parameters used in this work can provide accurate and reliable results. The subsequent study investigated the silica-water surface-charging mechanisms and energetics and was published in the Journal of Colloid and Interface Science.

4.2. Background: First Principles Quantum Chemistry Calculations

A detailed introduction to First Principles calculations can be found in standard texts [238, 239]. An introduction to *ab initio* quantum chemistry calculations can also be found in Appendix C. This section provides a brief introduction to Density Functional Theory.

The principle behind *ab initio* calculations is that, given only the atomic numbers and coordinates of atoms in a system, it should be possible to obtain the wavefunction of the system by solving the time-independent Schrödinger equation:

$$\hat{H}\phi = E\phi. \tag{4.1}$$

This simple but powerful equation states that by applying the Hamiltonian operator, $\hat{H}$, to the wavefunction, ϕ, the energy, E, of the wavefunction can be obtained. In practice, such a solution cannot be performed analytically for more than the simplest of systems, yet a variety of approximations can be made in order to make this problem tractable to a numerical solution. The Born-Oppenheimer approximation, in which it is assumed that the nuclear wavefunction can be separated from the electronic wavefunction, is almost ubiquitously utilised:

$$\hat{H}_{\text{elec}}\phi_{\text{elec}} = E_{\text{elec}}\phi_{\text{elec}}. \tag{4.2}$$

With the electronic wavefunction ϕ_{elec}, it is possible to predict many physical and chemical properties of the system, including the charges on each atom, and therefore electrostatic forces. Wavefunction-based approaches to solving Equation 4.2 include Hartree-Fock and Post-Hartree-Fock methods; however these methods scale poorly with increasing numbers of atoms, and therefore are often too computationally expensive for the study of more than a few tens of atoms.

4.2.1. Density Functional Theory

Density Functional Theory (DFT) represents a fundamentally different approach to this problem which is much less computationally expensive than wavefunction-based methods and can often obtain comparable accuracy [240]. The reduced computational cost of DFT, as compared to traditional wavefunction-based methods, results from the problem being reduced to a much lower dimensionality. In wavefunction-based methods, the problem of solving the Schrödinger equation involves, for an N-electron system, integration of $4N$ variables (x, y, z and spin for each N electrons). Instead, DFT solves equations based on the Schrödinger equation (Equation 4.5) in order to determine the electronic density, $n(\mathbf{r})$. The electronic density $n(\mathbf{r})$ can be thought of as the probability of finding any of the N electrons at a particular point in space $\mathbf{r}$. Once $n(\mathbf{r})$ is obtained, physical and chemical properties of the system can be calculated.

Most modern DFT codes are based on the Kohn-Sham formalism, which states that Equation 4.2 can be reformulated in terms of the kinetic energy operator and a set of functionals of the density, as shown in Equation 4.4. An exact functional is known for all but the electron kinetic energy and

electron-electron interactions. In Kohn-Sham DFT, these 'unknown' terms are replaced with the exact functional for hypothetical non-interacting electrons and an additional approximate exchange-correlational functional (Equation 4.3) which aims to correct for 'unknown' interaction terms.

The Kohn-Sham formalism makes the following approximation:

$$E_{\text{kin}}^{\text{exact}} + E_{e-e}^{\text{exact}}[n] = E_{\text{kin}}^{\text{non-inter}} + E_{e-e}^{\text{non-inter}}[n] + E_{xc}^{\text{approx}}[n]. \quad (4.3)$$

In making this approximation, we imagine a fictitious system containing 'non-interacting electrons in a set of i Kohn-Sham orbitals, ϕ_i, with energy ϵ_i. Using Equation 4.2, the full Kohn-Sham equations can thus be written as:

$$(E_{\text{kin}}^{\text{non-inter}} + E_{e-e}^{\text{non-inter}}[n] + E_{e-n}^{\text{exact}}[n] + E_{n-n}^{\text{exact}}[n] + E_{xc}^{\text{approx}}[n])\phi_i(\mathbf{r}) = \epsilon_i\phi_i(\mathbf{r}), \quad (4.4)$$

or more concisely:

$$(-\frac{1}{2}\nabla^2 + V_{\text{KS}}[n](\mathbf{r}))\phi_i(\mathbf{r}) = \epsilon_i\phi_i(\mathbf{r}), \quad (4.5)$$

where $-\frac{\nabla^2}{2}$ is the kinetic energy of the system (in atomic units) and V_{KS} is the sum of the Kohn-Sham functionals. By solving this equation self-consistently ϕ_i is obtained and from this, the density $n(\mathbf{r})$ can be obtained (Equation 4.6). The density can be used to calculate physical properties of interest.

$$n(\mathbf{r}) = \sum_{i=1}^{N} |\phi_i(\mathbf{r})|^2. \quad (4.6)$$

4.2.1.1. Numerical Solutions

In order to solve these equations on a computer, the system is discretised using a basis set expansion for ϕ_i, the choice of basis varying between DFT codes. In many DFT codes, such as CASTEP [241], this is implemented via a plane-wave pseudopotential approach, meaning that a sum of waves are utilised to build a numerical approximation for ϕ_i. The ONETEP DFT code also uses a pseudopotential approach and uses a localised basis set capable of plane-wave accuracy [242].

Plane wave codes often operate on an infinitely periodic system, and use Bloch's theorem in order to reduce the problem to something computationally tractable [241]. In brief, if the nuclei are arranged periodically, then the potential acting on them will also be periodic, and therefore Bloch's theorem states that the density must be periodic. The density is the magnitude of the wavefunction squared, and therefore the density can be written as:

$$n(\mathbf{r} + \mathbf{L}) = n(\mathbf{r}) = |\psi(\mathbf{r})|^2, \quad (4.7)$$

where $\mathbf{L}$ is any lattice vector and $\psi(\mathbf{r})$ represents the wavefunction of a system. As wavefunctions are complex functions, their magnitude is periodic but their phase might not be. The wavefunction can be split into two components, namely the magnitude $u_{\boldsymbol{k}}(\mathbf{r})$, which is fully periodic (i.e. $u_{\boldsymbol{k}}(\mathbf{r})$=$u_{\boldsymbol{k}}(\mathbf{r}+\mathbf{L})$) and an arbitrary phase factor $e^{i\mathbf{kr}}$ which varies over all vectors $\boldsymbol{k}$:

$$\psi_{\boldsymbol{k}}(\mathbf{r}) = u_{\boldsymbol{k}}(\mathbf{r})e^{i\boldsymbol{k}.\boldsymbol{r}}. \quad (4.8)$$

Here $\boldsymbol{k}$ is used to indicate a specific point in reciprocal space, and also as an index to label a particular

corresponding solution. $\boldsymbol{k}$ can take values of:

$$\boldsymbol{k} = \frac{2n\pi}{\boldsymbol{L}},\ n = 0,\ \pm1,\ \pm2,\ ...,\ N,$$

where N is the number of unit cells (which corresponds to a very large number in even microscopic solids). In order to find the electronic density of an infinite periodic system, the density can be integrated over all the $\boldsymbol{k}$ vectors. The significance of this is that the problem becomes computationally tractable by only sampling a subset of the $\boldsymbol{k}$ vectors. This process is known as $\boldsymbol{k}$-point sampling, and is done for each single-particle states of the Kohn-Sham Hamiltonian [243] in Equation 4.5:

$$n(\mathbf{r}) = \int |\phi_{\boldsymbol{k}}(\mathbf{r})|^2 d^3\boldsymbol{k} \approx \sum_{\boldsymbol{k}} |\phi_{\boldsymbol{k}}(\mathbf{r})|^2. \tag{4.9}$$

In the CASTEP software, each $\phi_k(\mathbf{r})$ is required to be orthonormal to each other and extend over the entire simulation cell, which results in a computational cost which scales cubically with system size. In the ONETEP software, linear scaling of computational cost with system size is achieved by using a different approach, instead using a localised non-orthogonal basis set composed of Non-orthogonal Generalized Wannier Functions (NGWFs) in a pseudopotentials approach which is capable of plane-wave accuracy [243]. Each NGWF is themselves composed of periodic cardinal sine (psinc) functions [243]. Before a ONETEP calculation is performed, radii of the NWGFs are defined which determine to what extent the wavefunctions are localised around the atoms.

4.2.1.2. Pseudopotentials

In both the ONETEP and CASTEP codes, the pseudopotential approximation is used. The principle behind this approximation is that the regions where the wavefunction changes its magnitude most rapidly are the regions that are most computationally expensive to model. These regions are near the core of the atoms and because the wavefunction in these regions have little effect on their chemical properties, a 'pseudopotential' can be defined which has much less variation near the core, but remains identical to the full electron wavefunction for the valence electrons. A further related approximation that is common in DFT codes is the 'frozen core' approximation, which assumes that the core electrons do not participate in bonding.

Two common types of pseudopotential are the 'norm-conserving' and 'Ultrasoft Pseudopotentials' (USPs). Norm-conserving pseudopotentials ensure that the total charge of the pseudopotentials is equal to the all-electron wavefunction (that is, the wavefunction without the pseudopotential approximation). In contrast, USPs relax this condition with the advantage of requiring less plane waves than the equivalent norm-conserving pseudopotential, and the further advantage of increased transferability to a wide-range of chemical environments. A disadvantage of USPs is that they lead to a variety of computational difficulties in their implementation and are not implemented in the ONETEP code.

4.2.1.3. Sources of Error

Whilst DFT can produce highly accurate calculations, it is not without sources of error. Most standard DFT software is based on four key physical approximations or limitations: Firstly, they assume the Born-Oppenheimer Approximation by fixing the nuclei and treating them essentially as classical particles. This is generally a very safe assumption, as the mass of the electron is significantly smaller than the nuclei. For the case of low-mass particles such as hydrogen, it can still hold as an approximation, but requires additional scrutiny. The second consideration is that DFT, in its standard formalism, is a ground-state theory and so can provide little insight into systems in which

excited electronic states are important. A third consideration with DFT is that because the density is calculated as a sum of Kohn-Sham orbitals, the calculation will introduce some repulsion energy even for singly occupied orbitals (i.e. an electron-electron repulsion interaction that does not exist); this is called the 'self-interaction error' and because of this, DFT is not suitable for the study of systems such as H_2^+ dissociation. Finally, as shown in (Equation 4.3), the largest source of systematic error in DFT calculations is the approximate exchange-correlation functional. [244]

Many exchange-correlation functionals have been proposed in the literature, each of which performs better or worse on certain types of system depending on the particular chemical environment. It is therefore important that a suitable functional is chosen for the system of interest. Because only an approximate exchange-correlation functional is used, the correlation energy does not generally include dispersion interactions between molecules, and therefore DFT is not applicable to systems with strong long-range dispersion interactions (e.g. coronene dimers); however, empirical functional exist to approximate these interactions. Furthermore, for some 'strongly correlated' systems, e.g. systems with partially occupied d- or f-states [244], the Kohn-Sham DFT approach (based on considering non-interacting electrons) fails to correctly describe the electronic properties.

Beyond these physical approximations, DFT requires numerical simulation and therefore a set of numerical approximations must also be made. Some of these are unavoidable, such as inaccuracy due to the limit of precision of numerical integration and rounding errors. DFT calculations often involve self-consistent field solutions to non-linear equations and the choice of tolerances for the level-of-convergence sets a limit to the accuracy of the solution. Other inaccuracies due to numerical approximations in DFT simulations can often be reduced by increasing the resolution of the simulation at the cost of increased computational expense. These properties include, for example, the number of plane waves (measured via the cut-off energy), Fast Fourier Transform (FFT) grid dimensions, the number of k-points in CASTEP and the size of the NWGF radii in ONETEP. For the study of surface systems, additional considerations apply: surface systems can be approximated as a periodic slab of matter separated by a vacuum gap, and it is important that any unphysical interactions between slabs are minimised by choosing a sufficiently large vacuum gap and that the slab is sufficiently thick to represent the bulk to the desired degree of accuracy.

4.3. Density Functional Theory Validation Study

This section provides a detailed description of the steps taken in order to ensure the DFT calculations were performed using a well-converged, reliable and accurate set of parameters.

In this work, various software packages were utilised. The NWChem software was used for validation on small molecules, providing calculations using the same level-of-theory (PBE-GGA exchange-correlation functional [245] and DFT) but at high accuracy (large basis set and tight solver-tolerances) and without the pseudopotential approximation ('all-electron'). DFT was performed primarily using the ONETEP software; as previously mentioned in Section 4.2.1.1, the computational cost of ONETEP scales linearly with the number of atoms such that systems of thousands of atoms can be approached using DFT which would be intractable using other software.

Unless otherwise specified, all ONETEP calculations were performed using the PBE-GGA functional [245] using 'fine_bl' settings (see Appendix D) and an effective kinetic energy cut-off of approximately 800 eV. Unless otherwise specified, all NWChem calculations were performed using the settings listed in Appendix D. The optimised geometry of silica slab model used in this work was validated by comparing the results of the geometry optimisation in both CASTEP and ONETEP; both providing good agreement with each other. The detailed methodology is described in the published work [158].

Forces were calculated by sampling the force upon a single oxygen atom in the system. In this work, the z-dimension refers to the direction normal to the surface plane.

In this validation study, firstly the pseudopotential approximation was validated against all-electron calculation in order to ensure their accuracy (Section 4.3.2). Various parameters were checked for convergence to suitable accuracy; in ONETEP, these parameters include the quantity and size of the NGWFs (Section 4.3.3 and Section 4.3.4) and the kinetic energy cut-off (Section 4.3.5). Parameters which are model-dependent were investigated such as the thickness of the 'slab' used to represent the surface (Section 4.3.6) and, finally, the spacing between periodic images in the direction normal to the surface ('vacuum gap') (Section 4.3.7).

4.3.1. Methods

In order to perform many of the tests within this validation study, all parameters are hold constant and a single parameter is varied from a low 'quality' to a high 'quality'; then the total energy of the system and forces within the system are calculated. The parameter is then chosen such that the forces and energies reach the desired accuracy. In order to assist this work, and future researchers performing simulation studies, a simple open-source tool was developed - 'ONETEPConv'. ONETEPConv a set of scripts, written in the Bash scripting language, which automates this process. The functionality of ONETEPConv includes convergence testing of the kinetic energy cut-off parameter, the radius of NGWFs and the number of NGWFs. The software can speed up calculations by re-using the result of a previous calculation, and it can be used to collate results into sorted .csv files for later analysis. Full documentation of the software is attached in Appendix E and the software is freely available online (doi:10.6084/m9.figshare.4001049.v1) [246].

4.3.2. Pseudopotential Approximation

ONETEP calculations utilise the pseudopotential approximation, in which an effective potential replaces the core electrons of the system. This has the advantage of decreased computational cost, and can produce very accurate results provided that the pseudopotential for the system of interest is of good quality. In order to ensure that the pseudopotentials were in good agreement with all-electron calculations, the geometry of a small model system was calculated using ONETEP and norm-conserving pseudopotentials, and this was compared to all-electron calculations using the NWChem software [247] at the same level of theory. A silanolate-water cluster and a silanol-water cluster were chosen as the model system as they represent the simplest model of the surface silanol functionality. Calculations were performed using a 58.2 Å cubic cell.

The optimised geometries of the silanol clusters and presented in Figure 4.1 with all-electron results (NWChem calculation) overlaid with the results using the pseudopotential approximation (ONETEP calculation).

Similar analysis was performed on a range of organic molecules, as shown in Table 4.1. In order to quantify the difference in the structure, the Root Mean Squared Deviation (RMSD) were calculated between the atomic coordinates of the simulations, a low RMSD corresponds to a similar structure. This confirmed that the norm-conserving pseudopotentials are transferable to a broad range of chemical systems and that ONETEP can accurately describe geometries of simple molecular systems.

The results above show a good agreement, with no significant discrepancies in geometry, between the all-electron and pseudopotential calculations.

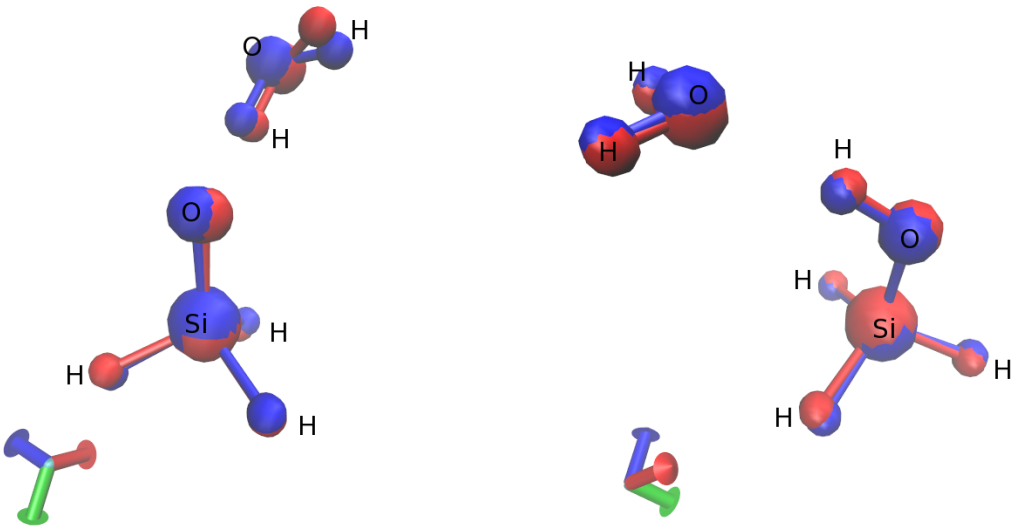

Figure 4.1.: Overlay of all-electron (blue) and pseudopotential (red) geometry optimised structures for small silica 'cluster' models: $SiH_3O^-...H_2O$ (left) and $SiH_3OH...H_2O$ (right). Good agreement between the geometries suggests the pseudopotentials are accurately describing the system. 3D axes are shown in the bottom left for reference.

Molecule	RMSD (Å)	Comment
2-methoxy-phenol	0.014	Almost identical
acetic acid	0.011	Almost identical
ammonia	0.0025	Almost identical
methyl ammonium	0.0041	Almost identical
5-aminopentan-1-ol	0.062	Minor Difference
glycine	0.24	Minor Difference
nitrate	0.066	Almost identical
$SiH_3OH...H_2O$	0.069	Minor Difference
$SiH_3O^-...H_2O$	0.20	Different water orientation, similar geometry

Table 4.1.: Root Mean Squared Deviation (RMSD) between all-electron and pseudopotential geometry optimised structures, good agreement was observed suggesting the pseudopotentials are accurately describing the system.

4.3.3. Number of NGWFs per Atom

The default number of NGWFs for Si of four have been previously shown to be insufficient for an accurate description of crystalline silicon, whereby nine NGWFs were required [248]. In order to test the relevance of this finding to silica-surface chemistry, a test system involving a silanoate...water hydrogen-bonded complex ($SiH_3O^-...H_2O$) was geometry optimised using NWChem and compared to ONETEP calculations with different numbers of NGWFs. Nine NGWFs per Si did not significantly affect the geometry (< 0.1 Å change in bond length, 1 degree change in bond angles) compared to four NGWFs per Si, however the interaction energy produced was significantly improved (as compared to the 'accurate' NWChem calculation), as shown in Table 4.2. The similarity between the all-electron calculations and ONETEP calculations also further demonstrate that the pseudopotentials are capable of an accurate description of silanol-water interactions.

As DFT code relies upon a non-linear solver, convergence of calculations requires a reasonable choice of solver parameters. Utilising 9 NGWFs per Si atom led to difficulties with the NGWF conjugate

gradients optimisation for periodic silica and 'slab' silica models, and therefore the kinetic energy preconditioning parameter K_0 was reduced. A K_0 value of 2.5 produced similar issues, but a value of 2.0 led to rapid convergence of the NGWFs. It can be seen from Table 4.2 that decreasing K_0 did not lead to a loss of accuracy in the interaction energy. The geometries were not significantly affected by the change in K_0. 9 NGWFs per Si and a K_0 of 2.0 were therefore used in subsequent calculations.

Software	Basis Set	K_0†	Interaction Energy (kJ/mol)
ONETEP	4 NGWFs per Si	3.0	-84.24
ONETEP	9 NGWFs per Si	3.0	-82.06
ONETEP	9 NGWFs per Si	2.0	-81.98
NWChem	all-electron	-	-80.78

Table 4.2.: Convergence of the number of NGWFs per Si atom for a SiH_3O^-... H_2O system. Increasing the number for 4 to 9 provided an interaction energy closer to the all-electron calculations. †kinetic energy preconditioning parameter.

4.3.4. Radius of NGWFs

The NGWFs radius controls the extent to which the density is localised around atoms in the ONETEP software. The default radius of 6 Bohr was insufficient for a well-converged Self-Consistent Field electronic minimisation of the NGWFs (i.e. the Root Mean Squared Gradient of the NGWFs was higher than the tolerance). Increasing the NGWF radii for a silica surface slab test system showed that system energy was converged (relative to extrapolated infinite NGWFs radius) to within approximately 0.005 eV per atom for a 9 Bohr radius. 9 Bohr has been shown to be sufficient for accurate calculations on other systems [249], whereas larger radii begin to become prohibitively computationally expensive, and therefore 9 Bohr was selected for use in subsequent calculations.

4.3.5. Kinetic Energy Cut-off

In the ONETEP implementation of DFT, the electronic density is expanded in terms of periodic cardinal sine (psinc) functions. In principle, an infinite number of psinc functions is required, however the expansion can be truncated to increase computational efficiency with a corresponding loss of accuracy, and this is controlled via the kinetic energy cut-off parameter. This parameter determines the approximate[1] maximum kinetic energy of the psinc functions. The convergence of the energy per atom and forces (on an example atom) with respect to the kinetic energy cut-off were investigated by performing a set of single-point energy calculations on the surface system at different kinetic energy values, the results of which are shown in Figure 4.2. Convergence of the energy to a threshold value of 0.1 eV/atom is suitable for most calculations with 0.01 eV/atom being considered very well converged [250]. The energy and forces were converged to within 0.021 eV/atom and 0.0012 eV/Å respectively by a kinetic energy cut-off of 800 eV, and therefore this cut-off was used for subsequent work.

4.3.6. Slab Thickness

Ideally, the surface would emulate the real structure of a surface, often containing thousands of atomic layers below it. However due to computational costs, a finite slab thickness of only a few layers could

[1] The precise kinetic energy cut-off is different for each dimension of the cuboidal cell and is determined by the spacing of the grid upon which the psinc functions are placed, which in turn is dependent upon the specific dimensions of the cell

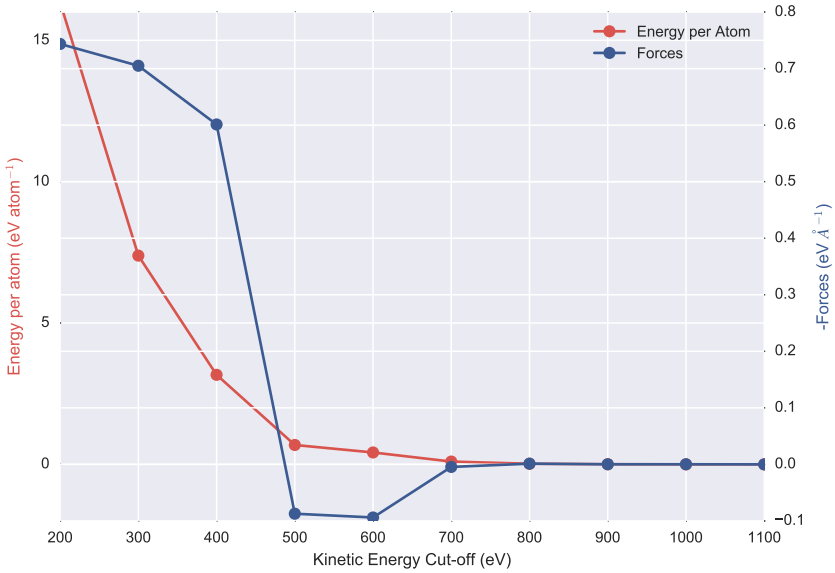

Figure 4.2.: Convergence of the energy per atom and forces (on an example atom) with respect to the kinetic energy cut-off parameter. The results are normalised to results of the 1100 eV kinetic energy cut-off. As expected, the energy decreased monotonically as a function of energy. The energy and forces were converged to within 0.021 eV/atom and 0.0012 eV/Å respectively by 800 eV.

be simulated. If the slab is too thin, its electronic properties will not be representative of the material and therefore it was important to validate that increasing the thickness does not significantly change the properties of the layer. A set of single-point energy calculations were run upon a fully hydrogen passivated (top and bottom) slab of (101) α-cristobalite at different slab thicknesses. A 50 Å vacuum layer was utilised in all calculations . Depending on where the slab was cut, the terminating groups would either be silane (Si−H) or silanol (Si−OH) groups on the top and bottom respectively. The systems investigated are summarised in Table 4.3.

As expected from theory, the total energy decreased monotonically with increased slab thickness due to increased electronic energy from additional atoms, as shown in Figure 4.3. The mean energy per atom of the bulk crystal was -324.42 eV per atom; with increasing slab thickness, the energy per atom is expected to converge towards this value. The energy per atom decreased towards the bulk value with increasing thickness until 16 Å thickness was reached, as shown in Figure 4.3. The energy per atom will not decrease monotonically due to the differences in surface functionalisation and system chemistry of the different slabs (Table 4.3). The energy per atom increased at 18 Å indicating the system was not completely converged; however as larger slab thicknesses become computationally prohibitive, a compromise must be made. The forces acting upon an example oxygen atom can be used to measure the stress induced by surface states, and therefore with increasing thickness the forces on the atom are expected to reduce non-monotonically. A plot of the forces per atom can be found in Appendix F. A minimum at 14 Å indicated that this choice of thickness was a good compromise and therefore this thickness was used in future work. This choice can be further justified by comparison to other simulations in the field which generally used thinner slabs [144, 237]. This system, shown in Figure 4.4, contains two sets of 10-membered Si-O-Si rings, or 3 'layers' of Si.

4.3.7. Vacuum Gap Convergence

Ideally periodic slabs should be sufficiently distant from each other in the direction normal to the surface such that there is negligible electrostatic interactions between them. In order to investigate this, single point energy calculations were performed over a range of increasing vacuum spacing for

Slab Thickness (Å)	Termination (Top/Bottom)	Number of Atoms
8	H/S	112
10	S/S	120
12	S/H	160
14	S/S	168
16	S/H	192
18	S/S	216

Table 4.3.: Summary of Different Silica Systems of different Slab Thickness. H = silane passivated, S = silanol passivated

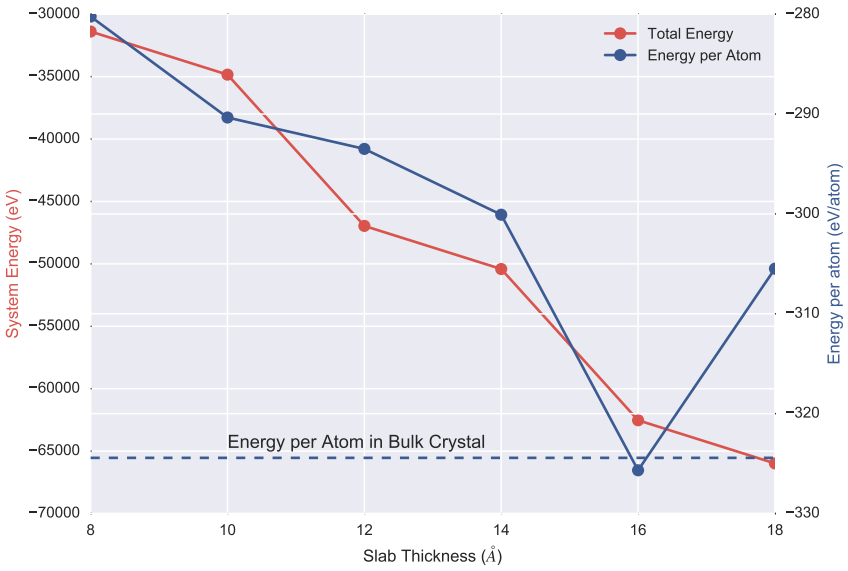

Figure 4.3.: Variation in total energy (red) and energy per atom (blue) as a function of silica slab thickness. As expected from theory, the total energy decreased monotonically with increased slab thickness due to increased electronic energy from additional atoms. The energy per atom is expected to converge to the bulk energy per atom (dashed line) at infinite thickness, however the decrease is not expected to be monotonic. It can be seen that by 18 Å the energy per atom has not converged to the bulk value, however 14-18 Å thickness slabs are approaching this value.

the neutral silica slab previously described and the results are presented in Figure 4.5(a). It can be seen from this figure that the forces and energies are converging as the periodic images of the slabs are separated further from each other.

This study was repeated for the same system, except for one silanol being deprotonated to form a silanolate, resulting in a system with a net negative charge. The result of this study can be seen in Figure 4.5(b). Unexpected behaviour was observed in that the total energy of the system was not convergent. The forces converged as would be expected, but the energy initially decreased with a z^{-1} relationship, then increased with a linear relationship, as can be seen from the close fit to an equation of this form. The initial decrease z^{-1} in energy is that expected from Coulomb's Law, due to reduced Coulombic interactions between periodic images. The linear relationship, however, is an unphysical artefact. Further analysis revealed that the linear increase in total energy of the system originates entirely from the electrostatic energy component of the system, which in ONETEP [113], is calculated using an Ewald summation [110].

In order to ascertain whether this artefact was an issue with the ONETEP code or a general issue with the Ewald summation, an Ewald calculation was performed using the Accelrys Material Studio

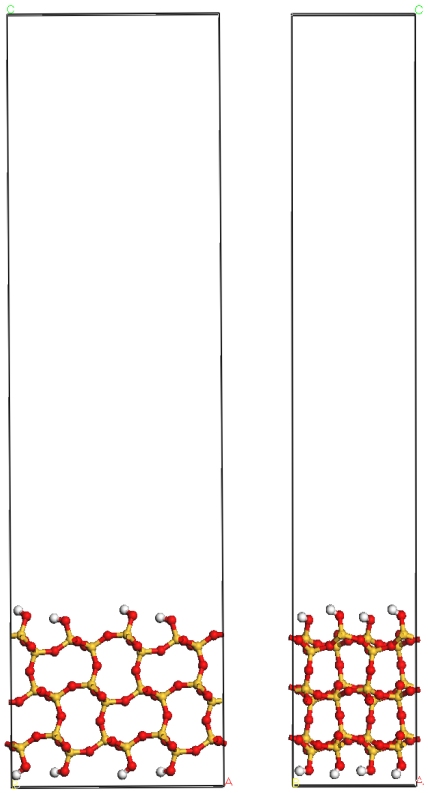

Figure 4.4.: Neutral Silica Slab with a 14 Å thickness, viewed in the xz plane (left) yz plane (right). Silicon (yellow), oxygen (red), hydrogen (white).

Forcite code for a hydroxide molecule in the same dimensions box. The results are shown in the blue circles of Figure 4.6, in which the same phenomenon was observed. Another set of calculations were performed but instead of cuboidal simulation cell, a cubic simulation cell was utilised. Increasing all dimensions of the box (x, y and z) simultaneously led to the expected Makov-Payne [251] convergence of the Ewald energy (red circles, Figure 4.6), and therefore demonstrated that the artefact was related to using an orthorhombic unit cell which is not neutral.

In order to understand this artefact, the Ewald summation implementation must be considered. For infinite 3D periodic systems with a net charge, the electrostatic energy would be undefined and therefore the Ewald summation imposes a compensating uniform background charge which reduces the net charge to zero. In the case of charged/polarised orthorhombic unit cells, it can be shown that extending one dimension leads to a density of compensating charge that tends towards zero, resulting in uncompensated charge and therefore an error in the energy and forces for systems [252–254]. Yeh and Berkowitz refer to the standard Ewald implementation as the 'conducting boundary condition' because when the polarisation of system is not accounted for in the formulation, it is physically analogous to the case when the outer boundary of the simulation has an infinite/metallic dielectric constant [254]. Yeh and Wallqvist [253] recognised that the limitations of the standard Ewald implementation were not well known and stated '...the vast majority of molecular dynamics simulations are still being performed with the conducting boundary condition regardless whether the simulated system has a net polarization or not.'.

Yeh and Berkowitza show that the error is minimal for short-range forces but increased in magnitude for long-range forces. Correction terms to the Ewald method ('EW3DC') exist which compensate for this error [252–254], but they are not widely implemented in software packages and calculations are often performed without these corrections, which may be due to poor awareness of this simulation artefact. In the ONETEP software, one approach to this issue could be to truncate the coulomb

potential in the z-direction, but this functionality remains largely untested and a preliminary tests on a simple system showed issues with the forces. An alternative solution, as suggested by Yeh et al., would be to apply a uniform electric field in the z-direction, which is a function of the instantaneous z-component of the cell dipole moment. However, this functionality is not available in Forcite and unavailable in ONETEP for dynamic or geometry optimisation simulations.

Yeh and Wallqvist showed that with increasing vacuum padding the forces from the conventional Ewald summation approach those of the corrected EW3DC forces. They also showed that for glass-water interfaces with a vacuum gap, the standard implementation of the Ewald sum is sufficient to provide accurate water orientation and density [253, 254]. Spohr (1997) studied simple interfacial systems and came to a similar conclusion, providing the vacuum padding is sufficient [255]. Therefore, the standard implementation of the Ewald sum was utilised in this work. A vacuum gap of approximately 90 Å was chosen as here the forces are converged to within approximately 0.001 eV/Å (compared to extrapolated 'infinite' vacuum gap).

4.3.8. Validation Study Summary

The parameters used for DFT simulations are found in Appendix D. In summary, a model of amorphous silica was constructed using a surface built from α-cristobalite as this model can replicate important properties of the silica-water interface such as the silanol density. The pseudopotentials used were validated against all-electron calculations and were shown to introduce negligible error into the optimised geometries of a range of simple chemical systems and shown to accurately model the interaction energy of silica-water to within 1 kJ/mol of the all-electron result. The default number of NGWFs was increased to nine for Silicon atoms and the radius of NGWFs was set to 9.0 Bohr for all atoms. An 800 eV kinetic energy cut-off was used which offered convergence of the forces to within 0.001 eV/Å with respect to the kinetic energy parameter. A 14 Å thick slab with silanol passivation was used, with an approximately 90 Å vacuum gap, resulting in forces converged to within 0.001 eV/Å with respect to the vacuum gap thickness. The parameters represent an optimal compromise between accuracy and computational expense for this system. In addition, a simple open-source utility was also developed to enable other researchers to rapidly perform similar validation studies for the ONETEP software [246].

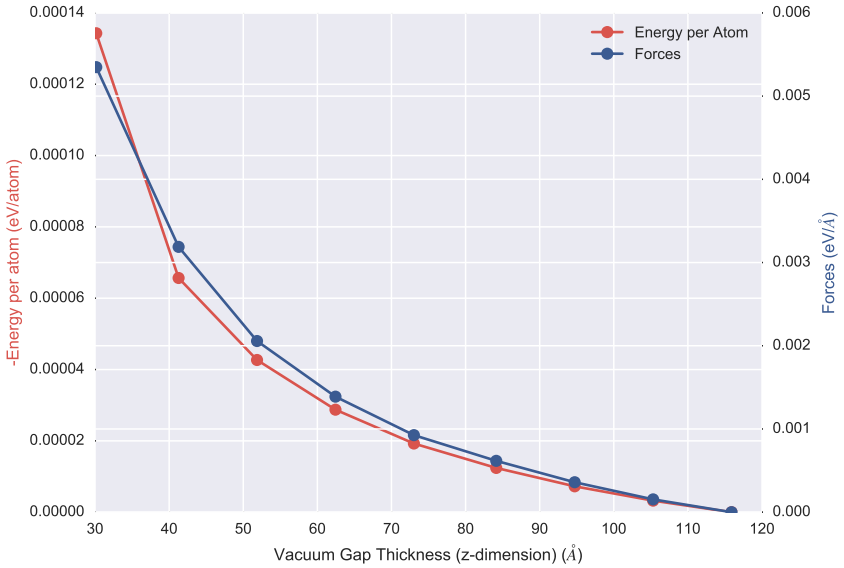

(a) Neutral Silica Slab

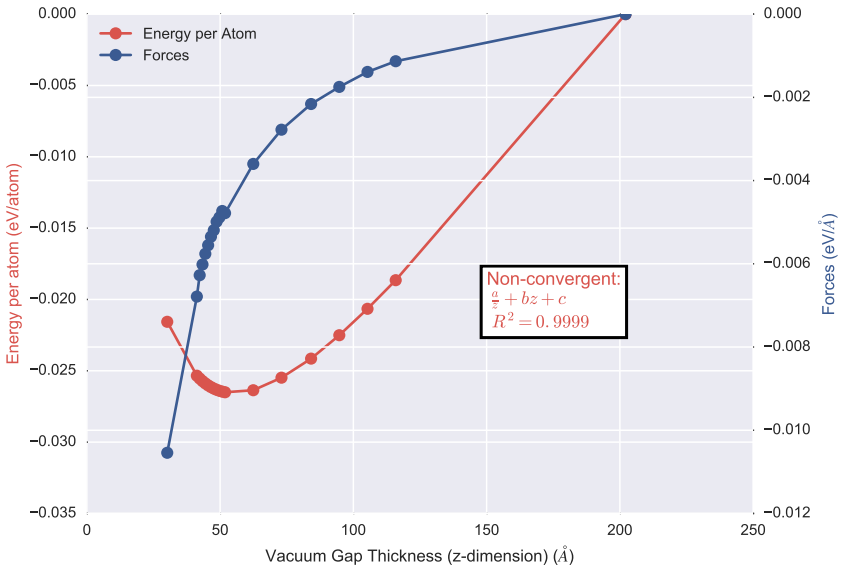

(b) Negative Silica Slab

Figure 4.5.: The effect of vacuum gap thickness (between periodic images) on the energy and forces of (a) a neutral silica slab system and (b) a negative silica slab system (-1 system charge). Calculations performed in ONETEP. The energies and forces are normalised to the value at largest system. For the neutral system in (a) both the energies and forces are converging with respect to the amount of vacuum spacing as expected. However for the negative system in (b) it can be seen that although the forces are converging, the total energy of the system has become a divergent property. A non-linear regression was performed on the energy per atom for the negative silica slab based on the formula: $\frac{a}{z} + bz + c$ where $a = 242.08$, $b = 0.022$, $c = -9.16$ and an excellent fit (R^2=0.9999) was obtained. The $\frac{1}{z}$ component is expected from Coulomb's Law, however the bz linearly divergent behaviour is indicative of an artefact in the Ewald summation method used, for an detailed explanation of this phenomenon, see Section 4.3.7.

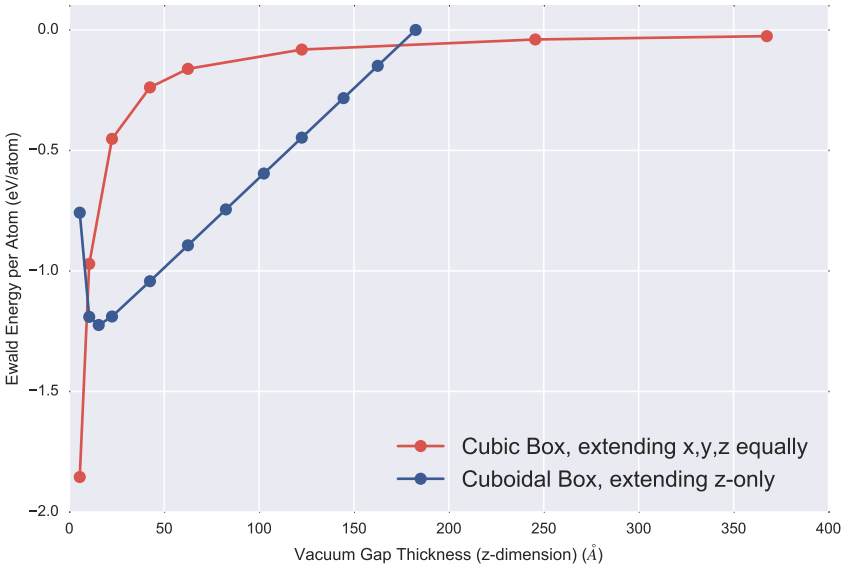

Figure 4.6.: Variation in the Ewald Energy of a single negatively charged hydroxide molecule in periodic box using the Forcite software. It can be seen that when only the Z-axis was extended (blue circles) the total energy did not converge; however when all cell dimensions were increased simultaneously (red circles), the Ewald energy converged. This demonstrates that the simulation artefact is related to cuboidal unit-cell usage.

4.4. Journal Paper

The following paper upon charging at the silica-water interface was published in the Journal of Colloid and Interface Science [158].

Acid-Base Dissociation Mechanisms and Energetics at the Silica-Water Interface: An Activationless Process

4.4.1. Abstract

Hypothesis

Silanol groups at the silica-water interface determine not only the surface charge, but also have an important role in the binding of ions and biomolecules. As the pH is increased above pH 2, the silica surface develops a net negative charge primarily due to deprotonation of the silanol group. An improved understanding of the energetics and mechanisms of this fundamentally important process would further understanding of the relevant dynamics.

Simulations

Density Functional Theory *ab initio* molecular dynamics and geometry optimisations were used to investigate the mechanisms of surface neutralization and charging in the presence of OH^- and H_3O^+ respectively. This charging mechanism has received little attention in the literature.

Findings

The protonation or deprotonation of isolated silanols in the presence of H_3O^+ or OH^-, respectively, was shown to be a highly rapid, exothermic reaction with no significant activation energy. This process occurred via a concerted motion of the protons through 'water wires'. Geometry optimisations of large water clusters at the silica surface demonstrated proton transfer to the surface occurring via the rarely discussed 'proton holes' mechanism. This indicates that surface protonation is possible even when the hydronium ion is distant (at least 4 water molecules separation) from the surface.

4.4.2. Introduction

Silica and water represent two of the most abundant chemical systems, and therefore it is unsurprising that understanding the interface between them is relevant to a wide variety of systems. Surface charging is fundamental to a range of phenomena such as dissolution rates [179, 180, 230] and the surface adsorption of ions and molecules [128, 231]. Chemical reactions of reactive silanol groups (Si−OH) with H^+/OH^- are thought to be the primary surface charging mechanism for silica [105], with electrolyte effects having a measurable but less significant effect [127].

4.4.2.1. Oxide Surface Charging

One of the most popular approaches to modelling surface proton reactions has been Surface Complexation Models (SCM). One such example is the 2-pK model which assumes that the surface state can be modelled as two consecutive protonation reactions, the equilibrium constants of which are often obtained empirically from acid-base titration data [133, 256]. This methodology has the advantage of being highly generalisable, but neglects any direct information obtained about the

oxide-water interfacial structure and dynamics obtained experimentally or via simulation. While the thermodynamic description of the 2-pK model is suitable for describing certain processes such as ion complexation and surface dissolution [133, 134], it provides little insight into the atomic-scale interactions which are present at water-surface interfaces and are required to understand many dynamic interfacial processes, such as double layer formation, solvent structure, surface-charging kinetics and non-equilibrium interfacial processes.

As the pH is increased above 2±1, the silica surface becomes increasingly negatively charged [257]. Silicon surface atoms (S_{surf}) are present as a neutral oxide that can dissociate or protonate according to the following chemical equilibria:

$$S_{surf}{-}OH + H_2O \underset{k_2}{\overset{k_1}{\rightleftharpoons}} S_{surf}{-}O^- + H_3O^+ \tag{4.10}$$

$$S_{surf}{-}OH + H_3O^+ \underset{k_4}{\overset{k_3}{\rightleftharpoons}} S_{surf}{-}OH_2{}^+ + H_2O\,. \tag{4.11}$$

X-ray photoelectron spectroscopy measurements have shown that significant quantities of $Si{-}OH_2{}^+$ are only present at extremely low pH (~2 or lower) [154]. High level *ab initio* calculations have demonstrated the chemical instability of this species in neutral water, supporting the notion that at conditions relevant to most applications (pH 2-14) this species is an insignificant component of the surface composition [144]. Given this observation, Borkovec explained how the 2-pK model should be interpreted as reactions between a pair of neighboring ionizable groups, as opposed to a single site as has often been assumed [131].

Although the 2-pK model can be used to describe the average surface charge from a system-scale perspective by considering only the reaction with hydronium ions, the surface at an atomistic scale presents a far more complex environment in which Equation 4.11 is competing with the analogous hydroxyl reaction show in Equation 4.12.

$$S_{surf}{-}OH + OH^- \underset{k_6}{\overset{k_5}{\rightleftharpoons}} S_{surf}{-}O^- + H_2O \tag{4.12}$$

4.4.2.2. Charge Transport in Pure Water

Given the chemical similarity between proton transfer of water-water proton transfers and of silanol-water proton transfers, the mechanism of proton transport in pure water is relevant. In pure water, solvated hydronium ions are transported via the Grotthuss mechanism [172] which involves interconversion between the symmetric Zundel cation $H_5O_2{}^+$ and the triply-hydrogen bonded Eigen cation $H_9O_4{}^+$ [199, 258]. The rate limiting step for proton transfer is believed to be the reorientation of water molecules, which necessarily involves breaking hydrogen bonds [258]. The concerted motion of protons along a chain of water molecules is sometimes referred to as a 'water wire'. Solvated hydroxide ions are thought to have a different mechanism for transport than hydronium ions and correspondingly demonstrate a lower ionic mobility [173]. This mechanism has been suggested to involve interconversion between the square planar $H_9O_5{}^-$ anion and the tetrahedral $H_7O_4{}^-$anion, with the rate limiting step being the formation of the latter [200, 201, 258].

4.4.2.3. Modelling the Silica-Water Interface

With regard to the silica-water interface, both *ab initio* and classical molecular modelling have been used to describe atomistic surface charge. Many classical forcefields capable of representing negative

charges have been developed, the majority of which require *a priori* knowledge of the surface charge, treating surface charges as predefined and fixed throughout the simulation [119, 161, 209, 210, 259–264]. In order to study time-varying surface charge using molecular dynamics, a force field must be used which can allow bond breaking and formation. Such a forcefield is usually referred to as reactive or dissociative. The reactive force field of Rustad et al. incorporated water dissociation and led to a fully hydroxylated surface with no surface charge [155], but was not designed to accurately represent surface charging and only considered a short timeframe of 10 ps. The dissociative force field of Mahadevan and Garofalini [171] was used to study formation of silanols and transfer of protons at the surface, similarly, the Hybrid-QM/MM study of Du et al. [265] was used to model formation of silanols at the surface, however none of these models were designed to investigate protonation-deprotonation dynamics of surface silanols and do not discuss this aspect of their model. The reactive forcefield 'reaxFF', developed by Goddard III et al. [266] and applied by Fogarty et al. [267], was utilised to study the silica-water interface. Their 600 ps dynamics implied that a fully hydroxylated surface was produced from a freshly cleaved slab after approximately 250 ps, the concentration of silanolate groups at the surface was not explicitly stated.

Ab initio molecular dynamics (AIMD) studies based on periodic Density Functional Theory (DFT) have investigated protonation-deprotonation involving hydronium ions in order to calculate pK_a values [144, 162, 268] and in order to investigate dissolution mechanisms involving hydronium ions [159, 171, 185]. DFT has shown that hydronium ions can facilitate transfer of negative charge across the surface via the Grotthuss mechanism [144]. Mahadevan and Garofalini have noted that hydronium ions are important in short lived proton transfer processes at the surface [171], which has been supported by experimental observations [174–176].

Reaction of hydronium ions with silanolate groups at the silica-water interface has been shown by Leung et al. to have no barrier along the reaction coordinate based on Potential of Mean Force calculations [144, 162]. In agreement with this result, Liu et al. have shown that there is no energetic barrier to acid dissociation of orthosilicic acid ($Si(OH)_4$) [162]. In contrast to silanol acid dissociation reactions, the counterpart basic reaction shown in Equation 4.12 has received much less attention within the literature using *ab initio* methods for silica surfaces.

It has long been known that the dynamics and energetics of hydroxyl-based proton transfer in pure water differs from hydronium-based proton transfers [258], and therefore Equation 4.12 must be considered separately from hydronium reactions (Equation 4.11) for an accurate representation of atomic interfacial proton transfer reactions. The hydroxyl transfer reaction shown in Equation 4.12 has received little attention with respect to *ab initio* studies, one of the key exceptions being the work of Xiao and Lasaga who have investigated this reaction as a possible precursor to silica dissolution [160]. Xiao and Lasaga used SiH_3OH and $(HO)_3Si{-}O{-}Si(OH)_3$ cluster models for the silica surface at the HF/6-31G* level (for geometries), and their results indicated that this reaction was activationless and exothermic.

4.4.2.4. Motivation

Understanding both Equation 4.10 and Equation 4.12 is important from two perspectives. Firstly, adsorption of H^+ and OH^- is thought to be important in determining the rate of dissolution of silicates, as indicated by Xiao and Lasaga [159]. One aim of this work is to improve on the limitations of the work of Xiao and Lasaga by exploring the hydroxyl-transfer reaction (Equation 4.12) using a more representative model of the silica (periodic slab), water (solvated hydroxide molecule) and a higher level of theory via Second Order Møller–Plesset (MP2) and DFT calculations. Secondly, an atomistic model that has been shown to accurately describe both water dynamics and surface protonation-deprotonation kinetics as a function of pH does not exist. Such a model is required for fundamental

understanding of double layer dynamics, for an improved understanding of the geochemical properties of oxides [269] and in order to interpret the response of charge-sensitive silica-water nanodevices such as silica nano-pore Field-Effect Transistors (FETs) [81] and Ion-Sensitive and Biologically-Sensitive FETs [263, 270]. A basic level of understanding of the available energetic barriers and mechanisms involved in proton transfer reactions at the surface is required before such a model can be considered. Thirdly, calculation of the transition states of these important reactions may allow a Transition State Theory description of the kinetics of the system which can be used to interpret the results of, for example, titration experiments. Understanding these reactions is important in the context of empirical macroscopic models such as SCMs in interpreting the physical significance of the reactions being modelled with empirical equilibrium constants.

In this work, DFT simulations in the form of AIMD and geometry optimisations have been used to investigate both the acid association mechanism (Equation 4.10) and the base-dissociation reaction (Equation 4.12) between silica and water. To our knowledge, this work represents the first *ab initio* simulation of the base-dissociation reaction which goes beyond a simple cluster-model for the silica surface, and the first *ab initio* simulation which explicitly explores the effect of differing solvent structure on both Equation 4.10 and Equation 4.12.

4.4.3. Computational Methods

Calculations were performed using DFT with the PBE-GGA exchange-correlation functional [245]. The PBE-GGA functional has been shown to produce accurate structures for crystalline silica [227]. The PBE functional is known to over-structure liquid water in dynamic simulations [271, 272] however it can provide reasonable geometries for optimised water clusters as compared to MP2 calculations [273, 274] and it has been used in various studies of the silica-water interface [144, 211, 237, 275].

Periodic boundary condition calculations were performed using the linear-scaling pseudopotential DFT software ONETEP version 3.5.9.8 [242, 276]. PBE OPIUM[2] norm conserving pseudopotential (NC-PPs) bundled with Accelerys Material Studio 6.0.0 were utilised in all ONETEP calculations. An effective kinetic energy cutoff of approximately 800 eV was used for the psinc basis set [243], which is equivalent to the energy cutoff used in conventional plane-wave DFT codes. DFT in ONETEP was performed using self-consistent field convergence criteria whereby the RMS gradient of the NGWFs must be equal to or less than $1.8375 \times 10^{-6}\, E_{\mathrm{h}}\, {a_0}^{-3/2}$. Geometry optimisations proceeded using the BFGS algorithm until the difference in energy between iterations was equal to or less than 1×10^{-5} eV, 0.03 eV Å^{-1} and 0.001 Å for the energies, forces and maximum atomic displacement respectively. Unless otherwise stated, all calculations were performed using these settings. NWChem software version 6.3 [247] was used to perform all-electron calculations. Unless otherwise specified, these calculations were performed using the driver module, DFT and the PBE-GGA functional. All calculations used a total energy SCF tolerance of $10 \times 10^{-8}\, E_{\mathrm{h}}$ and the aug-cc-pvtz basis set. For the data presented in Figure 4.11, NWChem geometry optimisations were performed using the stepper module and a 0.05 Å maximum displacement per iteration. Example input files used and unit conversions can be found within the Appendix G Section 1.

In order to validate the pseudopotential used, the geometry, deprotonation energy and adsorption energy of monomeric silanol-water and silanolate-water systems were compared with all-electron calculations, the results of which are presented in Table 4.4 and Table 4.5 respectively. It can be seen that there is good agreement (1-4% difference) in the calculated ONETEP NC-PPs and all-electron energies. Optimised geometries (not shown) demonstrated excellent agreement, with bond lengths within 0.01 Å and angles within 0.1 degrees.

Deprotonation Energy $\Delta E_{\mathrm{d,gas}}$ (kJ/mol)	Monomer (AE)‡	Monomer (NC-PP)§
SiH_3OH/SiH_3O^-	1506.4	1462.56
$SiH_3OH...H_2O/SiH_3O^-...H_2O$	1449.96†	1428.98

Table 4.4.: Deprotonation Energies $\Delta E_{\mathrm{d,gas}}$ (kJ/mol) calculated as calculated as the total energy of the deprotonated system minus the total energy of the protonated system. AE=All-electron. NC-PP=norm-conserving pseudopotential. ‡NWChem calculation †Basis Set Superposition Error (BSSE) Corrected §ONETEP calculation

Water Adsorption Energy $\Delta E_{\mathrm{ads,gas}}$ (kJ/mol)	Monomer (AE)‡	Monomer (NC-PP)§
$SiH_3OH...H_2O$	-24.26†(-23.04*†)	-25.18
$SiH_3O^-...H_2O$	-80.78†	-81.06

Table 4.5.: Water Adsorption Energy $\Delta E_{\mathrm{ads,gas}}$ (kJ/mol) calculated as $E_{\mathrm{complex}} - (E_{\mathrm{H_2O}} + E_{\mathrm{monomer}})$. AE=All-electron. NC-PP=norm-conserving pseudopotential. ‡NWChem calculation †BSSE corrected *MP2 level, DZ(p,d) basis set calculation from Reference: [214] § ONETEP calculation

Born-Oppenheimer AIMD simulations were performed using ONETEP to investigate the proton transfer dynamics of three water clusters (H_3O^+, OH^- or $H_3O_2^-$). Simulations were performed using the same electronic and simulation cell settings as the slab geometry optimisations, but without any

[2] See http://opium.sourceforge.net/index.html for information about the Opium pseudopotential generation project

geometry constraints. A 0.5 fs AIMD timestep and the Nosé-Hoover thermostat (one chain, 8.8 fs relaxation time). The water cluster was placed above the silica surface, and 200 fs of molecular dynamics was performed. A temperature of 300 K was utilised, consistent with the AIMD of Musso et al. [237] however it should be noted that the properties of bulk water are known to be poorly reproduced without the use of elevated temperature using this functional [271].

Implicit solvation calculations were performed using ONETEP, using a self-consistent cavity and a fine grid scale of 3.0 in a 47.5 Å cubic simulation cell with open boundary conditions [277].

Similarly to the work of Leung et al. [144], the calculations reported herein treat the nuclei classically and it is assumed that the effects of zero point motion and tunnelling do not affect the qualitative nature of proton transfer mechanisms. This has been shown to be the case for electron transfer and pure water proton transport [278, 279].

Visualisation was performed using the Visual Molecular Dynamics software [280] with O-H bonds and Si-O bonds drawn of internuclear separations of less than 1.1 Å and 1.7 Å respectively. Bond distances are given in Å. In some figures, hydrogen bonds have been drawn as unlabelled dotted lines using a cutoff of 3 Å and 20 degrees angles between hydrogen bond acceptors and donors.

4.4.3.1. Models

Musso et al. have performed a series of DFT studies on various silica polymorphs [221, 222, 237], including an investigation of the dynamics of water upon a (101) cleaved plane of the silica polymorph α-cristobalite. This surface is attractive from the point of view of modelling amorphous silica surface due to its surface hydroxyl density of approximately 5 OH per nm^{-2}, similar to fully hydroxylated silica [121]. Furthermore α-cristobalite itself has a bulk density (2.23 gcm^{-3} [235]) close to amorphous silica (2.20 gcm^{-3}) [236]. Therefore, α-cristobalite was chosen as a model crystal structure for the DFT calculations.

The initial silica structure of α-cristobalite was obtained from the structures bundled with Accelrys Material Studio 6.0.0 which was itself generated based on a paper by Dollase [281] (primitive tetragonal $P4_12_12$ space group, a=b=4.978 Å, c=6.948 Å). A variable-cell geometry optimisation using the CASTEP software [241] was performed on the primitive cell in order to obtain relaxed unit cell-parameters for use in future calculations (a=b=5.075 Å, c=7.085 Å). For this calculation, a 900 eV kinetic energy cutoff was utilised with a 4x4x4 k-point grid and the aforementioned NC-PPs.

Using the CASTEP relaxed crystal geometry, a supercell was created from these coordinates with doubled lattice parameters, and this was optimised using the ONETEP software, which is a fixed-cell dimension calculation. This produced no significant change in molecular geometry of the crystal. A (101)-plane slab of 14 Å thickness was cleaved from this crystal and passivated with a layer of hydrogen on both top and bottom, resulting in a system of 168 atoms of isolated silanol groups. The resulting lattice parameters were a=17.431 Å, b=10.150 Å, c=105.929 with approximately 90 Å of this being vacuum padding. The slab was relaxed using ONETEP, with no significant rearrangement of the bulk. The optimisation resulted in a contraction of approximately 0.1 Å slab thickness. The final coordinates are shown in Figure 4.7.

The optimised silica slab (Figure 4.7) demonstrated isolated silanols with an O...O distance of 4-5 Å and the closest O...H approach distance of 4.8 Å. This result deviates from that reported by Musso et al. [237], who reported a zig-zag pattern of hydrogen bonds. However, Musso et al. comment that these hydrogen bonds are weak and disrupted at room temperature and entirely broken in the presence of water [237]. This was investigated by repeating the geometry optimisation using CASTEP, (1000 eV kinetic energy cutoff, Γ-point sampling of the Brillouin zone and ultrasoft pseudopotentials of Civalleri

and Harrison [282]). This resulted in the same geometry as the previous ONETEP optimisation. This indicates that the deviation in structure between this work and that of Musso et al. is a result of the latter being in a different local minimum. The local minimum obtained herein provides an idealised model of a silica surface composed of isolated silanols.

Taking the neutral slab, a proton was removed from a surface silanol (indicated with a circle in Figure 4.7) to create a negatively charged silanolate group and the system was geometry optimised in ONETEP. In the protonated system the in-plane Si−O bond length was 1.638 Å and the out-of-plane (Si)-(OH) bond length was 1.643 Å, in the deprotonated system the in-plane Si-O bond was slightly stretched (1.692 Å) and the out-of-plane $Si-O^-$ bond was shortened (1.547 Å). The geometry of the bulk and the other surface silanols were not significantly affected by the deprotonation, demonstrating that the silanols are truly isolated even in the deprotonated system. The surface charge density used in this work (~0.05 $Si-O^-$ per nm^2) is similar to that calculated by Behrens and Grier for a silica plate in deionised water [124], however the surface charge density of silica is highly variable depending on surface preparation, ionic strength and pH.

Unless otherwise specified, calculations were performed using 3D periodic boundary conditions using ONETEP and a vacuum gap with a neutralising background charge to minimise periodic interactions. For systems with a net charge which are also orthorhombic, it has been shown that there will be some uncompensated neutralising background charge [252] that leads to a divergent system energy, though the forces remain convergent. The ONETEP implementation of DFT has the advantage that there is little computational cost to using a large vacuum gap, therefore allowing the forces within this work to be well converged with respect to the simulation cell size to within ~0.005 eV/Å.

For explicit solvent calculations, the isolated water clusters were initially optimised in vacuum. The PBE-GGA functional was found to provide a reasonable description of the ground-state geometry of simple water clusters (see Appendix G Section 2). The initial coordinates for the 11-water ($H_3O^+(H_2O)_{11}$) and 20-water ($H_3O^+(H_2O)_{20}$) hydronium clusters mentioned in this work were obtained from the work of Hodges and Wales [283] using the Kozack-Jordan potential [284] and are candidate global minimum for a solvated hydronium ion in 11- and 20- water molecules respectively. Experiments have shown the 20-water cluster is an unusually stable water cluster [285]. The optimised water geometries were placed approximately 2.3 Å distant from the optimised silica surface, and relaxation energies listed in the main text are simply calculated as the energy of the entire system (water cluster + silica) after optimisation minus the configuration they were initially placed. The bottom half of the slab was constrained during geometry optimisations, as shown in Figure 4.7 using stick representation.

A summary of all model systems geometry optimised in this work can be found in Table 4.6.

4.4.4. Results and Discussion

4.4.4.1. Acid-Base Dissociation Reactions of single Hydronium or Hydroxide molecules with Silica Surface Models

In order to investigate the proton transfer described in Equation 4.10, 200 fs of AIMD were performed on the $S_{surf}O^- + H_3O^+$ system. The same initial configuration was also used in a geometry optimisation. Similarly, in order to investigate the proton transfer reaction described in Equation 4.12, the model system $S_{surf}OH + OH^-$ was considered. As model systems for S_{surf}, both an isolated silanol cluster (SiH_3OH/SiH_3O^-) and a periodic silica slab ($S_{surf}OH/S_{surf}O^-$) was considered.

The initial and final coordinates of the geometry optimisation of the H_3O^+ system are shown in Figure 4.8a for the slab system, and Figure Appendix G Section 3 for the cluster system. Snapshots of the

Substrate	Adsorbate	Figures
Silica$-O^-$	H_3O^+	Figure 4.8a, Figure 4.9†
Silica$-O^-$	$H_5O_2^+$ ('Zundel Cation')	Figure 4.12
Silica$-O^-$	$H_9O_4^+$ ('Eigen Cation')	Figure 4.13
Silica$-O^-$	$H_3O^+(H_2O)_{11}$	Figure 4.14
Silica$-O^-$	$H_3O^+(H_2O)_{20}$	Figure 4.15, Figure 4.16, Figure 4.17
SiH_3O^-	H_3O^+	SI 3a, SI 3b§, SI 5a, SI 5b‡
$Si(OH)_3O^-$	H_3O^+	SI 8a
$(SiH_3OH)O(SiH_3O^-)$	H_3O^+	SI 7a
Silica$-$OH	OH^-	Figure 4.8a, Figure 4.10†
Silica$-$OH	$H_3O_2^-$	Figure 4.19, Figure 4.18†
Silica$-$OH	$H_7O_4^-$	Figure 4.20
Silica$-$OH	$H_9O_5^-$	SI 9
SiH_3OH	OH^-	SI 4a, SI 4§, SI 6a, SI 6b‡
$Si(OH)_3OH$	OH^-	SI 8b
$(SiH_3OH)O(SiH_3OH)$	OH^-	SI 7b

Table 4.6.: Geometry Optimisations were performed for the above systems at the PBE level of theory in vacuum. AIMD was additionally performed for those systems marked with †. 'Silica' refers to the α-cristobalite silica surface model. §MP2 level geometry optimisation. ‡Geometry optimisations performed using the implicit solvation model of ONETEP. 'SI' refers to Appendix G section.

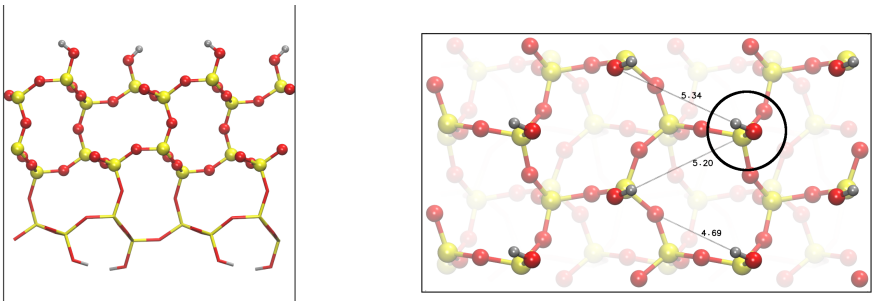

Figure 4.7.: α-cristobalite silica surface model, atomic coordinates from a fixed cell geometry optimisation in ONETEP (see Section 4.4.3.1) with orthorhombic cell parameters a=17.431 Å, b=10.150 Å, c=105.929 Å. Surface vectors were obtained from a bulk variable cell optimisation in CASTEP. Left image shows the lateral view of the slab, with constrained atoms in stick representation and non-constrained atoms as ball and stick. The right image shows a view normal to the slab with three Si-OH...O-Si bond distances shown. In order to generate a charged silica surface slab model, the highlighted silanol (black circle) was deprotonated and the system geometry optimised as described in the main text (Section Section 4.4.3.1). The surface has been hydrogen passivated. Silicon atoms are shown as yellow, oxygen atoms as red and hydrogen atoms as grey.

AIMD are shown in Figure 4.9 and a video of the AIMD trajectory can be found within Appendix G. Both the geometry optimisation and the AIMD simulation showed a proton transfer from the H_3O^+ to the $Si-O^-$ resulting in a $Si-OH\cdots H_2O$ hydrogen bonded system, as described in Equation 4.10. Within the AIMD simulation, proton transfer and reorientation of the H_3O^+ occur simultaneously, resulting in rapid transfer within ~25 fs, with strong oscillations of the silanol $O-H$ continuing until the end of the simulation as the energy of the reaction is dissipated.

The initial and final coordinates of the geometry optimisation of the hydroxide system is shown in Figure 4.8b for the slab, and in Appendix G Section 3 for the cluster model. The optimisation showed a proton transfer from the $Si-OH$ to the OH^-, resulting in a $Si-O^-\cdots H_2O$ hydrogen bonded system as described in Equation 4.12. Snapshots of the AIMD are shown in Figure 4.10 and a video of the AIMD trajectory can be found within the Appendix G. Reorientation of the OH^- occurred for the first 75 fs, followed by rapid proton transfer over the next ~50 fs, after which the H_2O diffused 4 Å away from the now negatively charged silanolate group.

Proton transfer during a geometry optimisation indicates that the initial encounter-pair is energetically unstable and that there is no activation energy to the proton transfer process. Figure 4.11 shows the energy profile for a geometry optimisation performed upon a cluster system at both the PBE-GGA and MP2 level of theory, and on the periodic slab model of the silica surface (PBE). It can be seen that the total energy of the system decreases smoothly and monotonically. Consistent with this observation, using both the ONETEP and NWChem transition state search functionality, no transition state could be identified for these proton transfer coordinates.

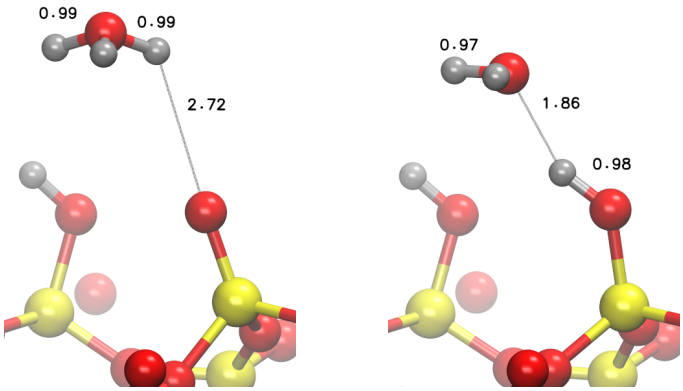

(a) Negative silica slab with H_3O^+ above a surface silanolate (Equation 4.10). The silanolate is protonated by the H_3O^+.

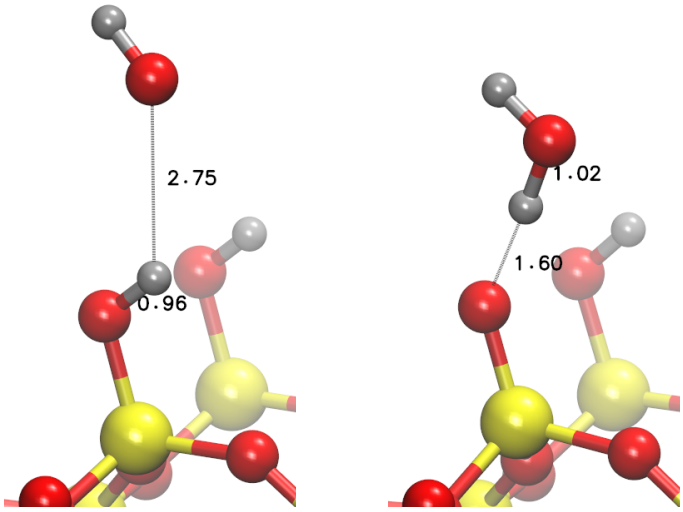

(b) Neutral silica slab with a OH^- above the surface (Equation 4.12). The silanol is deprotonated by the OH^-.

Figure 4.8.: Geometry optimisation of single gas-phase water ion (OH^- or H_3O^+) above the silica surface. Left image of each panel shows unoptimised structure, right image of each panel shows optimised structure.

It is possible that hydrogen bonding in geminal or vicinal silanols would introduce energetic barriers, for example Sulpizi et al. recently published a study indicating that silanols with in-plane hydrogen bonds of a hydroxylated quartz surface are 3 pK_a units more acidic than those forming hydrogen bonds out-of-plane with water [268]. Leung et al. have shown that highly strained sites can be significantly more acidic [144]. Geometry optimisations using geminal and vicinal silanol cluster models (shown in Supplimentary Information Section 3) indicated that these proton transfers remain activationless. This work will be restricted to the study of isolated silanols.

The results thus far presented have not taken into account the effect of solvation on hydronium and hydroxide ions, and therefore it is possible that the instability of the reactants in the above DFT studies may be a result of neglecting these interactions. It was found that the incorporation

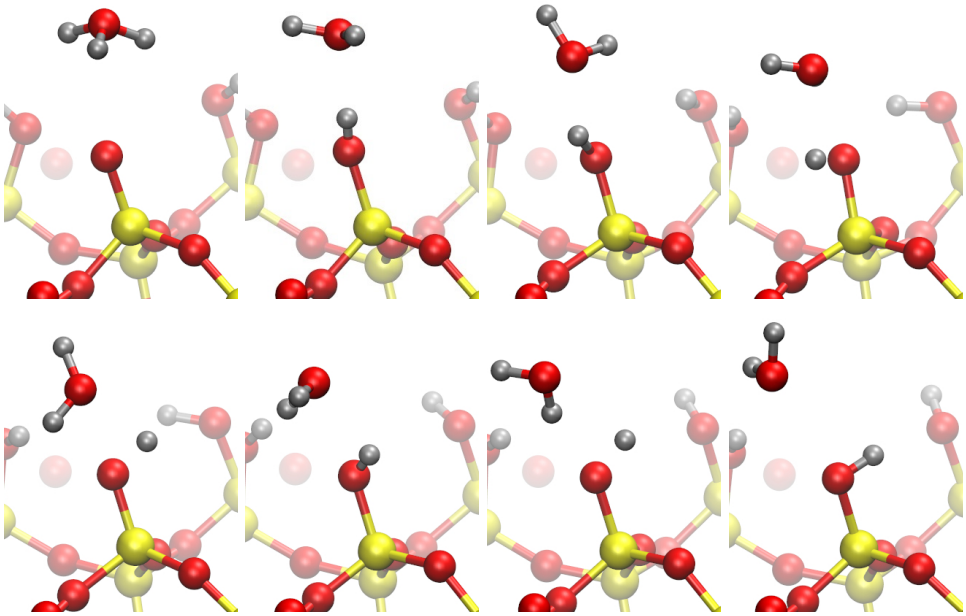

Figure 4.9.: AIMD Simulation of a neutral silica slab with a H_3O^+ above a silanolate group at the silica surface (Equation 4.10). The silanolate group is rapidly protonated by the H_3O^+ within the first 50 fs. Snapshots are shown at every 25 fs. Chronology proceeds starting from the first row, left to right, then the second row, left to right.

of implicit solvent also demonstrated activationless proton transfer during geometry optimisations of either the hydronium or hydroxide (Appendix G Section 3). The implicit solvent model cannot explicitly incorporate the effects of water cooperativity [286] and Grotthuss proton transport [172], and therefore solvation of the periodic silica slab model was investigated via explicit solvation, in terms of water clusters of increasing size placed at the silica surface.

4.4.4.2. Surface Protonation in the Presence of Explicitly Solvated Hydronium

Proton transport was investigated for hydrogen-bonded water clusters at the surface via geometry optimisations of water clusters in contact with the silica surface in vacuum. The following systems were investigated: H_3O^+, $H_5O_2{}^+$ ('Zundel cation'), $H_9O_4{}^+$ ('Eigen cation'), a hydronium ion solvated in 11 water molecules ($H_3O^+(H_2O)_{11}$), and a hydronium ion solvated in 20 water molecules ($H_3O^+(H_2O)_{20}$). See Appendix G Section 2 for images of these structures in isolation.

The initial structures and geometry optimised structures of Eigen cation and Zundel cation systems are shown in Figure 4.12 and Figure 4.13 respectively. Both of these simulations demonstrated proton transfer via the Grotthuss mechanism. A hydrogen bonded network between the water-cluster and the surface was formed prior to the proton transfer.

The optimisation for the larger $H_3O^+(H_2O)_{11}$ system is presented in Figure 4.14. Similarly to the previous hydronium systems, the surface was protonated within the first few iterations which was followed by a rearrangement of the protons in the system to stabilise the hydroxide ion produced. Unlike the previous simulations, the resulting water cluster demonstrated some structural character of both a Zundel cation and a $H_3O_2{}^-$dimer (Figure 4.14c), indicating that there is some charge separation within the water cluster and that the surface has been protonated via the H_3O^+ anion stabilising the deprotonation of a water molecule.

A Natural Population Analysis (NPA) (Appendix G Section 4) confirmed that the Zundel-like substructure had a Natural Charge significantly more positive that the other oxygen atoms in the simulation, however the H_3O_2 substructure did not show a particularly negative charge relative to other oxygens

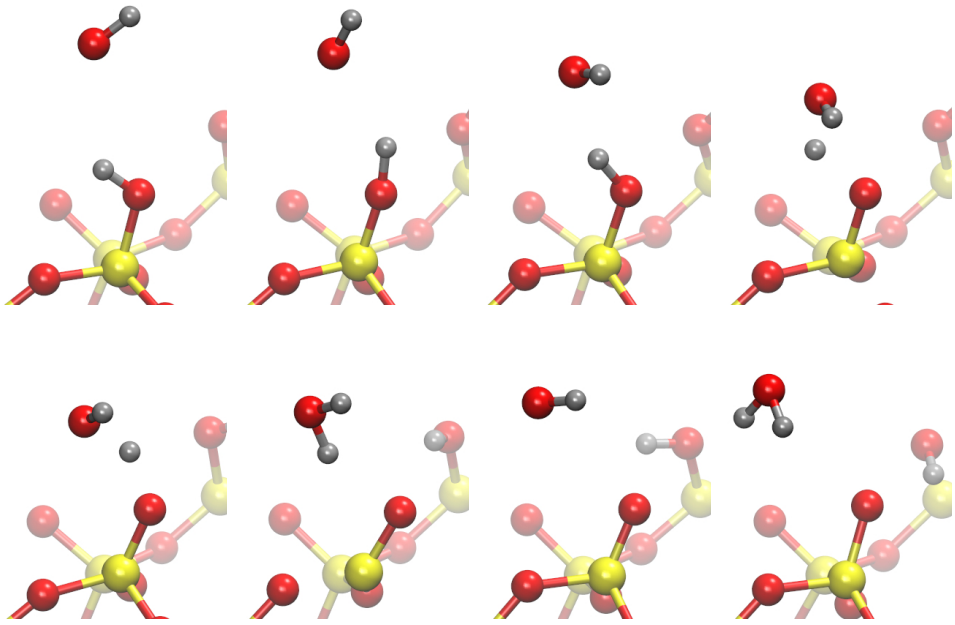

Figure 4.10.: AIMD Simulation of a neutral silica slab with a OH^- above a silanol at the silica surface (Equation 4.12). The silanol is rapidly deprotonated by the OH^- with ~50 fs after an initial period of ~75 fs. Snapshots are shown at every 25 fs. Chronology proceeds starting from the first row, left to right, then the second row, left to right. Proton transfer occurs rapidly within approximately 25 fs.

(Appendix G Section 4). Prior to optimisation, the silanolate group surface-terminal oxygen had a Natural Charge of -1.17 and all other surface-terminal oxygens showed a Natural Charge of -1.04 ± 0.01. After optimisation all surface-terminal oxygens showed a Natural Charge of -1.04 ± 0.01, which indicates that the silanolate had been neutralised. NPA analysis showed that water cluster itself is almost neutral, with a net natural charge of +0.04 relative to the net Natural Charge of -0.04 for the silica slab. It can be concluded that the silica surface has been protonated, and the system neutralised. However the water cluster has distributed itself so as to retain a structural defect analogous to a Zundel cation. The next section uses a larger water cluster to investigate how the distance of the hydronium ion from the surface may affect this mechanism of surface protonation.

The $H_3O^+(H_2O)_{20}$ water cluster system was studied, in which the H_3O^+ could be placed initially distant from the surface or close to the surface depending on the orientation of the cluster. Figure 4.15, Figure 4.16 and Figure 4.17 present the results of a geometry optimisation of this cluster in three different initial orientations respectively. Conformation A, shown in Figure 4.15, initialised the H_3O^+ ion at a distance from the surface with the shortest path between the silanolate and H_3O^+ being four water molecules. Using chemical notation, the initial structure can be described as $S_{surf}{-}O^-\cdots(H_2O)_{20}\cdots H_3O^+$. This conformation had four water molecules in the shortest path between the silanolate and H_3O^+. Rotation of this water cluster relative to the surface resulted in Conformation B (Figure 4.16) and Conformation C (Figure 4.17) which have three and two intervening water molecules, respectively.

Geometry optimisation of this cluster in all three Conformations A, B and C showed activationless protonation of the silanolate surface. In Conformation A (Figure 4.15), protonation of the surface silanolate occurred via water dissociation resulting in a substructure of water near the surface similar to a solvated hydroxide ion ($H_3O_2^-$) near the silica-water interface. NPA showed that the H_3O^+ remained positive compared to the rest of the water cluster, but the $H_3O_2^-$-like substructure was not negative. Using chemical notation, the optimised structure could be schematically drawn as $S_{surf}{-}OH\cdots H_3O_2\cdots(H_2O)_{18}\cdots H_3O^+$. Interestingly, the H_3O^+ ion in the cluster was unperturbed by the silanolate environment, indicating that, at least at 0 K, there is a distance beyond which H_3O^+

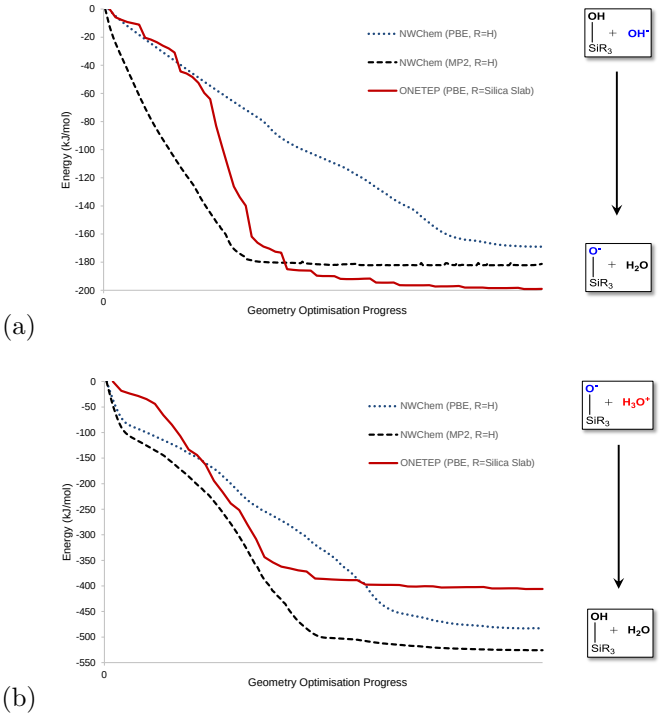

Figure 4.11.: Change in system energy with geometry optimisation progress. A geometry optimisation was performed upon the systems described within Equation 4.10 and Equation 4.12 and the respective system energy versus geometry optimisation step is shown in Figure (a) and Figure (b) respectively. A minimal cluster silanol model was used, and the chemical system is drawn as insets within each figure. The initial energy (y-axis) is normalised to zero. As each optimisation took a different number of steps, for comparison the optimisation progress (x-axis) is presented, in which the optimsation has been scaled to range from the initial structure (left of x-axis) to the fully optimised structure (far right of the x-axis). It can be seen that in both optimisations there was a smooth, monotonic decrease in energy upon optimisation, indicating an activationless proton transfer. Images of each geometry optimisation can be found in Figure 4.8 within the main text for the ONETEP optimisations, and in Section 3 of Appendix G for the NWChem optimisations.

will not recombine with the silanolate group directly (herein referred to as the 'basin of attraction') which in this case occurs at 4 water molecules separation from the silanolate. In contrast, for the optimisation of Conformation C (Figure 4.17), the initial proximity of the H_3O^+ facilitated complete proton transfer to the silanolate, resulting in a neutral system $S_{surf}-OH\cdots(H_2O)_{21}$. Conformation B showed a mechanism in between these two extremes: the optimised structure (Figure 4.16) can be seen schematically as $S_{surf}-OH\cdots OH\cdots H_5O_2{}^+\cdots(H_2O)_{18}$, and again showed a Natural Charge (Appendix G Section 4) which was positive for the $H_5O_2{}^+$ substructure but not negative for the OH^--like substructure.

By comparing these three conformations, the ground-state basin of attraction for activationless proton transport for isolated silanols on silica surfaces is seen to be 2-3 water molecules. The proton transfer mechanism observed in Figure 4.14, Figure 4.15 and Figure 4.16 involves initial deprotonation of the mediating water molecules stabilised by the hydronium ion, and resembles the 'proton holes' transport discussed by [163]. That is to say, these results suggest that even if the H_3O^+ is distant from the surface, its presence is enough to stabilise the surrounding waters such that the surface can be protonated without the H_3O^+ ion losing its localised proton, as shown most clearly in Figure 4.15.

Thermal fluctuations might be expected to reduce the basin of attraction by breaking the hydrogen-bonded water-wires required for Grotthuss mechanism-like proton transport, however, the thermal

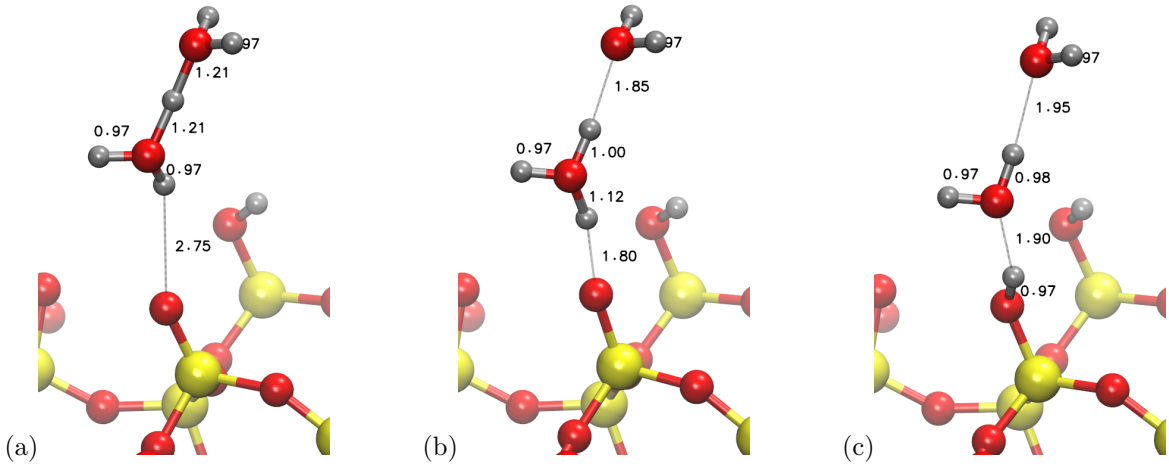

Figure 4.12.: Geometry optimisation of a Zundel cation ($H_5O_2^+$) above a silanolate group at the silica surface. As the geometry optimisation proceeds, the silanolate group is protonated by the cation (b), resulting in two water molecules hydrogen bonded to a silanol group (c).

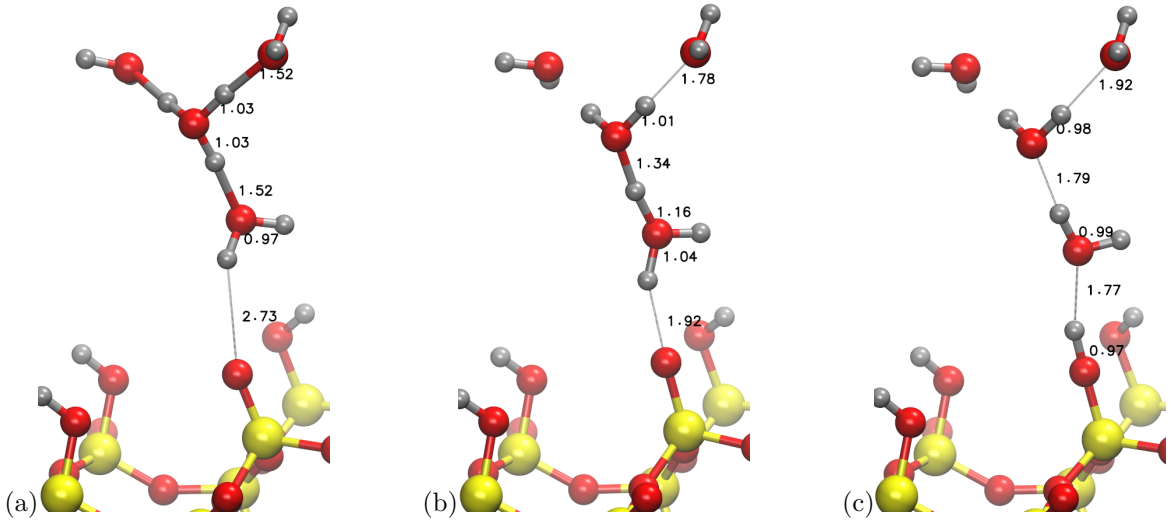

Figure 4.13.: Geometry optimisation of an Eigen cation ($H_9O_4^+$) above a silanolate group at the silica surface is shown in (a). As the optimisation proceeds a proton transfer occurs such that the silanolate is protonated by the Eigen cation (b), forming a water cluster which is hydrogen bonded to the silanol surface (c).

energy would also allow activated proton transfer, thereby increasing the size of the basin of attraction. It is interesting to compare these results with the results of the AIMD simulations of the water-silica interface by Leung et al., which indicated that once the H_3O^+ was further than 2-3 water molecules from the surface, then the H_3O^+ would diffuse away without protonating the surface. This suggests that the thermal contribution and/or screening from the bulk prevents proton transfer to the surface, however we note that these AIMD simulations were run at elevated temperature in order to preserve the liquid dynamics of water under the PBE functional [144].

4.4.4.3. Surface Deprotonation in Presence of Explicitly Solvated Hydroxide

In this section, AIMD simulation of the $H_3O_2^-$ cluster at the silica interface is presented, followed by geometry optimisations of the $H_3O_2^-$, $H_9O_5^-$ and $H_7O_4^-$ clusters at the silica interface. As discussed in the introduction, several of these clusters are of particular interest as they have been presented in the literature as important in the transfer of protons within pure water.

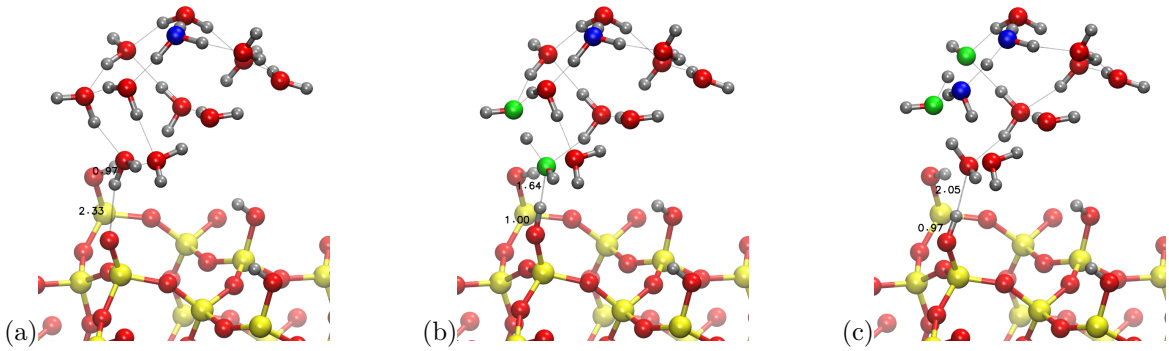

Figure 4.14.: Geometry optimisation of a hydronium ion (shown in blue) solvated in 11 water molecules ($H_3O^+(H_2O)_{11}$) above a silanolate group on the silica surface is shown in (a). The surface is protonated within the first few iterations, as shown in (b), forming a water network shown in (c). The water network contains a substructure which is structurally similar to a zundel cation (blue) and $H_3O_2^-$ dimer (green) near the surface, a shown in (c). Natural Population Analysis of the optimised system shown in (c) can be found in the Appendix G Section 4, and demonstrates that the blue-highlighted atoms are more positively charged than the rest of the water cluster. The green-highlighted oxygens showed a similar Natural Charge to the rest of the water cluster.

Snapshots of the $H_3O_2^-$ system AIMD simulation are shown in Figure 4.18 and a video is included in Appendix G. From the AIMD simulation it can be seen that during the first ~50 fs the symmetric structure of the $H_3O_2^-$ anion is broken as a $H_2O\cdot\cdot OH^-$ structure is formed, after which the silanol is deprotonated within the next ~25 fs.

The geometry optimisation of the same $H_3O_2^-$ system is shown in Figure 4.19. Similarly to the previously shown isolated hydroxyl system in Figure 4.8b, geometry optimisation of the $H_3O_2^-$ system resulted in deprotonation of the silanol surface by the hydroxide cluster and the formation of a pair of water molecules hydrogen bonded to a silanolate group on the surface.

The optimisation for the $H_7O_4^-$ system is shown in Figure 4.20. As with the previous optimisation of the $H_3O_2^-$ and OH^- systems, the $H_7O_4^-$ optimisation demonstrated deprotonation of the silanol group surface to form a silanolate group. A correlation can be observed between the number of waters in the cluster and the resulting $SiO^-\cdots HO{-}O$ hydrogen bond length between the geometry optimised OH^-, $H_3O_2^-$ and $H_7O_4^-$ systems which showed hydrogen bond lengths of 1.60 Å, 1.51 Å and 1.39 Å respectively (Figure 4.8b, Figure 4.19 and Figure 4.20 respectively). This decrease in bond lengths might well be explained as a result of positive hydrogen bonding cooperativity in which, when a hydrogen bond forms, a redistribution of electrons within the water molecules occurs which can reuslt in a reduction of hydrogen bond length with increasing cluster size [287]. It should be noted that this correlation is not guaranteed as many other factors can affect hydrogen bond lengths, for example, if the hydrogen bond conformation is nonoptimal then its strength will decrease (and thereby length increase). Hydrogen bonds at the periphery of a cluster may be expected to show a smaller change in hydrogen bond length [286]. This increased stabilisation of the $SiO^-\cdots HO{-}O$ hydrogen bond with increasing water cluster size is significant as this effect is often neglected in the parameterisation and validation of classical force-fields, which are often constructed using a single water molecule interacting with the surface [161, 288].

For the square planar $H_9O_5^-$ system (Appendix G Section 3), geometry optimisation did not deprotonate the silanol group at the surface and the hydroxyl cluster remained stable and relatively unperturbed by the silica surface environment, with only a slight distortion (0.1 to 0.2 Å) of the hydrogen bonds normal to the surface. The lack of proton transfer indicates that a significant activation barrier to deprotonation was present for this system. This result is consistent with the AIMD of pure water by Tuckerman et al., who observed no proton transfer for the more stable square planar $H_9O_5^-$ complex

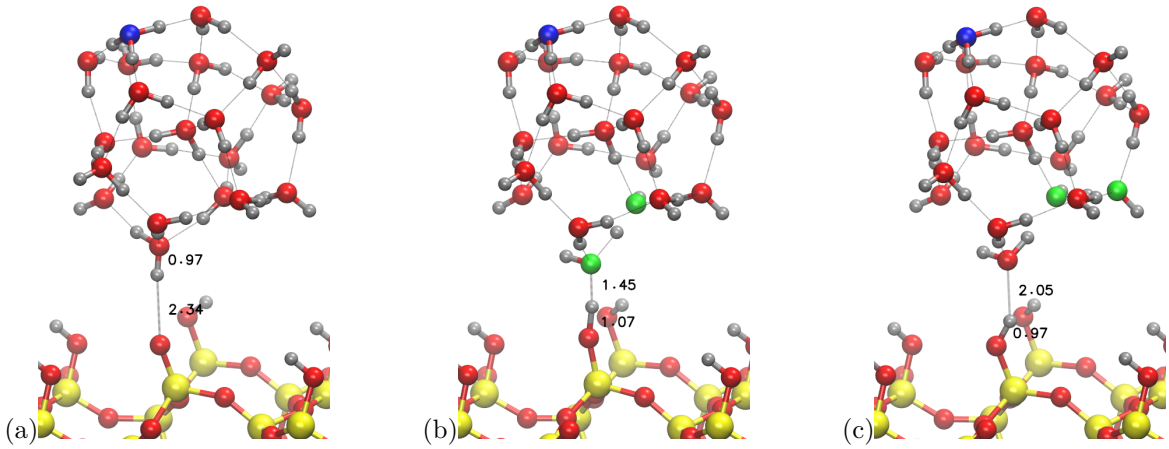

Figure 4.15.: Conformation A: Geometry optimisation of a hydronium ion solvated in 20 water molecules ($H_3O^+(H_2O)_{20}$)] above a silanolate group at the silica surface. The H_3O^+ is initially separated from the silanol by 4 water molecules (a). The hydronium ion remains stabilized by the cluster (shown in blue) throughout the optimisation steps (b) and (c), remaining unperturbed by the surface. The silanolate is protonated as the optimisation proceeds, as shown in (b), resulting in the formation of a water cluster substructure similar to a hydroxide ion near the surface (oxygen atoms shown in green in (b) and (c)). Natural Population Analysis showed that the blue-highlighted oxygen in the optimised structure is significantly more positive that the other oxygen atoms, as shown in Appendix G Section 4. The green-highlighted oxygen showed a similar Natural Charge to the rest of the water cluster.

[201, 258], and the experimental and theoretical study of Cwiklik et al. on pure water, who observed that this structure is more stable than the $H_7O_4^-$ tetrahedral cluster [289].

These simulations extend the work presented by Xiao and Lasaga [160] and, to our knowledge, represent some of the first dynamic and mechanistic *ab initio* descriptions of surface charging due to solvated hydroxide at the silica/water interface. An interesting find of this study is that the SiO^-....HO−O hydrogen bond length is strongly dependent upon the degree of solvation. Furthermore, this study indicates that, similarly to proton transfer in pure water, deprotonation of SiOH in the presence of OH^- demonstrates no significant activation energy, except in the case of the highly stable $H_7O_4^-$ solvated cluster.

4.4.4.4. Time-Scales and Energetics

All proton transfer events observed in geometry optimisations occurred within the first few optimisation steps, indicating a strong energy gradient driving the reaction. AIMD results already presented (Figure 4.9, Figure 4.10 and Figure 4.18) have shown these proton transfer events occur on a femtosecond time-scale (~25-100 fs). This result is consistent with Car-Parinello molecular dynamics studies on pure water, which have shown that once a water wire is formed, OH^-/H_3O^+ recombination occurs extremely rapidly (on a femtosecond time-scale) [190, 192].

In order to quantify the energetics of this proton transfer, all-electron calculations using NWChem were performed upon a silica cluster model of an isolated silanol molecule (SiH_3OH) and an orthosilicic acid molecule ($Si(OH)_4$). Three different reaction schemes were considered for each reaction in which a single additional water molecule stabilised the reactants, the full details of these calculations can be found within the Appendix G Section 5. Each different reaction scheme considers a different combination of hydrogen bonding between the products, which can lead to large differences in the reaction energies. Reaction energies of between -637 and -682 kJ/mol for orthosilicic acid, and of between -655 to -693 kJ/mol for silanol were calculated for Reaction Equation 4.10. Reaction energies of between -43.5 to -105 kJ/mol were calculated for orthosilicic acid, and of between -25.9 and -142 kJ/mol for silanol were calculated for Reaction Equation 4.12. For Reaction Equation 4.12, using

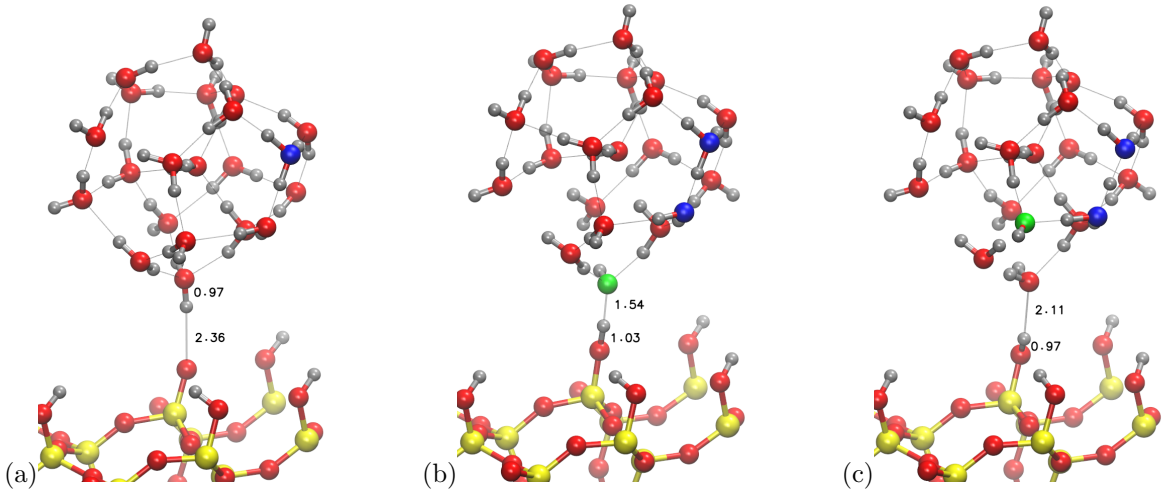

Figure 4.16.: Conformation B: Geometry optimisation of a hydronium ion solvated in 20 water molecules ($H_3O^+(H_2O)_{20}$) above a silanolate group at the silica surface. The H_3O^+ is initially separated from the silanol by 3 water molecules (a). This is the same water cluster as Figure 4.15, but rotated such that the hydronium ion (blue) is closer to the surface silanolate. As the optimisation proceeds the silanolate is protonated by a nearby water molecule (b) and the water cluster rearranges forming a substructure which contains what could be described as a solvated hydroxide ion (green) and a solvated hydronium ion (blue). Natural Population Analysis showed that the blue-highlighted oxygens in the optimised structure are more positive that the other oxygen atoms, as shown in Appendix G Section 4. The green-highlighted oxygen showed a similar Natural Charge to the rest of the water cluster.

a $(HO)_3Si{-}O{-}Si(OH)_2(OH)_3$ model of the surface, Xiao and Lasaga calculated a reaction energy of -232.6 kJ/mol at the MP2/6-31G* level, The resulting reaction energy is likely more exothermic than the silicic acid and silanol due to the formation of multiple hydrogen bonds in the resulting complex [160].

These values indicate that hydronium based protonation events are significantly more exothermic than their counterpart hydroxide deprotonation events, suggesting that the chemistry of silica deprotonation cannot be treated as simply the reverse of protonation at an atomistic scale. These calculations also demonstrate that both protonation and deprotonation reactions are highly exothermic; by comparison k_bT is approximately ~2.48 kJ/mol at 298 K. The fast time scale and high exothermicity of this reaction has significance for building dynamic models of surface charging, indicating that these reaction coordinates might be modeled as diffusion-limited once a hydrogen-bonded encounter pair has been formed.

4.4.5. Conclusions

Using AIMD and geometry optimisations, we have investigated the acid-base dissociation mechanism for protonation and deprotonation events of isolated silanol and silanolate groups by hydronium ions and hydroxide ions in solution. The reaction mechanism was observed to be rapid, highly exothermic and predominantly activationless. We believe that this work is the first to go beyond simple cluster models of the surface to study surface charging due to adsorption of solvated hydroxide at the silica-water interface.

The acid dissociation of isolated silanols (Equation 4.10) did not demonstrate an energetic barrier to the proton transfer, whether in the gas phase, implictly solvated or explicitly solvated using water clusters. Simulations of the $H_3O^+(H_2O)_{11}$ and $H_3O^+(H_2O)_{20}$ clusters demonstrated proton transfer via the 'proton holes' mechanism in which the hydronium ion stabilises water-dissociation which, in turn, protonates the silanolate group. This mechanism has rarely been considered in the literature,

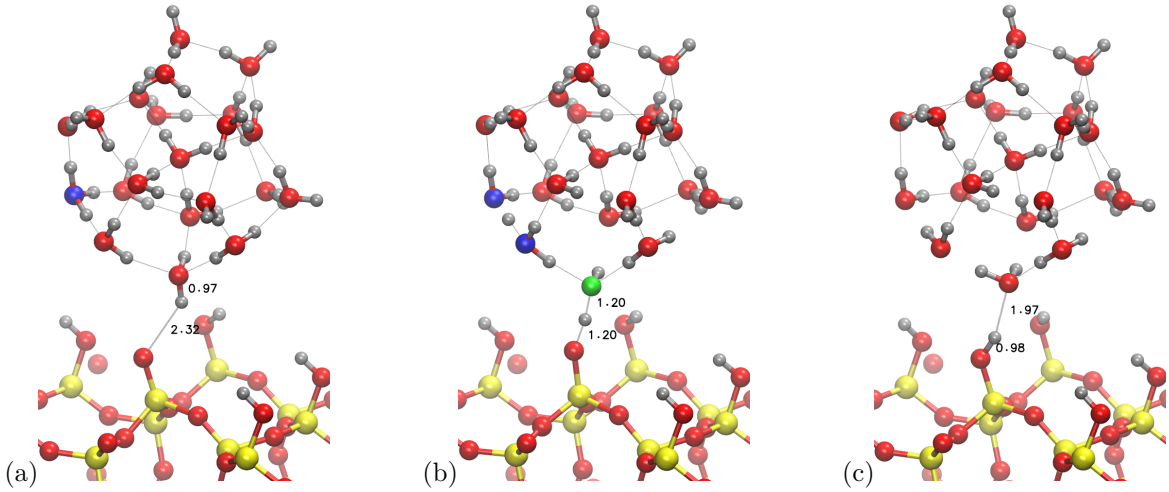

Figure 4.17.: Conformation C: Geometry optimisation of a hydronium ion solvated in 20 water molecules ($H_3O^+(H_2O)_{20}$) above a silanolate group at the silica surface. The H_3O^+ is initially separated from the silanol by 2 water molecules (a). This is the same water cluster as Figure 4.15 and Figure 4.16, but rotated such that the hydronium ion (blue) is closer to the surface silanolate . The closer proximity of the hydronium ion relative to Conformation A results in proton transfer from the hydronium ion to the silanolate group of the surface as shown in (b), ultimately producing a neutral water cluster hydrogen bonded to a neutral silanol group, as shown in (c). The intermediate hydroxide-like substructure is shown in green. Natural Population Analysis showed that oxygens in the optimised structure have similar Natural Charges, as shown in Appendix G Section 4.

but could indicate that surface protonation is possible even when the hydronium ion is distant (4 water molecules at least) from the surface.

The dissociation of isolated silanols in the presence of hydroxide (Equation 4.12) was also found to behave as an activationless process for the cases of both the gas phase hydroxide ions and the implicitly solvated hydroxide ions. For the case of explicitly solvated hydroxide ions, the local environment of hydrogen bonded silanols and waters was shown to be capable of creating an energetic barrier to deprotonation in the case of the $H_9O_5^-$ anion, but showed complete or partial deprotonation for the $H_3O_2^-$ and $H_7O_4^-$ hydroxide clusters. This energetic barrier to proton transfer for the $H_9O_5^-$ is consistent with the pure water simulations of Tuckerman et al. [201]. The $Si{-}O^-{\cdots}H_2O$ hydrogen bond length was found to be strongly dependent upon the degree of solvation, which could have significant implications for the accurate parameterisation of this bond in molecular dynamics force fields.

This work suggests that proton transfer events at the isolated silanol-water interface often do not exhibit a well-defined transition state and therefore Transition State Theory is likely inapplicable. Furthermore, the fast time scale and high exothermicity of the reactions discussed herein shows these hydronium/hydroxide systems will readily transfer protons, therefore surface scientists should be cautious when simulating such systems in the context of non-reactive forcefields.

Proton transfer was shown to involve first a reorientation of the water into hydrogen bonds with the surface group followed by proton transfer along a hydrogen bonded network of water to/from the surface group. This indicates that proton transfer for both hydroxide and hydronium ions is likely to be limited by the rate of reorientation of solvated hydroxide/hydronium clusters at the surface, as is thought to be the case for proton transfer in pure water [258, 290].

In this work, the silica geometry was assumed to be regular and composed of isolated silanols, however it is possible that the silica structure (e.g. geminal or vicinal silanols) could affect energetic barriers. Furthermore, this study does not incorporate the electrostatic effect of counterions in the double layer which will introduce stabilisation to negatively charged sites and can stabilise hydroxide molecules at

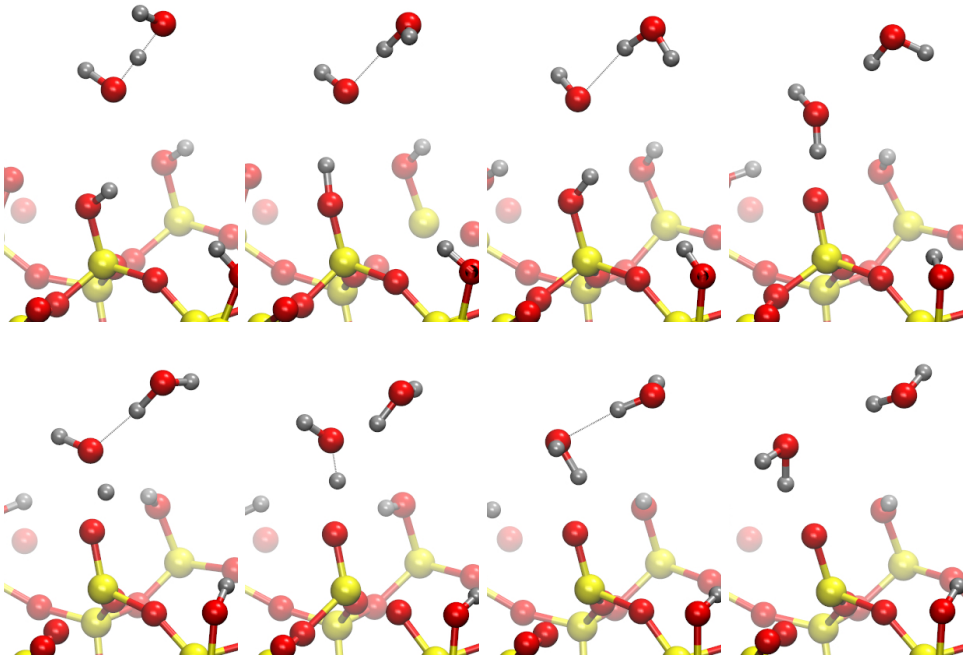

Figure 4.18.: AIMD Simulation of a neutral silica slab with the $H_3O_2^-$ anion above a silanol at the silica surface (Equation 4.12). Reorientation of the system occurs for the first ~50 fs from which the silanol is deprotonated by the $H_3O_2^-$ within another ~25 fs resulting in a water molecule hydrogen bonded to the silanolate group. From left to right, snapshots are shown at every 25 fs.

the surface [187].

As this study has been primarily focused upon static geometry optimisation calculations and short time-scale AIMD, it is the hope of the authors that this work will stimulate further work towards a model of the system which is capable of accurately describing the complex and dynamic nature of surface charging at an atomistic scale, without the need for surface-specific empirical parametrization or computationally expensive *ab initio* calculations.

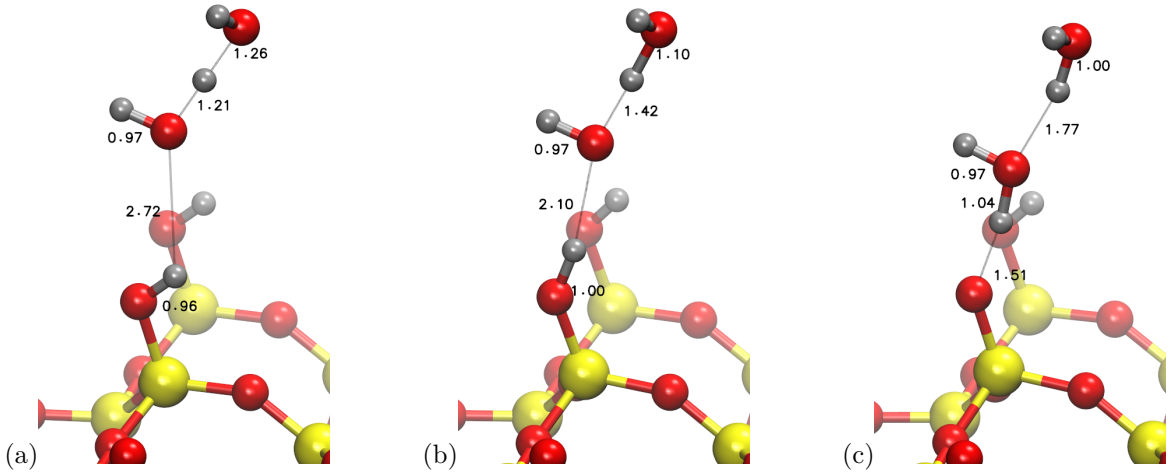

Figure 4.19.: Geometry optimisation of $H_3O_2^-$ above a silanol group at the silica surface. Initial structure is shown in (a). As the optimisation proceeds proton transfer from the silanol to the $H_3O_2^-$ anion occurs, as shown in (b). Image (c) shows the optimised structure, in which the silanol has been deprotonated.

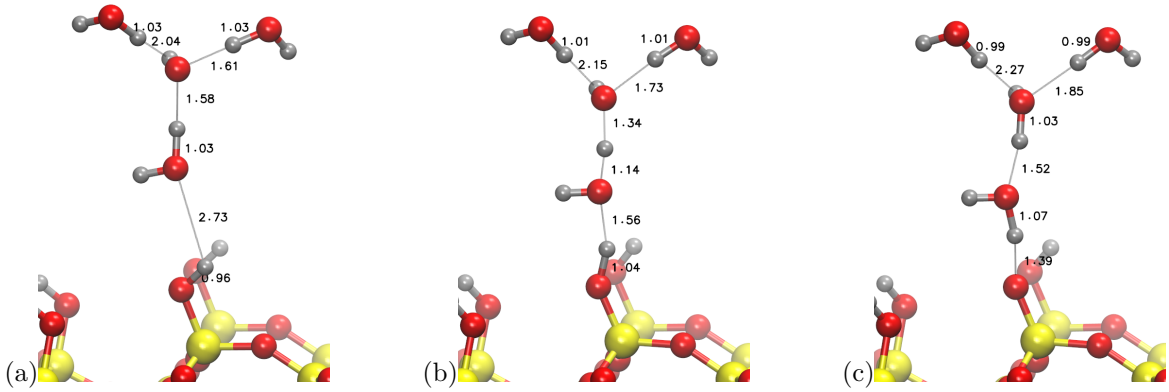

Figure 4.20.: Geometry optimisation of the $H_7O_4^-$ anion above a silanol group at the silica surface. The initial structure is shown in (a). As the optimisation proceeded, Grotthuss transfer of the proton from the surface occurs (b) resulting in a deprotonated silanolate group in the optimised structure (c).

4.5. Conclusions and Future Perspective

A study was performed to validate the DFT calculations and a freely available tool was produced which can assist researchers in similar studies using the ONETEP software. The subsequent DFT study investigated the atomistic nature of protonation-deprotonation processes at the silica-water interface. It showed that, based on ground-state electronic calculations, the hydronium and hydroxide ions can readily protonate silanolate groups and deprotonate silanol groups respectively, whereas water molecules will hydrogen bond (without proton transfer) to both silanol and silanolate groups.

Acid-base reactions were rapid and highly exothermic, which suggests that surface scientists should be cautious when simulating such systems in the context of molecular dynamics simulations which cannot describe bond-breaking and forming. The $Si{-}O^-{\cdots}H_2O$ hydrogen bond length was found to be strongly dependent upon the degree of solvation, which suggests that accurate parametrisation of this bond in classical molecular dynamics simulations requires careful consideration.

Some unexpected and novel observations were made with regard to the hydrogen-bonded structure of the water; for example, it was seen that the classical model of acid-base neutralisation by proton transfer from acid (hydronium ion) to base (silanolate group) can be an oversimplification in hydrogen-

bonded water clusters: the study revealed a new mechanism of protonation in which even hydronium ions distant from the surface can protonate the surface *without losing a proton,* by stabilising the dissociation of water molecules. Deprotonation via hydroxide ions was investigated, and transport via 'proton holes' was observed, which is a mechanism which is much less frequently investigated than proton transfer via the Grotthuss mechanism.

An original aim of this work was to support the development of a predictive and computationally inexpensive model which can capture macroscopic charging dynamics at the silica-water interface, as this is relevant to FET-sensor response. This study highlighted that prediction of the protonation-deprotonation kinetics at silica-water interfaces is non-trivial; one common approach to modelling this from an atomistic-simulation would be to identify the energetics of the transition-state and then utilise Transition State Theory to predict the kinetics. This work has shown that this atomistic approach is likely inapplicable due to difficulties in obtaining a distinct transition state in the complex interfacial hydrogen-bonded network at the surface. It demonstrated that the hydroxide and hydronium ion protonation mechanisms are distinct, despite often being treated as complimentary, indicating that a truly realistic model of protonation-deprotonation kinetics would likely need to treat these processes distinctly. The study suggests that protonation of the surface of water can be modelled as a diffusion-limited, activationless and highly exothermic process which is limited by reorientational motion of the water to form a hydrogen-bonded network. The challenge in building an accurate model of the dynamics of this process lie, however, in capturing the complexity of the energetic and entropic barriers involved in this reorientation. The new mechanism discovered showed that even hydronium ions distant from the surface might catalyse surface protonation, providing an additional layer of complexity to any system-scale modelling.

Due to lack of suitable experimental methods, there is little experimental data available upon surface charging kinetics at a molecular scale. After this work was completed, Agnello et al. published an experimental paper investigating silica surface charging at the silica-water-metal interface. Their experiment involved a rolling-sphere test in which a metal sphere was triboelectically charged and this charge was measured via a capacitively coupled electrode [291]. By investigating the charging rate (pC/s), zeta potential, surface energy and surface resistivity measurements as a function of humidity, they concluded that the charging kinetics are affected by the environment (humidity) and surface modification. As Agnello et al. studied the charging rate between triboelectically charged glass with water/metal, it was not measuring the inherent charging rate of spontaneous auto-ionisation of silica on exposure to water and therefore is not directly comparable to the work herein, however it does show the importance of water in silica-surface charging and represents one of the few available experimental techniques that might measure the kinetics of charging processes directly. Adding an organic film decreased the charging rate by obstruction, and this effect could be reversed by polarising the surface with nitrogen/oxygen plasma processing. This may have relevance to BioFET devices, in which an organic film is often utilised to functionalise the surface prior to biosensing and would suggest that that biofunctionalised sensors have different surface charging kinetics and thereby noise characteristics.

Whilst the work presented in this chapter has shown that the kinetics of protonation-deprotonation are difficult to model based on the fundamental proton-transfer reactions, it may be possible to build an empirical model which simplifies the entire multi-step process (involving water-reorientation followed by proton transfer) into an empirical constant. With this goal in mind, the focus of the following chapter was to find a empirically-parametrised simulation framework that might be suitable for modelling surface-charging at macroscopic time- and length-scales.

5. Kinetic Monte Carlo Model of Dynamic Surface Charging

5.1. Chapter Introduction

Oxide surfaces exposed to water develop a surface charge. This charge varies spatially over the space and in time as the oxide functional groups on the surface undergo protonation/deprotonation, as a consequence of chemical equilibria involving water, hydronium and hydroxide ions [292, 293]. While a detailed understanding of these equilibria can be obtained by the *ab initio* approaches described previously (Section 4.2), these simulation techniques cannot describe the macroscopic time- (minutes to hours) and length-scales (micrometres to centimetres) which are relevant to BioFET response.

Kinetic Monte Carlo (KMC) is a simulation framework that can reach macroscopic time- and length-scales. In this chapter, KMC simulations are presented which model the fluctuations of surface charge as a function of time and space. A motivating hypothesis for this work is that the kinetics of surface charging are vital to understanding some of the noise characteristics of BioFET/Ion-sensitive FET devices, in which the current flowing through the device is highly sensitive to fluctuations at the oxide/electrolyte interface.

For this work, a model based on the well-documented 'Ising Model' was utilised. In this model, the system is represented as a 2D lattice of discrete sites, where each 'site' corresponds to either a protonated ($s_i = 1$) or deprotonated site ($s_i = 0$) [294]. The system free energy was approximated to the electrostatic free energy of a rigid arrangement of point charges, where conformational degrees of freedom were assumed negligible. The probability of a transition from protonated to deprotonated (and *vice versa*) was determined by comparing the free energy between states (protonated/unprotonated) per site on the lattice (proton on a oxide group) and used to assign the relative probability of this transition. The time-scale of the transitions can be empirically parametrised such that the resulting model predicts surface charge fluctuations as a function of time.

This is the first time that this literature model [295, 296] has been implemented in the Zacros Software [297, 298], this software was chosen for its ability to deal with cluster expansions incorporating long-range lateral interactions in a computationally efficiently manner. [297, 298].

In this chapter, the general theory of KMC (Section 5.2), and its implementation in the specific model for surface charging (Section 5.2.2) are presented.. The validity of the model was tested in a comparison with the implementation by Zarzycki (2007) [296] (Section 5.4) and found to be functioning accurately (Section 5.5). The model could be used as a component in a future multi-scale model of BioFET response.

5.2. Background: Kinetic Monte Carlo

The kinetic Monte Carlo (KMC) method is a Monte Carlo method of computer simulation used to simulate the time evolution of processes. The algorithms underlying the KMC algorithm are known

by a variety of other names such as residence-time, n-fold way or the Bortz-Kalos-Liebowitz (BKL) algorithms. KMC is particularly useful for investigating the dynamics of systems in which there are rare events occurring, because the computational speed of the simulation is limited by the slowest event. Hence, KMC can reach much longer time scales than using other simulations techniques that proceed linearly with time, such as classical Molecular Dynamics simulations. KMC also offers the advantage over traditional Monte Carlo approaches that it can be used to study non-equilibrium processes as they evolve through time. The key disadvantage of the technique is that it provides no information of the time-scale of the elementary processes; these time-scales must be parametrised either from *ab initio* calculations or experiments.

5.2.1. General Theory

An overview of the theory and implementation of KMC was published by Chaterjee and Vlachos [299]. In brief, a founding assumption of KMC is that once a transition occurs, it stays in a potential energy basin for a significant period of time before the next basin is visited. Following on from this, a related assumption is that each event is independent of its history, and therefore can be modelled using Markovian state-to-state dynamics (in which only one event can occur at a time, followed by another event). Therefore the evolution of the system is described via the master equation:

$$\frac{\partial P_i(t)}{\partial t} = -\sum_{\mathbf{j}\neq\mathbf{i}} k_{ij} P_i(t) + \sum_{j\neq i} k_{ji} P_j(t), \tag{5.1}$$

where each sum is over all system states, where $P_i(t)$ is the probability of being in state i at a given time and where k_{ij} describes the average escape rate constant from basin i to basin j and therefore k_{ij} can be described as a probability of escape [300]. The KMC literature also describes k_{ij} using other terms such as the transition probability per unit time, microscopic rate, transition rate, jump rate and transition probability [299] and is referred to in this chapter as the 'microscopic rate constant'. The system is propagated via a set of stochastic transitions which satisfy the master equation.

The average time of escape can be written as: $\overline{\Delta t}_{\text{escape}} = k_{ij}^{-1}$. This is often modelled by a Boltzmann distribution for thermally activated processes. If the transition state of a chemical reaction can be obtained, then its microscopic rate constant, k_{ij}, can be predicted from *ab initio* calculations via Transition State Theory [300].

The microscopic rate constant, k_{ij}, has exponential decay statistics, a feature which is important in the derivation of the KMC algorithm. To show this, first consider that from the initial assumption of history independence, the transition probability, k, is a uniform function of time, i.e. for each short increment in time, the system is equally likely to escape from state i to state j.

Defining the transition probability density as $f(t)$, which describes the probability that over a set time dt there is a transition, then $f(t)$ is simply a product of the amount of time that has passed, the current time and the uniform transition probability, k:

$$df(t) = -kf(t)\,dt \Rightarrow \frac{\mathrm{d}f(t)}{\mathrm{d}t} = -kf(t). \tag{5.2}$$

The solution of Equation 5.2 is:

$$f(t) = ce^{-kt},$$

and applying the boundary condition $f(0) = k$ the following expression is obtained:

$$f(t) = ke^{-kt}. \tag{5.3}$$

Equation 5.3 shows that the transition state density of history-independent processes must obey exponential statistics [301]. Given this knowledge, if the correct rate constant 'k' for every fundamental process is provided then the time dependence ('dynamics') of transitions can be described, which is the goal of the KMC algorithm.

These assumptions describe a system in which the dynamics can be simulated as stochastic process, using Markovian state-to-state dynamics in which only one event can occur at a time, followed by another event. This type of process is well-known in the field of Mathematics as a 'Poisson Process' [302]. A useful property of Poisson processes is that a large number of them will have the same behaviour as the sum of the components, i.e. the transition probability density for the whole system, $F(t)$, can be written as:

$$F(t) = Re^{-Rt}, \tag{5.4}$$

where

$$R = \sum_{i=1}^{N} k_i.$$

The core principle of the KMC algorithm is to perform transitions between states whilst ensuring that the transition probability density for the whole system (Equation 5.4) is satisfied. To perform this stochastically, Equation 5.4 can be sampled using pseudo-random values drawn with the correct probability distribution. i.e. uniform deviates, u, ('random' numbers in the range 0 to 1) can be generated such that $Re^{-Rt} = u$. The resulting time between transitions is therefore:

$$t = -\frac{\ln(u)}{R}. \tag{5.5}$$

5.2.1.1. Kinetic Monte Carlo Algorithm

Any algorithm which uses Equation 5.5 is generally termed a KMC method. There are many variations of KMC algorithms with differing efficiencies; a common implementation of the KMC algorithm is as follows:

1. Set the time as $t = 0$.
2. Generate a list of all the rates k_i of all possible transitions in the system.

   Example: For a thermally activated process, generate k via $k = Ae^{\frac{-E_a}{k_b T}}$, where A represents collision frequency, E_a is the activation energy and $k_b T$ is the Boltzmann constant multiplied by Temperature.
3. Calculate the cumulative function $R = \sum_{j=1}^{i} k_j$ for $i = 1, ..., n$ where N is the total number of transitions
4. Obtain a uniform deviate $u \in [0, 1]$
5. Find the event to carry out transition i by finding the i for which $R_{i-1} < uR \leq R_i$
6. Carry out transition i
7. Find all possible transitions in the system and recalculate all of their k_i (if they have changed due to the transition)
8. Update the time with $t = t + \Delta t$ where $\Delta t = -\frac{\log(u)}{R}$
9. Return to step 1

5.2.2. Specific Model of Surface Charging

In this section, the application of the KMC algorithm to surface-charge modelling and the specific model used in this work is described and discussed.

An 'Ising Model' [294] is the basis of the model used in this work. In this model, the system is represented as a discrete 2D lattice of sites in which each is one of two states: either protonated ($s_i = 1$) or deprotonated ($s_i = 0$). This formalism has the advantage that there are many freely available software packages which can evaluate Ising Hamiltonians on regular lattices with high computational efficiency. The Ising model was also a natural choice given that protonation-deprotonation is assumed to be pairwise additive. Although experimental evidence of this assumption is not available, because charges are microscopically distant (approximately a nanometre apart at pH 7.4 for silica surface charge in water [32]), the electrostatic force is assumed to be the dominant interaction which is well known to be additive via the Superposition Principle. A further assumption is that the surface charges are localised. This is a justifiable assumption for oxides, as the surface charge is believed to be localised on hydroxyl functional groups at the surface [303].

The surface charge, σ, is a key experimental observable that the model can provide, calculated as:

$$\sigma = eN_{\mathrm{S}} \left(q_{\mathrm{H}} \theta_{\mathrm{H}} + q_{\mathrm{vacant}} (1 - \theta_{\mathrm{H}}) \right), \tag{5.6}$$

where N_{s} is the surface site density of hydroxyl groups, and θ_{H} is a value between 0 and 1 representing the proportion of the lattice with charged groups, e is the elementary charge and q_i represents the charge of site i. For simplicity, the 1-pK model (Section 3.3.2.1) is used, in which q_i is equal to $q_{\mathrm{H}} = +0.5$ and $q_{\mathrm{vacant}} = -0.55$ [133].

The probability of a transition is calculated by calculating the difference in the system energy before and after a transition (protonation/deprotonation). In order to calculate the system energy, the following Ising model Hamiltonian is used:

$$H = -\sum_i \mu_i^* s_i + \frac{1}{2} \sum_{i,j \neq i} W(\mathbf{r}_{ij}) s_i s_j, \tag{5.7}$$

where: each sum goes over all sites i within the entire lattice; μ_i is the chemical potential of each site and s_i is the 'spin' variable for each site, which represents whether the site is protonated ($s_i = 1$) or deprotonated ($s_i = 0$). $W(\mathbf{r_{ij}})$ represents the pairwise interaction energy between sites i and j, and is calculated within this work using the equation derived by Borkovec et al. for the electrostatic free energy of interaction of two point charges at planar surface-electrolyte interfaces [131, 295, 304, 305]:

$$W(\mathbf{r}_{ij}) = q_i q_j \left[\frac{e^2}{2\pi\epsilon_0\epsilon_w} \frac{e^{-\kappa \mathbf{r}_{ij}}}{\mathbf{r}_{ij}} + \frac{\epsilon_s}{2\pi\epsilon_0} \left(\frac{a}{\epsilon_s} + \frac{1}{\kappa\epsilon_w} \right)^2 \frac{e^2}{\mathbf{r}_{ij}^3} \right]. \tag{5.8}$$

In Equation 5.8, ϵ_0 is the permittivity of free space and ϵ_w is the dielectric constant of bulk unperturbed water. Point charges q_i, q_j are treated as being buried in a interfacial layer with dielectric constant, ϵ_s, at a distance a away from the electrolyte. In this work $a = 1$ Å $\epsilon_w = 80.0$ and $\epsilon_s = 3$. κ is the reciprocal Debye length which was given in Section 3.2.2. Equation 5.8 has previously been applied as part of both equilibrium Monte Carlo [126, 306–312] simulations and MC simulations by Zarzycki and Rosso [296, 313] where their model of the pH/surface-potential relationship of the hematite-electrolyte interface agreed with experimental data [306]. This KMC approach was used by Zarzycki and Rosso to explain the empirical observation that there are two characteristic relaxation times in proton-titration experiments [313].

Note that $W(|\mathbf{r}_i - \mathbf{r}_j|) > 0$, such that increased surface protonation ($s_i = 1$) will result in a more

positive contribution from the $W(\mathbf{r}_{ij})$ term, and therefore a higher energy surface from the Ising Hamiltonian (Equation 5.7).

The chemical potential is defined as $\mu_i = \mu_i^{\ominus} + k_b T \ln(a_i)$, where $\mu_i^{\ominus}$ is the chemical potential in its standard state. For the purpose of the work in this chapter, its choice is arbitrary and so taken to be zero. a_i is activity of protons, which is related to both the chemical equilibrium present and the bulk activity of protons:

$$\mu_i = k_{\mathrm{b}} T \ln(10)(\mathrm{p\hat{K}_i} - \mathrm{pH}), \tag{5.9}$$

where $\mathrm{p\hat{K}_i}$ is the microscopic equilibrium constant of the group given that all other sites are deprotonated and pH is defined as in Equation 5.10:

$$\mathrm{pH} = -\log_{10} a_{\mathrm{H}} \tag{5.10}$$

The charge of each site q_i and the microscopic $\mathrm{p\hat{K}_i}$ will depend upon the choice of model for the chemical equilibrium at the oxide surface. It can be seen from the Ising Hamiltonian (equation Equation 5.7) that decreasing the pH will increase the chemical potential of protons and therefore produce a lower energy surface.

The probability of a transition in the KMC scheme is related to the enthalpy change of the Hamiltonian of the system for that transition, e.g. for protonation:

$$\Delta H^{\mathrm{protonation}} = H(s_i = 1) - H(s_i = 0),$$

i.e. the probability of protonation will be related to More specifically, the functional form of this relationship is a Boltzmann distribution where:

$$r_i^{\mathrm{protonation}} = \min(1, Ae^{-\Delta H}), \tag{5.11}$$

and

$$r_i^{\mathrm{deprotonation}} = 1/r_i^{\mathrm{protonation}}. \tag{5.12}$$

In these expressions, $r_i^{\mathrm{protonation}}$ is the probability of protonation (the term 'transition rate' and various other terms have often used interchangeably, as discussed in Section 5.2). The minimum function in Equation 5.11 simply ensures that the probability of protonation does not exceed 1 (100% chance). 'A' is an empirical parameter which can be used to parametrise the time-scale of each elementary process (in this system, there are only two elementary processes - protonation and deprotonation); without this, the KMC algorithm would operate in arbitrary time.

In summary, it has been shown that the KMC algorithm involves selection of a time between events which is done stochastically, but is appropriately weighted by its respective probability of occurring (Equation 5.5). The most likely transition, and therefore the most frequent, will occur from a high-energy surface to a low-energy surface but the stochastic nature of the Monte Carlo algorithm means that it is entirely possible for a transition to occur that makes the system go from lower energy to higher energy. Hence, as in a real system, surface charge fluctuations over time occur, as opposed to rapidly equilibrating to a constant surface charge. This feature can be used to improve modelling the noise characteristics of FET-sensors as literature FET-sensor noise-modelling has neglected these dynamics, instead focused either on modelling noise within the semiconductor, or due to biomolecule motion [34, 314] and coupling of the electrolyte to the device [33, 80].

5.3. Model Validation: Methods

In order to validate the model, the simulation was performed in arbitrary time (i.e. no parameterisation for the time-scale of elementary processes, $A = 1$) with a surface site density of $1.0\,\mathrm{nm}^{-2}$, using the same settings as used by Zarzycki (2007) [296] . Lateral interactions were truncated to a maximum of the fifth nearest neighbour interactions, (i.e. 3.0 nm distance in the simulation). Zacros version 1.02 was used for this work. The Zacros software framework is well-suited for this particular KMC model because, in this software, the parallel efficiency *improves* with the number of nearest neighbour interactions [298] which means that the range of interactions can be extended to a longer-range at low computational expense. A simple 1-pK model is used (Section 3.3.2.1), in which the charges on each group are +0.5 or−0.5 for protonated and deprotonated sites, respectively. The intrinsic $\mathrm{pK_i}$ of the oxide functional group was set to 10. In the Borkovec model for the electrostatic free energy (Equation 5.8), the following parameters were used: $a = 0.1\,\mathrm{nm}$, $d = 1.0\,\mathrm{nm}$ and $\epsilon_s = 3$. $\kappa = 2.3255\,\mathrm{nm}^{-1}$, based on a 0.5 M 1:1 room temperature electrolyte. Periodic boundary conditions were employed.

The lattice configuration was initialised to empty (no bound protons) and the simulation was run until 25 Monte Carlo (arbitrary) time units had passed, which provided a surface coverage which fluctuated around a single value, assumed to be in equilibrium. A snapshot of the final configuration at pH 10 is shown in Figure 5.1.

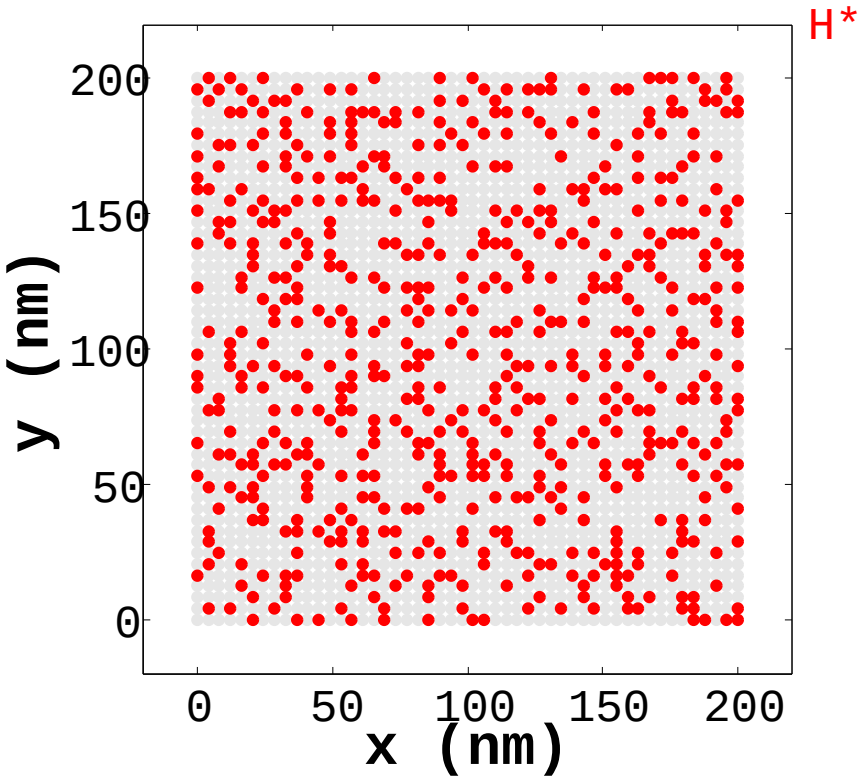

Figure 5.1.: Snapshot of KMC lattice after 30782 KMC Steps or 25 Monte Carlo Units of time. Each grey circle represents an unoccupied site (deprotonated) and red circle a proton bound site (protonated). Site spacing of $1.0\,\mathrm{nm}^{-2}$, pH=10.

5.4. Model Validation: Results

In this section, results of the KMC model are presented for comparison to the results of Zarzycki (2007) [296] to provide evidence that the model functioned as intended.

In order to analyse the results of the KMC simulation, a plot of the fractional coverage (proportion of sites occupied with protons) versus time was generated, as shown in Figure 5.2. This type of plot has a simple relationship to the predicted surface charge, as per equation Equation 5.6. Although surface charge is an experimental observable, the model was not parametrised (pK_i and A) so as to match an experimental system, but instead is used here to validate the KMC model against the result of Zarzycki (2007) [296].

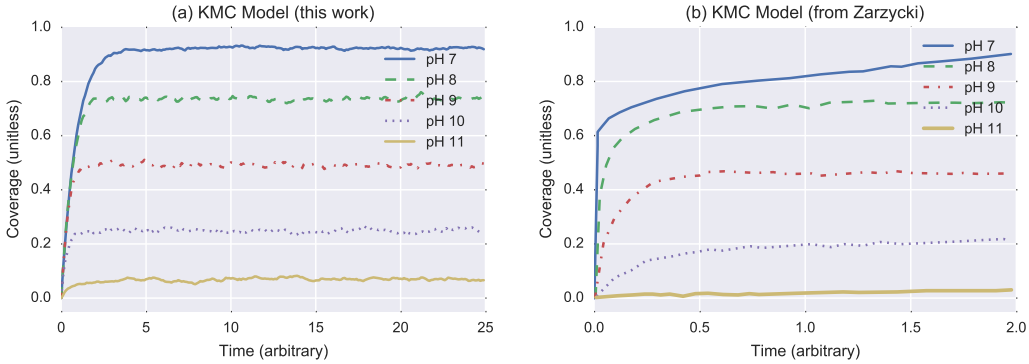

Figure 5.2.: Plot of surface coverage, $\phi_\theta(t)$ (proportion of sites occupied with protons), against arbitrary time over a range of pH (7-10). pK_i=10. The left-hand graph (a) is from the work described herein, whereas the right-hand graph (b) shows data which was extracted from Zarzycki (2007) [296]. Notably, at each of pH, the equilibrium coverage values in the two KMC studies are almost identical. In the 1-pK model used here, when the equilibrium coverage reaches $\phi_{\theta,eq} = 0.5$, the Point of Zero Charge is reached. The Point of Zero Charge in the two KMC studies are both in agreement, providing a Point of Zero Charge between pH values of 8 and 9.

In order to analyse the kinetics of the plot, Zarzycki calculated the non-linear relaxation function ($\phi_\theta(t)$) and relaxation time (τ_θ), which are defined as: [315]:

$$\phi_\theta(t) = \frac{< \theta(t;\mathrm{pH}) - \theta(t_{\mathrm{eq}};\mathrm{pH}) >}{< \theta(0;\mathrm{pH}) - \theta(t_{\mathrm{eq}};\mathrm{pH}) >} \quad \text{and} \quad \tau_\theta = \int_0^\infty \phi_\theta(t)\,\mathrm{d}t, \tag{5.13}$$

where $\theta(t;\mathrm{pH})$ is the surface coverage (proportion of sites occupied with protons) and $\theta(t_{\mathrm{eq}};\mathrm{pH})$ is the coverage at the time in which the simulation has equilibrated. The relaxation time, τ_θ, refers to the KMC 'time' for the system to equilibrate from its initial configuration. A plot comparing the results obtained in this work with those of Zarzycki (2007) [296] is shown in Figure 5.3.

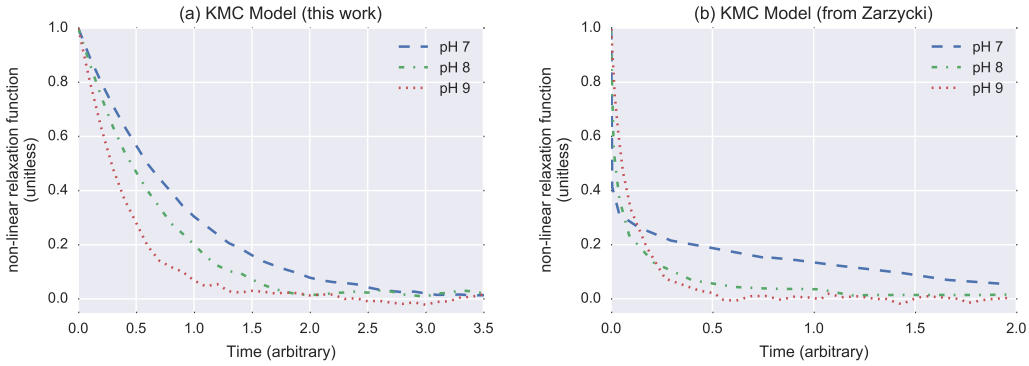

Figure 5.3.: Plot of the non-linear relaxation function (obtained using $\theta(t;\mathrm{pH}) = \theta(25;\mathrm{pH})$) against arbitrary time at pH 7, 8 and 9 for a system with pK_i=10. The left-hand graph (a) is from the work described herein, whereas the right-hand graph (b) is data extracted from Zarzycki (2007) [296]. Both the KMC model within this work (a) and the model of Zarzycki (b) show an decrease in relaxation time, τ_θ , calculated using Equation 5.13 (see Section 5.5 for discussion) with increasingly alkaline pH, but the two models different in the shape of the non-linear relaxation function.

5.5. Model Validation: Discussion

This work is the first time a KMC model based on the model of Zarzycki [296, 307–309] has been implemented in the Zacros software, and has been validated by comparison to the original literature model. The coverage-time plot shown in Figure 5.2 shows the simulated changes in the dynamics of surface protonation as a function of pH using both the Zacros implementation and the original implementation. It can be seen from Figure 5.2 that there is close agreement between them [296], predicting the same coverage value as the time tends towards infinity (equilibrium coverage). Another important property of the model is the Point of Zero Charge, an experimental observable that is defined as the pH at which the net charge of the surface appears to be zero [316]. In the 1-pK model, when the coverage is $\theta = 0.5$, the net charge of the surface is zero. From Figure 5.2, the point of zero charge observed both in this work and that of Zarzycki was between pH 8 and pH 9, supporting that the model used in this work was functioning correctly.

A plot of the non-linear relaxation function was used to calculate the time-scales involved in reaching the equilibrium state, shown in Figure 5.3. The two models differ in the shape of their non-linear relaxation functions: the non-linear relaxation function of this work shows a higher (steeper) initial gradient with increasingly alkaline pH, whereas the model of Zarzycki shows the opposite trend in initial gradient. Although, for example, the pH 7 result has a very steep initial gradient, it takes the longest time to reach equilibrium (with $\tau_\theta = 0$) of the three pH systems shown. This difference in the shape of the non-linear relaxation function might be due to Zarzycki performing their simulation with additional constraints such as, for example, surface heterogeneity, which they consider later in their paper but do not reference with respect to their result shown in Figure 5.3(b). Alternatively, it is possible that it is due to differences in the implementation of the KMC algorithm; Zarzycki did not use the Zacros software but instead utilised their own custom-written code which is not publicly available for comparison.

Relaxation times τ_θ were calculated using Equation 5.13 by integrating each non-linear relaxation curve up to the time of equilibration. For the KMC model presented within this work (a), the time of equilibration was taken to be $t_{\text{eq}} = 3.5$, resulting in an equilibrium coverage, τ_θ, of 0.82, 0.62 and 0.39 for pH 7, pH 8 and pH 9, respectively. For the Zarzycki model, if the time of equilibration is taken as the longest time available from their published data: $t_{\text{eq}} = 1.9$, then τ_θ is calculated to be 0.26, 0.12 and 0.10 for pH 7, pH 8 and pH 9 respectively. Their pH 8 and pH 9 results may have equilibrated by $t_{\text{eq}} = 1$, therefore the τ_θ was also calculated at $t_{\text{eq}} = 1$ and were found to be 0.09 and 0.10 for pH 8 and 9 respectively. Considering either t_{eq} values (1 or 1.9), it was found that $\tau_\theta \approx 0.1$ for both pH 8 and 9 systems. Based on these calculated equilibration times, τ_θ, it can seen that both the KMC model in this work (in Figure 5.3(a)) and the model of Zarzycki (in Figure 5.3(b)) show a decrease in relaxation time with increasingly alkaline pH.

Overall, agreement with the literature is sufficient to conclude that the model used in this work is performing correctly. Predictive use of the model in the context of FET-sensors requires two empirical parameters, the pK_i and the prefactor, A. The pK_i describes the free energy of the reactions, and experimental measurements of the pK_i for oxide-surfaces are available within the existing literature, although there is controversy over the values for silica surfaces, as discussed in the Thesis Background Section 3.3.2.2. The prefactor, A, describes an empirical parameter for the time-scale of each elementary process (in this system, there are only two elementary processes - protonation and deprotonation), without which, the KMC algorithm operates in arbitrary time (as was the case in this validation study). Once parametrised, the model can describe the length- and time-scales relevant to biosensor experiments. Accurate data for this parameter is not currently available from the existing literature, as the focus is mostly on equilibrium physics, rather than

the time-dependent physics required here. This might be obtainable using techniques such as the pressure-jump relaxation method [317] or a 'rolling-sphere' test [291].

5.6. Conclusions and Future Perspective

The model presented in this work, and related models, have been used in the literature to provide a link between the microscopic theory of protonation reactions and the experimental proton-titration data [296, 307–309]. In this work, a new implementation of a literature KMC model was produced using the Zacros software package. The model is capable of modelling changes in surface charge over macroscopic time (up to days) and length scales (up to micrometres) for an oxide-electrolyte interface. Although the values of the non-linear relaxation function differed slightly between this model and that of Zarzycki, the same trend with pH was observed. The equilibrium surface coverage and Point of Zero Charge were in excellent agreement with the model of Zarzycki, suggesting the model is functioning correctly.

Existing models of FET-sensor noise have neglected to consider the dynamics of surface charging, and once suitable experimental data is available for parameterisation of the model, it can be used as a component of a multi-scale FET-sensor model.

6. Modelling the Net Charge of Proteins

6.1. Chapter Introduction

BioFET sensors operate by detecting changes in the electric field at the oxide-water interface due to the binding of charged biomolecules to receptors on the surface. As a result of this, the charge of biomolecules is important for parametrising most models of BioFET response [2, 39, 44, 59]. The distribution of charge within a biomolecule is non-trivial to measure and predict because, like for aforementioned surfaces, it is a non-linear function of pH and ionic strength. Further, it can be modified by the local chemical environment, for example, the charge may differ between its bound or unbound form or due to conformational changes [86].

Proteins are zwitterions under biosensing conditions, typically performed in the pH range 6-8; only at extreme conditions of very low pH ($\text{pH} \ll 2$) are the carboxyl groups neutralised or of very high pH ($\text{pH} \gg 10$) are the amine groups neutralised. The charge of the protein can be experimentally characterised at least in part via its isoelectric point (pI), when the pH is equal to the pI then the mean net charge on the protein is zero. If a static electric field is applied to a medium containing proteins, the pI can be measured as the pH at which the electrophoretic mobility is zero [318].

The pI is very similar to the concept of Point of Zero Charge (PZC) earlier discussed (Section 5.5) in the context of surface protonation-deprotonation reactions. Importantly, electrophoresis measurements are unable to provide information on the spatial distribution of the charge on the biomolecule. In contrast, X-ray crystallography can provide information on the precise spatial arrangement of the atoms within the crystallised-form of the protein, this is often referred to as an X-ray structure. However, the resolution of X-ray structures of proteins is usually insufficient to resolve hydrogen atoms and therefore cannot reliably obtain the protonation state/charge of functional groups [319]. Nuclear Magnetic Resonance (NMR) spectroscopy can provide information on the $\text{p}K_\text{a}$, and therefore charge, of individual amino acids within a native protein, however, the process involves deconvolution of multiple titration events and therefore can be ambiguous [320]. As a consequence of the difficulty in obtaining accurate experimental data relevant to the required application (e.g. bound-state or unbound-state of the protein, pH and ionic strength), simulation is often used to calculate the $\text{p}K_\text{a}$ of each group.

Accurate modelling of biomolecule charge has relevance not only to biosensing, but also drug design [86] and bioengineering [321] which has led to many models being developed for this purpose [322]. In the work presented here, protein charge is estimated using the PROPKA model [85, 86], a popular semi-empirical model for calculating the $\text{p}K_\text{a}$ of amino acids in proteins [85]. The PROPKA algorithm considers the $\text{p}K_\text{a}$ of the groups as the sum of the empirically measured $\text{p}K_\text{a}$ for a small model amino acid plus a semi-empirical computed shift ($\Delta\text{p}K_\text{a}^\text{comp}$). This shift is based on the atomic coordinates within the 3D structure (usually obtained from X-ray crystallography experiments). $\Delta\text{p}K_\text{a}^\text{comp}$ is composed of solvation terms, hydrogen bonding terms and a charge-charge interaction term; these are computed using simple distance functions, with distance/angle functions for the backbone hydrogen bonded terms. This methodology has been shown to be able to predict $\text{p}K_\text{a}$ values to approximately ± 1 of experimental values [322]. Unlike other many other $\text{p}K_\text{a}$ prediction methodologies, PROPKA

does not solve the Poisson-Boltzmann equation and, as a result, no parameter is required to describe the 'effective' dielectric constant for the protein/solvent. Also as a result of this, PROPKA does not provide predictions as a function of ionic strength [323].

With knowledge of this mean net-charge on proteins, and assuming a fixed density of bound biomolecules bound to the sensor surface, it is possible to calculate a value for the change in surface charge density upon biomolecular binding which is used in many BioFET response models. Therefore, in this chapter, the net charge of two proteins are modelled an antibody-antigen system (Section 6.2) and streptavidin-biotin system (Section 6.3), both of which are relevant to biosensing experiments.

6.2. Study 1: Antibody (TNF-α) Charge Modelling

6.2.1. Introduction

Colleagues within the University of Southampton have been working on designing novel low-cost, disposable BioFET devices for biomedical diagnostic applications [58, 232, 324–327] and collaborating with the Sharp Corporation on this goal. In order to validate their sensor, a model biosensing system was chosen which has direct clinical relevance - biosensing of the antigen Tumor Necrosis Factor-α (TNF-α). TNF-α is an inflammatory cytokine which is important in acute inflammation and a diverse range of signalling events [328] and therefore represents an important biomarker which has been used in many biosensing studies [58, 329, 330].

The motivation for the work in this section (Section 6.2) was to provide the net charge at the pH of biosensing for this antibody-antigen system, a crucial parameter in many BioFET models [2, 39, 44, 59]. The results of this study were utilised by Sharp Corporation as part of their modelling efforts.

In the experimental work of the industrial collaborators, a BioFET surface was functionalised with the anti-TNF-α antibody and the BioFET could detect the binding of the protein antigen, TNF-α, when it is captured by the antibody. As the protein charge is affected by its environment, the variation of the protein charge between unbound to bound form is an important property and so calculations were also performed to investigate this phenomenon.

Although the precise structure (X-ray or NMR) of anti-TNF-α used in the experimental work were unavailable, several anti-TNF-α monoclonal antibodies have been commercially developed, and data is readily available for their structures. For example, X-ray structures of the F_{ab} binding regions of Imfliximab (Remicade®) [328] and Adalimubab (Humir®) [331] are available. Both these structures were used in the analysis, on the assumption that they have similar structures to the anti-TNF antibody used in the experiments.

In its native form, TNF-α is believed to present as a trimer, and it has been resolved as a trimer in its X-ray structure [332], but at subnanomolar concentrations, TNF-α has been reported to dissociate into its monomeric components [333, 334]. X-ray structures show that TNF-α binds to anti-TNF-α either as a dimer to the antibody Imfliximab [328] or as a monomer to the antibody Adalimubab [328, 331].

6.2.2. Computational Methodology

Three X-ray structure coordinates were obtained from the RCSB Protein Data Bank [335]. The TNF-α protein structure was in its trimeric form (PDB ID: 1TNF) [332]. The other two structures were of TNF-α protein complexed with the antibody Imfliximab (PDB ID: 4G3Y) [328] and with the antibody Adalimubab (PDB ID: 3WD5) [331]. The MOE 2013.08 Software [336] was utilised to

perform calculations using the frequently used PROPKA algorithm [85, 86]. Charges on the individual amino acids were set using the Henderson-Hasselbalch equation [337] based on their calculated pK_a values.

Infliximab binds to a TNF-α trimer in the X-ray structure but in order to provide a comparison to Adalimubab, which binds to a TNF-α *monomer*, the Infliximab structure was stripped down to a monomeric Antibody-TNF-α:TNF-α complex.

All structures were prepared as follows: All explicit water molecules were deleted and the MOE protein preparation tool was used to cap any unterminated groups not resolved in the X-ray structure. The 'Amber10:EHT' forcefield was used, with reaction-field implicit solvation. The 'Protonate3D' algorithm [336] was run using pH 7.4 and 0.1 M ionic strength and the protein was geometry optimised with a harmonic potential restraint of 0.5 Å deviation, so as remove energetically unfavourable contacts between atoms originating from error in the X-ray structure atomic coordinates. Finally the 'protein properties calculator' was used, which implements the PROPKA algorithm to rapidly calculate the total charge as a function of pH.

Figure 6.1 shows a cartoon of the experimental system, and ribbon representation of the X-ray structures (after preparation) used to calculate net charges.

6.2.3. Results and Discussion

The net charge on the TNF-α protein in its monomeric and trimeric form are presented in Figure 6.2 showing a variation in charge of between $40\,e$ to $-60\,e$ (elementary charge) as the pH ranged from pH 3 to pH 13 and a net charge of between $1\,e$ and $-2\,e$ as the pH ranged from pH 6 and pH 8. This suggests that over the pH range that many biosensing experiments are performed (around pH 7.4), there is a very small charge on the protein. The calculated pI for the trimer was 6.4, which is in reasonable agreement with the experimentally determined pI of 5.08 [329].

For the numerical biosensor model described in the introduction of this study (Section 6.2), the sensitivity of the biosensor is a function of the magnitude of the charge near the surface. In this model, a higher net charge is desirable for optimum biosensing response and therefore the results suggest extreme pH conditions would be ideal for biosensing. However this recommendation is only based on the charge on TNF-α whereas, in practice, large changes in pH away from physiological pH conditions will often denature the protein or alter solubility, resulting in reduced binding affinity. The effects of electrolyte concentration are also neglected in this model, which would have a significant affect on the screening of the biomolecule charges, and also be a function of pH [338]. Further, net charge arguments used within this simple biosensor model have been shown to be insufficient to predict biosensor response, as for example, the spatial distribution of charges will affect the electric field at the biosensor surface [31].

The biosensor works by detecting changes in signal upon binding, and therefore it is relevant to consider also how the charge already present at the surface (Surface/Anti-TNF-α charge) will be modified by the binding of the TNF-α. A fully resolved X-ray structure for the whole of Anti-TNF-α is unavailable, however an X-ray structure is available for the binding region (F_{ab} fragment). The change in charge of this region upon binding to the TNF-α protein was calculated.

The net change in charge of the TNF-α/antibody system was taken as simply the total charge of the antibody F_{ab}...TNF-α complex minus the sum of the charges on isolated TNF-α-monomer and the uncomplexed F_{ab} antibody charge, as expressed below:

$$\Delta\text{Charge} = (F_{ab}...TNF_{\alpha}) - (F_{ab} + TNF_{\alpha}).$$

A plot of the net change in charge for the Infliximab and Adalimubab proteins is presented in Figure 6.3. A broad similarity between the two antibody systems was observed but the differences suggest that for accurate quantitative prediction of the change in charge on complex formation, it would be recommendable to obtain an X-ray structure for the specific antibody being used in the study.

Using simple net charge arguments, these calculations predict that a weak BioFET response will be seen close to pH 8 and pH 10 for Infliximab/TNF-α binding and Adalimubab/TNF-α binding respectively. For both systems, highest response is predicted in highly acidic (pH<4) or basic (pH>11) conditions, which is unfortunate from the perspective of BioFET sensing because at these pH values the protein may be unstable or inactive as it is far from physiological conditions.

6.2.4. Conclusions

This study presents simple calculations which provide an estimation of the charge of the antigen in solution and as a trimer. At physiological pH ranges ($6 \lesssim \text{pH} \lesssim 8$), the results showed that the net charge is relatively insensitive to changes in pH and demonstrated a low-magnitude charge. More extreme pH values led to sharp increases in the magnitude of net charge of the antigen. This can be used to make informed decisions about the choice of experimental pH, although the protein may denature or become insoluble at more extreme pH values.

This study has also provided simple calculations which indicate that differences in structure between different commercially developed forms of the same antibody (anti-TNF-α) can have a significant effect on the optimum pH for biosensing experiments, with a variation of 2 pH units for the predicted point-of-no-signal between the Infliximab and Adalimubab structures. Although these calculations suffer from many limitations, they provide a simple-to-perform estimate from which to make informed decisions regarding an input parameter, the 'magnitude of charge on the biomolecules'. This parameter can be used in most existing models of BioFET response within the literature [2, 39, 44, 59] to estimate the change in surface charge density upon biomolecule binding, and was subsequently used by industrial collaborators (Sharp Corporation).

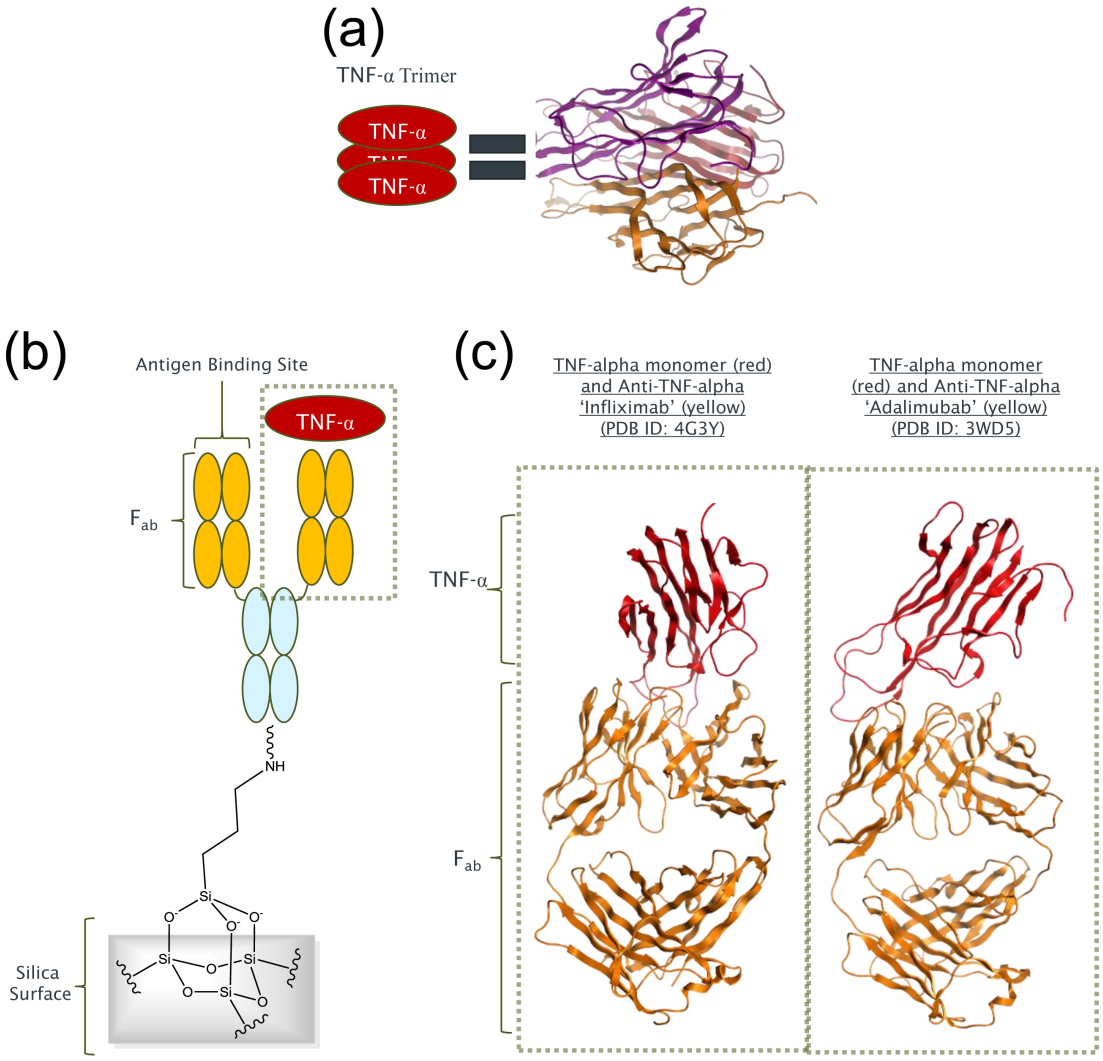

Figure 6.1.: (a) The protein TNF-α is proposed to exist as a trimer in solution, as shown in both a schematic depiction of the three subunits and the X-ray structure (PDB ID: 1TNF) represented using ribbons [332]. (b) A schematic of the antibody functionalised surface with a monomeric TNF-α protein complexed. (c) Ribbons are used to represent the X-ray structures used in this work, which include the F_{ab} region in complex with a monomeric TNF-α protein complexed. The Infliximab anti-TNF-α structure [328] differs slightly from the Adalimubab anti-TNF-α structure [331]. The two antibodies also bind to the antigen at different epitopes (i.e. binding sites). Infliximab has its trimeric antigen truncated to monomeric form, as discussed in the main text. The green dotted box(es) contain the modelled region i.e. the surface and core of the antibody were not modelled in this work.

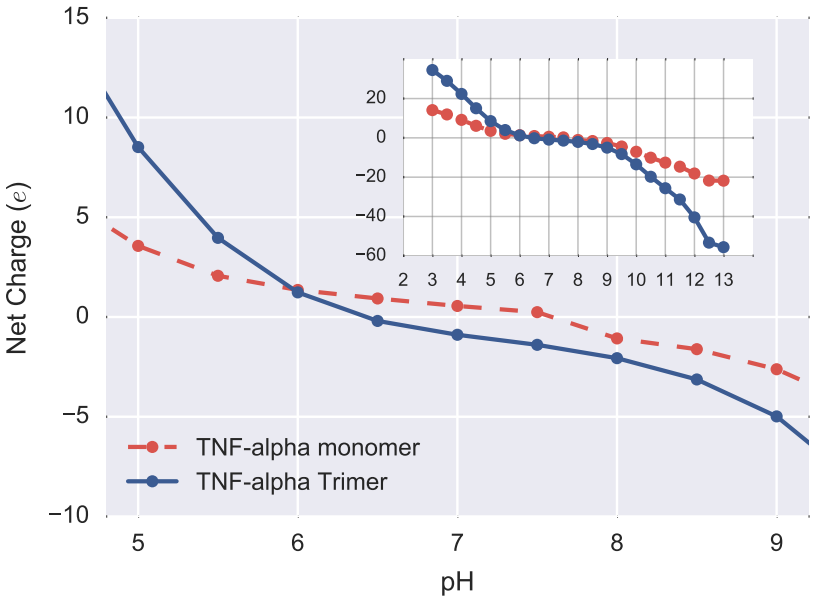

Figure 6.2.: Simulated variation in the net charge of the TNF-α protein, as a function of pH, for both the trimer (blue, solid) and the monomer (red, dashed). The inset shows the full pH range investigated. The monomer was prepared by removing two monomers from the trimer structure and geometry optimising the resulting structure.

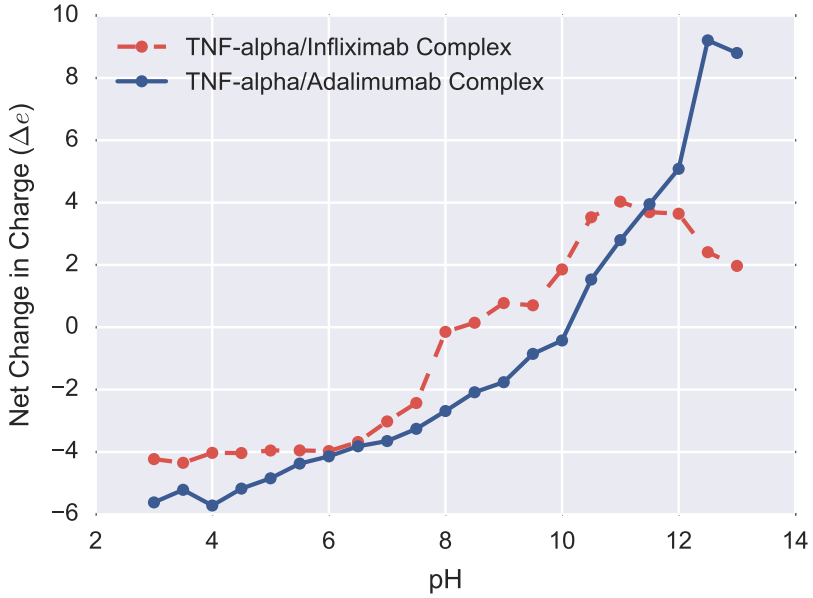

Figure 6.3.: Simulated change in the system charge due to 'binding' calculated as the net charge of the complex minus the sum of the net charges of the free monomer and free antibody. Both Infliximab (blue, solid) and Adalimubab (red,dashed) are shown. Using simple net charge arguments, a larger net change is expected correspond to a larger response by a BioFET sensor.

6.3. Study 2: Protein (Streptavidin) Charge Modelling

6.3.1. Introduction

Streptavidin is commonly used as a model protein in biosensing studies [339] and the ability to detect streptavidin is often used as the initial proof-of-concept for new biosensor designs [59, 78, 340]. The relevance of streptavidin extends beyond a useful model system, as, for example, Gupta et al. have shown that streptavidin has direct clinical relevance in capturing biotinylated interferon γ (MIG), which is a biomarker for several inflammatory and autoimmune disease states [341]. As BioFETs can, in principle, detect the electric field generated by a single elementary charge [233], even small changes in the electrodynamic properties of streptavidin might be detectable, making an understanding of its charge properties important. Surprisingly, despite its common usage in BioFET experiments and most other biosensors [339], a rigorous description of its expected charge as a function of pH is not available. Furthermore, many authors do not report the commercial origin of their streptavidin sample under the assumption that it is not relevant to its charging-properties [19, 70, 99, 342]; in this chapter, this assumption is shown to be a false assumption.

Streptavidin is a tetrameric protein composed of four identical subunits, each with a high-affinity binding site for its ligand, biotin [343]. Strong chaotropic agents (6M urea) result in its dissociation into a dimeric form [344].

Streptavidin is known to have a near-neutral pI; however the reported range of pI values are quite large. For example, Green reported that truncated streptavidin has a pI of 5-6 [345–347]. The pI of streptavidin is reported by Sivasankar et al. as approximately 6.3 [348]. Rockland inc.™, which sells commercial samples of streptavidin, reports a pI of 5-6 [349] whereas Thermo Scientific Pierce™ sell a recombinant, modified, form of streptavidin with a pI of 6.8-7.5. This variation in pI may be due to variation in the biomolecular structure and the difficulty in accurate pI measurement, and highlight the importance of reporting the source of streptavidin samples for both reproducibility and interpretability of BioFET results.

Further, surface-bound streptavidin can have different properties to the free protein. The pI of surface-bound streptavidin has been measured by the Surface Force Apparatus (SFA) experiments of Sivasankar et al. [348], their analysis resulted in a calculated pI of 5.0–5.5. This value may be an underestimate due to neglecting the contribution from the underlying layer. However, a similar, more recent study by Almonte et al. using Atomic Force Microscopy (AFM) calculated a pI of 5.0 +/- 0.5 [350], in good agreement with Sivasankar et al.. These studies might suggest that surface-bound streptavidin is slightly more negatively charged than when in bulk solution.

The net charge of streptavidin was also modelled by De Vico et al. [31] but their study did not present the charge as a function of pH; at pH 7.4 they calculated a charge of $-8.49\,e$ per tetramer. Windbacher et al. [45] state the charge of streptavidin is $-5\,e$ but do not provide their methodology. Neither studies consider how structural variation in streptavidin affects the net charge. Lloret et al. used PROPKA to model the charge of streptavidin as a function of pH predicting a charge of $-4\,e$ and $-5\,e$ for the 'folded' and 'unfolded' protein, but do not state what structure they used or how it was prepared [87]. This study aims to provide a more detailed analysis of streptavidin charge as a function of pH and structure.

6.3.2. Computational Methodology

The X-ray structure for streptavidin complexed with biotin was obtained from the RCSB Protein Data Bank (PDB ID: 1STP) [98]. The coordinates of this X-ray coordinates contain the monomeric

form of streptavidin which is be constructed into the tetramer using appropriate symmetry within the crystal. The MOE 2013.08 Software was used for charge calculations [336].

The structure contains a biotin ligand, which has a carboxyl group. However, in a typical biosensing experiment, this carboxyl group would usually not be present. This is because the biotin is covalently immobilised to a surface via its carboxyl group and a long hydrocarbon linker. Hence, in this model the carboxyl group of the biotin was replaced with a methyl group, making it a neutral molecule as would be the situation in a biosensor. Water was removed in all systems and, in order to generate the structure without its ligand, the biotin ligand was removed and the protein minimised using the same restraints as in the previous section (Section 6.2). The same methodology as Section 6.2 was also used to prepare the structures and calculate the net charges.

6.3.3. Results and Discussion

The simulated net charge for the streptavidin protein, as a function of pH, is shown in Figure 6.4. The stable tetrameric protein, in complex with biotin, showed a simulated pI of 5.04. As expected, on removal of the neutral biotin molecule, the net charge of the protein was insignificantly affected, showing a similar calculated pI of 5.01. This pI is in good agreement with experiments which show pI values in the range 5-6, suggesting the model is performing accurately. Strong chaotropic agents have been reported to result in streptavidin dissociation into its dimeric form [344], therefore for comparison, the highly solvated monomeric streptavidin structure was also studied. The pI of the monomer was calculated to be 5.66 (with and without the ligand bound), showing a slightly more negative net charge at physiological pH.

At pH 7.5, the tetramer was negatively charged with a net charge of approximately $-7.20\,e$, which is the middle of the predictions of the De Vico et al., of $-8.49\,e$ [31], Windbacher et al. of $-5\,e$ [45]. and Lloret et al. of $-4\,e$ to $-5\,e$ [87].

The full sequence of streptavidin, as encoded by the native gene which is naturally expressed in the bacterium *Streptomyces avidinii*, is presented in Figure 6.5, with residues that are often charged shown as coloured and underlined. The blue highlighted region is unlikely to be present in any commercial sample of streptavidin used for biosensing experiments as it is a signalling region that is removed *in vivo* [351]. The structure of streptavidin can vary between commercial preparations due to processing steps which result in artificial truncation of the protein. This has been done, for example, in order to increase the protein solubility [352]. In 1990, Green stated that most, but not all, commercial samples of streptavidin were truncated [347]. Since then, residues 15-159 of the native gene were used to express a recombinant form (i.e. artificially expressed in a non-natural bacterium) of streptavidin with increased solubility in the bacterium *Escherichia Coli,* and some modern commercial preparations of streptavidin[1] are this recombinant form, adding further possibilities for variability between different commercial preparations [353].

With regard to X-ray crystallography studies, Weber et al. reported that they were unable to crystallise non-truncated streptavidin, but successfully crystallised a truncated form of streptavidin, the structure of which was used in this work and is highlighted in green in Figure 6.5 [98]. Analysis of the sequence revealed that, depending on where in the sequence streptavidin is truncated, it is likely to differ in net charge by up to several elementary charges.

[1] e.g. Sigma-Aldrich (Product Id: S067, CAS Number 9013-20-1 MDL number MFCD00082035)

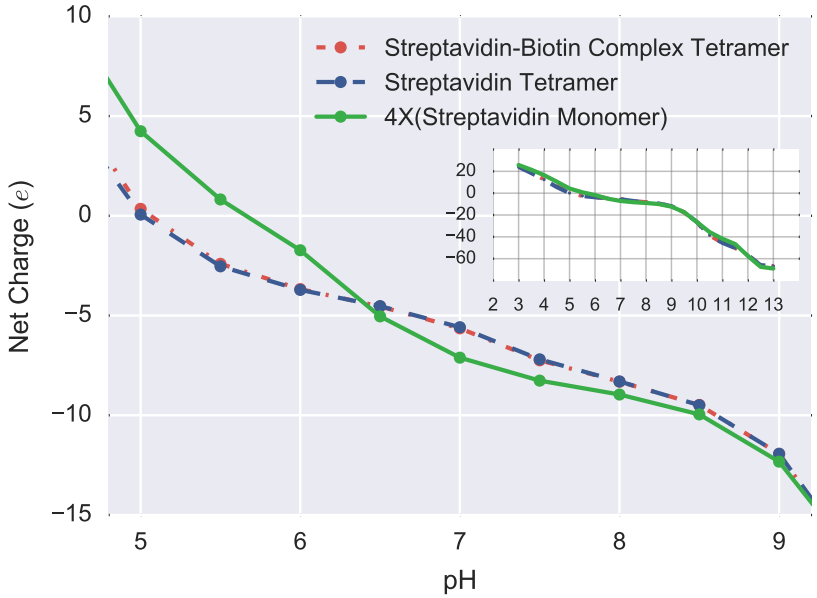

Figure 6.4.: Simulated variation in the net charge of streptavidin versus pH. Three systems were considered: The protein as tetramer in a complex with biotin (red, dashed), with the ligand removed (blue, dash-dot), and, finally, the monomeric form without ligand which is multiplied by four for comparison (green, solid). The inset shows the net charge as a function of pH over the full pH range (2-13). The change in charge due to binding of biotin can be seen by comparing the blue and red curves, and was negligible as expected for a small neutral ligand. Streptavidin is stable in its native tetrameteric form however the monomer is shown as an example of the case of dissociation extreme conditions. The monomer has a slightly different titration curve due to its increased solvation.

6.3.4. Conclusions

Depending on the commercial origin of streptavidin, its structure, and hence charge can vary, a fact which has been little appreciated within the BioFET literature. Given the ability of BioFET devices to, in principle, detect elementary charges, this has significant consequences for the comparability and reproducibility of biosensing experiments in which different streptavidin samples are used.

The pH-dependent charge of streptavidin was presented based on a truncated X-ray structure of streptavidin. The predicted pI was 5.04 which is in good agreement with experimental measurements which find a pI of between 5-6. The net charge at approximately pH 7.4 is relevant to biosensing conditions, and showed a net charge of $-7.20\,e$, for streptavidin, which is in between the predictions available within the literature of $-4\,e$ and $-8.49\,e$.

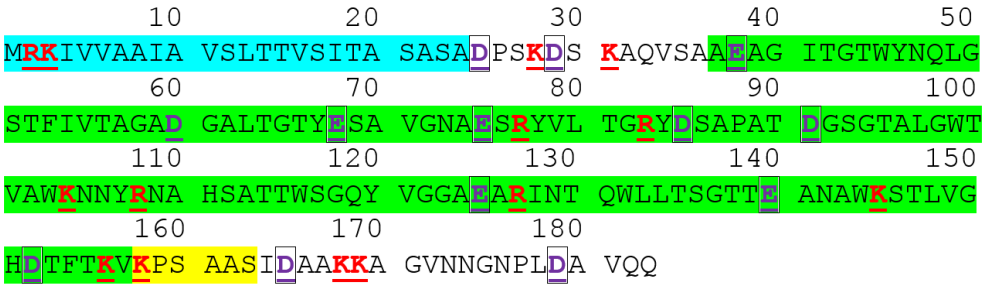

Figure 6.5.: Full sequence of streptavidin from the work of Argarana et al. [351]. The blue region (1-24) corresponds to the N-terminus signalling region that is likely removed *in vivo*. The green highlighted region (37-157) corresponds to the truncated-structure that was resolved in the X-ray crystal structure published by Weber et al. [98] (PBD ID: 1STP) and used in the simulation of net charges presented here. Pähler et al. [352]truncated streptavidin such that residues residues 37-163 were present (i.e. green and yellow regions). At pH 7, residues that based on the intrinsic pK_a of the individual amino acid are usually positively charged (red) or negatively charged (purple, black box outline) are both underlined. This analysis shows, for example, that the streptavidin used by Weber et al. is likely to be $1\,e$ more negative than the net charge of the streptavidin of Pähler et al., due to the positive lysine residue (K) labelled 160 in the figure. Weber et al. comment that the termini are likely flexible or disordered [98], suggesting that the intrinsic pK_a of the amino acids for the non-highlighted and yellow regions are likely reliable.

6.4. Conclusions and Future Perspective

Streptavidin, the most common model protein used in BioFET sensing experiments, as well as in most other biosensors, was investigated by collating literature for the measured sequence and pI of different samples. The analysis showed that the net charge of streptavidin can vary between different commercial sources of the protein, which has consequences for the reproducibility and comparability of biosensor experiments in which the commercial source is not reported. These results will be submitted for publication as part of a novel meta-analysis of the streptavidin-sensing BioFET literature, the results of will be presented in Chapter 8.

In this chapter, two biomolecule interactions (antigen/antibody and biotin/streptavidin) both relevant to BioFET sensing experiments were chosen as model systems and their net charges were calculated as a function of pH. BioFET response is dependent upon the electric field change at the interface upon binding of biomolecules. As a result of this, based on simple net charge arguments, the polarity and magnitude of the net change of charge corresponds to the expected polarity and magnitude of BioFET response. These simple net-charge arguments are commonly invoked to explain BioFET response, but are likely an oversimplification of the relevant physics. In practice, the relevant electric field is also a function of the position of charges upon the molecules on the biomolecule. De Vico et al. are one of few authors in this field to explicitly incorporate the contribution that the orientation and position of charges within a biomolecule might have [31], and the multi-scale BioFET response model of Heitzinger et al. also supports the notion that the position and orientation of charges are vital in modelling FET-response [37, 39, 40]. In the following chapter, simulations are presented which suggest that magnitude of the electric field is primarily determined, not by the magnitude of the charge on the biomolecule or its orientation, but instead by its influence on the surrounding counter-ion dynamics and orientational water polarisation.

7. Electrical Double Layer Dynamics at the Silica-Water Interface

7.1. Chapter Introduction

In results presented thus far, focus has been devoted to modelling the presence (or absence) of charges at oxide-water interface, with little explicit consideration of the dynamics and structure of ions within the electrical double layer. These properties are vital to improving fundamental understanding of biosensing [31, 342, 354], but also drug-delivery [115], prebiotic chemistry [116], geochemical processes (e.g. dissolution reactions [117]) and chemical engineering (e.g. water desalination [118]).

Literature BioFET response modelling is almost exclusively based upon the mean-field Poisson-Boltzmann equation [2, 35–45]. This model treats the charge introduced by the biomolecule as smeared out in an infinitely thin surface charge and therefore cannot accurately describe the changes in electrical double layer structure (and therefore electric field and sensor response) induced by binding of charged macromolecules. Sometimes the Poisson-Boltzmann model is modified to attempt to account for this 'biomolecule layer' as an ion-permeable membrane modelled via a Donnan potential [355–358] or an ion partition energy function [359–361]. Whilst these approaches can in some cases improve predictions from the model, they still neglect effects such as water polarisation, ion-ion correlations and finite-size effects. Given the limitation of current models, in the work presented here, classical Molecular Dynamics simulations were performed which can simulate all of these effects.

In this work, the term Molecular Dynamics, or MD, is used to refer to the simulation of the motion of atoms using classical physics. Distinction is made between other potential uses of the word, for example Born-Oppenheimer Molecular Dynamics (BOMD) in which the forces are computed using DFT, or to give another example, the dynamics of molecules observed in spectroscopic experiments. In MD simulations, chemical bond breaking/forming and electronic polarisation cannot be predicted, however, MD simulations can reach the time-scales required to study how ion dynamics are perturbed in the presence of surface charges and biomolecules. MD can also be used to investigate much larger systems spanning tens of thousands of atoms. Questions which are intractable using Poisson-Boltzmann approaches can be addressed, for example, 'how does the presence of a biomolecule affect the time-dependent fluctuations in the electric field?'

Maekawa et al. [263, 264] investigated the interfacial electrostatic potential at the silica-electrolyte interface. Their experimental work demonstrated a change in BioFET response on addition of increasing concentrations of monovalent electrolyte, and their MD simulations suggested that this effect can be explained as due to strong orientational polarisation of water induced by a compact Stern-like layer of cations at the silica surface. In the work presented within this chapter, the motivation was to extend this investigation to include: (a) how highly charged macromolecules can influence the structure and dynamics of the electrical double layer, and (b) to investigate how electrolyte systems containing multivalent ions behave, the latter of which has received relatively little attention within the atomistic simulation literature, despite their physiological [362, 363] and technological importance [361, 364, 365].

In order to study the behaviour of a charged macromolecule in the electrical double layer, DNA was chosen as the model system as it is well-studied both experimentally [366] and theoretically [367–369] and it has direct relevance to biosensing experiments [361]. A large body of work has been focused on the development of a set of MD parameters which can accurately describe the forces and energies ('forcefield') of DNA, and therefore its dynamics [367, 370]. Similarly, given its technological relevance, various forcefields specialised for the simulation of silica-electrolyte systems have been developed [119, 208–210]. In this work, the COMPASS II forcefield [114, 371] was used in order to retain comparability with the simulations of Maekawa et al. and because it has been parametrised to accurately describe ion-water interactions, and both organic and inorganic systems, making it suitable for interfacial dynamics. Further discussion of the motivation and validation of the choice of model system can be found within the publication in Section 7.3.

7.2. Background: Classical Molecular Dynamics Simulations

A detailed discussion of molecular dynamics is beyond the scope of this work, but several excellent resources are available in this field [372, 373]. A brief overview of the simulation technique is provided here:

Newton's second law of motion, shown in Equation 7.1, provides a major basis for MD simulations. Given an initial set of atomic positions, $\boldsymbol{r}_i(t=0)$, for each atom i, integration of Equation 7.1 provides the atomic positions as a function of time. The force acting on each atom due to all other atoms in the system, at a time t, is written as $\boldsymbol{F}_i(t)$. This can be expressed as the molecular mass, m, multiplied by the acceleration it is experiencing, $\boldsymbol{a}_i(t)$, where its acceleration is itself a function of its position, $\boldsymbol{r}_i(t)$:

$$\boldsymbol{F}_i(t) = m_i \boldsymbol{a}_i(t) = m_i \frac{\partial^2 \boldsymbol{r}_i(t)}{\partial t^2}. \tag{7.1}$$

The force can be expressed as the negative gradient of the potential energy ($\boldsymbol{F}_i(\boldsymbol{r}_i) = -\Delta_i V(\boldsymbol{r^N}, t)$) where $\boldsymbol{r^N}$ is the complete set of 3N atomic coordinates:

$$-\frac{\partial V(\boldsymbol{r^N}, t)}{\partial \boldsymbol{r}_i(t)} = m_i \frac{\partial^2 \boldsymbol{r}_i(t)}{\partial t^2}.$$

In MD, the potential energy expression, V, is parametrised empirically, or semi-empirically, using *ab initio* methods to describe the atomic interactions and is referred to as a 'forcefield'. Sometimes confusingly, the terms 'potential' and 'energy' are often used interchangeably in this field even though they differ by a factor of the charge of an electron; when using atomic units however, as done here, they are equivalent [374].

The potential energy expression is usually divided into an additive sum of intramolecular and intermolecular terms:

$$V = V_{\text{intramolecular}} + V_{\text{intermolecular}}$$

The bonded terms are usually expressed using a simple harmonic potential with corresponding force constant(s), k, similar to a spring. For bond lengths, the potential is a function of the distance between two atoms, and for bond angles, it is a function of the angle between three atoms. The energy of twisting a bond (torsion energy) is often modelled by a simple periodic function between four atoms. The relevant equations are summarised in Equation 7.2, where r_{eq} and θ_{eq} are the equilibrium bond

length, ϕ_{ijkl} is the dihedral angle, and γ_m is a phase which is either 0 or π.

$$\begin{aligned} V_{\text{intramolecular}} = & \frac{1}{2}\sum_{\text{bonds B}} k_{\text{B}}^{r}(\boldsymbol{r}_{\text{B}} - \boldsymbol{r}_{\text{eq}})^2 \\ & + \frac{1}{2}\sum_{\text{bend angles}} k_{ijk}^{\theta}(\theta_{ijk} - \theta_{\text{eq}})^2 \\ & + \frac{1}{2}\sum_{\text{torsion angles}}\sum_{m} k_{ijkl}^{\phi,m}(1 + cos(m\phi_{ijkl} - \gamma_m))^2. \end{aligned} \tag{7.2}$$

For the simplest forcefields, pair-wise interactions are used to represent intermolecular interactions. Between molecules, the attractive interaction potentials for: (a) permanent dipole-permanent dipoles (Keesome), (b) permanent dipole-induced dipoles (Debye), and (c) instantaneously induced dipoles (Dispersion/London) all decay as $\frac{1}{r^6}$. Collectively these terms are therefore often grouped into a 'Van der Waals' attraction term [375]. The short-range repulsion due to the Pauli exclusion principle (i.e. overlapping electron orbitals) is often modelled as a potential that decays as $\frac{1}{r^{12}}$, resulting in the commonly used Lennard-Jones potential, were σ and ϵ_d represents the radius of the minimum of the potential well, and the depth of the potential well, respectively:

$$V_{\text{intermolecular,VDW}} = 4\epsilon_d\left[\left(\frac{\sigma}{r}\right)^{12} - \left(\frac{\sigma}{r}\right)^{6}\right]. \tag{7.3}$$

Finally, electrostatic interactions are incorporated via Coulomb's Law, whereby each atom is assigned a single elementary charge (i.e. $\pm 1\,e$) or partial charge (e.g. $-0.82\,e$). Analytical evaluation of the pairwise sum is highly computationally expensive for large numbers of atoms and therefore, for periodic systems, numerical evaluation of this in periodic systems can be performed via various methods (Section 3.2.3).

Once the potential energy function has been defined, the equations of motion must be numerically integrated. The most common algorithm for this integration is via iterative finite-difference approaches such as the Verlet and Velocity Verlet algorithms [372].

The choice of thermodynamic ensemble is a final, and important, consideration in MD simulation. A detailed explanation of thermodynamic ensembles is beyond the scope of this overview [111]. In short, for a given number of molecules (N) in the simulation, the practice of maintaining a constant energy (E) in a fixed volume (V) represents the simplest ensemble and is referred to as the microcanonical or 'constant-NVE' ensemble. Although simple to implement, it does not provide many useful properties as the energy of the system is constrained. As a result of this, a commonly used ensemble known as the canonical ensemble constrains the number of molecules, the temperature (T) and the volume ('constant-NVT'). This complicates the implementation as an algorithm is needed to maintain the temperature. In real experiments, temperature can be maintained by exchange of heat between the sample and a 'heat bath', i.e. a thermal reservoir which has a heat capacity much larger than the sample, such that when places in contact with the sample the temperature of the reservoir is not significantly changed. Most successful NVT schemes utilise a similar principle which is termed a 'thermostat'.

Most biosensing experiments are done at atmospheric pressure, with the volume of the sample free to expand and contract. It is common to try and model this situation using MD simulations. In order to keep the pressure (P) constant in simulation (NPT, isothermal-isobaric ensemble), a barostat is required in addition to the thermostat. In general, the ensemble is chosen to suit the required thermodynamic properties whilst minimising computational complexity [374].

The primary source of error in any MD simulation originates from the parameterisation of the forcefield. This can be performed using experimental data or *ab initio* calculations, although usually a combination is used. Further sources of error originate from the numerical integration of the equations

of motion. This is particularly a problem for long time-scales, as small errors in the integration will accumulate. Similar errors to those already discussed for *ab initio* are also present, such as errors introduced in computationally efficient evaluation of the electrostatic interactions.

7.3. Journal Paper

This following research involving molecular dynamics simulations of the electrical double layer was published in the journal Physical Chemistry Chemical Physics (PCCP) [376].

Dynamic Behaviour of the Silica-Water-Bio Electrical Double Layer in the Presence of a Divalent Electrolyte

7.3.1. Abstract

Electronic devices are becoming increasingly used in chemical- and bio- sensing applications and therefore understanding the silica-electrolyte interface at the atomic scale is becoming increasingly important. For example, Field-Effect Biosensors (BioFETs) operate by measuring perturbations in the electric field produced by the Electrical Double Layer due to biomolecules binding on the surface. In this paper, explicit-solvent atomistic calculations of this electric field are presented and the structure and dynamics of the interface are investigated in different ionic strengths using Molecular Dynamics simulations. Novel results from simulation of the addition of DNA molecules and divalent ions are also presented, the latter of particular importance in both physiological solutions and biosensing experiments. The simulations demonstrated evidence of charge inversion, which is known to occur experimentally for divalent electrolyte systems. A strong interaction between ions and DNA phosphate groups was demonstrated in mixed electrolyte solutions, which are relevant to experimental observations of device sensitivity in the literature. The bound DNA resulted in local changes to the electric field at the surface; however, the spatial- and temporal- mean electric field showed no significant change. This result is explained by strong screening resulting from a combination of strongly polarised water and a compact layer of counterions around the DNA and silica surface. This work suggests that the saturation of the Stern layer is an important factor in determining BioFET response to increased salt concentration and provides novel insight into the interplay between ions and the electrical double layer.

7.3.2. Introduction

Silica and water form some of the most abundant chemical systems and understanding the interface between the two is important for a large range of applications such as biosensing [31, 342, 354], drug-delivery [115], prebiotic chemistry [116], improved fundamental understanding of geochemical processes (e.g. dissolution reactions [117]) and chemical engineering (e.g. water-desalination [118]). The precise structure and dynamics of this interfacial region, including the Electrical Double Layer (EDL) remains elusive, despite over a century of extensive study [106, 377–380].

Addition of charged macromolecules to oxide surfaces results in a perturbation of the EDL which cannot be accurately described by conventional mean-field models. In this work, electrolyte and biomolecule dynamics were studied with atomistic resolution, providing a detailed description of the electric field generated at the interface. DNA was chosen as an example of a highly-charged

macromolecular polyelectrolyte which is both well-characterised and has relevance to a range of biotechnology applications. In addition, divalent ions were included, which are known to have a strong influence on the structure of the EDL, important to silica dissolution processes [180] and prominent in physiological solutions [363] but despite this, have received surprisingly little attention in the atomistic simulation literature..

One application of this work is in improving understanding of the mechanism-of-action of a promising class of biosensors, termed Biologically-sensitive Field-Effect Transistors (BioFETs). These sensors operate by detecting changes in the electric field within the EDL as a result of biomolecule binding, as shown schematically in Figure 7.1. Reliable and quantitative prediction of changes in the electric field due to biomolecule adsorption, and hence BioFET response, is currently difficult primarily due to the complexity of the EDL.

Not only has the presence of divalent ions recently been shown to increase BioFET sensitivity [361, 364, 365], but the electric field and ion-dynamics at the interface are thought to be crucial in determining Field-Effect Biosensor response.

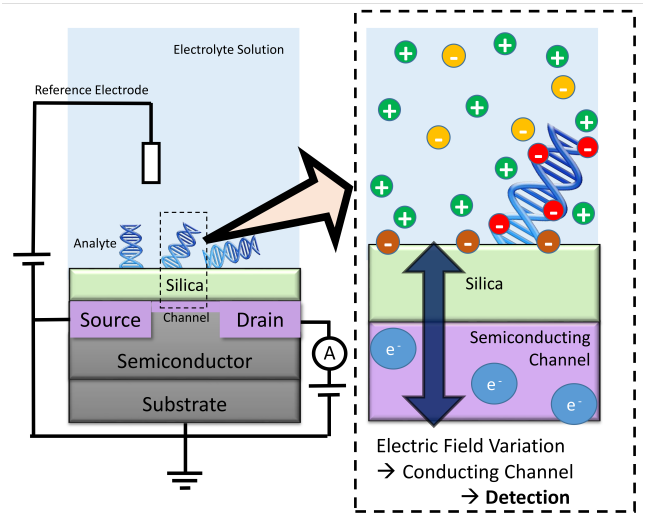

Figure 7.1.: Schematic of BioFET operation. Biomolecules can alter the electric field at the interface, resulting in a measurable change in conductance of the channel. Many factors: surface charge; biomolecule charge; biomolecule orientation; surface dipole; ionic strength; and pH, can affect the interfacial electric field.

7.3.2.1. Importance of EDL Structure and Ion Dynamics in the interfacial region

The most commonly discussed hypothesis for BioFET response is via detecting changes in the electric field due to changes in the 'surface' concentration of ionised groups forming the EDL or charges around biomolecules [84][1]. The interfacial region is thought to be significantly affected by biomolecules; for example the orientation of biomolecules is thought to be important in determining sensor response [31, 37] . The EDL structure in turn can be affected by dense biomolecule layers through ion-exclusion; mathematical models incorporating ion-exclusion effects have been shown to describe experimental signal measurements of DNA hybridisation better than more conventional EDL models [361].

[1] However, another more recently hypothesised mechanism of detection is via detecting changes in EDL dipole moment *in absence of changes* to the surface concentration of ionised groups (e.g. surface charge) or free charges (e.g. electrolyte ions or charged biomolecules like DNA) at the surface. This notion is supported by the experiments of Cahen et al. which showed FET response on addition of neutral organic monolayers, or simply oxygen-water vapour [15]. The importance of the dipole moment of the surface has been supported by the simulations of Heitzinger et al. based on the mean-field solution of the Poisson Equation [40]. This effect could be caused by electronic polarisation of neutral molecules at the silica-water interface.

Recent experimental work recognises the importance of ion dynamics in BioFET engineering, with deterministic information extracted from BioFET signals in the frequency domain of the response [314, 361, 381] which has been explained as a result of adsorption-desorption noise of biomolecules [382] and perturbed charge fluctuations in the EDL [34]. Chung et al. recently performed a particle-based simulation in which charged spherical particles approach the FET-surface [383]. In their work, the noise levels increased as the particles approached, and the results strongly suggest that the thermal-Coulombic motion of ions gathered around the particles induce the Lorentzian shapes in the noise spectrum. Experiments have shown a decrease in low frequency noise with increased ionic strength due to increased screening competition between the EDL and the semiconductor device [33]. Heitzinger et al. suggested a different trend for DNA-sensing, in which they calculated an increase in the standard deviation of the FET channel current with ionic concentration due to an increasingly variable orientation of the DNA [37]. These studies show that addition of a biomolecule, such as DNA, can affect EDL dynamics to the extent that a response can be observed in the frequency domain that is not apparent in the time-domain, even under high ionic strength conditions.

Experiments are not able to unambiguously decouple the signal noise originating from the semiconductor device and the EDL region in the electrolyte solution. Most current EDL theories used in the BioFET engineering field are based on equilibrium, mean-field solutions of the Poisson-Boltzmann Equation. These models offer the advantage of low computational cost and can be accurate for low ionic strength and low surface-charge systems. However, for BioFET systems, this is rarely the case and finite-size steric effects render the Poisson-Boltzmann equation inaccurate without modification. Modern advances in computational power have enabled the exploration of more detailed atomistic models of the structure and dynamics of the silica-water(-bio) interface [32] via both classical [210, 260, 263, 264, 384–388] and *ab initio* Molecular Dynamics (MD) [144, 158, 187, 237, 389].

This work presents MD simulations of EDL Structure and Ion Dynamics in the interfacial region to investigate how a) increased ionic strength and b) addition of DNA perturbs the electric field and charge density at the silica-water interface.

7.3.2.2. Divalent Ions

Physiological samples often contain divalent cations such as Mg^{2+} and Ca^{2+} which serve important biological functions. For example, diffusely associated divalent cations are thought to have a significant effect on reducing the internal stress in DNA/RNA due to screening of the negative charges on the phosphate backbone, as evidenced by experiment [362, 363] and simulation [390, 391].

Divalent ions are also known to be important in the phenomenon of charge inversion, in which the first diffuse layer in the EDL contains more counterions than needed to compensate for surface charge, which is then balanced by a second co-ion layer. This phenomenon has been attributed to two (non mutually-exclusive) mechanisms. One mechanism is via 'specific adsorption' of ions, via forces such as chemical bonding or water-mediated interactions [392]. The other mechanism is via many-body ion-ion correlations, in which the chemical potential near the surface is reduced due to spatial correlations between discrete ions, with the electrostatic interactions outweighing the entropic cost of forming such a highly correlated system [392, 393]. Atomic Force Microscopy (AFM) has measured the effects of charge inversion at the silica-water interface using trivalent and quadrivalent ions at low concentrations ($\leqslant 1\,\mu M$) [394]. These experiments did not demonstrate charge inversion for Mg^{2+}; however, it would be expected that divalent ions would require a higher concentration than trivalent ions. Edel and de Mello have measured the streaming current for silica nanochannels and Mg^{2+} counterions, observing charge inversion for concentrations exceeding approximately $400\,mM$ [395].

From the perspective of BioFET biosensing, the importance of adding divalent and multivalent

salts has also been shown. Jayant et al. have recently shown a significant enhancement in DNA-hybridisation sensitivity upon addition of trace amounts of multivalent salt (Mg^{2+} or Co^{3+}) to a low-concentration NaCl background buffer [359–361]. In their work, a background of 1 mM NaCl was used for hybridisation of ssDNA, and it was found that addition of the complementary strand in 1 mM NaCl with 100 µM Mg^{2+} produced a 350 ± 150% increase in potential shift relative to the control. They found that this effect was only significant when the initial concentration of monovalent salt was low, which supports an ion-competition mechanism. Modelling the DNA as a membrane, they putatively assigned the signal to a combination of (a) increased ion-exclusion of multivalent ions and (b) increased DNA-condensation in the presence of multivalent ions [361].

Other authors support the notion that multivalent salts can have a significant effect on BioFET signal, for example, Rica et al. have observed an increase in DNA hybridisation on addition of multivalent salt (spermidine) and observed a corresponding FET signal indicative of charge inversion at 10 µM spermidine. The signal changed polarity at higher concentrations of spermidine, which they attribute to increased screening of the charge inverted DNA molecule [364]. Shul'ga et al. have reported an almost 100% increase in glucose-sensitive enzyme-FET signal on addition of 0.1 M $MgCl_2$ which they attribute to divalent cations affecting the rate of charge transfer of the enzyme substrate oxidation [365].

Despite the importance of divalent ions, a monovalent electrolyte is typically assumed in MD simulations of hydrated surface-biomolecule systems or mathematical modelling of BioFET signals. Sakata et al. [263, 264, 384, 385] have recently used MD simulations to investigate the EDL structure and dynamics for hydrated silica-water [264, 384] and hydrated silica-DNA systems [385]. This paper extends this work to investigate the effect of divalent Mg^{2+} ions upon the structure and dynamics of the EDL at this technologically important interface.

7.3.3. Computational Methods

Figure 7.2(a) shows a schematic diagram of the simulation domain used in this work. The solid base was modelled as the (100) surface of alpha-quartz (SiO_2) with dimensions of 49.130 Å x 54.050 Å, and a depth of 16.5 Å. At open-circuit potential and biosensing conditions (usually $5 \lesssim \text{pH} \lesssim 9$), silica-water interfaces are negatively charged and therefore the upper surface was defined with a ratio of one fifth $SiO^-/SiOH$ ($0.2\,C\,m^{-2}$), as discussed further in the Appendix H Section 1. The surface charge was then neutralised with Na^+ to produce an electroneutral unit-cell and a solvent box was put into contact with this surface, similar to the method of Zhang et al. [388].

Solvent boxes were prepared with an initial density of $1\,gcm^{-3}$ and a vertical height of approximately 73 Å. Three different solvent boxes were considered: 0 M electrolyte (salt free, corresponding to deionised water); approximately 0.2 M ionic strength electrolyte; and approximately 1 M ionic strength electrolyte, each containing a 1:1 molar ratio of NaCl to $MgCl_2$. The system was geometry optimised for 5000 steps and then NVT dynamics **[372]** were performed at 300 K for 3 ns. Dynamics were performed with the Nosé-Hoover thermostat using a Q ratio of 0.01 **[372]**.

For comparison, three further systems were prepared at each ionic strength, incorporating DNA neutralised with Na^+. DNA was constructed and chemically bonded to the surface following the method of Maekawa et al. [385] and consisted of a d(AAAAAAAAAA) decamer with a complementary base-T strand and a net charge of $-19\,e$. The DNA was superimposed onto the solvent box, the DNA was kept fixed and a 5000 step geometry optimisation was performed for the three cases. Then, water molecules within the DNA were removed and electrolyte ions moved from inside to outside of the DNA. A further 5000 step geometry optimisation and 100 ps of NVT dynamics were performed in order to further relax the system. Similarly to Luan et al. [396], ionic strengths were calculated using the

number of electrolyte ions counted beyond those required to neutralise the silica and DNA. The volume of the liquid system (without DNA and after geometry optimisation) was used for this calculation with the result that stated ionic strengths (0.2 M/1 M) are only estimates. Systems referred to as 0 M contain no added electrolyte in the solvent box, but are electroneutral due to Na^+ associated with the surface layer and DNA. A summary of each the composition of each model is given in Table 7.1 and images of the initial configurations of the DNA systems at varying ionic strength are shown in Figure 7.2.

In the simulations, the COMPASS II 1.2 forcefield was used. This forcefield has been parametrised predominately using *ab initio* data for a wide range of condensed systems; both organic and inorganic systems and on a range of ionic liquids [114, 371]. In this forcefield, the charges are the same as in the COMPASS I forcefield (see for reference the previous work by Maekawa et al. [263, 264, 385]), with the exception of the phosphate group on DNA molecules. For this functional group, the COMPASS II defaults were used; -0.3 for the sugar-linking oxygens, -0.822 for the non-linking oxygens (=O and -O^-) and +0.9246 for phosphorus atoms resulting in a total charge of -1 for each $[RCH_2PO_4C(H)R]^-$substructure. Ewald summation was used for the electrostatic interactions with a 4.184 J mol threshold and an atom-based summation with a 12.5 Å cutoff for the van der Waals interactions. Unless otherwise specified, all analysis was performed over the mean of the last 1 ns with 1 ps windows.

The self-diffusion coefficient, D, was calculated using the Einstein relation. The mean squared displacement (MSD), defined as $[r_i(t) - r_i(t_0)]^2$, where $r_i(t)$ is the position of an ions at time t. The Einstein relation shows that the MSD increases linearly over time as shown in (Equation 7.4), where d is the dimensionality of the system (=3 in this work) and t_0 can be any time point as only relative time differences are considered [397].

$$D = \frac{\left\langle [r_i(t) - r_i(t_0)]^2 \right\rangle}{2d(t - t_0)} \tag{7.4}$$

Therefore self-diffusion coefficient was calculation by linear regression of the MSD against time.

The residence times of molecules coordinated with ions was calculated as per the definition of Impey et al. [398], based on the rate of decay of the time-correlation function with the parameter $t^* = 0$.

The electric field was calculated in this work from the electrostatic forces on a test charge evaluated using two methods: coulomb summation and Ewald summation. In the Ewald sum, the calculation is periodic in x,y and z, whereas in the coulomb summation method, a finite supercell is used. Details of these methodologies can be found in the Appendix H Section 2, each of which have advantages and disadvantages. Briefly, the Coulombic sum method has error from truncation of the full periodicity of the system to a finite sum, and the Ewald sum has error from the contribution of periodic interactions in the z-direction and from the introduction of a non-uniform compensating background charge for orthorhombic unit-cells [252].

7.3.4. Forcefield Verification

An accurate description of ion dynamics and structure is fundamental to simulations of charge dynamics in the EDL. The COMPASS II forcefield [114] was utilised in this study as it has been parametrised using a wide range of experimental data, including both organic compounds and biochemically relevant ions in the condensed phase. One important requirement of the forcefield is that it describes the solvation of ions accurately. In order to validate the forcefield, initial simulations of the interaction between the Mg^{2+} and Na^+ cations, and water were performed.

Element	0 mM	200 mM	1000 mM	0 mM & DNA	200 mM & DNA	1000 mM & DNA
O	8902	8850	8654	8724	8653	8494
H	13171	13067	12675	12830	12688	12370
Si	1200	1200	1200	1200	1200	8494
Cl	0	18	87	0	6	87
Mg	0	6	29	0	6	29
Na	0 (33)	6 (33)	29 (33)	0 (33) [19]	6 (33) [19]	29 (33) [19]

Table 7.1.: Total number of atoms of each element in each simulation. For the 'Na' row, the first number shown is the number of Na^+ ions in the solvent box, the number of round brackets is the number of ions initalised as ion pairs with silanolate ions at the surface, and the number is square brackets is the number of ions initialised to neutralise the DNA phosphate groups.

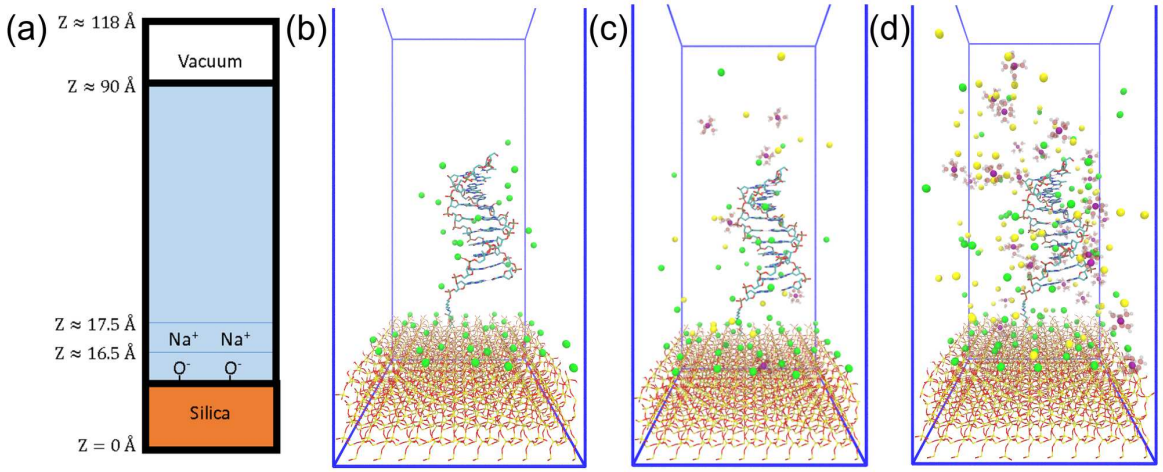

Figure 7.2.: System summary. (a) Side-on schematic of the simulation cell. (b, c, d) Initial configuration of the 0 mM, 200 mM and 1 M ionic strength systems with DNA. Mg^{2+} = Purple, Na^+ = Green, Cl^- = Yellow, O = Red, Si = Gold. Mg-coordinated water drawn as transparent. DNA drawn as stick representation. Videos of each trajectory can be found in the Appendix H.

Figure 7.3 shows a plot of the coordination number for each ion with respect to pure water (oxygen atoms), as well as snapshots of the equilibrium solvation sphere around the (a) Mg^{2+} and (b) Na^+ cations. The calculated coordination number of $Mg^{2+}$was approximately 6, in good agreement with neutron scattering data [399], whereas for Na^+ the coordination number was approximately 5 which is in agreement with neutron scattering of 4.9 ± 1 [400] and *ab initio* MD of 4.6 [401]. The Mg^{2+} cation showed a more ordered solvation sphere than Na^+, demonstrated by the initial steep rise and flat region of the curve for the first compared to the second. The secondary peak in the curve shows evidence of a structured secondary solvation sphere. The difference in structure between the ions is due to the smaller ionic radii and stronger Coulombic attraction of Mg^{2+} resulting in a much tighter, more ordered solvation sphere.

Another test parameter for the forcefield is the diffusion coefficient; the values for Cl^- , Na^+, Mg^{2+} and H_2O are presented in Table 7.2. The calculated diffusion coefficient for water and ions overestimates the experimental value by a factor of approximately 2, which is consistent with other common water forcefields such as TIP3P and is a consequence of the well-known difficulty of accurately capturing water dynamics in empirical forcefields. Agreement within 2- to 3- fold is considered reasonable for diffusion coefficients [402]. It is promising that the relative diffusivity of the ions is in good agreement with experiment, suggesting qualitatively correct dynamics.

Lastly, the calculated radial distribution function of Mg^{2+}/Na^+ ions to H/O atoms in bulk water

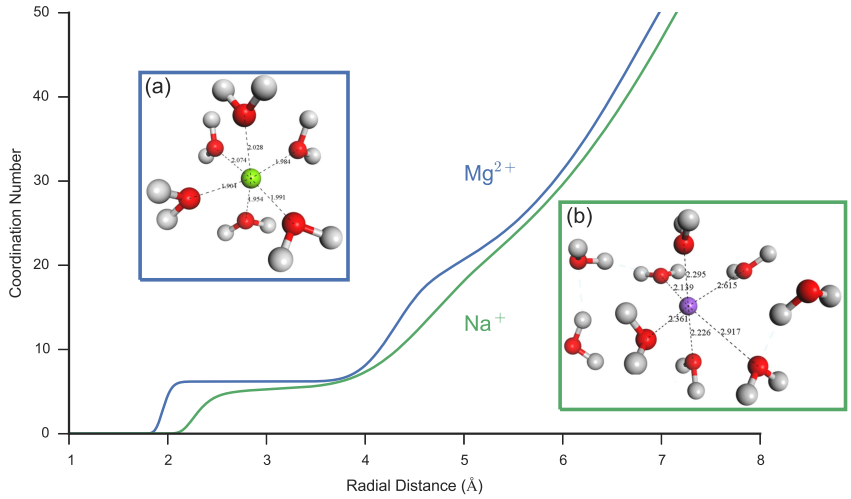

Figure 7.3.: Comparison of the water structure around $Mg^{2+}$and Na^{+} in pure water. Ion-O Coordination number (cumulative number of oxygen atoms) for a single Mg^{2+}(blue) and Na^{+} (green) in pure water. There is an initially steep rise for Mg^{2+} followed by an extended flat region, indicating that there is a highly ordered first solvation shell resulting in a radial region where oxygen is absent. Na^{+} by comparison has a more labile first solvation shell, with less distinct regions occupied by the oxygen atoms. The coordination number for Mg^{2+} is 6.2 in agreement with the expected octahedral coordination. For Na^{+} the coordination number is in the range 4.8-5.5, the lower coordination to Na^{+} is expected due to the less efficient packing around the molecule. The curves also show evidence of a second ordered region for Mg^{2+} compared to Na^{+}. Shown insets are representative snapshots of the first hydration shell of Mg^{2+}(a) and Na^{+} (b) also demonstrating the difference in ordering of the water molecules. Mg^{2+}shows a tighter binding octahedral structure, as opposed to the more diffuse Na^{+}ion. Snapshots were taken from the system after 2 ns of NVT MD. All molecules shown with atoms within 3.5 Å of the ion, bond lengths (Å) shown in black.

is shown in Figure 7.4. The coordination number previously shown in Figure 7.3 was calculated as the integral of this RDF, assuming a fixed box-volume based on the last frame of analysis. Excellent agreement is seen between the simulated RDF peak position for Mg^{2+}-O and Mg^{2+}-H versus neutron scattering experiments; however, exact agreement is not expected due to the higher concentration of the experimental data.

7.3.5. Results and Discussion

The main aim of the work presented in this paper was to investigate the interfacial EDL structure in a range of ionic strengths, with and without the presence of DNA as an example biomolecule. Simulations were performed using 0 mM, 200 mM & 1000 mM ionic strength 1:1 $MgCl_2$ to NaCl electrolyte, with and without DNA. Videos of each of these molecular dynamics simulations can be found in the Appendix H. The simulation results were analysed in sections to examine: ion dynamics in the interfacial region and comparison with accepted Double Layer models; variation of EDL structure with ionic strength; and the effect of the inclusion of the DNA molecule.

7.3.6. Ion Dynamics at the Silica-Water interface

Understanding ion dynamics at the silica-water interface is vital not only for improved biosensor design but also in other fields such as geochemistry, where Na^{+} and Mg^{2+} may be important in dissolution reactions [117], and chemical engineering for the improved design of water-desalination processes [118].

System	Simulated D $1 \times 10^{-5}\,cm^2s^{-1}$	Literature D $1 \times 10^{-5}\,cm^2s^{-1}$
Na^+ 0.2 M in Water	4.1	1.3 (expt.*) [403]
Mg^{2+} 1 M $MgCl_2$	1.3	0.71 (expt.*) [403] 0.50 (expt) [404] 0.60-0.79† [405]
Cl^- 1 M $MgCl_2$	3.6	2.0 (expt.*) [403] 1.4 (expt.) [404] 2.4-2.6† [405]
H_2O Bulk Water	5.9 [263]	2.3 (expt.) [406] 5.2-7.0‡ [407]

Table 7.2.: Simulated COMPASS II forcefield diffusion coefficients compared to literature data. The $Na^+/Mg^{2+}/Cl^-$ diffusion coefficients were calculated using the COMPASS II forcefield at 300 K (with at least 500 ps NPT equilibration) extracting the MSD gradient with respect to time over 8 ps and substituting this into Equation 7.4. The simulation cell was approximately 46.5 $Å^3$, and contained 20 Mg^{2+} and 40 Cl^-. The COMPASS II forcefield, like the widely used TIP3P model of water, overestimates the diffusion coefficient of water by approximately two fold from experiment, likely resulting in the overestimation of D for the ions. This disagreement reflects the difference in concentration between simulation results and experiment, and the difficulty of accurately parameterising the dynamics of water in a simple empirical forcefield; however, the relative ion diffusivities are in good agreement with experiment . * Extrapolated to infinite dilution. † Simulated using TIP4P and OPLS forcefield at very low ionic strength. ‡Simulated using TIP3P forcefield .

7.3.6.1. $Si{-}O^-[Na^+(H_2O)_n]$ Interfacial Structure

The simplest interfacial system, representing deionised bulk water or a concentration of 0 mM, contains the silica surface with sodium ions neutralising the negatively charged silanols. In order to investigate the structure of the interface at this and higher ionic strengths, as in the previous section, the radial distribution functions (Appendix H Section 3) and coordination numbers (Figure 7.5) were calculated for both silanolate-Na^+ and silanolate-water(H).

For the 0mM case, the RDF demonstrated that for the silanolate groups, the mean $O\cdot..H_{water}$ hydrogen bond length was 1.25-2.0 Å and each silanolate was coordinated to 2-3 water molecules. The silanolate-Na^+ coordination number increased with increasing ionic strength, resulting in coordination numbers of 0.95, 1.03 and 1.10 for 0 mM, 200 mM and 1000 mM respectively, as shown in Figure 7.5(a). The increased concentration of cations did not affect the ionic bond length or result in multiple sodium ions per silanolate, but did result in a slight reduction in silanolate-water (hydrogen) coordination resulting in coordination numbers of 2.83, 2.67 and 2.5 for 0 mM, 200 mM and 1000 mM ionic strength respectively, as shown in Figure 7.5(b). One explanation for this is that Na^+ accumulation near the interface results in increased displacement of interfacial water.

The residence time of water molecules to silanolate groups was calculated to be 80 ps (based on a silanolate to hydrogen distance cutoff of 3.5 Å) and showed no dependence on ionic strength. This indicates that with increasing interfacial ionic concentration, the water dissociation rate is not significantly affected (Appendix H Section 4).

In conclusion, increasing ionic strength reduced the equilibrium water coordination to silanolate groups, but the water-silanolate kinetics were not significantly affected.

7.3.6.2. Silica-Na^+ Dissociation

The dissociation of Na^+ions, initialised in contact with the silanolate ions, was examined by observing individual ions and calculating their MSD over time. In all three simulations of the silica-electrolyte interface (9 ns simulation time total), only 2 desorption events were observed, one for the 0 mM system after 600 ps and one for the 1 M system after 1700 ps. In both cases, the dissociation mechanism was the same. Examining the desorption event in the 0 mM system in more detail, the calculated diffusion coefficient for the dissociating ion and the roughly linear increase in MSD with time were typical of a

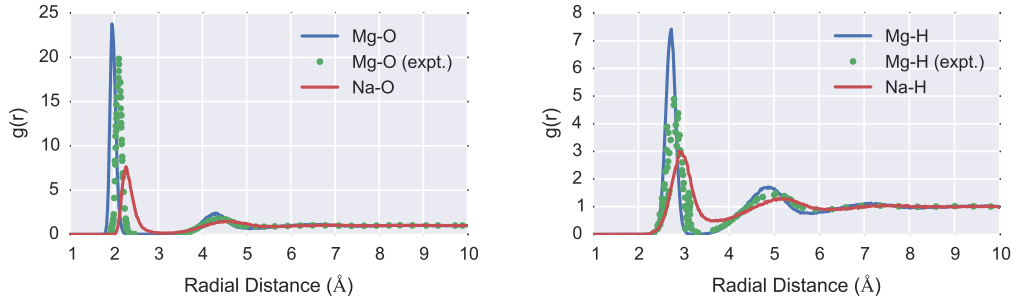

Figure 7.4.: Simulated (red/blue) Mg^{2+}-O (left) and Mg^{2+}-H (right) Radial Distribution Function (RDF) in bulk water, compared to experimental (green) data for Mg^{2+}. For the simulations, 268 water molecules and 1 ion (Mg^{2+}/Na^{+} respectively) were prepared in an approximately 20 Å box, NPT molecular dynamics were performed with 2 ns equilibration and a 8 ns production period over which the RDF was calculated. The neutron scattering data was obtained from Bruni et al. [399] and is measured at 1:83 $MgCl_2$:H_2O concentration. Excellent agreement is seen between the simulated RDF peak position for Mg^{2+} RDFs versus experiment; however, exact agreement is not expected due to the higher concentration of the experimental data. Na^{+} shows a smaller first peak due to its lower water coordination number and shows a more diffuse RDF for its second peak due to its weaker interaction with water. Na^{+} is also in good agreement with experiments; neutron diffraction data for Na^{+} puts the first RDF peak at 2.35 Å for oxygen and the first peak at 2.91 Å for H [400]. These results suggest the COMPASS II forcefield is accurately describing the equilibrium ion-water structural properties.

unbound stochastic ion (shown in Appendix H Section 5). The mechanism of dissociation is shown in Figure 7.6 and was a result of Na^{+} displacement by a fourth water molecule. This resulted in a highly solvated silanolate (coordination number of 4) compared to the average silanolate-water coordination number of 2.5. Sodium desorption kinetics may therefore require a two-step mechanism involving hypercoordination of the silanolate followed by desorption into the bulk.

7.3.6.3. Residence Time of the First Hydration Shell of Sodium

The ionic strength of the solution can affect the solvation dynamics of the ions and therefore the structure of the EDL. In order to quantify the characteristic time-scale that a water molecule remained coordinated with Na^{+}, two systems were considered: the condensed surface layer ($\lesssim 5$ Å from the surface) and the bulk ($\gtrsim 5$ Å from the surface). The calculated residence time was approximately 20 ps and 12 ps for the surface and bulk respectively, with a slight dependence on ionic strength (Appendix H Section 6). The demonstrated increase in residence time at the surface suggests a more kinetically-stable solvation sphere for surface-coordinated ions, and is likely a result of the structuring of water and ions found at the interface. Residence times on the order of picoseconds are consistent with other studies of Na^{+} hydration [408].

7.3.6.4. Magnesium Ion Dynamics

When free magnesium ions approach DNA, it is currently unknown whether the phosphate groups of the DNA displace any of the six Mg^{2+}-coordinated water molecules. Several experiments suggest that Mg^{2+} retains its solvation shell [366], for example, if Mg^{2+}-DNA direct binding was strongly favourable, then Mg^{2+} would be expected to be resolved in X-Ray crystal structures of DNA. Furthermore, fluorescence and thermal melting experiments show no indication of Mg^{2+} directly bound to the DNA [409].

For the duration of all simulated systems presented in this paper, the $Mg_{(aq)}{}^{2+}$ ions retained their octahedral water coordination sphere, essentially remaining a single hexahydrated cluster, $[Mg(H_2O)_6]^{2+}$,

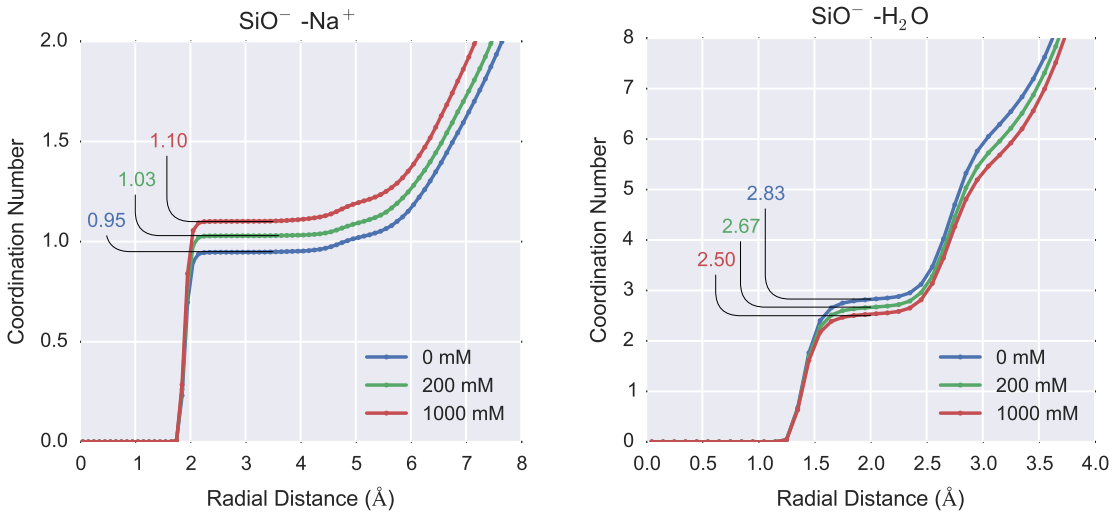

Figure 7.5.: Silanolate- coordination number as a function of 0 mM, 200 mM and 1000 mM ionic strength for silica-water systems. (left) Silanolate-sodium coordination number 0.95, 1.03 and 1.10 for 0 mM, 200 mM and 1000 mM respectively (right) Silanolate-water (hydrogen) coordination number 2.83, 2.67 and 2.5 for 0 mM, 200 mM and 1000 mM ionic strength respectively. Increasing ionic strength resulted in an increase in sodium ion coordination to silanolate ions and corresponding decrease in water coordination.

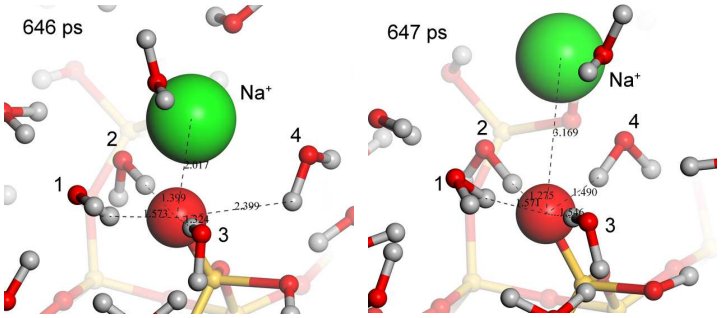

Figure 7.6.: Mechanism of dissociation of Na^+ from the silica surface. Snapshots taken from the 1 M system. At 646 ps water molecules (labeled 1-3) and the Na^+ (green) were bound to the silanolate ion (large red sphere). Water 4 was loosely associated with a $SiO^- \cdots H_2O$ distance of 2.39 Å. Over the next picosecond, Water 4 bound to the silanolate ($SiO^- \cdots H$ distance of 1.49 Å) resulting in dissociation of the Na^+. The Na^+ then remained within 5 Å of the silanolate (second solvation sphere) for 40 ps before diffusing into the bulk.

therefore supporting the notion that Mg^{2+} does not directly coordinate to the DNA. However, NMR experiments have measured a mean water-Mg^{2+}residence time of 1.5 µs [410] and therefore, micro-second time-scale molecular dynamics simulations would be required to sample the full configuration space of the solvent shell.

As discussed, magnesium ions are particularly important in nature and biological systems. Mg^{2+} is known to specifically adsorb to some oxides surface with the extent being highly surface and pH dependent[411, 412]. In this work, only on a few occasions did the magnesium ions remain near (<10 Å) the surface. In the 1 M simulation, a Mg^{2+} that was initialised near the surface remained near the surface for the first 1.5 ns and then adsorbed to a specific site, as shown in Figure 7.7. This was the only example observed of stable (> 500 ps residence time) adsorption of Mg^{2+} to the silica surface, and is the result of the formation of a hydrogen bonded network between two silanolate groups. This result contrasts with the CP/MAS NMR experiments of d'Espinose de la Caillerie et al. which suggested that Mg^{2+} forms direct Si-O-Mg bonds to the surface [413]; this disagreement may be because their system does not contain sodium ions at the surface. These results suggest that

magnesium ions do not readily displace silanolate-bound sodium ions, and that Mg^{2+} interacts with the surface via its solvation shell.

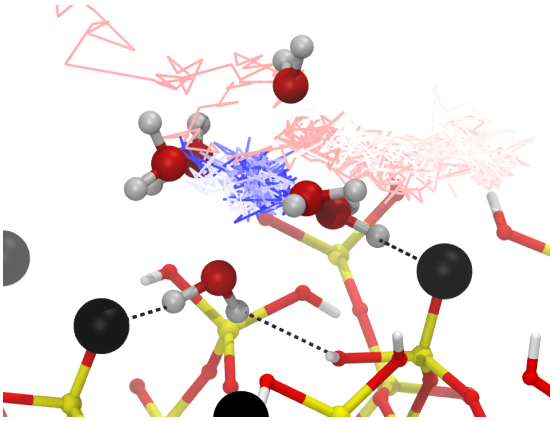

Figure 7.7.: Adsorption trajectory of an Mg^{2+}cation at the silica-electrolyte (1 M ionic strength) interface. Silica and Mg^{2+} coordinating waters are shown from a snapshot taken at 3 ns. Silanolate groups are shown as black spheres. Hydrogen bonds to the surface are shown with black dotted lines. The trajectory of the Mg^{2+} is shown as a time-colored line (red-white-blue) from approximately 750 ps (red) to 3 ns (blue). The blue cluster represents the Mg^{2+} reaching a stable adsorption site, the ion reached the site after 1.7 ns and remained there until the end of the simulation (1.3 ns duration). The Mg^{2+}did not bond directly with the negatively charged silanolate groups, instead forming a hydrogen bonded complex via its hexahydrate solvation sphere.

7.3.7. Poisson-Nernst-Planck (PNP) Double Layer Model

Direct experimental measurement of the distribution of interfacial charge is not available [388], however simulation of the EDL using a continuum model provides a theoretical comparison for expected ion distribution. Due to the high-surface potentials expected at oxide surfaces at the silica-water interface, linearisation of the Poisson-Boltzmann equation is invalid and so the full Poisson-Nernst-Planck equation [414] is solved here with a Stern layer, in a simple Gouy-Chapman-Stern (GCS) model [415] for a mixture of Mg^{2+}, Na^{+} and Cl^{-}. The details of this model are described in Appendix H Section 7.

The surface potential boundary condition was set to be equivalent to the surface charge density in the MD simulation of $0.2\,C\,m^{-2}$ (see Appendix H Section 1 and Section 7 for further discussion); for example, for the same ionic concentrations as the 1 M mixed-valency MD system, a surface potential of 190 mV was used. This surface potential is in quantitative agreement with experimental measurements at the silica-water interface [416]. At this surface potential, the ions have reached their bulk concentration within ~1 nm from the surface, independent of ionic strength (Appendix H Section 7).

The GCS has many limitations in high concentration systems. The dielectric constant of water will not be 80 near the surface due to the stronglocal interactions. Also, correlated motion between ions is not incorporated, which can be particularly important for systems containing divalent ions [392]. A further, well-known limitation of the GCS model is that it does not describe finite-size effects and cannot describe the adsorption of ions to specific sites on the surface or ion-water interactions.

In the GCS, high surface potentials can result in extremely high concentrations < 1 Å from the surface, which is physically unrealistic[2] due to steric constraints. By increasing the Stern layer thickness,

[2]The maximum concentration possible ($c_{max} = a^{-3}$ where a is the ionic radius) given steric constraints is 25 M to 207 M for 2-4 Å cations respectively.

the maximum concentration in the system is reduced, however it is possible to consider extensions to this models to better treat finite-size effects, for example, Kilic and Bazant [414] have presented a model which replaces the Stern layer with a layer of c_{max} cations, or Brown et al. [417] have presented a model incorporating hydration repulsion interactions which produced a Stern-like layer. These approaches share some findings in common, namely there is expected to be a high cationic concentration within ~1 nm of the surface under these surface conditions, followed by the smooth decay into the bulk [388].

In Figure 7.8, the 1 M MD simulation results are compared to the GCS model. As expected, both give the result that the bulk concentration is reached within approximately 1 nm and there is a high cationic concentration within a few angstroms of the surface in a Stern-like layer. The simulations showed that, as discussed previously, strongly favourable solvation of the Mg^{2+} ions resulted in them being distributed roughly evenly through the solvent and not displacing the sodium ions at the surface, with only a small accumulation of ions at the surface (Figure 7.8). This result is in good agreement with experimental observations for Mg^{2+} ions around DNA molecules in which the bound state is characteristic by almost complete hydration and free translation and rotational mobility [418]. These results provide a description that cannot be obtained from the GCS formalism.

These results might help to interpret the experimental results of Jayant et al. demonstrating an increase in DNA hybridisation sensitivity upon addition of trace amounts of divalent salt to a monovalent electrolyte system [361]. In their paper, this effect was modelled using a Poisson-Boltzmann model modified to include the effect of variable ion-permitivity due to a biomolecule layer. The results presented here suggest that the double-layer structure for Mg^{2+} containing electrolyte may not be adequately described by the Poisson-Boltzmann model. This discussion will be extended to the effect of DNA later.

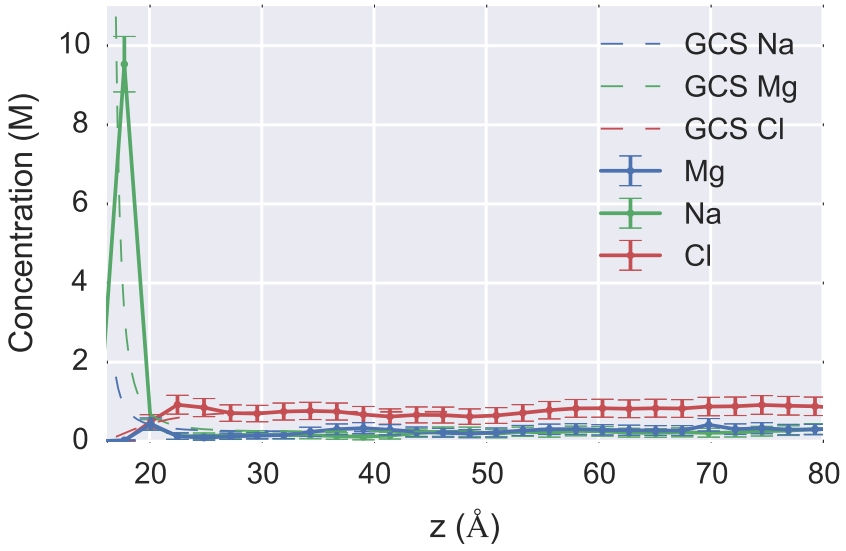

Figure 7.8.: Concentration as a function of z-distance from the surface for the 1 M system (solid lines) compared to the Gouy-Chapman-Stern (GCS) model with a 0.5 Å Stern-layer at 190 mV surface potential (dotted lines). The horizontal lines show the uniform bin size for which the concentration was calculated, and the vertical error bars show the Standard Error of the Mean (SEM). The maximum Na^+ concentration was 9.5 M and 1.6 M for the MD and GCS results respectively. The atomistic simulation corresponds well with the theory for the bulk concentration, and predicts a high concentration Stern-layer within a several angstroms of the surface. The Mg^{2+} concentration however is much more diffuse than predicted by the GCS because Mg^{2+} did not displace sodium ions from the Stern-layer; such atomistic-chemical effects cannot be described within the GCS formalism.

7.3.8. Effect of Ionic Strength on Electrical Double Layer

The effect of increasing the ionic strength on the interfacial charge distribution is shown in Figure 7.9 (A). The cumulative charge is plotted as a function of the distance from the unit-cell origin in the z-direction, this figure was obtained as an integral of the average charge distribution (shown in Appendix H Section 8). By plotting the cumulative charge, the zero-charge value corresponds to the position at which the double layer has fully compensated the surface charge. The charge due to silanolate ions is shown at z=17-18 Å. There is strong similarity between the charge profiles for all ionic strengths and shows positive peaks at 18.5 Å and 21.5 Å, and negative peaks at 20.7 Å and 23.0 Å. These peaks are caused by oriented water molecules; with positive/negative pairs corresponding to layers of oriented water. The similarity between the different ionic strengths indicates that the water is orienting primarily as a result of the surface charge $Si{-}O^{-}/Na^{+}$ layer, as opposed to as a result of the diffuse layer of ions.

The distribution of the diffuse-layer charge ($\gtrsim 3$ Å from the surface) due to the ions can be seen more clearly by plotting the same function but excluding charges from water atoms, as seen in Figure 7.9 (B). With increasing ionic strength, an increase in cationic charge at the interface was observed which overcompensates the surface charge up to around ~1.5 nm from the surface (z=30 Å). This was due to a significant increase of Na^{+} and Mg^{2+} ions within a few angstroms of the surface, outweighing the cumulative charge from increased chloride ion density in the bulk. This effect is sometimes referred to as charge inversion and is known to occur for multivalent electrolytes near highly charged surfaces and highly charged molecules such as DNA [391]. In this work, the charge inversion 1.5 nm from the surface was observed to be roughly proportional in magnitude to the ionic strength change (five-fold increase in ionic strength showed a five-fold increase in charge).

The orientation of the water with respect to the normal of the surface is shown in Figure 7.9 (C). With increasing ionic strength, orientational water polarisation increased. The water orientated H-down towards the negatively charged silica surface near the surface; this oxide-surface induced water polarisation is a well-known phenomenon [145, 157]. As expected, the water becomes isotropic as the bulk is reached.

In the high ionic strength simulations (0.2 M & 1 M), the water reoriented at 19-30 Å so as to be H-up towards chloride ions with oxygen towards the interfacial Mg^{2+} and Na^{+}. MD simulations of the wet-charged interface in the literature have demonstrated water polarisation in monovalent electrolytes [264, 419]. However, the simulations presented here showed that for high ionic strengths, the accumulation of negative charge in the 35 Å to 40 Å region resulted in a secondary layer of H-down orientated water.

In conclusion, with increasing ionic strength, the equilibrium interfacial charge distribution was found to be primarily determined by the water structure around the silanolate and sodium ions at the surface, rather than as a result of the diffuse layer of ions. Charge accumulation and inversion were observed, however, water polarisation lowered the electrostatic energy of the system so as to produce a charge distribution (and therefore potential profile and electric field) which was independent of ionic strength.

7.3.8.1. Local Electric Field in the Electrical Double Layer

In the literature, it has been shown in simulations that increased salt concentration led to positive charge accumulation near to the surface due to rearrangement of ions, partially compensated by oriented water at the Stern-like layer directly above the surface [264]. By taking the average charge density of atoms and solving the Poisson equation, a decrease in the calculated potential in the interfacial layer was observed. A uniform compensating background charge maintained electroneutrality.

In contrast, in the work presented here, the surface was initialised with a layer of compensating sodium ions; which represents an electroneutral system on the length-scale of the simulation domain. At high ionic strengths this is supported by both theory (Section 7.3.7) and experiment [420]. For the low ionic strength ('0 mM') system, this assumption may no longer hold, however the system provides a control against which to contrast the effect of increasing ionic strength. No increase in the interfacial charge density was observed with increasing the ionic strength of the bulk (Figure 7.9 (A) and Appendix H Section 8); this can be explained by the fact that the surface layer was initialised saturated with a 1:1 ratio of counterions. The presence of counterions in the Stern-like layer meant that cation accumulation (Figure 7.9 (B)) was necessarily weaker than the systems of Maekawa et al., and was completely compensated by water polarisation. This observation has significance for interpreting the response of Field-Effect Transistor-sensors which demonstrate a change in signal with changing ionic strength [263]; if many silanolate groups are ion-paired with cations or sterically obstructed from cation binding, e.g. proteins, an amorphous surface, then an increase in ionic strength is predicted to correspond to a weaker change in surface-charge accumulation and therefore device response.

A competing factor that could influence device response that is not considered in this work is the effect of variable surface charge. Titration experiments suggest that increasing ionic strength results in an larger apparent negative surface charge, which may be due to altering the chemical equilibrium of the silanol groups [421].

7.3.9. DNA and the Double Layer

A key aim of this work was to investigate the effect of including DNA molecules on the structure of the interfacial EDL, the electric field and therefore BioFET response. It should be noted that this work does not attempt to provide a detailed analysis of DNA-ion pairing and DNA conformational dynamics, since this topic has received much attention within the literature to date [366, 390, 422, 423].

7.3.9.1. Effect of DNA on Electrolyte Structure

The counterion atmosphere around DNA is an area of extensive research, in which it has been proven that there is a closely associated layer of counterions bound to the DNA regardless of their bulk concentration. The ions in this layer are referred to as 'condensed ions' in the theory of Manning[418] (Onsager-Manning-Oosawa condensation). For concentrations less than approximately 1 M excess NaCl, 76% of the phosphate groups of β-DNA are calculated to be compensated Na^+ within ~10 Å of the DNA surface[424] which has been confirmed to within 10% by NMR experiments [425]. For β-DNA in excess $MgCl_2$ at low concentrations, 44% of phosphate groups are calculated to be compensated by Mg^{2+} (88% charge neutralisation) [418], this percentage charge neutralisation is supported experimentally by Dialysis-monitor titration experiments in which addition of $Mg^{2+}$to 1:1 salt resulted in 85-85% neutralisation [426, 427], and ion condensation has been observed via NMR for divalent ions such as cobalt- and manganese- polyphosphate systems [428]. In mixed electrolyte, NMR experiments have shown Mg^{2+} can displace DNA-bound Na^+ [429].

For the MD simulations presented in this paper, there was significant structuring of the water surrounding the DNA whencompared to the simulations in absence of DNA (Appendix H Section 9). The RDF of the 1 M DNA-electrolyte system is shown in Figure 7.10, and shows that the DNA phosphate backbone attracted a structured counterion cloud in which sodium ions were associated closely with the phosphate groups at approximately 3 Å distance, and formed a secondary more diffuse layer at approximately 6 Å. Consistent with the literature [418], the magnesium ions were bound

to phosphate groups via hydrogen bonding through the solvation shell; the exception was a single magnesium ion that was initialised in contact with a phosphate group..

The percentage of ions per phosphate group was calculated by inspection of the phosphate-ion coordination number shown in the inset of Figure 7.10. Values of 76% and 42% for Na^+ and Mg^{2+} respectively, were calculated following the methodology of Young et al. [430, 431], in which the second inflection point in the RDF curve was used. These values are in excellent agreement with both the Manning condensation theory predictions and experiment, for non-mixed electrolytes NaCl and $MgCl_2$ solutions at low concentrations. It can be noted that, given the divalence of magnesium ions, each phosphate group has +1.69 e counterion charge within approximately 6 Å, which is evidence of charge inversion around the DNA. This is a phenomenon that is expected for multivalent systems at high concentrations[393] and is not described by Manning condensation theory, although more recent revisions of the theory have attempted to incorporate these effects [432].

Continuing from before, in the work of Jayant et al. [361] the enhanced FET-signal was attributed to a combination of (a) increased ion-exclusion of multivalent ions and (b) increased DNA-condensation in the presence of multivalent ions. The simulations presented here show no evidence of Mg^{2+} ion-exclusion in the DNA layer, suggesting that the previous observed increase in signal in multivalent salt was due to other effects, such as Mg^{2+} induced DNA-condensation onto the surface as supported by other MD studies, which discussed Mg^{2+} induced DNA aggregation [391].

7.3.9.2. Effect of DNA on the Surface Potential and Electric Field

The experimental response of BioFET devices is still poorly understood, due to a lack of understanding of the interfacial electric field. BioFETs are capable of detecting single molecules suggesting that even fluctuations in the electric field over nanoscale dimensions can be detected [72, 433]; despite the atomistic length-scale, there have been few atomistic studies which investigated this behaviour.

The full set of data from the simulations of the charge, potential and electric field in the interfacial region for all six cases, with and without DNA, is shown in Appendix H Section 8 for ease of comparison. In the simulations, DNA did not produce a strong effect on the time-average charge distribution of the systems. This might be seen as a counter-intuitive result given that the DNA has a negative charge, however the mechanical flexibility of the DNA-Na^+ system means that the time-averaged charge of DNA *w*ith respect to the surface normal, is expected to be small at any bulk ionic strength.

The electrostatic potential (relative to the silica substrate at 0 V) calculated from this charge distribution, demonstrates that the potential change at the surface ($\Delta_{\mathrm{DNA}}\psi = \psi_{\mathrm{DNA}}(z_{\mathrm{surf}}) - \psi_{\mathrm{noDNA}}(z_{\mathrm{surf}})$) on the addition of DNA was on the scale of millivolts, for example, at the position of the silanolate groups (z_{surf}=17 Å), $\Delta\psi$ =-18 mV, -0.5 mV and -37 mV for 0 mM, 200 mM and 1 M systems respectively. This is of the same order of magnitude as surface potential change measurements for biomolecule-oxide systems [97, 434], however these changes were highly sensitive to the choice of surface coordinate and therefore cannot be taken as accurate prediction of surface potential change due to DNA.

Due to natural thermal fluctuations, this mean potential is variable. In order to explore this variability over time due to DNA, the long-range electric field in to the EDL was calculated by measuring the electric field on a test charge 1 Å below the base of the silica. Figure 7.11 shows the z-component of the electric field as a function of time for all six cases. No significant difference was found between the electric field for the 0 mM ($M = -0.00604$, $SD = 0.00986$) and the 0 mM DNA system ($M = -0.00596$, $SD = 0.0102$) based on an independent samples t-test ($t(2999) = -0.306$, $p = 0.759$). For the higher ionic strength systems, a small but statistically significant change (200 mM system: p=5×10^{-51} ; 1 M system: p =7×10^{-27}) in electric field was observed upon addition of DNA

([E(DNA)−E(noDNA)]≈0.002 V/Å). If this change was a result of the DNA itself and not a result of noise, it would be expected that this response would be strongest in the 0 M system due to lowest ionic screening. Interestingly, the control 0 mM systems showed a 30-40% greater standard deviation in the electric field than the higher ionic strength systems; this indicates that bulk electrolyte may play a role in dampening transient fluctuations in the surface potential.

As discussed previously (Section 7.3.8.1), increasing ionic strength is expected to increase the surface potential [264]. The incorporation of an unsaturated Stern-like layer (silanolate groups at the surface without ion paired cations), produced an electric field which was screened as a result of bulk electrolyte and a compensating background charge introduced by the Ewald summation [264]. In order to compare these simulations with the work presented in this paper, the mean electric field was calculated (shown in the figure in Appendix H Section 10).

In addition, for the simulations presented in this paper, there was no compensating background charge and the system was neutralised by a Stern-like layer and the bulk electrolyte, resulting in a more compact double layer and therefore a weaker electric field by comparison. No trend in electric field change upon ionic strength increase was observed, in contrast to the strong changes in electric field for the unsaturated Stern layer systems of Maekawa et al. ($\Delta E_{[1M]-[0M]} \approx 0.02\,V/Å$) [264]. This comparison suggests that the electrolyte structure within several angstroms of highly-charged interfaces has a far more significant effect on the electric field, and therefore BioFET response, than biomolecule net-charge/orientation. This also emphasises the importance of developing atomistic models with a realistic description of the Stern layer in order to obtain quantitative atomistic prediction of surface potential.

Finally, for nanowire BioFETs, with small cross sections in the semiconducting region, and a correspondingly high sensitivity, the spatial variation of the field is crucial in understanding the response rather than a smeared out average approximation of the behaviour of an artificial one-dimensional system [31, 435, 436]. The spatial variation in the electric field at the surface of the silica was investigated for the control system ('0 mM') and is shown in Figure 7.12. This demonstrated that the DNA is having an effect on the local electric field at the surface; however screening from the condensed sodium ions and polarised water reduced the field such that the field perturbation due to DNA was weak compared to thermal noise.

These conclusions suggest that, with a compact neutralising Stern-like layer on the silica surface and around the DNA phosphate groups, that the electric field due to addition of DNA and ionic strength changes is negligible compared to thermal noise. The most likely explanation for this is that the double layer is more diffuse than determined by these simulations. Over time-scales not currently reachable within this MD model, a more diffuse layer might be formed via sodium ions in the Stern-like layer dissociating due to water- or DNA- induced displacement.

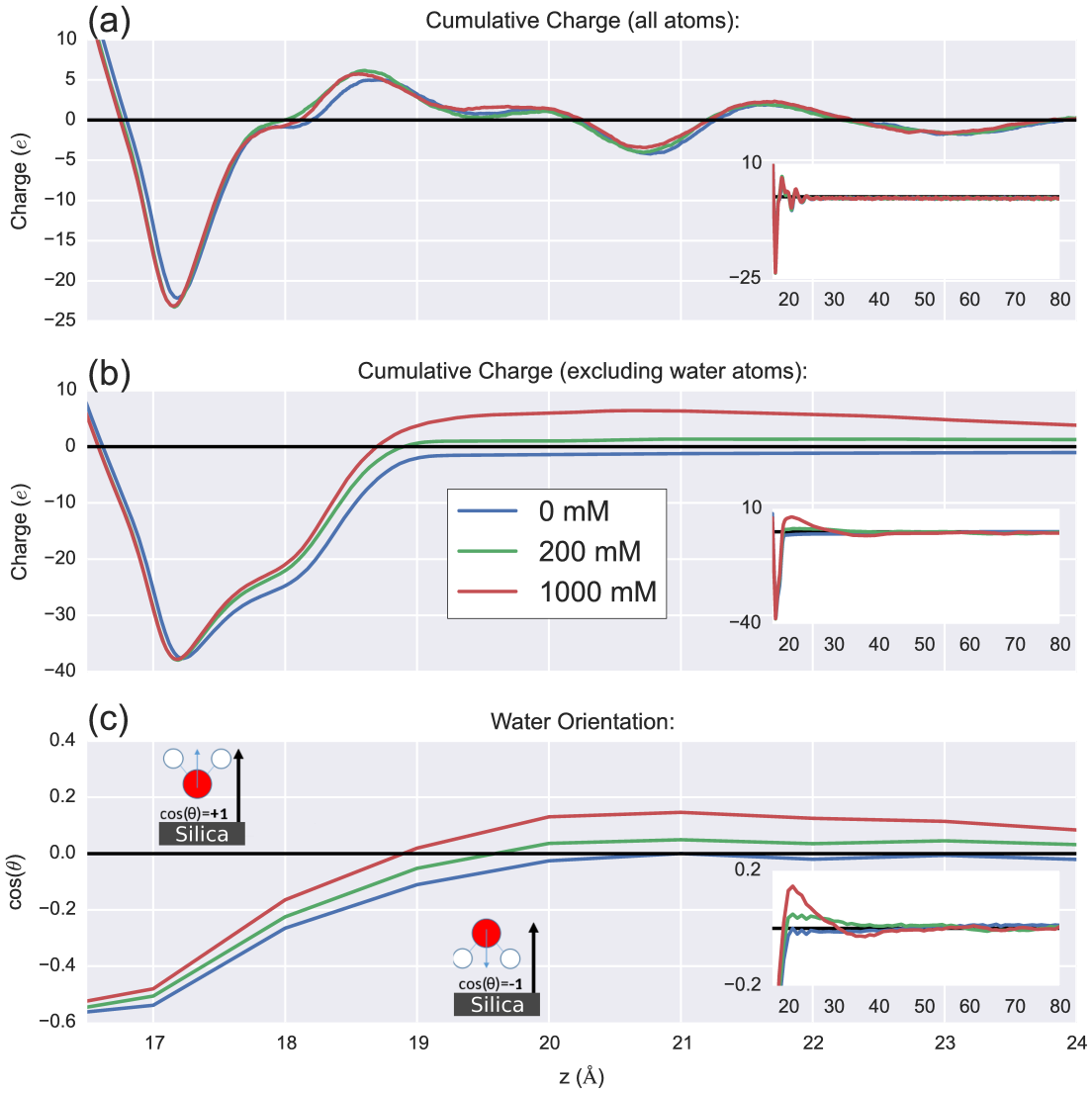

Figure 7.9.: (a) Cumulative charge as a function of distance normal to the silica surface for 0 M, 0.2 M and 1 M systems, this figure is calculated based on cumulative sum of charges in 0.01 Å thick slabs parallel to the xy plane. The negative cumulative charge 16-19 Å was due to silanolate groups at the surface. The subsequent peaks were due to oriented water around the Stern-like layer of electrolyte at the surface. The positive peaks were dominated by hydrogen atoms from water, and the negative peaks by oxygen atoms from water. (b) The same calculation with water charges are excluded. At ~3 Å from the surface (z=~19 Å), zero cumulative charge was reached due to sodium and magnesium cations neutralising the surface charge. At high salt ionic strength there was a net positive cumulative charge 4-15 Å from the surface (z=20-30 Å), sometimes called 'charge inversion' or 'concentration polarisation'. The inset shows the longer range interactions. For the 1 M case, the increased positive accumulated charge near the surface induced a negative layer at 30-40 Å due to chloride ions. (c) The mean orientation of water dipoles ($\cos(\theta)$) relative to the silica-surface normal, as a function of the z-distance from the surface, using 1 Å bins. A negative value indicates the water hydrogens are pointing towards the silica surface, positive that they are pointing away, and 0 indicates either parallel to the surface or isotrophic orientation. Within a few angstroms of the surface (z=15-19 Å) the water molecules are oriented H-down towards the silanolate groups. Further from the surface, with increasing with ionic strength, the water increasingly orientates H-up towards the chloride ions in the double layer and O-down towards the cations in the Stern-like layer. For high ionic strengths, at ~18-23 Å from the surface (z=35-40 Å), the accumulation of chloride anions was sufficient to orientate water H-down, as shown in the inset. As expected, the water became isotropic as the bulk was reached.

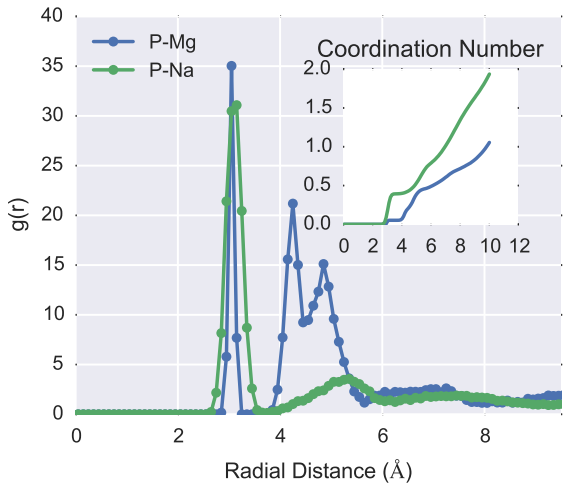

Figure 7.10.: RDF for the phosphate groups of DNA to Mg^{2+} (blue) and Na^{+} (green) respectively, taken from the 1 M silica-DNA system. Na^{+} bound to the phosphate group directly, as seen by the peak at 3 Å. The coordination number is shown as an inset, Mg^{2+} interacted primarily with the DNA through hydrogen bonding of their hexahydrate solvation shell (~5 Å distance).

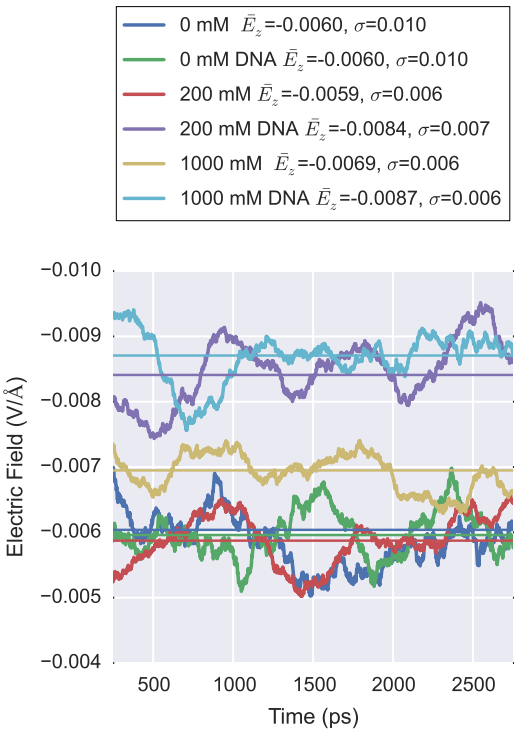

Figure 7.11.: 500 ps moving average of the electric field (z-component) of a test charge 1 Å below the silica substrate as a function of time, calculated using Ewald summation. For each system, the mean electric field, $\bar{E}_z$, is shown in the legend and drawn as a colored line, and the standard deviation, σ, is shown in the legend. The addition of DNA did not produce a significant change in $\bar{E}_z$ field for the 0 mM systems but demonstrated a small, statistically significant change for higher ionic strength.

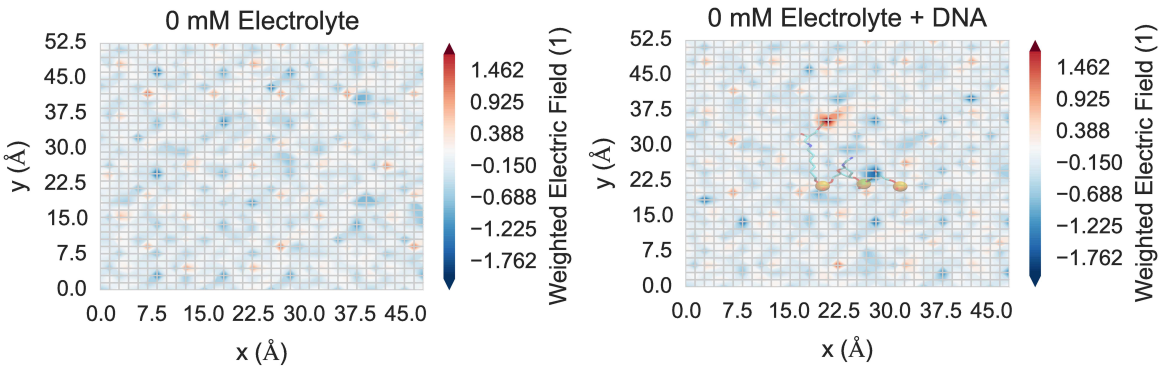

Figure 7.12.: Weighted electric field (z-component) as a function of space in the xy plane at $z = 17\,\text{Å}$ for the '0 mM' system without DNA (left) and with DNA (right). The weighted electric field is the electric field divided by its standard deviation, which acts to filter out highly variable thermal noise. The electric field is calculated using the coulomb summation method, taking the mean of the z-component of the field (1 ps frames over the last 100 ps) on a grid of test charges and displayed as a linear interpolated heat map. In the each figure, regular patterns of negative and positive field are due to the regular arrangement of silanolate and ion-paired sodium ions respectively. In the DNA system (right), DNA atoms close to the surface are shown as a transparent overlay, with negative phosphate atoms shown as orange spheres. The positive region at $y \approx 35\,\text{Å}$ is due to the positive hydrogen atom on the carbon linker and the negative regions at $y \approx 18\,\text{Å}$ and $y \approx 25\,\text{Å}$ are due to the negative charges of the DNA phosphate atoms, showing the DNA is having a local effect on the electric field. The magnitude of the electric field due to the DNA is low due to screening from condensed sodium ions and polarised water.

7.3.10. Conclusions

To the best of the knowledge of the authors, this work presents the first classical molecular dynamics investigation of the bare silica-water interface incorporating magnesium ions, and provides a novel atomistic analysis of the effect of ionic strength and DNA on the electric field and EDL structure at these technologically important interfaces. In this work, Molecular Dynamics simulations were performed using 0 mM, 200 mM & 1000 mM ionic strength 1:1 $MgCl_2$ to NaCl electrolyte, with and without DNA.

As discussed, understanding ion-dynamics at the silica-water interface is important for a range of systems. The simulations presented here demonstrate that increased ionic strength reduces the equilibrium water coordination to silanolate groups without significantly affecting the water-silanolate kinetics. Sodium ion surface-desorption kinetics required a two-step mechanism involving hypercoordination of the silanolate followed by desorption into the bulk. Sodium ions demonstrated a more kinetically-stable solvation sphere when coordinated to the silica-surface, relative to when positioned in the bulk. This was due to the structuring of water at the interface.

Direct experimental measurement of the distribution of interfacial charge is not available [388] and therefore the MD simulation results were compared to a continuum Poisson-Boltzmann model and revealed good agreement with regard to double-layer thickness and sodium ion accumulation. Mg^{2+} did not accumulate significantly at the interface, instead distributing more diffusely than predicted by the Poisson-Boltzmann model. This was as a result of the strong solvation of Mg^{2+} meaning it could not readily displace Na^{+} bound to the surface not described by the Poisson-Boltzmann formalism.

Fundamental understanding of the interfacial charge distribution and electric field is vital to understanding the mechanism of action of Field-Effect Transistor (FET)-sensors. Increasing ionic strength was shown to result in charge inversion due to cation accumulation, an effect which is observed experimentally for divalent ions. The charge inversion 1.5 nm from the surface was observed to be roughly proportional in magnitude to the ionic strength change (five-fold increase in ionic strength showed a five-fold increase in charge). This suggests that charge inversion can begin at lower ionic strengths than those measured by Edel and de Mello [395].

The results demonstrate that the equilibrium interfacial charge distribution was primarily determined by the water structure around the silanolate and sodium ions at the surface, rather than as a result of the diffuse layer of ions. Furthermore, the electrolyte structure within several angstroms of highly-charged interfaces had a far more significant effect on the electric field, and therefore FET-sensor response, than biomolecule net-charge/orientation. This supports the theory that the mechanism of action of FET-sensor is via modification of the surface chemistry (e.g. altering silanol/silanolate chemical equilibria) rather than the traditional picture based on directly sensing the electric field of the biomolecule [342].

As discussed, modelling of the FET-sensor response due to biomolecules is inhibited by a lack of understanding of the interfacial electric field and ion distribution in the presence of biomolecules. The results showed that with DNA present, there was minimal effect of the DNA due to water polarisation and strong screening by the condensed layer of electrolyte. The first calculation of the time-varying electric field for these systems was presented and, by comparison to a low ionic strength control, showed that bulk electrolyte plays a role in dampening transient fluctuations in the electric field and therefore device response.

These results have relevance to interpreting the experimental results of Jayant et al. [361] which demonstrated an increase in DNA hybridisation sensitivity upon addition of trace amounts of divalent salt to a monovalent-electrolyte system, attributed to ion-exclusion from the DNA region and/or DNA

aggregation. The simulations presented here showed no evidence of ion-exclusion from the DNA region and suggests that both (a) the Poisson-Boltzmann model may not be capable of accurately describing the EDL in the presence of mixed electrolyte, and (b) a mechanism other than ion-exclusion, such as DNA aggregation, explains the observed increase in response.

The results also emphasise the role of the Stern-like layer in understanding the response of FET sensors. Changes in the surface charge density (density of silanolate and condensed ions) would be expected to alter the electric field significantly, but in this work, surface charge is effectively fixed due to the long time-scale of cation desorption and no chemical reactions. Future work will address this limitation by varying the surface charge on the surface of the model, which can be compared directly with existing experimental titration data [416]. This will allow quantification of the extent to which the Stern-like layer modulates the electric field and therefore improve fundamental understanding of sensor response.

7.3.11. Supplementary Data

Data supporting this study are available from the University of Southampton repository in Appendix H and at:
http://dx.doi.org/10.5258/SOTON/401018

7.4. Conclusions and Future Perspective

This study investigated the behaviour of a silica-water mixed electrolyte ($NaCl : MgCl_2$) interface in the absence or presence of a highly-charged polyelectrolyte. Whilst many atomistic simulations have investigated the silica-water interface, surprisingly little attention has been given to solutions containing divalent ions given their importance in physiological solution [427, 437]. Divalent ions are known to have a strong influence on the structure of the EDL, be important to silica dissolution processes [180] and are prominent in physiological solutions [363].

The results showed that at nanosecond time-scales, magnesium ions do not displace sodium ions at the silica-water interface. This result can be explained in terms of the highly favourable solvation of magnesium ions, and has relevance to understanding surface-dissolution and the electrical double layer in a range of fields such as geochemistry [117] and nanotechnology [412]. In agreement, with experimental studies, divalent ions resulted in charge inversion within the electrical double layer. Increasing ionic strength reduced the equilibrium water coordination to silanolate groups, but the water-silanolate kinetics were not significantly affected.

With regards to biosensing, the simulations showed the unanticipated result that DNA did not induce a significant change in the spatial- and temporal- mean electric field. Comparison to the simulations of Maekawa et al. demonstrated that the polarisation of water around a Stern-like layer of cations, contributes to a strong reduction in the (long-range) electric field originating from the surface charge and DNA. These results suggest that BioFET response may be dominated not by the net charge of biomolecules, as traditionally thought, but instead by their ability to perturb the Stern-like layer of cations at the interface.

BioFET experiments have shown that changes in surface potential as small as ~10 mV can been measured [70, 78]. A finding of the work presented in this chapter was that the calculated change in surface potential due to biomolecule presence was highly sensitive to the choice of atomic coordinates from which the 'surface' was defined; making direct comparison to measured shifts non-trivial. A range of experimental work has provided the measurement of the interfacial potential at silica-water

surfaces as a function of pH [416] and also the surface charge density as a function of pH [32]. Using this experimental data, the link between the surface potential calculated in atomistic simulations and the experimental measurement might be obtained. This merits further investigation, and future work will study the relationship between the surface charge, Stern-like layer density and the electrostatic potential at the interface.

In the following chapter (Chapter 8), a model biomolecular system is used as part of a meta-analysis of the literature which aims to ascertain to what extent biomolecules can change the interfacial potential, and how biosensor design might be improved in light of this.

8. Quantitative Analysis of FET-Sensor Literature Data: From pH Sensing to Biosensing

8.1. Chapter Introduction

In the previous chapters, the physics at the oxide-water interface has been investigated from individual charging-reactions over femtosecond time-scales to rearrangement of water and ions in the electrical double layer over nanoseconds. These microscopic details provide insight into the physics underlying the mechanism of FET-sensor response, but in order to improve BioFET design, results from the experimental system should also be considered. Therefore in this chapter, a critical review and quantitative analysis was performed based on available experimental literature for real BioFET devices. Analytical modelling was performed, based on the drift-diffusion equations, in which the change in experimentally measured drain current was used to calculate the change in surface potential as a result of biomolecule binding. This provided information on the macroscopic device length-scales (nanometers to micrometers) over experimental time-scales (minutes to equilibration of the device).

Whilst the commercial application of FET-sensors for pH sensing has already been realised [21], their commercialisation for biomolecular sensing is hindered by a poor understanding of how to optimise device design for reliable operation and high sensitivity. In part, this stems from the highly interdisciplinary nature of the problems encountered in this field, in which a knowledge of biomolecular-binding kinetics, surface chemistry, electrical double layer physics and electrical engineering are required. Whilst many reviews in the field of BioFET research exist, they all compare disparate analytes, making quantitative comparisons impossible.

In this chapter, a quantitative analysis and critical review was performed comparing FET-sensor data for pH-sensing with data for sensing of biomolecular streptavidin binding to surface-bound biotin systems. Streptavidin is the most commonly used model protein, and the importance of this system for biosensing applications has already been outlined (Chapter 6). This critical review is the first to provide a systematic, quantitative comparison of BioFET results for a single biomolecular analyte. This review also highlights factors that can influence the response yet have not always been fully appreciated, thereby resulting in sub-optimal experimental design.

For pH sensing, the oxide material is shown to play a dominant role in determining the surface potential shift per pH. This means that the normalised change in drain current, often referred to as 'sensitivity', can be improved by optimising only two parameters - the oxide material at the surface and the transistor 'quality'. An important motivation for this work was therefore to investigate whether a similar trend holds for biomolecular BioFET experiments.

8.2. Background: FET-sensor Characterisation and Performance Metrics

8.2.1. Reference Electrode

An ideal reference electrode provides a stable reference potential which is independent of changes in the solution, and can also be biased in order to control the properties of the transistor in a similar way to the gate electrode of a MOSFET transistor, as outlined in Section 3.1.3.1. As previously introduced, the liquid gate voltage, V_{g}, set by the reference electrode is often stated to be required for a reliable and stable signals. Nonetheless, it is not uncommon for devices to be fabricated without a reference electrode in the liquid [61, 65, 77, 78, 438] and instead, a voltage is applied through the substrate, which acts as a pseudo-reference electrode and is referred to as a 'back-gate' voltage (V_{bg}) [73].

8.2.2. Threshold Voltage

The threshold voltage (V_{T}) can be qualitatively described as the gate voltage at which the device turns 'on', i.e. a significant drain current flows through the device. More quantitatively, it is defined in MOSFET theory as the gate voltage that causes the potential at the surface of the semiconductor to reach significant inversion; 'significance' being judged to be the point at which the concentration of charges in the inversion layer (Section 3.1) are much greater than the impurity concentration in the semiconductor substrate [30]. Binding of analyte to the surface of a FET-sensor results in a change in the oxide-electrolyte surface potential which is equal to the change in surface potential at the semiconductor-oxide interface. Consequently, the measured shift in threshold voltage, ΔV_{T}, is directly proportional to analyte binding, assuming that the transistor is operated under an electrostatic-gating mechanism [53].

An example of a violation of the assumption of electrostatic gating would be when the metal contacts to the semiconductor are not well-passivated and therefore insufficiently protected from direct interaction with the analyte. This can result in changes to the metal-semiconductor work function and thereby a signal which is not originating from an electrostatic gating mechanism [53, 439, 440]. Heller et al. have described how plots of the drain current (I) against the reference electrode voltage (V_{g}), herein referred to as '$I - V_{\mathrm{g}}$ graphs' can be used to as a tool to identify the mechanism of FET operation [53].

8.2.3. Subthreshold Region

In a traditional MOSFET, when the gate voltage is less than the threshold voltage ($V_{\mathrm{g}} < V_{\mathrm{T}}$) and the semiconductor is only weakly inverted, the drain current is usually referred to as the 'subthreshold current' and the device is said to be operating in the 'subthreshold region'. This region is often used for FET-sensors [60, 73, 441, 442] as the drain current increases exponentially with the shift in threshold voltage:

$$I \propto \exp\left(\frac{\ln(10)(V_{\mathrm{g}} - V_{\mathrm{T}})}{\mathrm{SS}}\right), \tag{8.1}$$

where 'SS' is the 'Subthreshold Slope' - a parameter which measures the susceptibility of the transistor to generate a change in drain current for a change in the gate voltage (V_{g}) [30].

If a larger gate voltage is used and the drain current is low (i.e. when $V_{\mathrm{g}} > mV_{\mathrm{ds}} + V_{\mathrm{T}}$, where m is a constant related to the Subthreshold Slope [30]), then the change in drain current becomes linearly dependent upon changes in the threshold voltage and this region is referred to as the 'linear region'

[443]. Parasitic resistance occurs when analyte-insensitive regions of the device contribute significantly to the resistance; this is low in the subthreshold region as the semiconducting channel resistance is much higher than the parasitic resistance in this region [324]. Upon sensing analyte, the change in drain current divided by the initial drain current is a common measure of sensor performance (as discussed in Section 8.2.4) and is optimal when the device is operated in the subthreshold region. This has been shown both experimentally [232, 441] and theoretically, based on the drift-diffusion equations [73].

Rajan et al. defined signal-to-noise ratio as the ratio of the change in drain current to the measured low frequency noise of the system. Most literature supports that the signal-to-noise ratio is optimal in the subthreshold region [53, 70, 441, 444], but the work of Rajan et al. has shown that the region of optimal signal-to-noise can be device-dependent [53, 73, 441, 442, 444, 445]. The disagreement with other devices in the literature was explained as due to their device having a different regime of mobility fluctuation noise [446]. Not all publications are carried out in the subthreshold region (as shown in the summary table of literature in Appendix J), which might be due to lack of awareness of the significance of this region, or it may be because the signal-to-noise was indeed found to be suboptimal in the subthreshold region for a given device.

8.2.4. Device Characterisation, Performance Parameters and Metrics

FET-sensors operate on the principle that binding of analyte to the sensor surface results in a change in surface potential ($\Delta\psi_s$) via electrostatic gating. This induces an equivalent change in the device threshold voltage, which can be measured via the transistor as an amplified signal in the form of a change in the drain current. By measuring the variation in drain current (I) as a function of the reference electrode potential (V_g), the change in threshold voltage (ΔV_T) and the change in drain current (ΔI) can be measured. Either of these properties are termed device 'response' here. From these measurements, metrics important for characterising FET-sensors can be calculated. Two commonly used metrics, the 'Subthreshold Slope' and Normalised Change in Current, are illustrated in Figure 8.1 and described and discussed in this section.

The Subthreshold Slope is defined as the 'change in gate voltage (V_g) required to reduce the subthreshold current I by one decade' [447]. The Subthreshold Slope provides a measure of the transistor quality in terms of its susceptibility to respond to changes in the gate voltage. The reciprocal of the Subthreshold Slope is called the 'gate voltage swing' or 'subthreshold swing' [447]. The Subthreshold Slope can be extracted from the $\log(I) - V_g$ by measuring the inverse of the slope of the constant-gradient region (assuming constant drain current and backgate voltage). The lower limit that the Subthreshold Slope can reach in a classical FET is theoretically bounded to be no lower than ~59 mV/dec at room temperature [30].

The field of research requires the definition of appropriate quantitative and clearly-defined metrics in order to properly compare the performance of BioFET sensors and their ability to detect and quantify analytes. Particularly so, as publications in this field have not consistently used well-defined, and standardized nomenclature or parameters. Authors in the field of BioFET research have sometimes quantified sensor performance using a definition of the word 'sensitivity' which differs from the IUPAC definition. For example, some authors refer to the absolute change in current as 'sensitivity'. More frequently, the change in current divided by the initial current is referred to as the 'sensitivity'. Neither of these metrics provide reference to the change in analyte concentration.

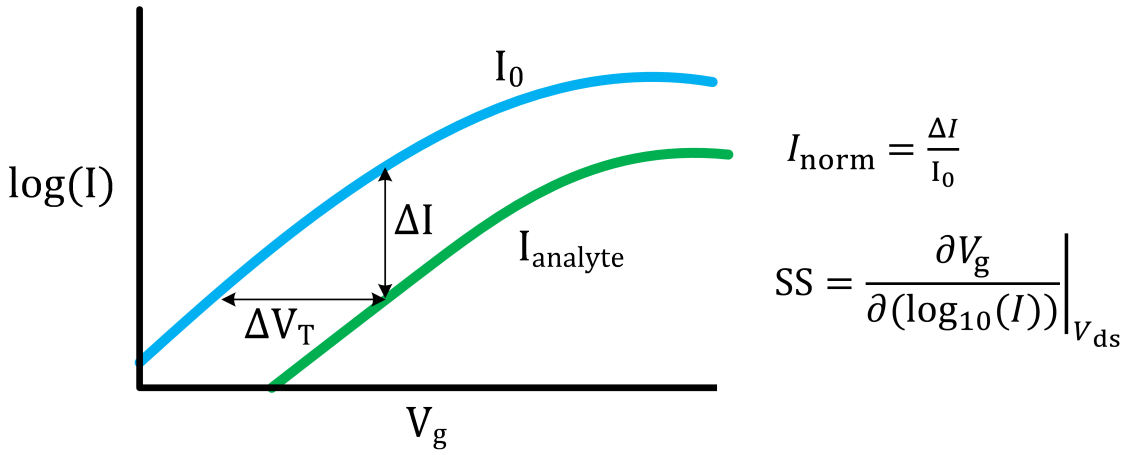

Figure 8.1.: Schematic $\log(I) - V_g$ graph showing the subthreshold region for an n-type FET, $V_{ds} \neq 0$ and a gate voltage sweep before (blue line) and after (green line) interaction with an added negatively charged analyte, with currents I_0 and $I_{analyte}$, respectively. The direction of response shown is typical of analytes such as streptavidin (at pH 7.4) or a change to more alkaline pH. There is a parallel shift in the $\log(I) - V_g$ curves such that, at constant I, the corresponding shift in threshold voltage ΔV_T can be measured. Assuming electrostatic gating, ΔV_T is equal in magnitude to the change in surface potential at the oxide-electrolyte interface, and can therefore be used for quantitative sensing of analyte binding. At constant V_g there is a shift in current response (ΔI), which can be divided by the initial current to produce the Normalised Change in Current, I_{norm}. The measured Subthreshold Slope (SS) is approximately constant in the subthreshold region.

8.2.4.1. IUPAC Definitions

IUPAC defines 'sensitivity' as a metric of the specific response as a function of the analyte concentration. More specifically, it is defined by IUPAC as 'the slope of the calibration curve'. IUPAC defines the calibration curve as 'the functional (not statistical) relationship for the chemical measurement process, relating the expected value of the observed (gross) signal or response variable to the analyte amount. The corresponding graphical display for a single analyte is referred to as the calibration curve'. [448]

The IUPAC definition of sensitivity is not a measure of the ability to detect the minimal amount of an analyte, and therefore another relevant metric is the Limit of Detection which IUPAC defines as the smallest measure that can be reasonably detected for a given analytical procedure, and is expressed as a concentration or quantity. More specifically: 'The limit of detection, expressed as the concentration, c_L, or the quantity, q_L, is derived from the smallest measure, x_L, that can be detected with reasonable certainty for a given analytical procedure. The value of x_L is given by the equation $x_L = \overline{x}_{bi} - ks_{bi}$, where $\overline{x}_{bi}$ is the mean of the blank measures, s_{bi} is the standard deviation of the blank measures, and k is a numerical factor chosen according to the confidence level desired.' [448]

8.2.4.2. Analysis of Sensitivity

The IUPAC definition of sensitivity incorporates two elements: the measurement of a specific response, and its dependence upon analyte concentration. Within the BioFET literature there is inconsistency or absence in both aspects. So the analysis required a careful examination of the presented data to evaluate the data quality and conclusions, and to use a clear set of nomenclature and criteria for any comparisons. These are outlined below.

Here the symbol I_{norm} is used to refer to the Normalised Change in Current, which is defined as:

$$I_{norm} = \frac{I_f - I_0}{I_0} = \frac{|\Delta I|}{I_0}, \tag{8.2}$$

where I_f and I_0 are final and initial values of the current, respectively.

Although some publications have simply used the absolute measured change in current from the device (ΔI) as the readout, this metric results in a large device-to-device variation and therefore the practice of normalising the current ($\Delta I/I_0$) has become common since it reduces this variation [97]. The change in current (ΔI) can either be positive or negative, and consequently the Normalised Change in Current, I_{norm}, also has an associated sign. Some authors (e.g. [70]) reported the Normalised Change in Current without this sign which makes the polarity of the measured change ambiguous, and because the polarity of this response is related to the polarity of the electric field at the interface, this can obscure a key result of the experiment.

In the subthreshold region, using the MOSFET drift-diffusion equations, the shift in threshold voltage (due to analyte binding) can be related to the Normalised Change in Current as: [232, 449]:

$$\Delta V_T = \frac{SS}{\ln(10)} \ln(I_{norm} + 1) = SS(\log_{10}(I_{norm} + 1)). \tag{8.3}$$

This can be used to calculate the expected magnitude of the Normalised Change in Current for a given analyte. For example, considering the case of an ideal n-type transistor with a Subthreshold Slope of 59 mV/dec, and an analyte that induces a shift in threshold voltage of 10.39 mV, the calculated Normalised Change in Current is approximately -33%. For the equivalent analyte, but for a p-type semiconductor, the calculated change in I_{norm} is +50%. A negative I_{norm} and a positive I_{norm} are qualitatively different, this is because a current that is decreasing is 'bounded' by zero and therefore a maximum of -100% is possible, whereas an increasing current has no mathematical upper limit for the Normalised Change in Current, I^+_{norm}, and it is referred to in this chapter as 'unbounded' to indicate that is always positive, and can reach large positive values. In the subthreshold region, direct comparison an unbounded signal from one device (i.e. with an n-type semiconductor) with the bounded signal of another (i.e. with a p-type semiconductor) is uninformative.

In order to compare the signal between devices based on different semiconductors, the change in current can be normalised by the current obtained either before the response (I_0) or after the response (I_f) , whichever is lower, these lowest and highest values are referred to as I_{low} and I_{high} respectively. If divided by This results in a Normalised Change in Current which is always positive and 'unbounded' with no mathematical upper limit. The differences between the unbounded and bounded Normalised Change in Current are illustrated schematically in Figure 8.2. Note that, for consistency with the quantitative analysis of the literature performed by Sun et al. [232] for pH sensing, I^+_{norm} was used in this analysis. It would be equivalently possible to compare the 'bounded' change in current, whereby the current is normalised by the higher of the before/after binding current (I^-_{norm}).

Normalised Change in Current is a commonly used metric in the field and its value is a function of the amount of bound analyte as well as the sensors ability to amplify response. This can be problematic from the perspective of biosensor design, because if an experiment is performed on a very poor sensor with a high concentration of bound analyte, then the resulting I_{norm} value can be the same as that measured by an experiment on a good sensor with a very low concentration of bound analyte. The response per 10-fold increase in concentration of analyte is a more useful biosensor figure-of-merit and is similar to the IUPAC definition of sensitivity [448]. In the BioFET literature, the Normalised Change in Current is often calculated based on the change in drain current after the introduction of an arbitrary concentration of analyte. In contrast, in the pH sensing literature, it is often defined over a single pH unit (i.e. per 10-fold increase in concentration of analyte). In the analysis presented within this chapter, a metric which is similar to the IUPAC definition will be used in which the Normalised Change in Current per 10-fold increase in concentration is presented (e.g. % per unit pH or % per 10-fold increase in streptavidin concentration). Within this work, this metric will referred to

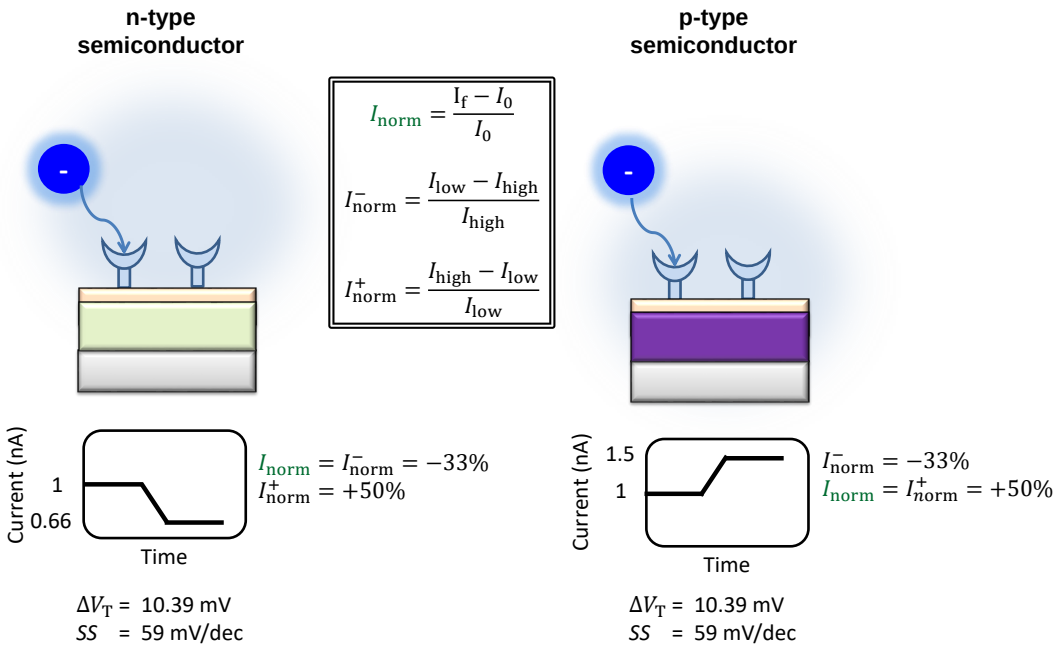

Figure 8.2.: Schematic of the change in current upon sensing a negatively charged analyte by an n-type semiconductor (left) and p-type semiconductor (right) is shown. The device is assumed to operating in the subthreshold region. The values shown are calculated using Equation 8.3 assuming an ideal device (59 mV/dec) and an analyte which can induce a shift in the threshold voltage of 10.39 mV. The polarity of the response is reversed between the two types of semiconductor, and therefore the Normalised Change in Current is different between an n-type semiconductor and a p-type semiconductor. The Normalised Change in Current is often obtained by $I_{norm} = \Delta I/I_0$, where I_0 is the initial current prior to analyte addition. In a sensing experiment, the lowest value of the current recorded is referred to here as I_{low} and the highest value as I_{high}. The change in current can be instead normalised by I_{low} instead of I_0, resulting in the 'unbounded' Normalised Change in Current (I^+_{norm}). An alternative method would be to normalise by I_{high} (I^-_{norm}). Inspection of the above figure illustrates that in order to compare the sensing results for a particular analyte between devices of different semiconductor, the Normalised Change in Current must be calculated consistently (i.e. I^+_{norm} cannot be directly compared to $|I^-_{norm}|$).

as 'Sensitivity' due to its similarity to the IUPAC definition and is rigorously defined in the Methods (Section 8.3).

Other than its use in producing a figure-of-merit, there are important reasons as to why measurement of the response as a function of analyte concentration is useful in the context of biosensors. The affinity (i.e equilibrium dissociation constant, K_d) of an analyte binding to a sensor can be estimated by fitting the concentration-dependent response data to an appropriate binding model [72]. Further, the concentration at which the response saturates can be used to estimate the density of bound molecules [59].

Performance metrics have also been discussed by Rajan et al.[73, 450], who highlighted a few examples from the literature of concentration-response curves for BioFETs over different analytes and stress the importance of considering, not only the IUPAC sensitivity, but also the signal-to-noise ratio which they define as the ratio of absolute drain current change to low frequency noise. At this time, unfortunately, most BioFET data is reported without noise analysis or sufficient repeats to obtain an estimate of the statistical uncertainty of measurements, and so quantitative estimation of this signal-to-noise ratio or IUPAC Limit of Detection is rare. Given these limitations, the analysis presented in this chapter uses the Normalised Change in Current per 10-fold increase in analyte concentration ('Sensitivity') as a performance metric to compare sensing results between different experiments.

8.2.5. Effect of Ionic Strength on Sensing Performance

The ionic strength of the buffer in which the analyte is presented can affect biosensing response in several ways: apart from any affect on the affinity of the interaction, it can modify the extent to which the charge of the biomolecule affects the charge in the semiconductor via electrostatic screening (Section 8.2.5.1) and it can modify the surface charge or chemistry (Section 8.2.5.2).

8.2.5.1. Electrostatic Screening

Phoshate Buffered Saline (PBS), i.e an aqueous solution of 138 mM NaCl, 2.7 mM KCl in 10 mM sodium phosphate at pH 7.4 [87], is often utilised in biosensing experiments. It is often referred to in this field as 1X PBS in order to contrast it to diluted forms, for example, 0.1X PBS which is a 10-fold dilution [87]. 1X PBS has an ionic strength of approximately 160 mM, which is comparable to that in many physiological situations, and so is particularly relevant to biosensing studies.

The Debye length is a characteristic length scale for electrostatic screening by electrolytes in the Debye-Hückel model of the electrical double layer (introduced in Chapter 7). One way of understanding the physical significance of the Debye length is to consider an ion as a point charge in a bulk electrolyte. Counterions surround the ion due to electrostatic attraction and thermal motion, and the Debye length is the radial distance at which the total compensating charge density is maximal [107].

Consideration of Debye length can be useful for BioFET experimental design. In high ionic strength solutions, the Debye length is short and therefore if the analyte, which is bound to the surface of the sensor, is a large biomolecule then it is likely to contain charges which are several Debye lengths away from the sensor surface and therefore have no significant effect on the surface potential of the sensor and consequently no measurable response. Dilution is often performed to reduce the ionic strength of the solution and extend the Debye length; however, this can cause ancillary issues such as a reduction in buffering capacity and instability of the biomolecule in solution [451] or reduced affinity of the biomolecule-target interaction, although the latter is not the case for the biotin-streptavidin interaction [87]. For PBS dilutions of 1X, 0.1X and 0.01X, the calculated Debye lengths are 0.76 nm, 2.41 nm and 7.61 nm respectively. Stern et al. demonstrated a significant BioFET response for binding of streptavidin in solution to biotin on the sensor at 0.01X PBS, but no significant response at 1X PBS. Approximating streptavidin as ~5 nm from the surface [98], they found that this result agrees with the Debye-Hückel theory. [61]

8.2.5.2. Surface Chemistry

The surface chemistry can change at different ionic strengths, resulting in alteration of the response. For oxide surfaces, the 'surface charge', which is calculated from potentiometric titration data, is known to be a function of ionic strength [452, 453]. Further, Tarasov et al. have used silicon nanowire FETs with highly pH sensitive HfO_2 or Al_2O_3 surfaces and shown clearly that at fixed pH, changes in electrolyte concentration can have a significant response [454]. They observed a linear increase in response with increasing pH in the pH range 2-10 ($\Delta V_T = 56 \pm 3$ mV/pH). At pH 6, they observed that electrolyte concentration has negligible effect on response below 10 mM, but that above 10 mM the response rapidly increased to 'Nernstian' [455] response (59 mV for every 10-fold increase in KCl concentration). Their empirical model attributes this to pH independent selective adsorption of anions, possibly via chloride ion adsorption to the surface displacing surface-bound water molecules.

These empirical observations are supported by the molecular dynamics simulation study by Criscenti et al. [456]. Experimentally, Maekawa et al. did not observe significant FET response to addition

of electrolyte on silica surfaces with concentrations up to 1 M of NaCl, but upon increasing the concentration above 1 M there was a significant increase in response corresponding to roughly 30 mV for every 10-fold increase in NaCl concentration [264]. Maekawa et al. performed molecular dynamics simulations to investigate this [263, 264] but in direct contrast to Criscenti et al. did not observe significant water displacement by chloride ions. The simulation work of Maekawa et al. did however predict a decrease in surface potential with increasing ionic strength, which is in agreement with their experimental results. In their simulations, reorientational water polarisation dominated the surface potential, and increased electrolyte concentration reduced the surface potential, suggesting that ion-induced water reorientation was the cause of the surface potential drop. In summary, whilst the conclusions from atomistic simulations are under debate, experiments show ionic strength can have a significant effect on BioFET response.

8.2.5.3. Recent Developments

An alternative mode-of-operation of FETs has been proposed which has the possibility of offering enhanced Sensitivity for devices whilst retaining the use of high ionic strength solution. It may also be beneficial for systems in which there is an undesirable 'drift' in the measured drain current that is not related to the analyte. In this mode-of-operation, which was first proposed in the 1990s with the work of Schasfoort et al. [22, 457] and recently demonstrated for detection of poly-l-lysine [458], a sudden change in ionic strength change is made ('ion-step') and the initial non-equilibrium response is measured before the system fully equilibrates. By using this transient response of the system, biomolecules can potentially be detected in higher ionic strength buffers to that using conventional 'equilibrium' sensing experiments. Speculative reasons for the lack of wide-spread adoption of this methodology may be due to the additional step required for biosensing, thus making the resulting mode-of-operation less commercially appealing, lack of awareness, or lack of reproducibility.

8.3. Methods

This analysis is focused upon pH-sensing and streptavidin/biotin interactions on FET devices, operating in the subthreshold region. Data from this region was chosen because it provides the optimal Normalised Change in Current (as introduced in Section 8.2.3) and there is less availability of concentration-dependent streptavidin-sensing measurements in the linear region. Where available, the Subthreshold Slope was directly extracted from the streptavidin literature, and where this was not reported explicitly it was extracted manually from $I - V_g$ graphs.

As discussed in Section 8.2.4, when comparing Normalised Change in Current between devices of different semiconductor type (p- or n-) type, normalisation simply using the 'initial' drain current in time is insufficient. In all results presented in this chapter, the change in drain current was normalised by the lower drain current (I_{low}) to give the parameter I^{+}_{norm}:

$$I^{+}_{norm} = \frac{I_{high} - I_{low}}{I_{low}} = \frac{|\Delta I|}{I_{low}}, \tag{8.4}$$

where I_{high} is the higher value of the drain current, whether it be before or after a change in concentration of analyte. As an example, for streptavidin on an n-type device, the drain current will decrease after addition of streptavidin and therefore I_{low} will be the drain current after addition of streptavidin and I_{high} before addition. This retains consistency with the quantitative analysis of the literature performed by Sun et al. [232] for pH sensing. Many publications only provide the change in response due to addition of (an arbitrary concentration) of streptavidin, and therefore the

Normalised Change in Current per 10-fold increase in concentration of analyte could not be calculated for such papers, only the Normalised Change in Current, I^{+}_{norm}. For publications which present streptavidin-sensing data as a function of concentration of streptavidin, it is possible to calculate the Normalised Change in Current for a 10-fold increase in streptavidin concentration, and equivalently for pH sensing, the response due to a change of 1 pH unit was used (Equation 5.10). This was repeated for each 10-fold increase in concentration available within the paper, resulting in a set of $I_{\mathrm{norm,i}}$ for each i changes in drain current. Finally, the 'Sensitivity' was calculated from the geometric mean of Normalised Change in Currents ($I_{\mathrm{norm,i}}$) over n measurements each performed at a 10-fold higher concentration than the previous:

$$\text{Sensitivity} = \left(\prod_{i=1}^{n} I^{+}_{\mathrm{norm,i}} \right)^{\frac{1}{n}}. \tag{8.5}$$

Here the metric in Equation 8.5 will be referred to as 'Sensitivity', and is similar to the IUPAC definition of sensitivity [448].

In this calculation, the value of ΔI used in calculating each $I_{\mathrm{norm,i}}$ was taken to be between each subsequent measurement, as opposed to an initial control drain current and each measurement. A mean is used so as to calculate the representative value of I_{norm} per-unit-analyte. A geometric mean was used as it is more appropriate than the arithmetic mean for ratios/percentages [459].

Not all publications presented their data both unambiguously and with completeness. Hence, sometimes paper-specific assumptions had to be made for this analysis, and these assumptions are explained in detail in Appendix I.

A table summarising published works to-date which detect streptavidin using a BioFET device can be found in Appendix J. A total of twenty distinct experimental systems were identified. Seven of these devices were operated in the linear region of FET operation and were not included in the this quantitative analysis as explained in Section 8.3. Five publications either did not report the region of operation or did not provide sufficient data for analysis and were excluded.

8.4. Results

Data obtained from nine publications on streptavidin binding to biotin-coated FET-Sensors is shown in Figure 8.3. The Normalised Change in Current, I^{+}_{norm}, is plotted against the device Subthreshold Slope. The data was obtained from experiments which were not all performed at the same concentration of streptavidin and at more than one ionic strength. Where experiments were performed at several concentrations of streptavidin, or at differing ionic strength, this is indicated in the figure. For experiments performed at a higher concentration of streptavidin, there is a higher density of bound analyte (until the sensor surface is saturated) and there is a corresponding increase in the Normalised Change in Current (I^{+}_{norm}).

This increase in Normalised Change in Current with concentration can be seen in measurements on the graph for which measurements at several concentrations were available, the relative concentration used being indicated via the size of the marker symbol. No clear relationship between the Normalised Change in Current and Subthreshold Slope was observed. High ionic strength can reduce response and therefore increasing ionic strength is indicated in Figure 8.3 with a thicker marker outline.

Each solid curve shown in Figure 8.3 shows the calculated shift in threshold voltage for a given Subthreshold Slope and I^{+}_{norm} (Equation 8.3), therefore it can be seen that most measurements correspond to a shift in the threshold voltage, ΔV_{T}, of approximately 5 mV to 165 mV.

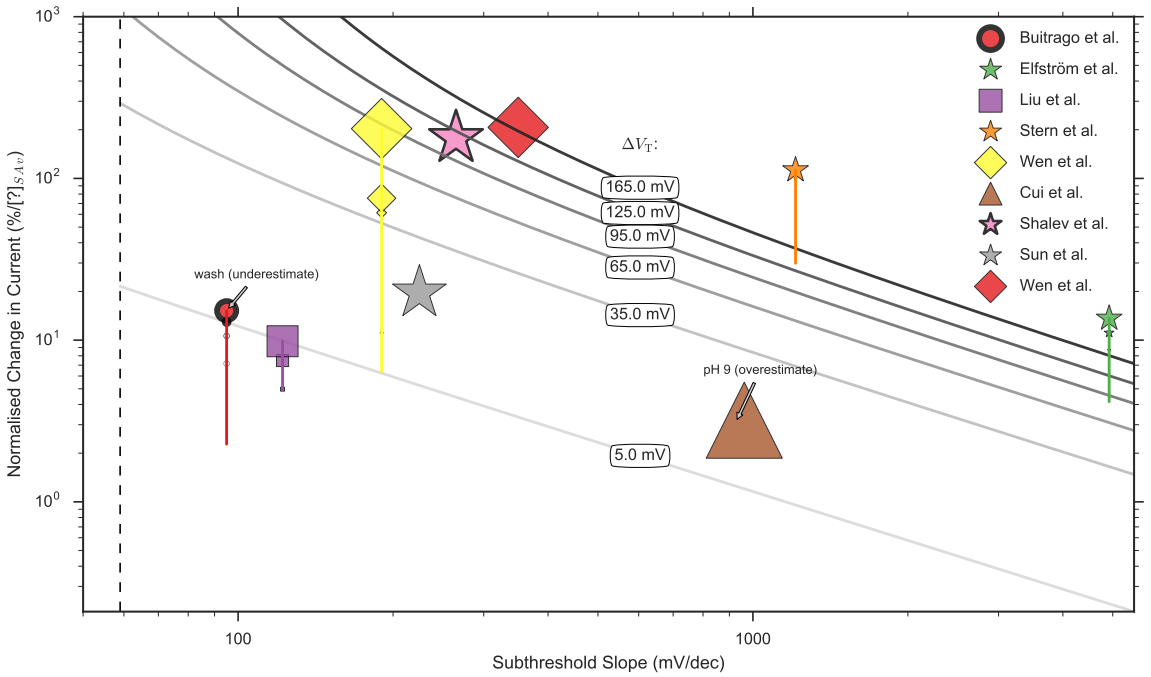

Figure 8.3.: Measured 'unbounded' Normalised Change in Current (I^{+}_{norm}) versus measured Subthreshold Slope for sensing operating in the subthreshold region. [19, 59, 70, 71, 460, 461] The shape of marker symbol corresponds to the type of device: 3D nanowire stack = ●, nanoribbon = ★, nanobelt = ■, planar = ♦, nanowire = ▲. The size of the marker symbol is proportional to the log(concentration) of streptavidin used. The vertical lines joining some markers corresponds to a series of measurements under different concentrations . A thicker outline of a marker symbol indicates an experiment made under high ionic strength, where the maximum ionic strength was 1X PBS and the minimum 0.01X PBS. The dashed line shows the theoretical lower limit of the Subthreshold Slope of 59 mV/dec available to classical FETs at room temperature. The solid grey lines are isocontours calculated by inserting the shift in threshold voltage, ΔV_{T}, into Equation 8.3, the value inserted is labelled upon each line. i.e. for a data point on top of a line, it represents its calculated shift in threshold voltage and therefore the calculated change in surface potential. The results of Buitrago et al. [462] and Cui et al.[78] are likely to be an underestimate and overestimate respectively for the reasons given in the Appendix I; a more detailed explanation of the data extraction, the marker thickness, and a replot with a linear x-axis can be found in Appendix I. A clear relationship between I^{+}_{norm} and Subthreshold Slope is not apparent.

In order to improve the comparability between measurements performed at different concentrations, the Sensitivity was calculated and plotted in Figure 8.4. Unfortunately many published BioFET experiments were performed with only a single analyte concentration, making the calculation of Sensitivity impossible. Sun et al. [232] published a collation of pH sensing data, using a metric equivalent to Sensitivity, and this data is included in Figure 8.4 and Figure 8.5 for comparison to the biosensing data.

As shown in Figure 8.4, the Sensitivity values ranged between 2% and 60% per 10 fold increase in Streptavidin, whereas the pH Sensitivity values varied between 1% and 600% per pH. Therefore, on the basis of available streptavidin sensing data, it can seen that a streptavidin-sensing Sensitivity comparable to optimal pH sensing results has not been obtained. The pH sensing data showed a shift in threshold voltage which was consistent for a particular oxide material, whereas the streptavidin-binding data showed no clear trend in threshold voltage shift. In order to better visualise the calculated shift in threshold voltage, the Subthreshold Slope of each data point and corresponding Sensitivity value was inserted into Equation 8.3 to obtain the calculated shift in threshold voltage per 10-fold increase in analyte concentration for that measurement. This was then used to plot Figure 8.5. In this figure, isosurfaces calculated using Equation 8.3 are drawn from red to blue for values of the Sensitivity increasing in 1% increments in the range 1-150%.

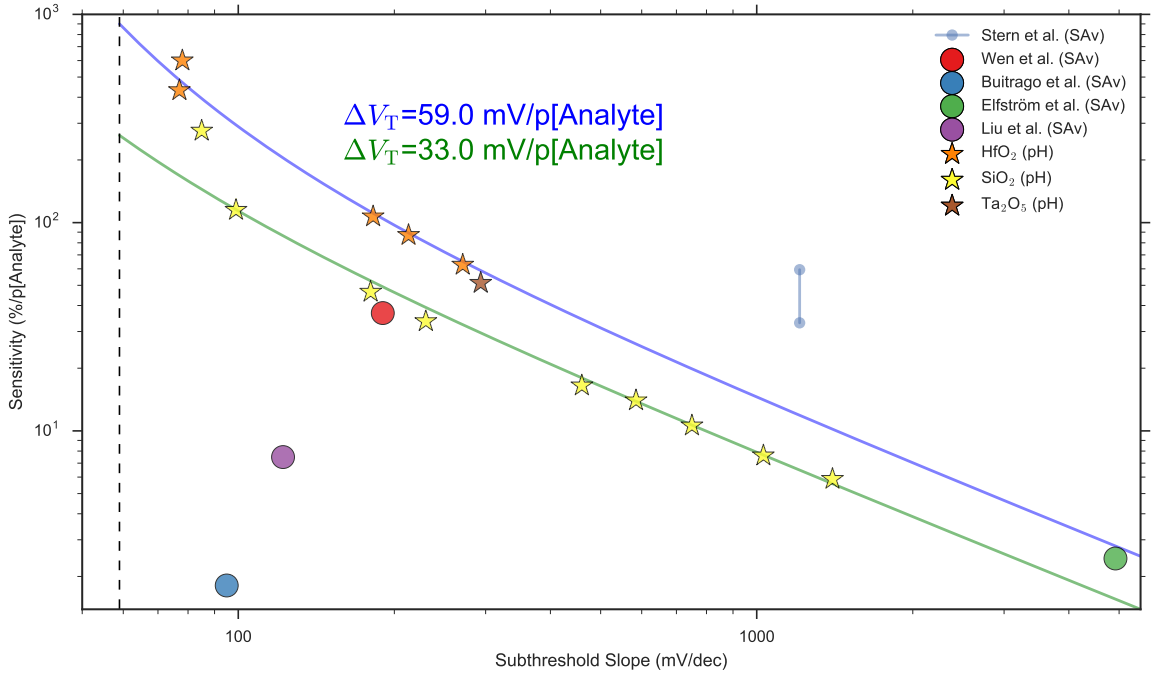

Figure 8.4.: The relationship between Sensitivity and Subthreshold Slope, for measurements obtained within the subthreshold region. Both streptavidin sensing [19, 59, 61, 70, 460] (●) and pH sensing data (★) [232, 441, 449, 463–469] are shown. The Subthreshold Slope from the data of Stern et al may not be accurate and two points are shown to represent the range of uncertainty in the Sensitivity value (see for details Appendix I). Dielectrics have a shift in threshold voltage per change in pH unit that is ~33 mV/pH for SiO_2 and ~59 mV/pH for HfO_2. Curves calculated using Equation 8.3 for a threshold voltage shift per 10 fold increase in analyte concentration of 33 mV and 59 mV are shown using solid lines. The dashed line indicates the theoretical lower limit of the Subthreshold Slope at room temperature of 59 mV/dec available to classical FETs. Details of method used to obtain the data and a replot of the same data but on a linear x-axis can be found in Appendix I.

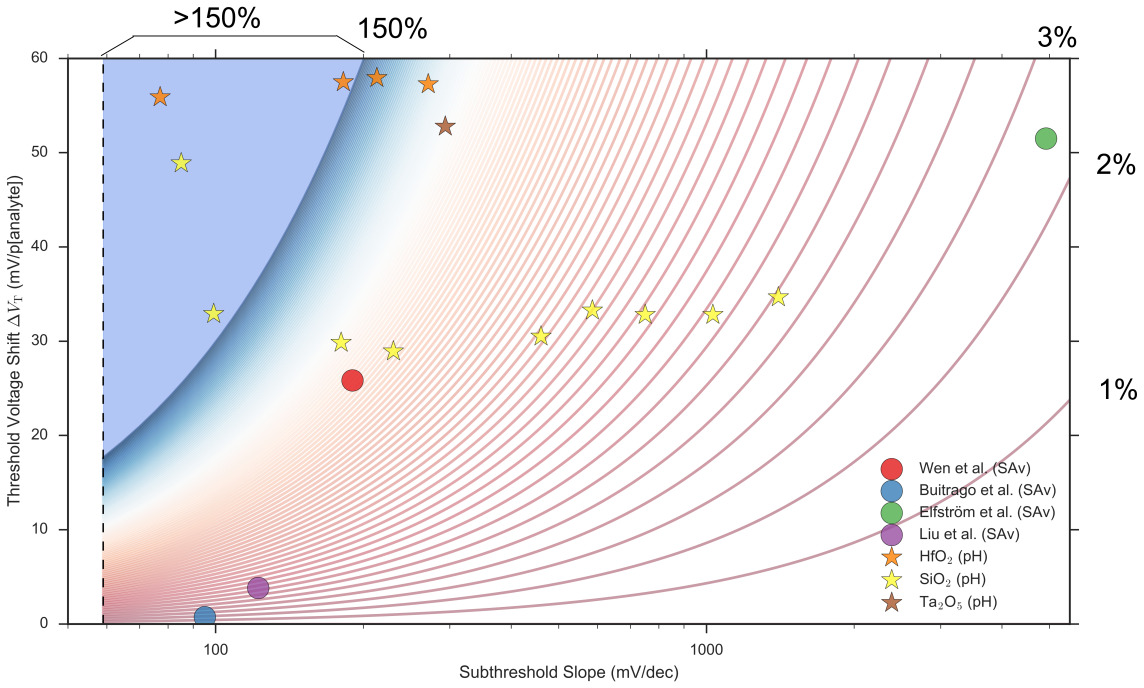

Figure 8.5.: The relationship between the calculated shift in threshold voltage per 10-fold increase in analyte concentration and measured Subthreshold Slope, for measurements obtained within the subthreshold region. This is a replot of the experimental data shown in Figure 8.4, but in this figure, the shift in threshold voltage per 10-fold increase in analyte concentration is calculated by inserting both its Subthreshold Slope and Sensitivity into Equation 8.3. Both streptavidin sensing [19, 59, 61, 70, 460] (●) and pH sensing (★) results [232, 441, 449, 463–469] are shown. Isocontours are drawn, using Equation 8.3, in 1% increments using values of the Sensitivity between 1% (red) and 150% (dark blue), with >150% being shown as a pale blue region. The theoretically optimal Subthreshold Slope of 59 mV/dec is shown as a dashed line. Equation 8.3 predicts that with a Subthreshold Slope of 59 mV/dec, it is impossible to obtain greater than ~100% Sensitivity with a shift in threshold voltage < 10 mV per 10-fold increase in analyte concentration, and this can be seen graphically within the figure. The calculated data for Stern et al. has high uncertainty, as discussed in the Appendix I, with a calculated shift in threshold voltage per 10-fold increase in streptavidin concentration of 150-250 mV, therefore their data is not shown on this scale. Details of method used to obtain the data and a copy of the plot with a linear x-axis can be found in Appendix I.

8.5. Discussion

8.5.1. Detection at High Ionic Strength

The Normalised Change in Current versus measured Subthreshold Slope for streptavidin-sensing experiments from various literature sources were collated and presented in Figure 8.3. The isocontours drawn allow inspection of the (calculated) shift in threshold voltage (ΔV_{T}). Assuming electrostatic gating, then the shift in threshold voltage is directly proportional to the change in surface potential and therefore the amount of surface-bound analyte. The maximum calculated shift in threshold voltage corresponds to approximately 165 mV. If these systems are saturated at maximal density of streptavidin, it indicates the maximum surface potential shift possible for this system. Oxide surfaces demonstrate characteristic changes in surface potential per unit of pH and therefore it is possible to consider what analogous pH sensing stimulus would result in the same ΔV_{T} observed in streptavidin sensing experiments. For silica, a shift from pH 4 to pH 9.5 would correspond to a surface potential shift with a magnitude of ~165 mV (~30 mV/pH in this region), and proton titration experiments of an amorphous silica suspension show that the surface charge density varies by about 0.15 Cm^{-2} through this range [204]. This suggests that streptavidin binding can change the surface potential by a comparable magnitude to that which occurs upon large pH changes.

Given that some of these experiments were performed at high ionic strength (~160 mM), these significant changes in the electrostatic potential at the interface disprove early assumptions about BioFET operation. For example, Bergveld (1996) [470] used the Debye-Hückel model of the electrical double layer (Section 3.2.2) to argue that large biomolecules cannot be detected at high ionic strengths, having written:

> 'The resulting double layer, with a thickness of the Debye length, is of the order of 1 nm thick in moderate electrolyte concentrations. Beyond this distance no external electric field exists. Hence the idea that a layer of charged molecules at the surface of an ISFET modulates the electric field in the gate oxide should definitely be forgotten.'

In the Debye-Hückel model, the Debye length is ~1 nm at ~160 mM ionic strength and yet streptavidin has been detected at this ionic strength by various authors [19, 341, 471]. Even providing the Debye-Hückel model can describe the system accurately (an assumption that this thesis contests), the flaw in this argument remains two-fold: firstly, the Debye length is not a hard cut-off beyond which no electrostatic effect is felt because the screened Coulombic interactions reach to infinity[1] and only become negligible at a region of approximately 1-3 Debye lengths. Secondly, the argument assumes that the molecules are rigid and bound in a fixed orientation, whereas in reality they are flexible and dynamic and therefore some orientation of the analyte can bring the molecular charges closer to the surface than other orientations [472].

8.5.2. Biomolecule Sensitivity Compared to pH Sensitivity

A large degree of the variability in the response illustrated in Figure 8.3 is due to the variety of concentrations of analyte used between different experiments. The measured Sensitivity versus measured Subthreshold Slope for streptavidin-sensing experiments were presented in Figure 8.4. A low Sensitivity (3-60%) was observed for all streptavidin-sensing experiments as compared to pH sensing (which show Sensitivity up to 600%), despite the excellent Subthreshold Slopes obtained in many of the BioFET devices. This can be explained as a consequence of the fact that none of the

[1] In the Debye-Hückel model for the electrode-electrolyte interface the surface potential $\psi_x = \psi_0 e^{-\kappa x}$ therefore the electric field $E_x = -\psi_0 \kappa e^{-\kappa x}$

biosensing experiments demonstrated both the high shift in surface potential and low Subthreshold Slope that is required for a high change in Sensitivity. It should be noted that the low Sensitivity of 2% seen in the study of Buitrago et al. [19] may be simply a consequence of the response not being measured at equilibrium, as in Buitrago (2014) it was stated that analyte was 'immediately washed away by PBS' [462].

The data shown in Figure 8.5 shows that most oxide surfaces demonstrate surface potential shifts as a function of pH which are above approximately 25 mV/pH. As this value is a shift per 10-fold increase in analyte (pH=-log([H^+]), this can be contrasted to streptavidin sensing experiments, which showed both: (a) a greater variation in possible shifts in threshold voltage per 10-fold increase in streptavidin concentration and, (b) some shifts of less than 15 mV. If a device has a shift in threshold voltage per 10-fold increase in streptavidin concentration that is this low, it can be clearly seen in Figure 8.5 that it is theoretically impossible to obtain greater than approximately 75% Sensitivity. This form of analysis can be used to inform BioFET design; it suggests that if a device shows a low threshold voltage shift per 10-fold increase in analyte, then design focus should be put upon enhancing the change in surface potential by optimising the surface chemistry.

8.5.3. Biomolecule-induced versus pH-induced Threshold Voltage Shifts

The calculated shift in threshold voltage per 10-fold increase in analyte concentration can be seen most clearly in Figure 8.5. For pH sensing, the results showed a shift in threshold voltage per pH which was consistent with the material of the oxide, as previously observed in the literature [232]. Specifically, despite the fact that the pH sensing results are from disparate literature sources, they show highly consistent threshold voltage shifts of ~30 mV/pH (SiO_2) and ~60 mV/pH (HfO_2). The physical origin for these material-consistent surface potential shifts can be explained in terms of surface complexation models (Section 3.3.2.1), which were first introduced by Yates et al. [473] and later refined by Healy et al. [474]. In these models, an increased density of hydroxyl groups on the surface corresponds to an increase in surface potential shift per unit pH [455, 475]. This theory is supported by experimental work which has shown that blocking hydroxyl groups on the surface with organic functionality can reduce the surface potential shift per pH [93, 455, 476].

Given the ability of Surface Complexation Models to explain the shift in threshold voltage for pH sensing data, it is plausible a similar mechanism can explain much of the variation in biosensing data. In pH sensing, the density of analyte receptors is described by the density of hydroxyl groups at the oxide surface, whereas for streptavidin-biotin biosensing the density of analyte receptors is the density of biotin available at the sensor surface. Using analogous arguments to those used in Surface Complexation Models, an intuitive hypothesis is that the shift in threshold voltage per 10-fold increase in analyte concentration is primarily limited by the density of receptors (and therefore bound-analyte) on the surface.

In order to investigate this hypothesis the density of bound molecules was estimated by making some simple assumptions and utilising the concentration at which the sensor response saturates ($c_{\max}$). Due to the (untypically) high affinity of the streptavidin-biotin interaction, in which the affinity has a $K_d \approx 1$ fM [72], if the concentration of analyte at the surface is much greater K_d then, based on the Langmuir isotherm model, approximately 100% of streptavidin will be in its surface-bound form at equilibrium [477].

Taking the work of Elfström et al. as an example, given their sample volume, V_{vol}, of 200 µL solution and concentration, $c_{\max}$, of 0.5 nM, the total number of molecules in the solution ($=c_{\max}V_{\text{vol}}$) can be obtained. Assuming all molecules bind to the surface and that they bind homogeneously, then the bound density, ρ, will simply be $c_{\max}V_{\text{vol}}$ divided by the functionalised area exposed to analyte, A, (10 mm^2).

From this calculation, the surface density of biomolecule is calculated to be 0.015 molecules/nm^2. This can be compared with the maximum streptavidin density, $\rho_{\max}$, theoretically possible for streptavidin, assuming each molecule occupies 25 nm^2 [98] which is equivalent to 0.04 molecules/nm^2. This comparison suggests that the surface-bound density for the device of Elfström et al. is close to ideal, suggesting a sufficiently high density of biotin receptors on the surface to efficiently capture streptavidin. Under the hypothesised Surface Complexation-like Model, a large shift in threshold voltage per 10-fold increase in concentration of streptavidin is therefore expected. It can be seen in Figure 8.5, that for the work of Elfström et al. there was a ~50 mV shift in threshold voltage per 10-fold increase in streptavidin concentration, which is large compared to the majority of other streptavidin measurements and pH sensing measurements shown. This supports the hypothesis that the biosensing shift in threshold voltage per 10-fold increase in streptavidin concentration is largely determined by the density of surface receptors.

In addition to receptor density (discussed above) as one factor that may affect the threshold voltage shift, there are many other potential factors which could explain the observed differences between pH-sensing and biosensing experiments. Several factors relate to the surface and its chemistry. Figure 8.6 shows a schematic which attempts to summarise possible differences in the surface chemistry, and therefore measured surface potential shifts, between pH and biosensing experiments. Each of these factors are explained in the following paragraphs.

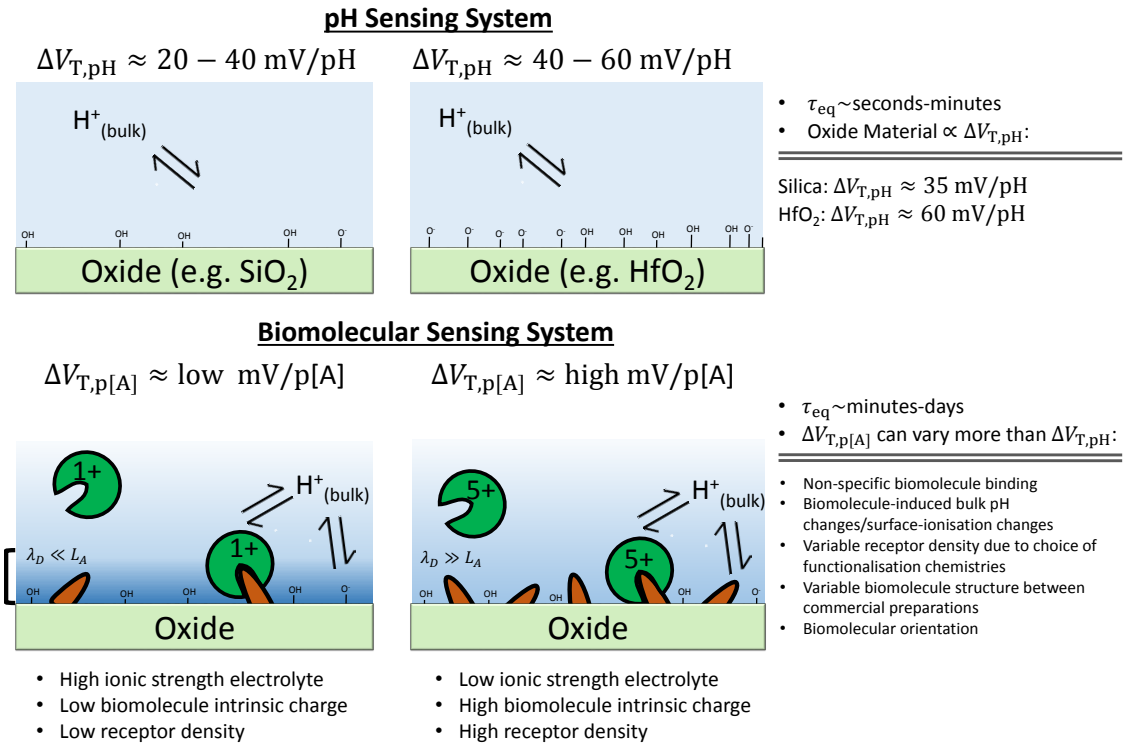

Figure 8.6.: Comparison of factors influencing the surface potential in a pH sensing experiment (above) with those in a biomolecular sensing experiment (below). The systems on the left and right have a low and high receptor density, respectively. Receptors for pH sensing are hydroxide groups, whereas for biomolecular detection specific receptors (shown as yellow wedges) are required. For pH sensing, the receptor density is the determining factor the change in surface potential, and therefore the shift in threshold voltage per pH $\Delta V_{T,pH}$. In contrast, for biomolecular systems, many more factors can affect the shift in threshold voltage per 10-fold increase in concentration of analyte, $\Delta V_{T,p[A]}$. The net charge of the biomolecular system (shown as green circles) can influence response. The Debye length (λ_D) is compared to the distance of the analyte from the surface (L_A) on the figure, which can significantly affect BioFET signal. τ_{eq} is used to refer to the typical time-scale to equilibration.

Firstly, the shift in threshold voltage per 10-fold increase in analyte concentration for biosensing

may be lower than that for a 10-fold increase in H^+ concentration in pH sensing simply because transport of the biomolecule to the surface and the subsequent reaction can take long times to equilibrate compared to the equilibration of the acid-base reactions relevant to pH sensing. For example, considering diffusive flux, it can be shown that a typical nanowire-based geometry has an expected response time on the order of an hour for a fM concentration of analyte with a diffusion constant of $150\,\mu m^2\,s^{-1}$ typical of single-stranded DNA about 20 base-pairs long [478]. In contrast, the diffusion constant for H^+ is orders of magnitude higher due to Grotthuss transport, which was introduced in Section 3.3.4[2]. In contrast to pH sensing, the limitations imposed by mass transport, binding kinetics and device-geometry choices must be considered when designing for optimal response [73, 83, 477].

Secondly, the concentration of biomolecular analyte available to bind to the surface may be lower than that expected based on the initially added bulk concentration due to binding to non-sensitive regions of the device, an issue which is often caused by non-specific binding but can also occur if the receptor chemistry used on the sensor surface is elsewhere in the device. Non-specific is particularly problematic for nanoscale dimension devices in which the biosensitive regions of the device can have a small surface area relative to the total exposed surface area [460].

Thirdly, from the results shown in Chapter 6, variation between different experiments may occur due to different commercial preparations of the same biomolecule having different electrodynamic properties.

Fourthly, in principle, the biomolecular orientation can affect the response [31, 472].

A final consideration is that of the buffering capacity of the solution. Lloret et al. measured the change in pH of bulk solution using a pH microelectrode in response to addition of streptavidin. This showed that addition of 1 µM streptavidin to 0.01X PBS (i.e. containing 1.627 mM ionic strength, pH 7.4) resulted in a change of 0.5 pH units [87]. In contrast, at 1X PBS the shift in pH was negligible as expected from its high buffering capacity. If this result is found to be reproducible, the significance of this cannot be understated; for example, for a typical PBS concentration of 0.01X, and a typical SiO_2 surface in the pH 5-9 region ($\Delta V_T = 30\,mV/pH$ response), this 0.5 pH unit shift due to streptavidin addition would correspond to a non-specific response of $\Delta V_T = 15\,mV$. This would be on the same order of magnitude as many measured streptavidin signals, as shown in Figure 8.3. It is noteworthy that the practice of using minimal buffering capacity and high biomolecule concentration (added in a single aliquot) is not uncommon [96, 97, 341, 449, 460, 479]. A simple solution is to ensure low concentrations of analyte are used; this also puts the experiment closer to the application of medical diagnostics in which biomolecules often must be detected at low-concentrations from blood samples, or alternatively to use a solution which can obtain lower ionic strengths than PBS for the same buffering capacity, for example, using just the Sodium Phosphate component of the PBS buffer. [87]

This quantitative analysis of the literature suggests that in order to optimise BioFET Sensitivity, device-design should focus upon simultaneous optimisation of the device Subthreshold Slope and the electrolyte-oxide surface chemistry. Taking the device geometry as an example, much literature is focused upon the investigation of new device-geometries which might offer enhanced Sensitivity, however this analysis showed that using a simple planar transistor, Wen et al. [480] achieved a comparable streptavidin Sensitivity to the work of Stern et al. [61] who utilised a nanoribbon. The nanobelt arrays of Liu et al. [460] and Cheng et al. [65] showed even lower Sensitivity values. The commonly stated assumption that increased surface area-to-volume ratio increases Sensitivity is the rationalisation for much of the focus in publications on building new nanoscale dimensions devices

[2]Detection of changes in pH can also involve a detection of changes in OH^- (Section 3.3.4), and therefore the time taken to sense a single H^+ is non-trivial to calculate, as it non-linearly related to the acid-base chemical equilibria in the system

[18, 59–61]. This assumption is still subject to debate, with some authors suggesting that the nanoscale dimensions offer increased Sensitivity via a different mechanism [62, 481] or not generally applicable to all structures [63]. While the analysis presented in this chapter suggest that device geometries may not be the limiting factor in Sensitivity enhancement, increasing surface-area-to-volume ratios of the device geometry may provide benefits in terms of signal-to-noise enhancement or improved biomolecule binding kinetics, whilst smaller-size devices offer increased portability.

8.6. Conclusions and Future Perspective

Whilst numerous reviews in the field of BioFET research have been published, they have generally provided examples of devices across a range of analytes, making direct comparison of Sensitivity near impossible. This review provides the first comprehensive analysis of the FET-sensor response due to a single biomolecular analyte. Streptavidin-sensing was primarily chosen as a model system due to its general wide spread usage and well-understood (bio)chemistry. This was contrasted with pH sensing, which is a better understood application of FET sensors, and has already been well-characterised.

For pH sensing, it is known that the Sensitivity can be increased by optimising the transistor design such as to have a low value of the Subthreshold Slope and by choosing an oxide material which has a large shift in surface threshold voltage per pH such as HfO_2. In contrast to pH sensing Sensitivity, the analysis of the literature which was presented in this chapter revealed that streptavidin-sensing Sensitivity showed no clear dependence on Subthreshold Slope, with a much greater variation in the shift in threshold voltage per 10-fold increase in streptavidin concentration between devices, even for the same oxide material. Even with a poor choice of oxide material on the surface (e.g. SiO_2 is poor due to its relatively low characteristic shift in threshold voltage per pH of ~33 mV/pH), good pH sensing Sensitivity can be obtained without an optimal (~59 mV/dec Subthreshold Slope) transistor. This study shows that the same design-strategy *does not* hold for biosensing, because, for example, a poorly functionalised biosensor surface will always have negligible Sensitivity regardless of the choice of oxide. This addressed one of the original motivations of this work to investigate whether optimisation strategies that had been employed for pH sensors would be directly transferable to optimisation of biomolecular sensing. The analysis presented suggested that Subthreshold Slope improvement is not as likely to be as beneficial for biosensor optimisation as it is for pH sensing because the limiting factor for Sensitivity is often the surface chemistry.

The variability in the shift in threshold voltage per 10-fold increase in analyte concentration for biosensing responses was greater than that found for pH sensing responses. This higher variability can be explained by a variety of factors. pH models predict the most important factor in influencing this shift is the density of analyte-receptor at the surface, and therefore this may be an important factor determining the variability in biomolecular response. Further, the effects of ionic strength and buffering capacity in biosensing are much more pronounced than for pH sensing due to the biomolecule distance from the surface, and due to the ability of the biomolecule to change the pH of the buffer. Additional variability in biosensing threshold voltage shift per 10-fold increase in analyte concentration can originate from loss of biomolecule due to non-specific binding. This is particularly problematic for nanoscale dimension devices in which the biosensitive regions of the device can have a small surface area relative to the total exposed surface area. A fundamental source of variability can originate from the biomolecule itself; depending on the particular commercial preparation of a biomolecule such as streptavidin, the structure and isoelectric point and thus sensing response of the biomolecule can vary (Section 6.3).

In conclusion, the analysis presented in this chapter suggests that in order to optimise BioFET Sensitivity, device design optimisation should focus upon the Subthreshold Slope of the device and the

electrolyte-oxide surface chemistry. For example, even using an ideal classical transistor (Subthreshold Slope$\approx 59\,\mathrm{mV/dec}$), if the surface is poorly functionalised then it is will have a low Sensitivity. Devices even of simple (microscopic) planar geometry were shown capable of obtaining comparable Sensitivity to more elaborate nanodevice geometries (such as nanowires), suggesting nanoscale device design is not a requisite for high biomolecular Sensitivity.

By measuring the response-curve as a function of analyte concentration, researchers are provided with important information for device design: the saturation point of the curve can indicate the density of bound analyte, the response per 10-fold increase in analyte concentration can provide a figure-of-merit for the device and by fitting the curve to an appropriate binding model, the binding affinity of the analyte to its receptor can be estimated. Simple calculations can be used to estimate the density of bound analyte based on the concentration at which the sensor response saturates, and both this value and measurement of the shift in threshold voltage per 10-fold increase in analyte concentration can be useful in determining whether Sensitivity enhancement efforts are limited by surface chemistry or transistor performance.

As highlighted in this chapter, biosensor design is a highly interdisciplinary field. Understandably, this has led to lack of appreciation of the importance of reporting parameters such as the commercial origin of the biomolecule used, the value of the Subthreshold Slope of the device and proper controls to ensure that the response is due to specific binding of the biomolecule. Some common pitfalls were highlighted: Firstly, many experiments have been performed without a reference electrode in the liquid, which is a requirement for a reproducible and reliable response. Secondly, the practice of reporting only the absolute value of the Normalised Change in Current without the polarity can lead to ambiguity in interpreting the results of experiments. Finally, many BioFET experiments are performed at high concentration of biomolecules with deliberately low buffering capacity solution (diluted buffer), which could result in a significant non-specific response due to changes in the bulk pH of the solution and experiment reproducibility.

Many of these limitations are similar to those that have been encountered for other emerging biosensing technologies. The current 'gold standard' for label-free biosensing is Surface Plasmon Resonance (SPR) biosensors. In a highly extensive review published in 2005, Rich and Myszka analysed 1113 articles (103 reviews, 1010 papers) and discussed common issues within the Surface Plasmon Resonance biosensor literature such as: authors only considering high concentrations of analyte, response being normalised inappropriately or the data was reported in insufficient detail [482]. Surface chemistry optimisation has played an important part of Surface Plasmon Resonance biosensor development [483]. In principle, BioFET devices have the potential to surpass Surface Plasmon Resonance biosensors due to their ability to detect low-mass analyte and the lack of requirement for additional optical equipment (which can be high cost and low throughput). As highlighted in this chapter, currently advances in the field of BioFET research are being obstructed by the lack of consensus upon which quantitative metrics (i.e. figure-of-merit) should be used to compare devices, as a result, most published studies can only be compared qualitatively. Despite these limitations, BioFET research is a rapidly advancing field in which novel device design and operation methodologies are constantly being developed which increase the viability of BioFET devices for commercial use.

9. Research Conclusions

Most models describing FET-sensor response have relied upon mean-field assumptions which neglect the multi-scale nature of the system. Even qualitative predictions of FET-sensor response remain challenging. Many examples exist of FET-sensor measurements which cannot be explained using conventional electrostatic-gating arguments. These arguments were originally developed to explain MOSFET response, as opposed to FET-sensor response.

In this work, the interfacial physics of FET-sensors were modelled using a variety of simulation techniques with different length- and time-scales, with the aim of both improving understanding of the underlying electrodynamics at the surface of the sensor (the oxide-water interface), and improving BioFET device design. The following outline summarises the structure of the thesis, starting with microscopic simulations and ending with modelling of the entire (macroscopic) BioFET systems. As FET-sensors detect changes in the electric field induced by changes in surface charge, in Chapter 4, Density Functional Theory was used to model the microscopic charging processes at the silica-water interface over an approximately one nanometre length-scale over hundreds of femtoseconds. In Chapter 5, Kinetic Monte Carlo simulations were performed, which are capable of modelling the kinetics of these charging processes over much longer length- and time-scales (e.g. micrometre and seconds), at the expense of microscopic detail of the mechanisms involved.

BioFET sensors not only detect changes in the electric field induced by surface-charge modification, but crucially can also detect changes in the electric field induced by the introduction of biomolecular charge. Therefore, in Chapter 6, a semi-empirical model was used to estimate the charge of typical biomolecules used in biosensing experiments, TNF-α and streptavidin. In Chapter 7, classical Molecular Dynamics simulations were used to model the dynamics of charges at the silica-water-biomolecule interface over several nanometres, which is a sufficient length-scale for the study of typical small biomolecules such as DNA oligomers. The simulations were performed over nanosecond time-scales, which is sufficient to accurately describe water reorientation dynamics and to study the effect of ion- and biomolecule-dynamics on the electric field. Finally, in Chapter 8, a quantitative analysis of experimental BioFET results for the detection of Streptavidin was performed. This study used the MOSFET drift-diffusion equations to relate reported changes in measured drain current to changes in surface potential, and therefore provided a description of the surface potential behaviour at the oxide-water-biomolecule interface over macroscopic (i.e. experimental) length- and time-scales.

Charging at the Silica-Water Interface

Despite decades of study, the detailed structure and dynamics of the oxide-water interface, which is present in many FET-sensors, remain elusive. Acid-base reactions are established to be the dominant charge-determining process, and the literature has primarily focused upon quantification of these reactions via study of their equilibrium structure, for example in the measurement of the pK_a of silanol groups at the silica surface. Small changes in pH can be detected by FET-sensors, and therefore the dynamics of these acid-base reactions is expected to be important in modelling FET-sensor noise. In order to build a dynamic model of the system, first an improved understanding of the energetics and mechanisms of surface charging at the silica-water interface must be obtained.

In Chapter 4, Density Functional Theory calculations were used to investigate charging at this interface. A model of amorphous silica was constructed using a surface built from α-cristobalite as this model can replicate important properties of the silica-water interface such as the silanol density. The pseudopotentials used were validated against all-electron calculations and were shown to introduce negligible error into the optimised geometries of a range of simple chemical systems and shown to accurately model the interaction energy of silica-water to within 1 kJ/mol of the all-electron result. The chosen parameters represent an optimal compromise between accuracy and computational expense for this system. Additionally, a simple, freely available, open-source tool was created which can help automate the process of convergence-testing when using the ONETEP software.

The results of the study showed that the protonation of isolated silanols in the presence of H_3O^+ exhibit a highly rapid, exothermic reaction with no significant activation energy. In the simulations, this process occurred via a concerted motion of the protons through hydrogen-bonded water molecules known as 'water wires'. Geometry optimisations of large water clusters containing hydronium ions ($H_3O^+(H_2O)_{11}$ and $H_3O^+(H_2O)_{20}$) at the silica surface demonstrated proton transfer to the surface occurring via the rarely discussed 'proton holes' mechanism. This mechanism is when a hydroxyl ion mediates the transfer of a proton from the proton donor (a hydronium ion) to an acceptor (the surface). This study also identified a novel mechanism of surface protonation in which even those hydronium ions distant (4 water molecules at least) from the surface, *without losing a proton,* can protonate the surface by supporting the dissociation of water molecules.

The dissociation of isolated silanols in the presence of hydroxide ions was also investigated using several cluster systems and also found to behave as an activationless process for the cases of both the gas phase hydroxide ions and the implicitly solvated hydroxide ions. For the case of explicitly solvated hydroxide ions, in the case of the $H_9O_5^-$ anion, the local environment of hydrogen bonded silanols and waters was shown to be capable of creating an energetic barrier to deprotonation, but showed complete or partial deprotonation for the $H_3O_2^-$ and $H_7O_4^-$ hydroxide clusters. In support of this result, a similar energetic barrier has been observed for proton transport of $H_9O_5^-$ in the pure water simulations of Tuckerman et al. [201]. These findings demonstrate the microscopic complexity of the acid-base equilibria present at the silica-water interface. Whilst the study of proton transfer in pure water has received considerable attention, given that silica and water are some of the most abundant materials on the planet, this work highlights the need for a greater focus on research into silica-water chemistry.

The short time-scale and high exothermicity of these reactions shows that these hydronium/hydroxide systems will readily transfer protons, and therefore surface scientists should be cautious when simulating such systems in the context of non-reactive forcefields. The $Si{-}O^-\cdots H_2O$ hydrogen bond length was found to be strongly dependent upon the degree of solvation, which suggests that accurate parametrisation of this bond in classical molecular dynamics simulations requires careful consideration.

Currently, problems of undesirable drift and noise in the response are key limitations of FET-sensors which are likely to be a result of surface-charging acid-base reactions. The kinetics of these acid-base reactions are therefore important to understanding the response of FET-sensors, which can, in principle, detect surface-charge changes as small in magnitude as an elementary charge. A common methodology for obtaining the kinetics of a chemical reaction is via Transition State Theory, but this work suggested that proton transfer events at the isolated silanol-water interface often do not exhibit a well-defined transition state and therefore dynamic modelling using Transition State Theory is likely inapplicable. Considering the future of the field, given that the rate-limiting step is the formation of a suitable hydrogen-bonded water network, predictive modelling of the kinetics of surface-charging reactions over large length- and time-scales requires a model that incorporates the probability of formation of a suitable hydrogen-bonded network.

Kinetic Monte Carlo Model of Dynamic Surface Charging

For a given surface-water interface, it might be possible to accurately model surface charging dynamics simply by empirically parameterising the kinetics of surface charging reactions into a set of constants. Given this motivation, in Chapter 5, a Kinetic Monte Carlo model was produced, which is capable of describing protonation-deprotonation events over the macroscopic time- and length-scales relevant to FET-sensor operation. The model presented in this work, as well as related models, have been used within the literature to provide a link between the microscopic theory of protonation reactions and the experimental proton-titration data. In this work, a new implementation of this literature KMC model was produced using the Zacros software package, in which the parallel computational efficiency improves with the number of nearest neighbour interactions, facilitating the study of large systems in a computationally efficient manner. This Kinetic Monte Carlo model was based on a framework in which the electrostatic free energy of protons binding to an oxide surface is considered in the context of a Poisson-Boltzmann model for the electrolyte interface.

The key predictions of the model from this work (time-scale and equilibrium surface coverage) were in good agreement with the literature model, and it could be used as part of future multi-scale BioFET modelling efforts. Limitations in the field primarily stem from the difficulty in obtaining experimental kinetic data for microscopic protonation-deprotonation events, which make accurate parametrisation of the time-scale of microscopic protonation-deprotonation events difficult to obtain.

Modelling the Net Charge on Proteins

BioFET sensors operate by detecting changes in the electric field at the oxide-aqueous interface due to the binding of charged biomolecules to receptors on the surface. As a result of this, the charge of biomolecules is important for parametrising most current models of BioFET response which are based on the Poisson-Boltzmann equation. Using simple net-charge/electrostatic gating arguments, the magnitude and sign of the charge of a biomolecule is expected to correspond to the magnitude and polarity of BioFET response to the binding of that biomolecule.

The distribution of charge within a biomolecule is non-trivial to measure and predict because it is a non-linear function of pH and ionic strength and can be modified by the local chemical environment. In Chapter 6, the net charge on the biomolecules was calculated using the semi-empirical PROPKA model which uses the positions of atoms within the protein to predict their charge, as a function of pH.

In Study 1 (Section 6.2) a typical antibody-antigen system, that of anti-TNF-α (which, in a device, would be attached to the biosensor surface) binding to the antigen TNF-α in solution, was investigated by calculating both the net charge of the analyte (antigen) and the change in net charge on protein binding to the receptor (antibody). This particular system was chosen because it was of interest to industrial (Sharp Corporation) and academic collaborators, for whom the net-charge calculations would be of value, but also because it is an important biomarker for inflammatory response and therefore a typical biomolecular system for biosensing applications.

At physiological pH ranges ($6 \lesssim \text{pH} \lesssim 8$), the results showed that the net charge of the antigen is relatively insensitive to changes in pH and demonstrated a low magnitude charge ($|q| < 4\,e$). More extreme pH values led to sharp increases in the magnitude of net charge of the antigen. Such information can be used to make informed decisions about the choice of pH for BioFET-sensing experiments, although there are also practical limitations, for instance the protein can denature or become insoluble at more extreme pH values.

Based on simple net-charge arguments, the differences in structure between different commercially developed forms of the same antibody (anti-TNF-α) were shown to have a significant effect on the expected optimum pH for biosensing experiments, with a variation of 2 pH units for the predicted point-of-no-signal between the two commercial antibody structures investigated. The calculated net charge on the protein can be used in most existing models of BioFET response within the literature [2, 39, 44, 59] to estimate the change in surface charge density upon biomolecule binding, and was subsequently used by the industrial collaborators (Sharp Corporation).

In Study 2 (Section 6.3), the net charge of streptavidin, an archetypal model protein in biosensing, was investigated. Many authors do not report the commercial origin of their streptavidin sample under the assumption that it is not relevant to its charging properties, however this assumption was shown to be false via a review of experimentally reported pI values which showed a range of pI values between 5–7.5 for solution-phase streptavidin, with surface-bound streptavidin showing pI values at the lower range (pI ≈ 5). Further, it is not uncommon for different commercial preparations of streptavidin to have different structures and therefore analysis of the sequence of the native gene was used to highlight the potential for variation in the charge of streptavidin based on either natural or artificial variation in its structure. This variability in streptavidin charge demonstrates that it is important that authors report the origin of the sample (i.e. how was it expressed - is it recombinant or native? Was it artificially truncated by the vendor?) in order to ensure reproducible results.

Surprisingly, despite its common usage in BioFET experiments and most other biosensors, a rigorous description of the expected charge of streptavidin as a function of pH was not available in the literature. In novel simulations using the PROPKA model based on a truncated X-ray structure of streptavidin, the pH-dependence of the charge on streptavidin was predicted. The predicted pI was 5.04 which is in good agreement with experimental measurements, which found a pI of between 5–6. The net charge at approximately pH 7.4 is relevant to biosensing conditions and for streptavidin this was calculated to be $-7.20\,e$, which is in the middle of the predictions available within the literature that range between $-5\,e$ and $-8.49\,e$.

The calculated net charge provides a simple-to-calculate estimate from which to make informed decisions regarding an input parameter (the 'magnitude of charge on the biomolecules') for usage within many models of biosensor response. This approach is insufficient to accurately capture the complexity of the relevant physics, and various simulations over the last decade have suggested that net-charge arguments are insufficient for accurate modelling of BioFET response [31, 37, 39, 40]. In order to more accurately describe the electric field change induced by the biomolecule, a model that can capture the spatial arrangement of charges in the system would be required. To model the time-dependent response of the device (e.g. noise or 'drift'), a dynamic model would also be required.

As presented in Section 3.1.5, an additional open-research question in this field is related to the unexplained phenomenon in which neutral molecules can induce a change in BioFET response. Responses have also been observed with opposite polarity to that expected based on net-charge modelling arguments. In both these cases (neutral molecules and 'reversed' signals), net-charge modelling arguments are fundamentally insufficient to explain FET-sensor response. This further supports the notion that a model is required which goes beyond net-charge modelling, for example, by incorporating the spatial arrangement of charges in the system.

Electrical Double Layer Dynamics at the Silica-Water interface

An electrical double layer is present at all liquid-solid interfaces, and therefore its structure and dynamics have relevance to a broad range of fields, from geochemistry to chemical engineering. With regards to BioFET research, the electrical double layer is often modelled using mean-field approaches

based upon the Poisson-Boltzmann equation. These models treat the biomolecule as a uniform, infinitely thin layer or modify the Poisson-Boltzmann equation to attempt to describe the biomolecules as a membrane. Such models are fundamentally limited by an inability to model finite-size effects, ion-ion correlations and water polarisation, all of which are likely to be important in generating the detected changes in electric field on biomolecule binding. Classical Molecular Dynamics is a simulation technique that can model these effects and was used in this work.

In Chapter 7, classical Molecular Dynamics simulations were performed to study the silica-water interface in different ionic strengths. Novel results from simulation of the addition of DNA molecules and divalent ions were also presented, the latter of particular importance in both physiological solutions and biosensing experiments. Divalent ions have received surprisingly little attention in the literature by the atomistic simulation community in the context of oxide-water interfaces, but the interaction of divalent ions with DNA systems in bulk solution has been characterised using both experiments and simulations.

Direct experimental measurement of the interfacial charge distribution is not available and therefore the MD simulation results presented in Chapter 7 were compared to a continuum Poisson-Boltzmann model and revealed good agreement with regard to double-layer thickness and sodium ion accumulation. Mg^{2+} did not accumulate significantly at the interface, instead distributing more diffusely than predicted by the Poisson-Boltzmann model. This result can be explained in terms of the highly favourable solvation of magnesium ions, and has relevance to the understanding of interfacial processes such as surface-dissolution, which has been proposed in the literature to be catalysed by magnesium adsorption [117]. In agreement, with experimental studies, divalent ions resulted in charge inversion within the electrical double layer, 1.5 nm from the surface. The magnitude of the charge inversion was approximately proportional to the ionic strength change (five-fold increase in ionic strength showed a five-fold increase in charge). This suggests that charge inversion can occur at lower ionic strengths than those previously measured by experimental work within the literature.

Increasing ionic strength reduced the equilibrium water coordination to silanolate groups, but the dissociation rate of water molecules to silanolate groups was not significantly affected. Sodium ion surface-desorption kinetics required a two-step mechanism involving hypercoordination of the silanolate followed by desorption into the bulk. Sodium ions demonstrated a more kinetically-stable solvation sphere when positioned at the silica-surface relative to when positioned in the liquid bulk. This was due to the structuring of water at the interface. These results, originating from explicit ion-water interactions, cannot be described by the commonly used Poisson-Boltzmann formalism.

Modelling of FET-sensor response due to biomolecules is currently inhibited by a lack of understanding of the interfacial electric field and ion distribution which occurs in the presence of biomolecules. In the MD simulations presented in Chapter 7, the first calculation of the time-varying electric field for these systems was presented. By comparison to a low ionic strength control, this calculation showed that bulk electrolyte plays a role in dampening transient fluctuations in the electric field and therefore device response. The bound DNA resulted in local changes to the electric field at the surface; however, calculation of the spatial- and temporal-mean electric fields showed no significant change. This unanticipated result was explained as due to strong screening originating from a combination of strongly polarised water and a compact 'Stern-like' layer of Na^{+} around the DNA and silica surface. The conclusion that water polarisation in the Stern-like layer can compose a major part of the electric field originating from the biomolecular-silica-water interface, suggests that BioFET response might be determined primarily by the ability of the biomolecule to modify the Stern-like layer, as opposed to its 'net charge' as traditionally thought. With regard to the understanding and optimisation of BioFET sensors, this result would suggest that even neutral or low net-charge biomolecules are able to be detected if they can disrupt the Stern layer, as the net charge of the biomolecule is not the

dominant causal component of the response. It also suggests that optimal surface chemistry design would require a surface system in which electrolyte ions are only weakly bound to the surface.

Experiments have shown that BioFET sensors can detect changes in surface potential as small as approximately 10 mV. A finding of the work presented in this chapter was that calculation of the change in surface potential due to biomolecule was highly sensitive to the choice of atomic coordinates from which the 'surface' was defined; making direct comparison to measured shifts problematic. A range of experimental work however has provided measurements of the interfacial potential and surface charge density at silica-water surfaces as a function of pH. Using this experimental data, the link between the surface potential calculated in atomistic simulations and the experimental measurement might be obtained. This merits further investigation, and future work will study the relationship between the surface charge, Stern-like layer density and the electrostatic potential at the interface.

With regards to modelling BioFET response, the simulation technique used in this study is not able to model how biomolecules modify the surface protonation-deprotonation equilibria. Looking to the future of the field, a more accurate model of BioFET response would account for changes in the protonation state of the surface due to biomolecule binding, but the work presented in Chapter 5 is potentially a first step in this field. For the equilibrium properties, models are already available which can predict changes in the protonation state due to the local chemical environment (such as that used in Chapter 6) but they are generally restricted to biomolecular systems in aqueous solution, as opposed to interfacial systems.

Quantitative Analysis of FET-Sensor Literature Data: From pH Sensing to Biosensing

Whereas IS-FETs have achieved commercial success as pH sensors, BioFETs remain unsuitable due to a lack of reliable-detection capability and stable response. Whilst many reviews exist in the field of BioFET research, they compare disparate surface-bound molecules, surfaces, analytes and experimental conditions, making quantitative comparisons near impossible. In Chapter 8, a critical review was presented which is the first to provide a systematic, quantitative comparison of BioFET results for a single biomolecular analyte. Streptavidin-sensing was chosen as the model system, primarily due to its common usage in biosensing experiments and well-understood (bio)chemistry. Streptavidin-sensing data was contrasted with pH sensing, which is a simpler-to-perform and hence well-understood and well-characterised application of FET sensors.

The signal-to-noise ratio is a desirable figure-of-merit, but it is rarely presented in published sensing data, instead, the presented data is often only sufficient to extract the Normalised Change in Current (I_{norm}) as a metric of the signal, with the 'noise' values unreported. Analysis was performed by comparing available streptavidin-sensing and pH-sensing data for both the Normalised Change in Current per 10-fold increase in analyte concentration ('Sensitivity'), and the shift in threshold voltage (ΔV_{T}) per log-unit of analyte, as a function of the Subthreshold Slope. For pH sensing, the oxide material is known to play a dominant role in determining the surface potential shift per pH. As a result of this, current pH sensing Sensitivity enhancement strategies are dominated by the choice of oxide material and transistor optimisation. Even an affordable and easy to fabricate oxide (e.g. SiO_2, as opposed to HfO_2) can demonstrate a high ΔV_{T} per pH (~33 mV/pH) which means that high Sensitivity can be obtained even without an optimal Subthreshold Slope (~59 mV/dec). For pH sensing applications of FET-sensors (i.e. IS-FETs), a clear strategy for device-optimisation for increased Sensitivity is available.

In contrast to pH-sensing Sensitivity, the analysis of the literature presented in this chapter showed that streptavidin-sensing Sensitivity does not have clear dependence on Subthreshold Slope, with

much more variable values of ΔV_T per 10-fold increase in analyte concentration between devices, and in some cases very low ($< 10\,\text{mV}$ per 10-fold increase in analyte concentration). This addressed one of the original motivations of this work to investigate whether optimisation strategies that had been employed for pH sensors would be directly transferable to optimisation of biomolecular sensing. The analysis presented suggested that Subthreshold Slope improvement is not as likely to be beneficial for biosensor optimisation as it is for pH sensing because the surface chemistry can reduce the Sensitivity of biosensors (which may have no sites available for analyte binding) more than that of pH sensors.

The variability in threshold voltage shifts due to streptavidin-binding to the biotin sensor surface, as compared to due to changes in pH, was explained as a result of a combination of factors. The most important factor is proposed, in this work, to be due to variation in the functionalised receptor site density between sensor surfaces. This was evidenced by the success of receptor-site density models in rationalising pH sensing results. Further, based on the results of Elfström et al., it was shown in Chapter 8, how simple analysis of the concentration at which the sensor saturates is useful in estimating the relative density of surface-bound biomolecules. This simple strategy could be used by researchers to decide whether to focus their efforts on surface chemistry- or transistor- optimisation.

The increased variability in published threshold voltage shifts relative to pH sensing can also be due to other factors: One factor is a consequence of the fact that the effects of ionic strength and buffering capacity in biosensing are much more pronounced than for pH sensing. At high ionic strength, a charge which is distant from the surface will not be sensed. As a result of this, the relatively large distance of the charges on the biomolecule from the surface, compared to protons binding to an oxide surface (in which the charge of the proton is in contact with the surface), results in more pronounced dependence of the shift in threshold voltage on the ionic strength for biosensing compared to pH sensing. Further, acid-base reactions of the amino acids on the biomolecule can change the pH of the buffer, or potentially disrupt the oxide-water acid-base equilibria, and therefore biosensing systems show a more pronounced dependence of the threshold voltage on the buffering capacity of the aqueous solution. A further factor which introduces variability into the measured threshold voltage shift originates from a loss of biomolecule from aqueous solution due to non-specific binding. This is particularly problematic for nanoscale devices in which the biosensitive regions of the device can have a small surface area relative to the total exposed surface area. In Section 6.3 it was also shown that a fundamental source of BioFET response variability can originate from the biomolecule itself, because depending on the particular commercial preparation of a biomolecule, as was found for streptavidin, the structure and isoelectric point of the biomolecule can vary.

A key conclusion of this analysis is that in order to optimise BioFET sensitivity, device-design optimisation should focus upon simultaneous optimisation of the device Subthreshold Slope and the electrolyte-oxide surface chemistry. For example, even an ideal classical transistor (Subthreshold Slope$\approx 59\,\text{mV/dec}$) with a low-density of receptors on the surface will show a small change in surface potential and therefore a small Normalised Change in Current and Sensitivity. Optimised response requires a large change in surface potential, for example, via a high density of receptors on the surface. Devices even of simple (microscopic) planar geometry were shown capable of obtaining comparable Sensitivity to more elaborate nanodevice geometries (such as nanowires), suggesting nanoscale device design is not a requisite for high biomolecular Sensitivity.

Measurement of the sensor-response as a function of analyte concentration (i.e. pH) is common in the pH sensing community. This measurement is effectively the same as the IUPAC definition of sensitivity. Yet despite this, in the BioFET-sensing community, measurement of response as a function of biomolecular concentration is still uncommon. In this work it was argued that equivalent measurements are a vital figure-of-merit for comparing BioFET devices.

The critical review Chapter 8 highlights how biosensor design requires interdisciplinary input and

understanding. Lack of this has led to underappreciation of the importance of reporting parameters such as the precise nature of the biomolecules used, the value of the Subthreshold Slope of the device and proper controls to ensure that the response is due to specific binding of the biomolecule. Some common pitfalls were highlighted: Firstly, many experiments are performed without a reference electrode in the liquid, which is required for reproducible and reliable response. Secondly, the practice of reporting only the absolute value of the Normalised Change in Current without the polarity can lead to ambiguity in interpreting the results of experiments. Finally, many BioFET experiments have been deliberately performed at high biomolecule concentrations and low buffering capacity solutions (diluted buffer) to increase the signal and apparent sensitivity. However, not only is this non-physiological, but is also likely to result in significant non-specific responses due simply to changes in the bulk pH of the solution.

Many of these limitations and pitfalls are similar to those that were encountered when other biosensing technologies were emerging. For example, for surface plasmon resonance (SPR) biosensors, many authors originally reported their data with insufficient detail for reproducibility and reliability, and it took many decades before a standardised framework of experimental design and performance-metrics was established. BioFET performance is currently usually quantified via the Normalised Current Change, which neither describes the relationship between signal and concentration, nor the minimum detectable concentration (or amount) of an analyte. Once reliable figures-of-merit for BioFET devices have become established, progress in optimising BioFET sensors for practical usage in the field should proceed more rapidly and with more reliability.

Despite these limitations, BioFET research is a rapidly advancing field in which novel device design and operation methodologies are constantly being developed which increase the viability of BioFET devices for commercial use. An example of a promising recent advance is the discovery of the ability to detect biomolecules using a characteristic change in the BioFET frequency response [34, 63, 314, 383] or detecting the transient signal upon a step-wise change in ion concentration [458]. These techniques offer the potential of reducing noise and to circumvent the requirement of low ionic strength buffers to achieve sufficient magnitude of signal.

Multi-Scale Simulation and Future Perspective

In this section, a perspective on the future of FET-sensor simulation is provided, highlighting literature that is exemplary of current open research questions within the field.

FETs are relatively well understood as solid-state devices, whereas FET-sensors are much less well understood due to the complexity introduced by the aqueous media and surface chemistry, including surface ionisation and ion dynamics. A key challenge of modelling FET-sensors has been that the time-scales of interest span far longer than their solid-state counterparts. For example, the time-scales involved range from approximately 10^{-3} to 10^{3} seconds for biomolecule binding events compared to approximately 10^{-12} seconds for the changes in conductivity of the sensor. In this work, disparate simulation techniques were employed to investigate the interfacial physics across the many-scales of the problem, from individual surface charging reactions, to ion dynamics in the electrical double layer and finally to the modelling of the surface potential changes experimentally measured using BioFET devices.

Often modelling of BioFET response is performed via mean-field Poisson-Boltzmann approaches in which response caused by binding of the biomolecule to the sensor surface is modelled as the equilibrium response to the introduction of a uniform sheet of charge. These models have been unsuccessful in explaining many aspects of BioFET response, and the work within this thesis suggests that the

contribution of acid-base equilibria kinetics and ion dynamics has been hitherto underestimated. A reliable model of FET-sensor response requires an accurate description of the electric field across the disparate time- and length-scales involved. One promising methodology for such a simulation framework is via Brownian Dynamics simulations. For example, in the multi-scale model of Asenov et al. [80, 81], Brownian Dynamics simulations were used to explicitly model the effect of ion dynamics on FET-sensor response. They used the model to improve understanding of the drain current noise originating from the ion-dynamics, however it was not applied to biomolecular systems. In future work in this field, such a model could be used to investigate the effect of biomolecule binding on the device noise. Furthermore, as their models lacks a description of noise originating from the acid-base equilibria at the surface, this would be an informative extension to this model. This extension could be implemented either as an equilibrium model of surface charging via traditional surface complexation models, or as a dynamic model using a Kinetic Monte Carlo model such as that presented in this thesis.

The lack of a reliable model for BioFET response has resulted in experimental work in the field which is performed with limited rational design. Some general principles have emerged to improve BioFET response, such as reducing the amount of screening of the analyte-charges by lowering the ionic strength of the electrolyte and operating in the subthreshold region for maximum normalised change in current. Nonetheless, many design principles remain disputed due to a lack of consensus on the underlying physical mechanism. For example, maximising the surface-area-to-volume ratio has been shown to increase device response (Section 3.1.3). The theoretical explanation, however, remains disputed and the literature review within this thesis (Chapter 8) showed similar Sensitivity for a range of devices of significantly different surface-area-to-volume ratios. Improved understanding of the relationship between device nanostructure and response therefore represents one of the most important research questions for device design, and in the coming years, multi-scale simulations will likely provide a tool to address this.

As introduced in Chapter 7, analysis of the BioFET noise has been shown in the literature to be another strategy for improving BioFET response. More specifically, biomolecules have been shown to be capable of producing a distinctive change in BioFET noise, such that frequency-mode detection can be used for improved detection capability [314, 361, 381]. This observation has been proposed to be a result of thermal noise of ions associated with the biomolecule [34], but prediction of the characteristic frequency at which this occurs remains an open research question. In a recent 2016 publication by Chung et al., a simple particle-based dynamic model was used to evaluate the effect of charged spheres (representing biomolecules) on ion dynamics and therefore FET-noise [383]. The noise levels increased as the charged spheres approached the surface, and the results strongly suggest that the thermal-Coulombic motion of ions gathered around the particles induce the Lorentzian shapes in the noise spectrum. With increased understanding of the precise relationship between biomolecule structure and noise-response, research in this field should provide another tool for rational enhancement of BioFET response.

It has been proposed in the literature that the issue of drain current drift (i.e. a monotonic change in drain current over time) in FET-sensor response is a result of chemical modification of the oxide surface on exposure to aqueous solution [205, 234]. Chemical modification could occur via acid-base reactions at the surface, or penetration of ions through the surface dielectric. The issue of drain-current drift remains a common problem for FET-sensors, and a multi-scale model of device response could be used to investigate the details of how these phenomena affect FET-sensor response, and therefore provide rational design guidelines for the optimal dielectric surface of FET-sensors.

In conclusion, modelling BioFET response is an inherently multi-scale problem, and in order to address the open questions in the field of BioFET design, future work will require suitable multi-scale models

to address current limitations in understanding.

10. List of Publications

Journal Publications

B. M. Lowe, C.-K. Skylaris & N. G. Green, 'Acid-base dissociation mechanisms and energetics at the silica-water interface: An activationless process'. *Journal of Colloid and Interface Science.* 451, 231–244, (2015). doi: 10.1016/j.jcis.2015.01.094

B. M. Lowe, Y. Maekawa, Y. Shibuta, T. Sakata, C.-K. Skylaris & N. G. Green, 'Dynamic Behaviour of the Silica-Water-Bio Electrical Double Layer in the Presence of a Divalent Electrolyte'. *Physical Chemistry Chemical Physics.* Accepted for Publication, (2016). doi: 10.1039/C6CP04101A

B. M. Lowe, K. Sun, I. Zeimpekis, C.-K. Skylaris & N. G. Green, 'Field-Effect Sensors – From pH sensing to Biosensing: Sensitivity Enhancement using Streptavidin-Biotin as a Model System'. *In preparation.*

Software

B. M. Lowe. ONETEP Convergence Automation Utility (OnetepConv) - A free, open-source utility for performing convergence testing with the ONETEP software. doi: 10.6084/m9.figshare.4001049.v1

Conference Presentations

B. M. Lowe, K. Sun, I. Zeimpekis, Y. Maekawa, Y. Shibuta, T. Sakata, C.-K. Skylaris & N. G. Green, 'Limitations and Possibilities for Biologically-sensitive Field-Effect Transistor-sensor Design (BioFET): Complexity of the Oxide-Electrolyte Interface'. Presented at 2016 5th International Conference on Material Science and Engineering Technology (ICMSET), October 2016, Tokyo, Japan.

B. M. Lowe, Y. Maekawa, Y. Shibuta, T. Sakata, C.-K. Skylaris & N. G. Green, 'Complexity at the Glass-Water Interface: Molecular Dynamics and Nanotechnology'. Presented at Complex Systems Simulation (CSS) Warm-up Event, September 2016, Amsterdam, Netherlands.

B. M. Lowe, Y. Maekawa, Y. Shibuta, T. Sakata, C.-K. Skylaris & N. G. Green, 'Multiscale Simulation of Field Effect Biosensors: from Quantum Mechanics to Electrostatics'. Presented at Nanoelectronics and Nanotechnology Group Annual Conference 2016: 'Sensors', July 2016, Southampton, UK.

B. M. Lowe, Y. Maekawa, Y. Shibuta, T. Sakata, C.-K. Skylaris & N. G. Green, 'Charge Dynamics at the Silica-Electrolyte Interface'. Presented at the 251st Spring 2016 American Chemical Society National Meeting, March 2016, San Diego, CA, USA.

B. M. Lowe, Y. Maekawa, Y. Shibuta, T. Sakata, C.-K. Skylaris & N. G. Green, 'The Importance of Understanding Electrodynamics in Understanding Field Effect Biosensors'. Presented at the Institute of Physics Early Career Researchers Colloquium, September 2015, London, UK.

B. M. Lowe, Y. Maekawa, Y. Shibuta, T. Sakata, C.-K. Skylaris & N. G. Green, 'Investigation of the Complex Water-Biomolecule-Silica Interface via Molecular Dynamics Simulations'. Presented at the Student Conference on Complexity Science, September 2015, Grenada, Spain.

Poster Presentations

B. M. Lowe, Selected to present and communicate research at the Science, Engineering and Technology (SET) for Britain. March 2016, House of Commons, Westminster, UK.

B. M. Lowe, C.-K. Skylaris & N. G. Green, 'Deprotonation at the silica/water interface: a DFT study'. Poster presented at the Theory, Modelling and Computational Methods for Semiconductors Conference, January 2014, Manchester, UK.

B. M. Lowe, C.-K. Skylaris & N. G. Green, 'Simulation of Silicon Nanowire Field Effect Sensors'. Poster presented at the Student Complexity Conference 2014, August 2014, Brighton, UK. Poster also presented at the Centre for Doctoral Training in Next Generation Computational Modelling Open Day, Match 2014, Southampton, UK.

Bibliography

[1] T. Hyeon. Chemical synthesis of magnetic nanoparticles. *Chem. Commun.*, (8):927–934, 2002.

[2] P. Nair and M. Alam. Design Considerations of Silicon Nanowire Biosensors. *IEEE Trans. Electron Devices*, 54(12):3400–3408, 2007.

[3] W. L. Zhang, R. J. Tang, H. C. Jiang, W. Zhang, B. Peng, and H. Zhang. Magnetization reversal simulation of diamond-shaped NiFe nanofilm elements. *IEEE Trans. Magn.*, 41(12):4390–4393, 2005.

[4] J. Xiang, W. Lu, Y. Hu, Y. Wu, H. Yan, and C. M. Lieber. Ge/Si nanowire heterostructures as high-performance field-effect transistors. *Nature*, 441(7092):489–493, 2006.

[5] H. W. C. Postma, T. Teepen, Z. Yao, M. Grifoni, and C. Dekker. Carbon Nanotube Single-Electron Transistors at Room Temperature. *Science*, 293(5527):76–79, 2001.

[6] W. U. Huynh, J. J. Dittmer, and A. P. Alivisatos. Hybrid Nanorod-Polymer Solar Cells. *Science*, 295(5564):2425–2427, 2002.

[7] J. L. West and N. J. Halas. Engineered nanomaterials for biophotonics applications: Improving sensing, imaging, and therapeutics. *Annu. Rev. Biomed. Eng.*, 5:285–292, 2003.

[8] J. Riu, A. Maroto, and F. Rius. Nanosensors in environmental analysis. *Talanta*, 69(2):288–301, 2006.

[9] L. Senesac and T. G. Thundat. Nanosensors for trace explosive detection. *Mater. Today*, 11(3):28–36, 2008.

[10] P. Arora, A. Sindhu, N. Dilbaghi, and A. Chaudhury. Biosensors as innovative tools for the detection of food borne pathogens. *Biosens. Bioelectron.*, 28(1):1–12, 2011.

[11] D. R. Thévenot, K. Toth, R. A. Durst, and G. S. Wilson. Electrochemical biosensors: Recommended definitions and classification. *Biosens. Bioelectron.*, 16(1-2):121–131, 2001.

[12] D. M. Kemeny. *Elisa and Other Solid Phase Immunoassays: Theoretical and Practical Aspects*. John Wiley & Sons, Chichester ; New York, 1988. ISBN 978-0-471-90982-8.

[13] A. Ramanavieius, F. W. Herberg, S. Hutschenreiter, B. Zimmermann, I. Lapënaitë, A. Kaušaitë, A. Finkelšteinas, and A. Ramanavièienë. Biomedical application of surface plasmon resonance biosensors (review). *Acta Medica Litu.*, 12(3):1–9, 2005.

[14] S. G. Patching. Surface plasmon resonance spectroscopy for characterisation of membrane protein–ligand interactions and its potential for drug discovery. *BBA-Biomembranes*, 1838(1, Part A):43–55, 2014.

[15] D. Cahen, R. Naaman, and Z. Vager. The Cooperative Molecular Field Effect. *Adv. Funct. Mater.*, 15(10):1571–1578, 2005.

[16] P. Bergveld, J. Wiersma, and H. Meertens. Extracellular Potential Recordings by Means of a Field Effect Transistor Without Gate Metal, Called OSFET. *IEEE Trans. Biomed. Eng.*, BME-23(2):136–144, 1976.

[17] K.-I. Chen, B.-R. Li, and Y.-T. Chen. Silicon nanowire field-effect transistor-based biosensors for biomedical diagnosis and cellular recording investigation. *Nano Today*, 6(2):131–154, 2011.

[18] N. Elfström, R. Juhasz, I. Sychugov, T. Engfeldt, A. E. Karlström, and J. Linnros. Surface Charge Sensitivity of Silicon Nanowires: Size Dependence. *Nano Lett.*, 7(9):2608–2612, 2007.

[19] E. Buitrago, M. Fernández-Bolaños, Y. M. Georgiev, R. Yu, O. Lotty, J. D. Holmes, A. M. Nightingale, and A. M. Ionescu. Attomolar streptavidin and pH, low power sensor based on 3D vertically stacked SiNW FETs. In *Proceedings of Technical Program - 2014 International Symposium on VLSI Technology, Systems and Application (VLSI-TSA)*, pages 1–2. 2014.

[20] G. Zheng, F. Patolsky, Y. Cui, W. U. Wang, and C. M. Lieber. Multiplexed electrical detection of cancer markers with nanowire sensor arrays. *Nat. Biotech.*, 23(10):1294–1301, 2005.

[21] P. Bergveld. Thirty years of ISFETOLOGY: What happened in the past 30 years and what may happen in the next 30 years. *Sens. Actuat. B-Chem.*, 88(1):1–20, 2003.

[22] P. Bergveld. A critical evaluation of direct electrical protein detection methods. *Biosens. Bioelectron.*, 6(1):55–72, 1991.

[23] P. Bergveld. Development of an Ion-Sensitive Solid-State Device for Neurophysiological Measurements. *IEEE Trans. Biomed. Eng.*, BME-17(1):70–71, 1970.

[24] L. Bousse, N. F. D. Rooij, and P. Bergveld. Operation of chemically sensitive field-effect sensors as a function of the insulator-electrolyte interface. *IEEE Trans. Electron Devices*, 30(10):1263–1270, 1983.

[25] M. J. Schöning and A. Poghossian. Recent advances in biologically sensitive field-effect transistors (BioFETs). *Analyst*, 127(9):1137–1151, 2002.

[26] Y. Cui and C. M. Lieber. Functional Nanoscale Electronic Devices Assembled Using Silicon Nanowire Building Blocks. *Science*, 291(5505):851–853, 2001.

[27] R. S. C. Cobbold. Historical Review. In *Theory and Applications of Field-Effect Transistors*, pages 2–4. Wiley-Interscience, New York, 1970.

[28] J. W. Toliver. *Theory and Applications of Field-Effect Transistors*. Kansas State University, 1st edition, 1967.

[29] L. J. Sevin. *Field-Effect Transistors*. McGraw-Hill, 1st edition, 1965. ISBN 978-0-07-056355-1.

[30] Y. Taur and T. H. Ning. *Fundamentals of Modern VLSI Devices*. Cambridge University Press, second edition edition, 2013. ISBN 978-1-107-39399-8.

[31] L. De Vico, L. Iversen, M. H. Sørensen, M. Brandbyge, J. Nygård, K. L. Martinez, and J. H. Jensen. Predicting and rationalizing the effect of surface charge distribution and orientation on nano-wire based FET bio-sensors. *Nanoscale*, 3(9):3635, 2011.

[32] A. Rimola, D. Costa, M. Sodupe, J.-F. Lambert, and P. Ugliengo. Silica Surface Features and Their Role in the Adsorption of Biomolecules: Computational Modeling and Experiments. *Chem. Rev.*, 113(6):4216–4313, 2013.

[33] M.-P. Lu, E. Vire, and L. Montès. Ionic screening effect on low-frequency drain current fluctuations in liquid-gated nanowire FETs. *Nanotechnology*, 26(49):495501, 2015.

[34] K. Georgakopoulou, A. Birbas, and C. Spathis. Modeling of fluctuation processes on the biochemically sensorial surface of silicon nanowire field-effect transistors. *J. Appl. Phys.*, 117(10):104505, 2015.

[35] M. H. Sørensen, N. A. Mortensen, and M. Brandbyge. Screening model for nanowire surface-charge sensors in liquid. *Appl. Phys. Lett.*, 91(10):102105–102105–3, 2007.

[36] P. R. Nair and M. A. Alam. Screening-Limited Response of NanoBiosensors. *Nano Lett.*, 8(5):1281–1285, 2008.

[37] C. Heitzinger, Y. Liu, N. J. Mauser, C. Ringhofer, and R. W. Dutton. Calculation of Fluctuations in Boundary Layers of Nanowire Field-Effect Biosensors. *J. Comput. Theor. Nanosci.*, 7(12):2574–2580, 2010.

[38] C. Heitzinger and G. Klimeck. Computational aspects of the three-dimensional feature-scale simulation of silicon-nanowire field-effect sensors for DNA detection. *J. Comput. Electron.*, 6(1-3):387–390, 2007.

[39] C. Heitzinger, R. Kennell, G. Klimeck, N. Mauser, M. McLennan, and C. Ringhofer. Modeling and simulation of field-effect biosensors (BioFETs) and their deployment on the nanoHUB. *J. Phys.: Conf. Ser.*, 107(1):012004, 2008.

[40] C. Heitzinger, N. J. Mauser, and C. Ringhofer. Multiscale Modeling of Planar and Nanowire Field-Effect Biosensors. *SIAM J. Appl. Math.*, 70(5):1634–1654, 2010.

[41] S. Baumgartner, C. Heitzinger, A. Vacic, and M. A. Reed. Predictive simulations and optimization of nanowire field-effect PSA sensors including screening. *Nanotechnology*, 24(22):225503, 2013.

[42] S. Baumgartner, M. Vasicek, A. Bulyha, and C. Heitzinger. Optimization of nanowire DNA sensor sensitivity using self-consistent simulation. *Nanotechnology*, 22(42):425503, 2011.

[43] T. Windbacher, V. Sverdlov, and S. Selberherr. Modeling of Low Concentrated Buffer DNA Detection with Suspend Gate Field-Effect Transistors (SGFET). In *Computational Electronics, 2009. IWCE'09. 13th International Workshop on*, pages 1–4. IEEE, 2009.

[44] T. Windbacher, V. Sverdlov, S. Selberherr, C. Heitzinger, N. Mauser, and C. Ringhofer. Simulation of field-effect biosensors (BioFETs) for biotin-streptavidin complexes. In *AIP Conference Proceedings*, volume 1199, page 507. 2010.

[45] T. Windbacher, V. Sverdlov, and S. Selberherr. Biotin-streptavidin sensitive biofets and their properties. In *Biomedical Engineering Systems and Technologies*, pages 85–95. Springer, 2010.

[46] J. E. Lilienfeld. Method and apparatus for controlling electric currents. Patent Number: US1745175 (A). Application Number: US19260140363 19261008. Priority Numbers: CAT272437 19251022, 1930.

[47] J. W. Han, J. S. Oh, and M. Meyyappan. Cofabrication of Vacuum Field Emission Transistor (VFET) and MOSFET. *IEEE Trans. Nanotechnol.*, 13(3):464–468, 2014.

[48] J. J. Liou, A. Ortiz-Conde, and F. Garcia-Sanchez. *Analysis and Design of Mosfets: Modeling, Simulation, and Parameter Extraction*. Springer, 1st edition, 1998. ISBN 978-0-412-14601-5.

[49] M. E. Agnes. *Webster's New World College Dictionary*. Webster's New World, Boston, 5th edition edition, 2016. ISBN 978-0-544-59822-5.

[50] J. Go, P. R. Nair, and M. A. Alam. Theory of signal and noise in double-gated nanoscale electronic pH sensors. *J. Appl. Phys.*, 112(3):034516, 2012.

[51] H. H. Nguyen, J. Park, S. Kang, and M. Kim. Surface Plasmon Resonance: A Versatile Technique for Biosensor Applications. *Sensors*, 15(5):10481–10510, 2015.

[52] S. Sang, Y. Wang, Q. Feng, Y. Wei, J. Ji, and W. Zhang. Progress of new label-free techniques for biosensors: A review. *Crit. Rev. Biotechnol.*, pages 1–17, 2015.

[53] I. Heller, A. M. Janssens, J. Männik, E. D. Minot, S. G. Lemay, and C. Dekker. Identifying the Mechanism of Biosensing with Carbon Nanotube Transistors. *Nano Lett.*, 8(2):591–595, 2008.

[54] T. Sakata, M. Kamahori, and Y. Miyahara. DNA Analysis Chip Based on Field-Effect Transistors. *Jpn. J. Appl. Phys.*, 44(4S):2854, 2005.

[55] M. W. Shinwari, M. J. Deen, and D. Landheer. Study of the electrolyte-insulator-semiconductor field-effect transistor (EISFET) with applications in biosensor design. *Microelectron. Reliab.*, 47(12):2025–2057, 2007.

[56] V. Lakshminarayanan. Personal Communication regarding FET-sensor Signal-to-Noise Ratio. URL: https://www.researchgate.net/post/Why_do_FET-sensors_BioFETs_IS-FETs_increase_the_signal-to-noise_ratio_relative_to_simply_measuring_the_surface_potentail_directly, 2016.

[57] P. Bergveld. Development, Operation, and Application of the Ion-Sensitive Field-Effect Transistor as a Tool for Electrophysiology. *IEEE Trans. Biomed. Eng.*, BME-19(5):342–351, 1972.

[58] M. M. A. Hakim, M. Lombardini, K. Sun, F. Giustiniano, P. L. Roach, D. E. Davies, P. H. Howarth, M. R. R. de Planque, H. Morgan, and P. Ashburn. Thin Film Polycrystalline Silicon Nanowire Biosensors. *Nano Lett.*, 12(4):1868–1872, 2012.

[59] N. Elfström, A. E. Karlström, and J. Linnros. Silicon Nanoribbons for Electrical Detection of Biomolecules. *Nano Lett.*, 8(3):945–949, 2008.

[60] N. K. Rajan, K. Brower, X. Duan, and M. A. Reed. Limit of detection of field effect transistor biosensors: Effects of surface modification and size dependence. *Appl. Phys. Lett.*, 104(8):084106, 2014.

[61] E. Stern, J. F. Klemic, D. A. Routenberg, P. N. Wyrembak, D. B. Turner-Evans, A. D. Hamilton, D. A. LaVan, T. M. Fahmy, and M. A. Reed. Label-free immunodetection with CMOS-compatible semiconducting nanowires. *Nature*, 445(7127):519–522, 2007.

[62] K. Shoorideh and C. O. Chui. On the origin of enhanced sensitivity in nanoscale FET-based biosensors. *PNAS*, 111(14):5111–5116, 2014.

[63] H. Ghosh, D. Kundu, and C. RoyChaudhuri. Design Issues for Performance Enhancement in Nano-structured Silicon Oxide Biosensors: Modeling the Frequency Response. *IEEE Trans. Electron Devices*, 63(8):3241–3248, 2016.

[64] E. Buitrago, M. F.-B. Badia, Y. M. Georgiev, R. Yu, O. Lotty, J. D. Holmes, A. M. Nightingale, H. M. Guerin, and A. M. Ionescu. Electrical characterization of high performance, liquid gated vertically stacked SiNW-based 3D FET biosensors. *Sens. Actuat. B-Chem.*, 199:291–300, 2014.

[65] Y. Cheng, K.-S. Chen, N. L. Meyer, J. Yuan, L. S. Hirst, P. B. Chase, and P. Xiong. Functionalized SnO2 nanobelt field-effect transistor sensors for label-free detection of cardiac troponin. *Biosens. Bioelectron.*, 26(11):4538–4544, 2011.

[66] S. Chen, L. Nyholm, N. Jokilaakso, A. E. Karlström, J. Linnros, U. Smith, and S.-L. Zhang. Current Instability for Silicon Nanowire Field-Effect Sensors Operating in Electrolyte with Platinum Gate Electrodes. *Electrochem. Solid-State Lett.*, 14(7):J34–J37, 2011.

[67] J. Janata. Historical review. Twenty years of ion-selective field-effect transistors. *The Analyst*, 119(11):2275, 1994.

[68] U. Guth, F. Gerlach, M. Decker, W. Oelßner, and W. Vonau. Solid-state reference electrodes for potentiometric sensors. *J. Solid State Electrochem.*, 13(1):27–39, 2009.

[69] T. Rim, K. Kim, N. Hong, W. Ko, C.-K. Baek, S. Jeon, M. J. Deen, M. Meyyappan, Y.-H. Jeong, and J.-S. Lee. Investigation of the electrical stability of Si-nanowire biologically sensitive field-effect transistors with embedded Ag/AgCl pseudo reference electrode. *RSC Adv.*, 3(21):7963–7969, 2013.

[70] X. Wen, S. Gupta, Y. Wang, T. R. N. Iii, S. C. Lee, and W. Lu. High sensitivity AlGaN/GaN field effect transistor protein sensors operated in the subthreshold regime by a control gate electrode. *Appl. Phys. Lett.*, 99(4):043701, 2011.

[71] X. Wen, M. L. Schuette, S. K. Gupta, T. R. Nicholson, S. C. Lee, and W. Lu. Improved Sensitivity of AlGaN/GaN Field Effect Transistor Biosensors by Optimized Surface Functionalization. *IEEE Sens. J.*, 11(8):1726–1735, 2011.

[72] X. Duan, Y. Li, N. K. Rajan, D. A. Routenberg, Y. Modis, and M. A. Reed. Quantification of the affinities and kinetics of protein interactions using silicon nanowire biosensors. *Nat. Nano.*, 7(6):401–407, 2012.

[73] N. K. Rajan. *Limit of Detection of Silicon BioFETs*. Ph.D. thesis, Yale University, 2013.

[74] C. Toumazou and P. Georgiou. Piet Bergveld - 40 years of ISFET technology: From neuronal sensing to DNA sequencing. *Electron. Lett.*, 47(26):S7–S12, 2011.

[75] E. D. Minot, A. M. Janssens, I. Heller, H. A. Heering, C. Dekker, and S. G. Lemay. Carbon nanotube biosensors: The critical role of the reference electrode. *Appl. Phys. Lett.*, 91(9):093507, 2007.

[76] M. Lambrechts and W. Sansen. Ion-Sensitive Field Effect Transistors. In *Biosensors: Microelectrochemical Devices*, page 69. CRC Press, 1992. ISBN 978-0-7503-0112-1.

[77] M. T. Martínez, Y.-C. Tseng, M. González, and J. Bokor. Streptavidin as CNTs and DNA Linker for the Specific Electronic and Optical Detection of DNA Hybridization. *J. Phys. Chem. C*, 116(42):22579–22586, 2012.

[78] Y. Cui, Q. Wei, H. Park, and C. M. Lieber. Nanowire Nanosensors for Highly Sensitive and Selective Detection of Biological and Chemical Species. *Science*, 293(5533):1289–1292, 2001.

[79] B. Ashcroft, B. Takulapalli, J. Yang, G. M. Laws, H. Q. Zhang, N. J. Tao, S. Lindsay, D. Gust, and T. J. Thornton. Calibration of a pH sensitive buried channel silicon-on-insulator MOSFET for sensor applications. *Phys. Status Solidi B*, 241(10):2291–2296, 2004.

[80] I. Moore, C. Millar, S. Roy, and A. Asenov. Brownian noise in FET based nano-pore sensing: A 3D simulation study. In *2010 14th International Workshop on Computational Electronics (IWCE)*, pages 1–4. 2010.

[81] I. Moore, C. Millar, S. Roy, and A. Asenov. FET based nano-pore sensing: A 3D simulation study. *J. Comput. Electron.*, 11(3):266–271, 2012.

[82] M. Z. Bazant, K. Thornton, and A. Ajdari. Diffuse-charge dynamics in electrochemical systems. *Phys. Rev. E*, 70(2):021506, 2004.

[83] T. M. Squires, R. J. Messinger, and S. R. Manalis. Making it stick: Convection, reaction and diffusion in surface-based biosensors. *Nat. Biotech.*, 26(4):417–426, 2008.

[84] L. De Vico, M. H. Sørensen, L. Iversen, D. M. Rogers, B. S. Sørensen, M. Brandbyge, J. Nygård, K. L. Martinez, and J. H. Jensen. Quantifying signal changes in nano-wire based biosensors. *Nanoscale*, 3(2):706, 2011.

[85] H. Li, A. D. Robertson, and J. H. Jensen. Very fast empirical prediction and rationalization of protein pKa values. *Proteins*, 61(4):704–721, 2005.

[86] D. C. Bas, D. M. Rogers, and J. H. Jensen. Very fast prediction and rationalization of pKa values for protein–ligand complexes. *Proteins*, 73(3):765–783, 2008.

[87] N. Lloret, R. S. Frederiksen, T. C. Møller, N. I. Rieben, S. Upadhyay, L. De Vico, J. H. Jensen, J. Nygård, and K. L. Martinez. Effects of buffer composition and dilution on nanowire field-effect biosensors. *Nanotechnology*, 24(3):035501, 2013.

[88] D. Nozaki, J. Kunstmann, F. Zörgiebel, W. M. Weber, T. Mikolajick, and G. Cuniberti. Multiscale modeling of nanowire-based Schottky-barrier field-effect transistors for sensor applications. *Nanotechnology*, 22(32):325703, 2011.

[89] A. Matsumoto, H. Matsumoto, Y. Maeda, and Y. Miyahara. Simple and robust strategy for potentiometric detection of glucose using fluorinated phenylboronic acid self-assembled monolayer. *Biochim. Biophys. Acta BBA - Gen. Subj.*, 1830(9):4359–4364, 2013.

[90] A. Matsumoto, N. Sato, T. Sakata, K. Kataoka, and Y. Miyahara. Glucose-sensitive field effect transistor using totally synthetic compounds. *J. Solid State Electrochem.*, 13(1):165–170, 2009.

[91] C. S. Ah, C. W. Park, J.-H. Yang, J. S. Lee, W.-J. Kim, K. H. Chung, Y. H. Choi, I. B. Baek, J. Kim, and G. Y. Sung. Detection of uncharged or feebly charged small molecules by field-effect transistor biosensors. *Biosens. Bioelectron.*, 33(1):233–240, 2012.

[92] K. Gartsman, D. Cahen, A. Kadyshevitch, J. Libman, T. Moav, R. Naaman, A. Shanzer, V. Umansky, and A. Vilan. Molecular control of a GaAs transistor. *Chem. Phys. Lett.*, 283(5–6):301–306, 1998.

[93] A. Tarasov, M. Wipf, K. Bedner, J. Kurz, W. Fu, V. A. Guzenko, O. Knopfmacher, R. L. Stoop, M. Calame, and C. Schönenberger. True Reference Nanosensor Realized with Silicon Nanowires. *Langmuir*, 28(25):9899–9905, 2012.

[94] G. S. Kulkarni, W. Zang, and Z. Zhong. Nanoelectronic Heterodyne Sensor: A New Electronic Sensing Paradigm. *Acc. Chem. Res.*, 49(11):2578–2586, 2016.

[95] K. Bradley, M. Briman, A. Star, and G. Grüner. Charge Transfer from Adsorbed Proteins. *Nano Lett.*, 4(2):253–256, 2004.

[96] A. Star, J.-C. P. Gabriel, K. Bradley, and G. Grüner. Electronic Detection of Specific Protein Binding Using Nanotube FET Devices. *Nano Lett.*, 3(4):459–463, 2003.

[97] F. N. Ishikawa, M. Curreli, H.-K. Chang, P.-C. Chen, R. Zhang, R. J. Cote, M. E. Thompson, and C. Zhou. A Calibration Method for Nanowire Biosensors to Suppress Device-to-Device Variation. *ACS Nano*, 3(12):3969–3976, 2009.

[98] P. C. Weber, D. H. Ohlendorf, J. J. Wendoloski, and F. R. Salemme. Structural origins of high-affinity biotin binding to streptavidin. *Science*, 243(4887):85–88, 1989.

[99] S. Upadhyay, R. Frederiksen, N. Lloret, L. De Vico, P. Krogstrup, J. H. Jensen, K. L. Martinez, and J. Nygård. Indium arsenide nanowire field-effect transistors for pH and biological sensing. *Appl. Phys. Lett.*, 104(20):203504, 2014.

[100] W. J. Duffin. *Electricity and Magnetism*. McGraw Hill Book Co., London; New York, 3rd edition, 1980. ISBN 0-07-084111-X 978-0-07-084111-6.

[101] P. Politzer and D. G. Truhlar. Introduction: The Role of the Electrostatic Potential in Chemistry. In P. Politzer and D. G. Truhlar, editors, *Chemical Applications of Atomic and Molecular Electrostatic Potentials*, pages 1–6. Springer US, 1981. ISBN 978-1-4757-9636-0 978-1-4757-9634-6.

[102] J. O. Bockris, A. K. Reddy, and M. E. Gamboa-Aldeco. *Modern Electrochemistry 2A*, volume 2A. Kluwer Academic Publishers, Boston, 2002. ISBN 0-306-46166-8.

[103] R. R. Pethig and S. Smith. *Introductory Bioelectronics: For Engineers and Physical Scientists*. John Wiley & Sons, 2012. ISBN 978-1-118-44328-6.

[104] R. J. Hunter. *Foundations of Colloid Science*. Oxford University Press, 2001. ISBN 978-0-19-850502-0.

[105] J. Lyklema. *Fundamentals of Interface and Colloid Science: Solid-Liquid Interfaces*. Academic Press, 1995. ISBN 978-0-08-050712-5.

[106] D. Grahame. The Electrical Double Layer and the Theory of Electrocapillarity. *Chem. Rev.*, 41(3):441–501, 1947.

[107] J. O. Bockris and A. K. Reddy. *Modern Electrochemistry 1*, volume 1. Kluwer Academic Publishers, Boston, 1998. ISBN 978-0-306-45554-4.

[108] Q. Zheng and G.-W. Wei. Poisson–Boltzmann–Nernst–Planck model. *J. Chem. Phys.*, 134(19):194101, 2011.

[109] S. A. Ghasemi, A. Neelov, and S. Goedecker. A particle-particle, particle-density algorithm for the calculation of electrostatic interactions of particles with slablike geometry. *J. Chem. Phys.*, 127(22):224102, 2007.

[110] J. M. Ziman. *Principles of the Theory of Solids*. Cambridge University Press, 1972. ISBN 978-0-521-29733-2.

[111] D. Frenkel and B. Smit. Chapter 6 - Molecular Dynamics in Various Ensembles. In *Understanding Molecular Simulation*, pages 139–163. Academic Press, San Diego, second edition, 2002. ISBN 978-0-12-267351-1.

[112] J. P. Hansen. Molecular-dynamics simulations of Coulomb systems in two and three dimensions. In *Molecular Dynamics Simulation of Statistical-Mechanical Systems*, Proceedings of the 97th Int. "Enrico Fermi" School of Physics, pages 89–129. Elsevier Science, North Holland, Amsterdam, 1986.

[113] N. D. M. Hine, J. Dziedzic, P. D. Haynes, and C.-K. Skylaris. Electrostatic interactions in finite systems treated with periodic boundary conditions: Application to linear-scaling density functional theory. *J. Chem. Phys.*, 135(20):204103, 2011.

[114] H. Sun. COMPASS: An ab Initio Force-Field Optimized for Condensed-Phase ApplicationsOverview with Details on Alkane and Benzene Compounds. *J. Phys. Chem. B*, 102(38):7338–7364, 1998.

[115] C. Barbé, J. Bartlett, L. Kong, K. Finnie, H. Q. Lin, M. Larkin, S. Calleja, A. Bush, and G. Calleja. Silica Particles: A Novel Drug-Delivery System. *Adv. Mater.*, 16(21):1959–1966, 2004.

[116] J. V. Smith. Biochemical evolution. I. Polymerization on internal, organophilic silica surfaces of dealuminated zeolites and feldspars. *PNAS*, 95(7):3370–3375, 1998.

[117] J. D. Kubicki, J. O. Sofo, A. A. Skelton, and A. V. Bandura. A New Hypothesis for the Dissolution Mechanism of Silicates. *J. Phys. Chem. C*, 116(33):17479–17491, 2012.

[118] T. Metke, A. S. Westover, R. Carter, L. Oakes, A. Douglas, and C. L. Pint. Particulate-free porous silicon networks for efficient capacitive deionization water desalination. *Sci. Rep.*, 6:24680, 2016.

[119] E. R. Cruz-Chu, A. Aksimentiev, and K. Schulten. Water-Silica Force Field for Simulating Nanodevices. *J. Phys. Chem. B*, 110(43):21497–21508, 2006.

[120] F. A. Ahmed, A. K. Elraies, A. A. Mohammed, and R. G. Gaafar. An Investigation Study on the Effect of Brine Composition on Silica Dissolution. In *Advances in Environmental and Geological Science and Engineering*, pages 188–192. 2015. ISBN 978-1-61804-314-6.

[121] L. Zhuravlev. The surface chemistry of amorphous silica. Zhuravlev model. *Colloids Surf. A Physicochem. Eng. Asp.*, 173(1-3):1–38, 2000.

[122] E. F. Vansant, P. V. D. Voort, and K. C. Vrancken. *Characterization and Chemical Modification of the Silica Surface*. Elsevier, 1995. ISBN 978-0-08-052895-3.

[123] F. Li and A. Nathan. Silicon Dioxide. In *CCD Image Sensors in Deep-Ultraviolet: Degradation Behavior and Damage Mechanisms*, page 61. Springer Science & Business Media, 2006. ISBN 978-3-540-27412-4.

[124] S. H. Behrens and D. G. Grier. The charge of glass and silica surfaces. *J. Chem. Phys.*, 115(14):6716–6721, 2001.

[125] R. K. Iller. *The Chemistry of Silica*. Wiley-Interscience, New York, 1979.

[126] P. Zarzycki, K. M. Rosso, S. Chatman, T. Preočanin, N. Kallay, and W. Piasecki. Theory, experiment and computer simulation of the electrostatic potential at crystal/electrolyte interfaces. *Croat. Chem. Acta*, 83(4):457–474, 2010.

[127] E. Tombácz. pH-dependent surface charging of metal oxides. *Chem. Eng.*, 53(2):77–86, 2007.

[128] C. J. Brinker and G. W. Scherer. *Sol-Gel Science: The Physics and Chemistry of Sol-Gel Processing*. Gulf Professional Publishing, 1990. ISBN 978-0-12-134970-7.

[129] P. Somasundaran. *Encyclopedia of Surface and Colloid Science*. CRC Press, 2006. ISBN 978-0-8493-9608-3.

[130] M. H. Kurbatov, G. B. Wood, and J. D. Kurbatov. Isothermal Adsorption of Cobalt from Dilute Solutions. *J. Phys. Chem.*, 55(7):1170–1182, 1951.

[131] M. Borkovec. Origin of 1-pK and 2-pK Models for Ionizable Water-Solid Interfaces. *Langmuir*, 13(10):2608–2613, 1997.

[132] W. Piasecki, W. Rudziński, and R. Charmas. 1-pK and 2-pK Protonation Models in the Theoretical Description of Simple Ion Adsorption at the Oxide/Electrolyte Interface: A Comparative Study of the Behavior of the Surface Charge, the Individual Isotherms of Ions, and the Accompanying Electrokinetic Effects. *J. Phys. Chem. B*, 105(40):9755–9771, 2001.

[133] S. Goldberg. Surface Complexation Modeling. In *Reference Module in Earth Systems and Environmental Sciences*. Elsevier, 2013. ISBN 978-0-12-409548-9.

[134] J. Lutzenkirchen. *Surface Complexation Modelling*. Academic Press, 2006. ISBN 978-0-08-046778-8.

[135] P. W. Schindler and H. Gamsjäger. Acid-base reactions of the TiO2 (Anatase)-water interface and the point of zero charge of TiO2 suspensions. *Kolloid Z. Z. Polym.*, 250(7):759–763, 1972.

[136] W. Stumm, C. P. Huang, and S. R. Jenkins. Specific chemical interaction affecting the stability of dispersed systems. *Croat. Chem. Acta*, (42):233, 1970.

[137] K. F. Hayes and J. O. Leckie. Modeling ionic strength effects on cation adsorption at hydrous oxide/solution interfaces. *J. Colloid Interf. Sci.*, 115(2):564–572, 1987.

[138] T. Hiemstra, W. H. Van Riemsdijk, and G. H. Bolt. Multisite proton adsorption modeling at the solid/solution interface of (hydr)oxides: A new approach: I. Model description and evaluation of intrinsic reaction constants. *J. Colloid Interf. Sci.*, 133(1):91–104, 1989.

[139] T. Hiemstra and W. H. Van Riemsdijk. A Surface Structural Approach to Ion Adsorption: The Charge Distribution (CD) Model. *J. Colloid Interf. Sci.*, 179(2):488–508, 1996.

[140] M. Kosmulski. *Surface Charging and Points of Zero Charge*. CRC Press, 2009. ISBN 978-1-4200-5189-6.

[141] K. F. Hayes, G. Redden, W. Ela, and J. O. Leckie. Surface complexation models: An evaluation of model parameter estimation using FITEQL and oxide mineral titration data. *J. Colloid Interf. Sci.*, 142(2):448–469, 1991.

[142] G. H. Bolt. Determination of the Charge Density of Silica Sols. *J. Phys. Chem.*, 61(9):1166–1169, 1957.

[143] B. R. Bickmore, C. J. Tadanier, K. M. Rosso, W. D. Monn, and D. L. Eggett. Bond-valence methods for pKa prediction: Critical reanalysis and a new approach. *Geochim. Cosmochim. Ac.*, 68(9):2025–2042, 2004.

[144] K. Leung, I. M. B. Nielsen, and L. J. Criscenti. Elucidating the Bimodal Acid-Base Behavior of the Water-Silica Interface from First Principles. *J. Am. Chem. Soc.*, 131(51):18358–18365, 2009.

[145] S. Ong, X. Zhao, and K. B. Eisenthal. Polarization of water molecules at a charged interface: Second harmonic studies of the silica/water interface. *Chem. Phys. Lett.*, 191(3–4):327–335, 1992.

[146] M. S. Azam, C. N. Weeraman, and J. M. Gibbs-Davis. Specific Cation Effects on the Bimodal Acid–Base Behavior of the Silica/Water Interface. *J. Phys. Chem. Lett.*, 3(10):1269–1274, 2012.

[147] N. Sahai and D. A. Sverjensky. Evaluation of internally consistent parameters for the triple-layer model by the systematic analysis of oxide surface titration data. *Geochim. Cosmochim. Ac.*, 61(14):2801–2826, 1997.

[148] Encyclopedia of nuclear magnetic resonance. In *Encyclopedia of Nuclear Magnetic Resonance*, page 4370. Wiley, Chichester, UK, 1996.

[149] M. J. Wirth, M. D. Ludes, and D. J. Swinton. Spectroscopic Observation of Adsorption to Active Silanols. *Anal. Chem.*, 71(18):3911–3917, 1999.

[150] H.-F. Fan, F. Li, R. N. Zare, and K.-C. Lin. Characterization of Two Types of Silanol Groups on Fused-Silica Surfaces Using Evanescent-Wave Cavity Ring-Down Spectroscopy. *Anal. Chem.*, 79(10):3654–3661, 2007.

[151] J. P. O'Reilly, C. P. Butts, I. A. I'Anso, and A. M. Shaw. Interfacial pH at an Isolated Silica-Water Surface. *J. Am. Chem. Soc.*, 127(6):1632–1633, 2005.

[152] J. D. Fisk, R. Batten, G. Jones, J. P. O'Reill, and A. M. Shaw. pH Dependence of the Crystal Violet Adsorption Isotherm at the Silica-Water Interface. *J. Phys. Chem. B*, 109(30):14475–14480, 2005.

[153] P. Schindler and H. R. Kamber. Die Acidität von Silanolgruppen. Vorläufige Mitteillung. *Helv. Chim. Acta*, 51(7):1781–1786, 1968.

[154] Y. Duval, J. A. Mielczarski, O. S. Pokrovsky, E. Mielczarski, and J. J. Ehrhardt. Evidence of the Existence of Three Types of Species at the Quartz-Aqueous Solution Interface at pH 0-10: XPS Surface Group Quantification and Surface Complexation Modeling. *J. Phys. Chem. B*, 106(11):2937–2945, 2002.

[155] J. R. Rustad, E. Wasserman, A. R. Felmy, and C. Wilke. Molecular Dynamics Study of Proton Binding to Silica Surfaces. *J. Colloid Interf. Sci.*, 198(1):119–129, 1998.

[156] Y. Dong, S. V. Pappu, and Z. Xu. Detection of Local Density Distribution of Isolated Silanol Groups on Planar Silica Surfaces Using Nonlinear Optical Molecular Probes. *Anal. Chem.*, 70(22):4730–4735, 1998.

[157] V. Ostroverkhov, G. A. Waychunas, and Y. R. Shen. New Information on Water Interfacial Structure Revealed by Phase-Sensitive Surface Spectroscopy. *Phys. Rev. Lett.*, 94(4):046102, 2005.

[158] B. M. Lowe, C.-K. Skylaris, and N. G. Green. Acid-base dissociation mechanisms and energetics at the silica-water interface: An activationless process. *J. Colloid Interf. Sci.*, 451:231–244, 2015.

[159] Y. Xiao and A. C. Lasaga. Ab initio quantum mechanical studies of the kinetics and mechanisms of silicate dissolution: H+(H3O+) catalysis. *Geochim. Cosmochim. Ac.*, 58(24):5379–5400, 1994.

[160] Y. Xiao and A. C. Lasaga. Ab initio quantum mechanical studies of the kinetics and mechanisms of quartz dissolution: OH- catalysis. *Geochim. Cosmochim. Ac.*, 60(13):2283–2295, 1996.

[161] A. A. Hassanali, H. Zhang, C. Knight, Y. K. Shin, and S. J. Singer. The Dissociated Amorphous Silica Surface: Model Development and Evaluation. *J. Chem. Theory Comput.*, 6(11):3456–3471, 2010.

[162] X. Liu, X. Lu, E. J. Meijer, R. Wang, and H. Zhou. Acid dissociation mechanisms of Si(OH)4 and Al(H2O)63+ in aqueous solution. *Geochim. Cosmochim. Ac.*, 74(2):510–516, 2010.

[163] D. Riccardi, P. König, X. Prat-Resina, H. Yu, M. Elstner, T. Frauenheim, and Q. Cui. "Proton Holes" in Long-Range Proton Transfer Reactions in Solution and Enzymes: A Theoretical Analysis. *J. Am. Chem. Soc.*, 128(50):16302–16311, 2006.

[164] D. R. Kinney, I. S. Chuang, and G. E. Maciel. Water and the silica surface as studied by variable-temperature high-resolution proton NMR. *J. Am. Chem. Soc.*, 115(15):6786–6794, 1993.

[165] Q. Du, E. Freysz, and Y. R. Shen. Vibrational spectra of water molecules at quartz/water interfaces. *Phys. Rev. Lett.*, 72(2):238–241, 1994.

[166] V. Ostroverkhov, G. A. Waychunas, and Y. R. Shen. Vibrational spectra of water at water/α-quartz (0 0 0 1) interface. *Chem. Phys. Lett.*, 386(1–3):144–148, 2004.

[167] M.-P. Gaigeot, M. Sprik, and M. Sulpizi. Oxide/water interfaces: How the surface chemistry modifies interfacial water properties. *J. Phys.: Condens. Matter*, 24(12):124106, 2012.

[168] L. T. Zhuravlev. Concentration of hydroxyl groups on the surface of amorphous silicas. *Langmuir*, 3(3):316–318, 1987.

[169] S. Iarlori, D. Ceresoli, M. Bernasconi, D. Donadio, and M. Parrinello. Dehydroxylation and Silanization of the Surfaces of β-Cristobalite Silica: An ab Initio Simulation. *J. Phys. Chem. B*, 105(33):8007–8013, 2001.

[170] D. Ceresoli, M. Bernasconi, S. Iarlori, M. Parrinello, and E. Tosatti. Two-Membered Silicon Rings on the Dehydroxylated Surface of Silica. *Phys. Rev. Lett.*, 84(17):3887–3890, 2000.

[171] T. S. Mahadevan and S. H. Garofalini. Dissociative Chemisorption of Water onto Silica Surfaces and Formation of Hydronium Ions. *J. Phys. Chem. C*, 112(5):1507–1515, 2008.

[172] C. J. T. de Grotthuss. Sur la décomposition de l'eau et des corps qu'elle tient en dissolution à l'aide de l'électricité galvanique. *Ann. Chim.*, 58:54–73, 1806.

[173] M. Eigen and L. de Maeyer. Self-Dissociation and Protonic Charge Transport in Water and Ice. *Proc. R. Soc. Lond. A*, 247(1251):505–533, 1958.

[174] M. Nogami and Y. Abe. Evidence of water-cooperative proton conduction in silica glasses. *Phys. Rev. B*, 55(18):12108, 1997.

[175] Y. Daiko, T. Kasuga, and M. Nogami. Pore size effect on proton transfer in sol-gel porous silica glasses. *Micropor. Mesopor. Mat.*, 69(3):149–155, 2004.

[176] M. Nogami, Y. Tarutani, Y. Daiko, S. Izuhara, T. Nakao, and T. Kasuga. Preparation of P2O5 SiO2 Glasses with Proton Conductivity of ~100 mS/cm at Room Temperature. *J. Electrochem. Soc.*, 151(12):A2095–A2099, 2004.

[177] F. Tielens, C. Gervais, J. F. Lambert, F. Mauri, and D. Costa. Ab Initio Study of the Hydroxylated Surface of Amorphous Silica: A Representative Model. *Chem. Mater.*, 20(10):3336–3344, 2008.

[178] M. C. Gurau, G. Kim, S.-M. Lim, F. Albertorio, H. C. Fleisher, and P. S. Cremer. Organization of Water Layers at Hydrophilic Interfaces. *ChemPhysChem*, 4(11):1231–1233, 2003.

[179] P. M. Dove and S. F. Elston. Dissolution kinetics of quartz in sodium chloride solutions: Analysis of existing data and a rate model for 25°C. *Geochim. Cosmochim. Ac.*, 56(12):4147–4156, 1992.

[180] P. M. Dove and C. J. Nix. The influence of the alkaline earth cations, magnesium, calcium, and barium on the dissolution kinetics of quartz. *Geochim. Cosmochim. Ac.*, 61(16):3329–3340, 1997.

[181] I. Li, J. Bandara, and M. J. Shultz. Time Evolution Studies of the H2O/Quartz Interface Using Sum Frequency Generation, Atomic Force Microscopy, and Molecular Dynamics. *Langmuir*, 20(24):10474–10480, 2004.

[182] S.-W. Hwang, G. Park, H. Cheng, J.-K. Song, S.-K. Kang, L. Yin, J.-H. Kim, F. G. Omenetto, Y. Huang, K.-M. Lee, and J. A. Rogers. 25th Anniversary Article: Materials for High-Performance Biodegradable Semiconductor Devices. *Adv. Mater.*, 26(13):1992–2000, 2014.

[183] K. G. Knauss and T. J. Wolery. The dissolution kinetics of quartz as a function of pH and time at 70°C. *Geochim. Cosmochim. Ac.*, 52(1):43–53, 1988.

[184] H. Strandh, L. G. M. Pettersson, L. Sjöberg, and U. Wahlgren. Quantum chemical studies of the effects on silicate mineral dissolution rates by adsorption of alkali metals. *Geochim. Cosmochim. Ac.*, 61(13):2577–2587, 1997.

[185] L. J. Criscenti, J. D. Kubicki, and S. L. Brantley. Silicate Glass and Mineral Dissolution: Calculated Reaction Paths and Activation Energies for Hydrolysis of a Q3 Si by H3O+ Using Ab Initio Methods. *J. Phys. Chem. A*, 110(1):198–206, 2006.

[186] A. Tilocca and A. N. Cormack. Exploring the Surface of Bioactive Glasses: Water Adsorption and Reactivity. *J. Phys. Chem. C*, 112(31):11936–11945, 2008.

[187] A. Tilocca and A. N. Cormack. Modeling the Water-Bioglass Interface by Ab Initio Molecular Dynamics Simulations. *ACS Appl. Mater. Interfaces*, 1(6):1324–1333, 2009.

[188] S. Nangia and B. J. Garrison. Reaction Rates and Dissolution Mechanisms of Quartz as a Function of pH. *J. Phys. Chem. A*, 112(10):2027–2033, 2008.

[189] R. D. Levine. *Molecular Reaction Dynamics*. Cambridge University Press, Cambridge, reprint edition edition, 2009. ISBN 978-0-521-14071-3.

[190] P. L. Geissler, T. Van Voorhis, and C. Dellago. Potential energy landscape for proton transfer in (H2O)3H+: Comparison of density functional theory and wavefunction-based methods. *Chem. Phys. Lett.*, 324(1-3):149–155, 2000.

[191] W. C. Natzle and C. B. Moore. Recombination of hydrogen ion (H+) and hydroxide in pure liquid water. *J. Phys. Chem.*, 89(12):2605–2612, 1985.

[192] P. L. Geissler, C. Dellago, D. Chandler, J. Hutter, and M. Parrinello. Autoionization in Liquid Water. *Science*, 291(5511):2121–2124, 2001.

[193] D. Rapaport. Hydrogen bonds in water. *Mol. Phys.*, 50(5):1151–1162, 1983.

[194] G. K. Lockwood and S. H. Garofalini. Lifetimes of Excess Protons in Water Using a Dissociative Water Potential. *J. Phys. Chem. B*, 117(15):4089–4097, 2013.

[195] S. H. Lee and J. C. Rasaiah. Proton transfer and the mobilities of the H+ and OH- ions from studies of a dissociating model for water. *J. Chem. Phys.*, 135(12):124505, 2011.

[196] M. L. Soudijn. *Proton Transport in Aqueous Ionic Solutions*. Ph.D. thesis, University of Amsterdam, 2012.

[197] O. F. Mohammed, D. Pines, J. Dreyer, E. Pines, and E. T. J. Nibbering. Sequential Proton Transfer Through Water Bridges in Acid-Base Reactions. *Science*, 310(5745):83–86, 2005.

[198] U. W. Schmitt and G. A. Voth. The computer simulation of proton transport in water. *J. Chem. Phys.*, 111(20):9361, 1999.

[199] D. Marx, M. E. Tuckerman, J. Hutter, and M. Parrinello. The nature of the hydrated excess proton in water. *Nature*, 397(6720):601–604, 1999.

[200] M. E. Tuckerman, D. Marx, and M. Parrinello. The nature and transport mechanism of hydrated hydroxide ions in aqueous solution. *Nature*, 417(6892):925–929, 2002.

[201] M. E. Tuckerman, A. Chandra, and D. Marx. Structure and dynamics of OH-(aq). *Acc. Chem. Res.*, 39(2):151–158, 2006.

[202] A. Botti, F. Bruni, S. Imberti, M. A. Ricci, and A. K. Soper. Solvation shell of OH- ions in water. *J. Mol. Liq.*, 117(1–3):81–84, 2005.

[203] P. J. Scales, F. Grieser, T. W. Healy, L. R. White, and D. Y. C. Chan. Electrokinetics of the silica-solution interface: A flat plate streaming potential study. *Langmuir*, 8(3):965–974, 1992.

[204] S. Dixit and P. Van Cappellen. Surface chemistry and reactivity of biogenic silica. *Geochim. Cosmochim. Ac.*, 66(14):2559–2568, 2002.

[205] S. Jamasb, S. Collins, and R. L. Smith. A physical model for drift in pH ISFETs. *Sens. Actuat. B-Chem.*, 49(1–2):146–155, 1998.

[206] P. L. F. Hemment and S. Cristoloveanu. *Silicon-on-Insulator Technology and Devices: Proceedings of the Ninth International Symposium on Silicon-on-Insulator Technology and Devices*. The Electrochemical Society, 1999. ISBN 978-1-56677-225-9.

[207] A.A. Agzamkhodzhaev, L. Zhuravlev, A. Kiselev, and K. Shengeliya. Rehydroxylation of surface of amorphous silicas. *Colloid J. USSR+*, 36:1145, 1974.

[208] H. Heinz. Computational screening of biomolecular adsorption and self-assembly on nanoscale surfaces. *J. Comput. Chem.*, 31(7):1564–1568, 2010.

[209] H. Heinz, T.-J. Lin, R. Kishore Mishra, and F. S. Emami. Thermodynamically Consistent Force Fields for the Assembly of Inorganic, Organic, and Biological Nanostructures: The INTERFACE Force Field. *Langmuir*, 29(6):1754–1765, 2013.

[210] S. V. Patwardhan, F. S. Emami, R. J. Berry, S. E. Jones, R. R. Naik, O. Deschaume, H. Heinz, and C. C. Perry. Chemistry of aqueous silica nanoparticle surfaces and the mechanism of selective peptide adsorption. *J. Am. Chem. Soc.*, 134(14):6244–6256, 2012.

[211] H.-P. Cheng, L.-L. Wang, M.-H. Du, C. Cao, Y.-X. Wan, Y. He, K. Muralidharan, G. Greenlee, and A. Kolchin. Quantum, classical, and multi-scale simulation of silica-water interaction: Molecules, clusters, and extended systems. *J. Comput-aided Mater. Des.*, 13(1-3):161–183, 2006.

[212] S. B. Trickey, S. Yip, H.-p. Cheng, K. Runge, and P. A. Deymier. A Perspective on Multi-scale Simulation: Toward Understanding Water-silica. *J. Comput-aided Mater. Des.*, 13(1-3):1–12, 2006.

[213] C. Lomenech, G. Bery, D. Costa, L. Stievano, and J. F. Lambert. Theoretical and Experimental Study of the Adsorption of Neutral Glycine on Silica from the Gas Phase. *ChemPhysChem*, 6(6):1061–1070, 2005.

[214] P. Ugliengo, V. Saunders, and E. Garrone. Silanol as a model for the free hydroxyl of amorphous silica: Ab-initio calculations of the interaction with water. *J. Phys. Chem.*, 94(6):2260–2267, 1990.

[215] B. M. Lowe. MSc Module: Independent Research Project. 'First principles simulation of glycine absorbtion to silica'. Technical report, University of Southamapton, 2013.

[216] P. Ugliengo, M. Sodupe, F. Musso, I. J. Bush, R. Orlando, and R. Dovesi. Realistic Models of Hydroxylated Amorphous Silica Surfaces and MCM-41 Mesoporous Material Simulated by Large-scale Periodic B3LYP Calculations. *Adv. Mat.*, 20(23):4579–4583, 2008.

[217] C. Mischler, W. Kob, and K. Binder. Classical and ab-initio molecular dynamic simulation of an amorphous silica surface. *Comput. Phys. Commun.*, 147(1–2):222–225, 2002.

[218] M. Dračínský, L. Benda, and P. Bouř. Ab initio modeling of fused silica, crystal quartz, and water Raman spectra. *Chem Phys Lett*, 512(1-3):54–59, 2011.

[219] D. E. Taylor, K. Runge, M. G. Cory, D. S. Burns, J. L. Vasey, J. D. Hearn, and M. V. Henley. Binding of Small Molecules to a Silica Surface: Comparing Experimental and Theoretical Results. *J. Phys. Chem. C*, 115(50):24734–24742, 2011.

[220] F. Vigné-Maeder and P. Sautet. Theoretical Study of Hydroxylated and Dehydroxylated Surfaces of a Cristobalite Model of Silica. *J. Phys. Chem. B*, 101(41):8197–8203, 1997.

[221] F. Musso, P. Ugliengo, X. Solans-Monfort, and M. Sodupe. Periodic DFT Study of Radical Species on Crystalline Silica Surfaces. *J. Phys. Chem. C*, 114(39):16430–16438, 2010.

[222] F. Musso, M. Sodupe, M. Corno, and P. Ugliengo. H-Bond Features of Fully Hydroxylated Surfaces of Crystalline Silica Polymorphs: A Periodic B3LYP Study. *J. Phys. Chem. C*, 113(41):17876–17884, 2009.

[223] P. Ugliengo, B. Civalleri, R. Dovesi, and C. M. Zicovich-Wilson. Periodic B3-LYP calculations on H-Edingtonites, both alone and interacting with acetylene. *Phys. Chem. Chem. Phys.*, 1(4):545–553, 1999.

[224] A. Rimola and P. Ugliengo. The role of defective silica surfaces in exogenous delivery of prebiotic compounds: Clues from first principles calculations. *Phys. Chem. Chem. Phys.*, 11(14):2497–2506, 2009.

[225] G. Ferandez-Cata, A. Peerez-Gramatges, L. J. Alvarez, H. Comas-Rojas, and C. M. Zicovich-Wilson. On the Interaction between Silica Surfaces and Surfactants. A 2D Periodic B3LYP Investigation. *J. Phys. Chem. C*, 113(30):13309–13316, 2009.

[226] B. Civalleri, E. Garrone, and P. Ugliengo. Cage-like clusters as models for the hydroxyls of silica: Ab initio calculation of 1H and 29Si NMR chemical shifts. *Chem. Phys. Lett.*, 299(5):443–450, 1999.

[227] T. P. M. Goumans, A. Wander, W. A. Brown, and C. R. A. Catlow. Structure and stability of the (001) alpha-quartz surface. *Phys. Chem. Chem. Phys.*, 9(17):2146, 2007.

[228] S. Tosoni, B. Civalleri, and P. Ugliengo. Hydrophobic Behavior of Dehydroxylated Silica Surfaces: A B3LYP Periodic Study. *J. Phys. Chem. C*, 114(47):19984–19992, 2010.

[229] A. Rimola, B. Civalleri, and P. Ugliengo. Physisorption of aromatic organic contaminants at the surface of hydrophobic/hydrophilic silica geosorbents: A B3LYP-D modeling study. *Phys. Chem. Chem. Phys.*, 12(24):6357–6366, 2010.

[230] P. M. Dove. The dissolution kinetics of quartz in sodium chloride solutions at 25 degrees to 300 degrees C. *Am J Sci*, 294(6):665–712, 1994.

[231] T. P. Goloub, L. K. Koopal, B. H. Bijsterbosch, and M. P. Sidorova. Adsorption of Cationic Surfactants on Silica. Surface Charge Effects. *Langmuir*, 12(13):3188–3194, 1996.

[232] K. Sun, I. Zeimpekis, C. Hu, N. M. J. Ditshego, O. Thomas, M. R. R. de Planque, H. M. H. Chong, H. Morgan, and P. Ashburn. Effect of subthreshold slope on the sensitivity of nanoribbon sensors. *Nanotechnology*, 27(28):285501, 2016.

[233] N. Clément, K. Nishiguchi, J. F. Dufreche, D. Guerin, A. Fujiwara, and D. Vuillaume. A silicon nanowire ion-sensitive field-effect transistor with elementary charge sensitivity. *Appl. Phys. Lett.*, 98(1):014104, 2011.

[234] S. Jamasb. An analytical technique for counteracting drift in ion-selective field effect transistors (ISFETs). *IEEE Sens. J.*, 4(6):795–801, 2004.

[235] Pennsylvania State University. Mineral Industries Extension Services, E. P. McNamara, and I. Dulberg. Fundamentals of Ceramics. In *Fundamentals of Ceramics*, page 91. Pennsylvania State University, University Park, 2 edition, 1958.

[236] J. M. Stallons and E. Iglesia. Simulations of the structure and properties of amorphous silica surfaces. *Chem. Eng. Sci.*, 56(14):4205–4216, 2001.

[237] F. Musso, P. Mignon, P. Ugliengo, and M. Sodupe. Cooperative effects at water-crystalline silica interfaces strengthen surface silanol hydrogen bonding. An ab initio molecular dynamics study. *Phys. Chem. Chem. Phys.*, 14(30):10507, 2012.

[238] C. J. Cramer. *Essentials of Computational Chemistry: Theories and Models*. John Wiley & Sons, 2013. ISBN 978-1-118-71227-6.

[239] P. W. Atkins and R. S. Friedman. *Molecular Quantum Mechanics*. OUP Oxford, 2011. ISBN 978-0-19-954142-3.

[240] J. L. Atwood and J. W. Steed. Molecular Modeling and Related Computational Techniques. In *Encyclopedia of Supramolecular Chemistry*, page 902. CRC Press, 2004. ISBN 978-0-8247-4724-4.

[241] S. J. Clark, M. Segall, C. J. Pickard, P. J. Hasnip, M. J. Probert, K. Refson, and M. Payne. First principles methods using CASTEP. *Z. Kristallogr.*, 220(5-6):567–570, 2005.

[242] C. K. Skylaris, P. D. Haynes, A. A. Mostofi, and M. C. Payne. Introducing ONETEP: Linear-scaling density functional simulations on parallel computers. *J. Chem. Phys.*, 122:084119, 2005.

[243] C.-K. Skylaris, A. A. Mostofi, P. D. Haynes, O. Diéguez, and M. C. Payne. Nonorthogonal generalized Wannier function pseudopotential plane-wave method. *Phys. Rev. B*, 66(3):035119, 2002.

[244] A. J. Cohen, P. Mori-Sánchez, and W. Yang. Insights into Current Limitations of Density Functional Theory. *Science*, 321(5890):792–794, 2008.

[245] J. P. Perdew, K. Burke, and M. Ernzerhof. Generalized Gradient Approximation Made Simple. *Phys. Rev. Lett.*, 77(18):3865–3868, 1996.

[246] B. M. Lowe. OnetepConv - A free, open-source utility for performing convergence testing with the ONETEP software. doi: 10.6084/m9.figshare.4001049.v1. *Available Online*, 2016.

[247] M. Valiev, E. Bylaska, N. Govind, K. Kowalski, T. Straatsma, H. Van Dam, D. Wang, J. Nieplocha, E. Apra, T. Windus, and W. de Jong. NWChem: A comprehensive and scalable open-source solution for large scale molecular simulations. *Comput. Phys. Commun.*, 181(9):1477–1489, 2010.

[248] C.-K. Skylaris and P. D. Haynes. Achieving plane wave accuracy in linear-scaling density functional theory applied to periodic systems: A case study on crystalline silicon. *J. Chem. Phys.*, 127(16):164712, 2007.

[249] M. J. S. Phipps, T. Fox, C. S. Tautermann, and C.-K. Skylaris. Energy Decomposition Analysis Based on Absolutely Localized Molecular Orbitals for Large-Scale Density Functional Theory Calculations in Drug Design. *J. Chem. Theory Comput.*, 12(7):3135–3148, 2016.

[250] Biovia Corp. Materials Studio: CASTEP Guide. `http://www.tcm.phy.cam.ac.uk/castep/documentation/WebHelp/content/pdfs/castep.htm`, 2014.

[251] G. Makov and M. C. Payne. Periodic boundary conditions in ab initio calculations. *Phys. Rev. B*, 51(7):4014–4022, 1995.

[252] E. Wasserman, J. R. Rustad, and A. R. Felmy. Molecular modeling of the surface charging of hematite: I. The calculation of proton affinities and acidities on a surface. *Surf. Sci.*, 424(1):19–27, 1999.

[253] I.-C. Yeh and A. Wallqvist. On the proper calculation of electrostatic interactions in solid-supported bilayer systems. *J. Chem. Phys.*, 134(5):055109, 2011.

[254] I.-C. Yeh and M. L. Berkowitz. Ewald summation for systems with slab geometry. *J. Chem. Phys.*, 111(7):3155–3162, 1999.

[255] E. Spohr. Effect of electrostatic boundary conditions and system size on the interfacial properties of water and aqueous solutions. *J. Chem. Phys.*, 107(16):6342–6348, 1997.

[256] K. Bourikas, C. Kordulis, and A. Lycourghiotis. The mechanism of the protonation of metal (hydr)oxides in aqueous solutions studied for various interfacial/surface ionization models and physicochemical parameters: A critical review and a novel approach. *Adv. Colloid Interface.*, 121(1-3):111–130, 2006.

[257] L. Bousse, S. Mostarshed, B. Van Der Shoot, N. F. de Rooij, P. Gimmel, and W. Göpel. Zeta potential measurements of Ta2O5 and SiO2 thin films. *J. Colloid Interf. Sci.*, 147(1):22–32, 1991.

[258] M. Tuckerman, K. Laasonen, M. Sprik, and M. Parrinello. Ab Initio Molecular Dynamics Simulation of the Solvation and Transport of H3O+ and OH- Ions in Water. *J. Phys. Chem.*, 99(16):5749–5752, 1995.

[259] S. V. Patwardhan and C. C. Perry. Interactions of biomolecules with inorganic materials: Principles, applications and future prospects. *J. Mater. Chem.*, 17(28):2875–2884, 2007.

[260] C. D. Lorenz, P. S. Crozier, J. A. Anderson, and A. Travesset. Molecular Dynamics of Ionic Transport and Electrokinetic Effects in Realistic Silica Channels. *J. Phys. Chem. C*, 112(27):10222–10232, 2008.

[261] A. A. Hassanali and S. J. Singer. Model for the water-amorphous silica interface: The undissociated surface. *J. Phys. Chem. B*, 111(38):11181–11193, 2007.

[262] A. A. Hassanali and S. J. Singer. Static and dynamic properties of the water/amorphous silica interface: A model for the undissociated surface. *J. Comput-aided Mater. Des.*, 14(1):53–63, 2007.

[263] Y. Maekawa, Y. Shibuta, and T. Sakata. Charge Behaviors around Oxide Device/Pseudo-Physiological Solution Interface with Molecular Dynamic Simulations. *Jpn. J. Appl. Phys.*, 52(12R):127001, 2013.

[264] Y. Maekawa, Y. Shibuta, and T. Sakata. Distinctive Potential Behavior at the Oxidized Surface of a Semiconductor Device in a Concentrated Aqueous Salt Solution. *ChemElectroChem*, 1(9):1516–1524, 2014.

[265] M.-H. Du, A. Kolchin, and H.-P. Cheng. Water-silica surface interactions: A combined quantum-classical molecular dynamic study of energetics and reaction pathways. *J. Chem. Phys.*, 119(13):6418, 2003.

[266] A. C. T. van Duin, S. Dasgupta, F. Lorant, and W. A. Goddard. ReaxFF: A Reactive Force Field for Hydrocarbons. *J. Phys. Chem. A*, 105(41):9396–9409, 2001.

[267] J. C. Fogarty, H. M. Aktulga, A. Y. Grama, A. C. T. van Duin, and S. A. Pandit. A reactive molecular dynamics simulation of the silica-water interface. *J. Chem. Phys.*, 132(17):174704, 2010.

[268] M. Sulpizi, M.-P. Gaigeot, and M. Sprik. The Silica-Water Interface: How the Silanols Determine the Surface Acidity and Modulate the Water Properties. *J. Chem. Theory Comput.*, 8(3):1037–1047, 2012.

[269] W. Casey, J. Rustad, and L. Spiccia. Minerals as Molecules - Use of Aqueous Oxide and Hydroxide Clusters to Understand Geochemical Reactions. *Chem. Eur. J.*, 15(18):4496–4515, 2009.

[270] C.-S. Lee, S. K. Kim, and M. Kim. Ion-Sensitive Field-Effect Transistor for Biological Sensing. *Sensors-Basel*, 9(9):7111–7131, 2009.

[271] I.-C. Lin, A. P. Seitsonen, I. Tavernelli, and U. Rothlisberger. Structure and Dynamics of Liquid Water from ab Initio Molecular Dynamics-Comparison of BLYP, PBE, and revPBE Density Functionals with and without van der Waals Corrections. *J. Chem. Theory Comput.*, 8(10):3902–3910, 2012.

[272] J. C. Grossman, E. Schwegler, E. W. Draeger, F. Gygi, and G. Galli. Towards an assessment of the accuracy of density functional theory for first principles simulations of water. *J. Chem. Phys.*, 120(1):300–311, 2004.

[273] B. Santra, A. Michaelides, and M. Scheffler. On the accuracy of density-functional theory exchange-correlation functionals for H bonds in small water clusters: Benchmarks approaching the complete basis set limit. *J. Chem. Phys.*, 127(18):184104, 2007.

[274] B. Santra, A. Michaelides, M. Fuchs, A. Tkatchenko, C. Filippi, and M. Scheffler. On the accuracy of density-functional theory exchange-correlation functionals for H bonds in small water clusters. II. The water hexamer and van der Waals interactions. *J. Chem. Phys.*, 129(19):194111, 2008.

[275] H.-P. Cheng, R. N. Barnett, and U. Landman. Structure, collective hydrogen transfer, and formation of Si(OH)4 in SiO2-(H2O)n clusters. *J. Chem. Phys.*, 116(21):9300, 2002.

[276] N. D. M. Hine, M. Robinson, P. D. Haynes, C.-K. Skylaris, M. C. Payne, and A. A. Mostofi. Accurate ionic forces and geometry optimization in linear-scaling density-functional theory with local orbitals. *Phys. Rev. B*, 83(19):195102, 2011.

[277] J. Dziedzic, H. H. Helal, C.-K. Skylaris, A. A. Mostofi, and M. C. Payne. Minimal parameter implicit solvent model for ab initio electronic-structure calculations. *Europhys. Lett.*, 95(4):43001, 2011.

[278] J. S. Bader, R. A. Kuharski, and D. Chandler. Role of nuclear tunneling in aqueous ferrous-ferric electron transfer. *J. Chem. Phys.*, 93(1):230–236, 1990.

[279] D. Marx, M. E. Tuckerman, and M. Parrinello. Solvated excess protons in water: Quantum effects on the hydration structure. *J. Phys.: Condens. Matter*, 12(8A):A153, 2000.

[280] W. Humphrey, A. Dalke, and K. Schulten. VMD: Visual molecular dynamics. *J. Mol. Graphics*, 14(1):33–38, 1996.

[281] W. A. Dollase. Reinvestigation of the structure of low cristobalite. *Z. Kristallogr.*, 121(5):369–377, 1965.

[282] B. Civalleri and N. M. Harrison. New ultrasoft pseudopotentials for the study of silicates. *Mol. Simul.*, 28(3):213–237, 2002.

[283] M. P. Hodges and D. J. Wales. Global minima of protonated water clusters. *Chem. Phys. Lett.*, 324(4):279–288, 2000.

[284] R. E. Kozack and P. C. Jordan. Empirical models for the hydration of protons. *J. Chem. Phys.*, 96(4):3131–3136, 1992.

[285] J. A. Fournier, C. J. Johnson, C. T. Wolke, G. H. Weddle, A. B. Wolk, and M. A. Johnson. Vibrational spectral signature of the proton defect in the three-dimensional H+(H2O)21 cluster. *Science*, 344(6187):1009–1012, 2014.

[286] R. Ludwig. The effect of hydrogen bonding on the thermodynamic and spectroscopic properties of molecular clusters and liquids. *Phys. Chem. Chem. Phys.*, 4(22):5481–5487, 2002.

[287] J. D. Cruzan, L. B. Braly, K. Liu, M. G. Brown, J. G. Loeser, and R. J. Saykally. Quantifying hydrogen bond cooperativity in water: VRT spectroscopy of the water tetramer. *Science*, 271(5245):59–62, 1996.

[288] A. Butenuth, G. Moras, J. Schneider, M. Koleini, S. Köppen, R. Meißner, L. B. Wright, T. R. Walsh, and L. C. Ciacchi. Ab initio derived force-field parameters for molecular dynamics simulations of deprotonated amorphous-SiO2/water interfaces. *Phys. Status Solidi B*, 249(2):292–305, 2012.

[289] L. Cwiklik, J. P. Devlin, and V. Buch. Hydroxide Impurity in Ice. *J. Phys. Chem. A*, 113(26):7482–7490, 2009.

[290] D. Marx, A. Chandra, and M. E. Tuckerman. Aqueous Basic Solutions: Hydroxide Solvation, Structural Diffusion, and Comparison to the Hydrated Proton. *Chem. Rev.*, 110(4):2174–2216, 2010.

[291] G. Agnello, J. Hamilton, R. Manley, E. Streltsova, W. LaCourse, and A. Cormack. Investigation of contact-induced charging kinetics on variably modified glass surfaces. *Appl. Surf. Sci.*, 356:1189–1199, 2015.

[292] M. A. Lill and V. Helms. Molecular dynamics simulation of proton transport with quantum mechanically derived proton hopping rates (Q-HOP MD). *J. Chem. Phys.*, 115(17):7993–8005, 2001.

[293] G. Tocci and A. Michaelides. Solvent-Induced Proton Hopping at a Water–Oxide Interface. *J. Phys. Chem. Lett.*, 5(3):474–480, 2014.

[294] M. Borkovec and G. J. M. Koper. Ising Models of Polyprotic Acids and Bases. *J. Phys. Chem.*, 98(23):6038–6045, 1994.

[295] M. Borkovec, J. Daicic, and G. J. M. Koper. Ionization properties of interfaces and linear polyelectrolytes: A discrete charge Ising model. *Physica A*, 298(1–2):1–23, 2001.

[296] P. Zarzycki. Kinetic Monte Carlo study of proton binding at the metal oxide/electrolyte interface. *J. Colloid Interf. Sci.*, 315(1):54–62, 2007.

[297] M. Stamatakis and D. G. Vlachos. A graph-theoretical kinetic Monte Carlo framework for on-lattice chemical kinetics. *J. Chem. Phys.*, 134(21):214115, 2011.

[298] J. Nielsen, M. d'Avezac, J. Hetherington, and M. Stamatakis. Parallel kinetic Monte Carlo simulation framework incorporating accurate models of adsorbate lateral interactions. *J. Chem. Phys.*, 139(22):224706, 2013.

[299] A. Chatterjee and D. G. Vlachos. An overview of spatial microscopic and accelerated kinetic Monte Carlo methods. *J. Comput-aided Mater. Des.*, 14(2):253–308, 2007.

[300] K. Reuter. First-principles kinetic Monte Carlo simulations for heterogeneous catalysis: Concepts, status, and frontiers. *Model. Heterog. Catal. React. Mol. Process Tech. Syst. O Deutschmann Ed Wiley-VCH*, pages 71–111, 2011.

[301] A. F. Voter. Introduction to the Kinetic Monte Carlo Method. In K. E. Sickafus, E. A. Kotomin, and B. P. Uberuaga, editors, *Radiation Effects in Solids*, number 235 in NATO Science Series, pages 1–23. Springer Netherlands, 2007. ISBN 978-1-4020-5295-8.

[302] K. A. Fichthorn and W. H. Weinberg. Theoretical foundations of dynamical Monte Carlo simulations. *J. Chem. Phys.*, 95(2):1090–1096, 1991.

[303] S. M. Ahmed. Studies of the Dissociation of Oxide Surfaces at the Liquid–Solid Interface. *Can. J. Chem.*, 44(14):1663–1670, 1966.

[304] M. Borkovec, J. Daicic, and G. J. M. Koper. On the difference in ionization properties between planar interfaces and linear polyelectrolytes. *PNAS*, 94(8):3499–3503, 1997.

[305] M. Borkovec, B. Jönsson, and G. J. M. Koper. Ionization Processes and Proton Binding in Polyprotic Systems: Small Molecules, Proteins, Interfaces, and Polyelectrolytes. In E. Matijević, editor, *Surface and Colloid Science*, number 16 in Surface and Colloid Science, pages 99–339. Springer US, 2001. ISBN 978-1-4613-5448-2.

[306] P. Zarzycki. Comparison of the Monte Carlo estimation of surface electrostatic potential at the hematite (0 0 0 1)/electrolyte interface with the experiment. *Appl. Surf. Sci.*, 253(18):7604–7612, 2007.

[307] P. Zarzycki. Effective adsorption energy distribution function as a new mean-field characteristic of surface heterogeneity in adsorption systems with lateral interactions. *J. Colloid Interf. Sci.*, 311(2):622–627, 2007.

[308] P. Zarzycki. Monte Carlo simulation of the electrical differential capacitance of a double electrical layer formed at the heterogeneous metal oxide/electrolyte interface. *J. Colloid Interf. Sci.*, 297(1):204–214, 2006.

[309] P. Zarzycki. Monte Carlo modeling of ion adsorption at the energetically heterogeneous metal oxide/electrolyte interface: Micro- and macroscopic correlations between adsorption energies. *J. Colloid Interf. Sci.*, 306(2):328–336, 2007.

[310] P. Zarzycki and K. M. Rosso. Nonlinear response of the surface electrostatic potential formed at metal oxide/electrolyte interfaces. A Monte Carlo simulation study. *J. Colloid Interf. Sci.*, 341(1):143–152, 2010.

[311] P. Zarzycki, P. Szabelski, and R. Charmas. Role of the surface heterogeneity in adsorption of hydrogen ions on metal oxides: Theory and simulations. *J. Comput. Chem.*, 26(10):1079–1088, 2005.

[312] P. Zarzycki, R. Charmas, and P. Szabelski. Study of proton adsorption at heterogeneous oxide/electrolyte interface. Prediction of the surface potential using Monte Carlo simulations and 1-pK approach. *J. Comput. Chem.*, 25(5):704–711, 2004.

[313] P. Zarzycki and K. M. Rosso. Origin of Two Time-Scale Regimes in Potentiometric Titration of Metal Oxides. A Replica Kinetic Monte Carlo Study. *Langmuir*, 25(12):6841–6848, 2009.

[314] G. Zheng, X. P. A. Gao, and C. M. Lieber. Frequency Domain Detection of Biomolecules Using Silicon Nanowire Biosensors. *Nano Lett.*, 10(8):3179–3183, 2010.

[315] D. P. Landau and K. Binder. *A Guide to Monte Carlo Simulations in Statistical Physics*. Cambridge University Press, 2014. ISBN 978-1-316-06263-0.

[316] J. Sonnefeld. On the influence of background electrolyte concentration on the position of the isoelectric point and the point of zero charge. *Colloid. Surface. A*, 190(1–2):179–183, 2001.

[317] M. Ashida, M. Sasaki, H. Kan, T. Yasunaga, K. Hachiya, and T. Inoue. Kinetics of proton adsorption-desorption at TiO2-H2O interface by means of pressure-jump technique. *J. Colloid Interf. Sci.*, 67(2):219–225, 1978.

[318] O. Smidsrød, S. Moe, and S. T. Moe. *Biopolymer Chemistry*. Tapir Academic Press, 2008. ISBN 978-82-519-2384-2.

[319] M. Elias, D. Liebschner, J. Koepke, C. Lecomte, B. Guillot, C. Jelsch, and E. Chabriere. Hydrogen atoms in protein structures: High-resolution X-ray diffraction structure of the DFPase. *BMC Res. Notes*, 6:308, 2013.

[320] M. A. Hass and F. A. Mulder. Contemporary NMR Studies of Protein Electrostatics. *Annu. Rev. Biophys.*, 44:53–75, 2015.

[321] M. H. M. Olsson. Protein electrostatics and pKa blind predictions; contribution from empirical predictions of internal ionizable residues. *Proteins*, 79(12):3333–3345, 2011.

[322] G. Kieseritzky and E. W. Knapp. Improved pKa prediction: Combining empirical and semimicroscopic methods. *J. Comput. Chem.*, 29(15):2575–2581, 2008.

[323] P. Barth, T. Alber, and P. B. Harbury. Accurate, conformation-dependent predictions of solvent effects on protein ionization constants. *PNAS*, 104(12):4898–4903, 2007.

[324] I. Zeimpekis, K. Sun, C. Hu, O. Thomas, M. R. de Planque, H. M. Chong, H. Morgan, and P. Ashburn. Study of parasitic resistance effects in nanowire and nanoribbon biosensors. *Nanoscale Res. Lett.*, 10(79), 2015.

[325] K. Sun, I. Zeimpekis, C. Hu, N. M. J. Ditshego, O. Thomas, M. R. R. de Planque, H. M. H. Chong, H. Morgan, and P. Ashburn. Low-cost top-down zinc oxide nanowire sensors through a highly transferable ion beam etching for healthcare applications. *Microelectronic Engineering*, 153:96–100, 2016.

[326] K. Sun, I. Zeimpekis, M. Lombardini, N. M. J. Ditshego, S. J. Pearce, K. S. Kiang, O. Thomas, M. R. R. de Planque, H. M. H. Chong, H. Morgan, and P. Ashburn. Three-Mask Polysilicon Thin-Film Transistor Biosensor. *IEEE Trans. Electron Devices*, 61(6):2170–2176, 2014.

[327] I. Zeimpekis, K. Sun, C. Hu, N. M. J. Ditshego, O. Thomas, M. R. R. de Planque, H. M. H. Chong, H. Morgan, and P. Ashburn. Dual-gate polysilicon nanoribbon biosensors enable high sensitivity detection of proteins. *Nanotechnology*, 27(16):165502, 2016.

[328] S. Liang, J. Dai, S. Hou, L. Su, D. Zhang, H. Guo, S. Hu, H. Wang, Z. Rao, Y. Guo, and Z. Lou. Structural Basis for Treating Tumor Necrosis Factor α (TNFα)-associated Diseases with the Therapeutic Antibody Infliximab. *J. Biol. Chem.*, 288(19):13799–13807, 2013.

[329] T.-S. Pui, A. Agarwal, F. Ye, Y. Huang, and P. Chen. Nanoelectronic detection of triggered secretion of pro-inflammatory cytokines using CMOS compatible silicon nanowires. *Biosens. Bioelectron.*, 26(5):2746–2750, 2011.

[330] T. Decker and M.-L. Lohmann-Matthes. A quick and simple method for the quantitation of lactate dehydrogenase release in measurements of cellular cytotoxicity and tumor necrosis factor (TNF) activity. *J. Immunol. Methods*, 115(1):61–69, 1988.

[331] S. Hu, S. Liang, H. Guo, D. Zhang, H. Li, X. Wang, W. Yang, W. Qian, S. Hou, H. Wang, Y. Guo, and Z. Lou. Comparison of the inhibition mechanisms of adalimumab and infliximab in treating tumor necrosis factor α-associated diseases from a molecular view. *J. Biol. Chem.*, 288(38):27059–27067, 2013.

[332] M. J. Eck and S. R. Sprang. The structure of tumor necrosis factor-alpha at 2.6 A resolution. Implications for receptor binding. *J. Biol. Chem.*, 264:17595–17605, 1989.

[333] C. M. Petersen, A. Nykjaer, B. S. Christiansen, L. Heickendorff, S. C. Mogensen, and B. Møller. Bioactive human recombinant tumor necrosis factor-alpha: An unstable dimer? *Eur. J. Immunol.*, 19(10):1887–1894, 1989.

[334] P. Ameloot, W. Fiers, P. De Bleser, C. F. Ware, P. Vandenabeele, and P. Brouckaert. Identification of tumor necrosis factor (TNF) amino acids crucial for binding to the murine p75 TNF receptor and construction of receptor-selective mutants. *J. Biol. Chem.*, 276(40):37426–37430, 2001.

[335] H. M. Berman, J. Westbrook, Z. Feng, G. Gilliland, T. N. Bhat, H. Weissig, I. N. Shindyalov, and P. E. Bourne. The Protein Data Bank. *Nucl. Acids Res.*, 28(1):235–242, 2000.

[336] *Molecular Operating Environment (MOE) Software*. Chemical Computing Group Inc, 010 Sherbooke St. West, Suite #910, Montreal, QC, Canada, H3A 2R7, 2013.

[337] S. O. Farrell, F. A. Bettelheim, O. Torres, M. K. Campbell, and W. H. Brown. *Introduction to General, Organic and Biochemistry*. Brooks/Cole, Pacific Grove, Calif.; Andover, international ed of 10th revised ed edition edition, 2011. ISBN 978-1-133-10911-2.

[338] E. Stern, R. Wagner, F. J. Sigworth, R. Breaker, T. M. Fahmy, and M. A. Reed. Importance of the Debye Screening Length on Nanowire Field Effect Transistor Sensors. *Nano Lett.*, 7(11):3405–3409, 2007.

[339] E. H. Williams, A. V. Davydov, A. Motayed, S. G. Sundaresan, P. Bocchini, L. J. Richter, G. Stan, K. Steffens, R. Zangmeister, J. A. Schreifels, and M. V. Rao. Immobilization of streptavidin on 4H–SiC for biosensor development. *Appl. Surf. Sci.*, 258(16):6056–6063, 2012.

[340] X. Duan, N. K. Rajan, M. H. Izadi, and M. A. Reed. Complementary metal oxide semiconductor-compatible silicon nanowire biofield-effect transistors as affinity biosensors. *Nanomed.*, 8(11):1839–1851, 2013.

[341] S. Gupta, M. Elias, X. Wen, J. Shapiro, L. Brillson, W. Lu, and S. C. Lee. Detection of clinically relevant levels of protein analyte under physiologic buffer using planar field effect transistors. *Biosens. Bioelectron.*, 24(4):505–511, 2008.

[342] G. Shalev, Y. Rosenwaks, and I. Levy. The interplay between pH sensitivity and label-free protein detection in immunologically modified nano-scaled field-effect transistor. *Biosens. Bioelectron.*, 31(1):510–515, 2012.

[343] R. A. Sperling and W. J. Parak. Surface modification, functionalization and bioconjugation of colloidal inorganic nanoparticles. *Philos. T. Roy. Soc. A*, 368(1915):1333–1383, 2010.

[344] T. Sano and C. R. Cantor. Cooperative biotin binding by streptavidin. Electrophoretic behavior and subunit association of streptavidin in the presence of 6 M urea. *J. Biol. Chem.*, 265(6):3369–3373, 1990.

[345] N. M. Green. Avidin. In J. T. E. C.B. Anfinsen and F. M. Richards, editors, *Advances in Protein Chemistry*, volume 29, pages 85–133. Academic Press, 1975.

[346] L. Chaiet and F. J. Wolf. The properties of streptavidin, a biotin-binding protein produced by Streptomycetes. *Arch. Biochem. Biophys.*, 106:1–5, 1964.

[347] N. M. Green. Avidin and streptavidin. In M. W. Bayer and E. A., editors, *Methods in Enzymology*, volume 184 of *Avidin-Biotin Technology*, pages 51–67. Academic Press, 1990.

[348] S. Sivasankar, S. Subramaniam, and D. Leckband. Direct molecular level measurements of the electrostatic properties of a protein surface. *Proc. Natl. Acad. Sci.*, 95(22):12961–12966, 1998.

[349] Rockland Inc. Streptavidin Properties and Characterization. Data Sheet Code: S000-01.

[350] L. Almonte, E. Lopez-Elvira, and A. M. Baró. Surface-Charge Differentiation of Streptavidin and Avidin by Atomic Force Microscopy–Force Spectroscopy. *ChemPhysChem*, 15(13):2768–2773, 2014.

[351] C. E. Argarana, I. D. Kuntz, S. Birken, R. Axel, and C. R. Cantor. Molecular cloning and nucleotide sequence of the streptavidin gene. *Nucleic Acids Res.*, 14(4):1871–1882, 1986.

[352] A. Pähler, W. A. Hendrickson, M. A. Kolks, C. E. Argaraña, and C. R. Cantor. Characterization and crystallization of core streptavidin. *J. Biol. Chem.*, 262(29):13933–13937, 1987.

[353] A. Gallizia, C. de Lalla, E. Nardone, P. Santambrogio, A. Brandazza, A. Sidoli, and P. Arosio. Production of a soluble and functional recombinant streptavidin in Escherichia coli. *Protein Expr. Purif.*, 14(2):192–196, 1998.

[354] M.-Y. Shen, B.-R. Li, and Y.-K. Li. Silicon nanowire field-effect-transistor based biosensors: From sensitive to ultra-sensitive. *Biosens. Bioelectron.*, 60:101–111, 2014.

[355] B. K. Wunderlich, P. A. Neff, and A. R. Bausch. Mechanism and sensitivity of the intrinsic charge detection of biomolecular interactions by field effect devices. *Appl. Phys. Lett.*, 91(8):083904, 2007.

[356] D. Landheer, G. Aers, W. R. McKinnon, M. J. Deen, and J. C. Ranuarez. Model for the field effect from layers of biological macromolecules on the gates of metal-oxide-semiconductor transistors. *J. Appl. Phys.*, 98(4):044701, 2005.

[357] D. Landheer, W. R. McKinnon, W. H. Jiang, and G. Aers. Effect of screening on the sensitivity of field-effect devices used to detect oligonucleotides. *Appl. Phys. Lett.*, 92(25):253901, 2008.

[358] W. R. McKinnon, D. Landheer, and G. Aers. Sensitivity of field-effect biosensors to charge, pH, and ion concentration in a membrane model. *J. Appl. Phys.*, 104(12):124701, 2008.

[359] K. Jayant, K. Auluck, M. Funke, S. Anwar, J. B. Phelps, P. H. Gordon, S. R. Rajwade, and E. C. Kan. Programmable ion-sensitive transistor interfaces. I. Electrochemical gating. *Phys. Rev. E*, 88(1):012801, 2013.

[360] K. Jayant, K. Auluck, M. Funke, S. Anwar, J. B. Phelps, P. H. Gordon, S. R. Rajwade, and E. C. Kan. Programmable ion-sensitive transistor interfaces. II. Biomolecular sensing and manipulation. *Phys. Rev. E*, 88(1):012802, 2013.

[361] K. Jayant, K. Auluck, S. Rodriguez, Y. Cao, and E. C. Kan. Programmable ion-sensitive transistor interfaces. III. Design considerations, signal generation, and sensitivity enhancement. *Phys. Rev. E*, 89(5):052817, 2014.

[362] A. M. Soto, V. Misra, and D. E. Draper. Tertiary Structure of an RNA Pseudoknot Is Stabilized by "Diffuse" Mg2+ Ions. *Biochemistry*, 46(11):2973–2983, 2007.

[363] D. E. Draper, D. Grilley, and A. M. Soto. Ions and RNA Folding. *Annu. Rev. Bioph. Biom.*, 34(1):221–243, 2005.

[364] R. de la Rica, C. Fernández-Sánchez, C. Jiménez-Jorquera, and A. Baldi. Spermine-Induced Hybridization and Charge Inversion at the Diffuse Layer of a DNA-FET. *J. Phys. Chem. B*, 112(25):7614–7617, 2008.

[365] A. A. Shul'ga, M. Koudelka-Hep, and N. F. de Rooij. The effect of divalent metal ions on the performance of a glucose-sensitive ENFET using potassium ferricyanide as an oxidising substrate. *Sens. Actuat. B-Chem.*, 27(1–3):432–435, 1995.

[366] C. Maffeo, J. Yoo, J. Comer, D. B. Wells, B. Luan, and A. Aksimentiev. Close encounters with DNA. *J. Phys.: Condens. Matter*, 26(41):413101, 2014.

[367] A. Pérez, F. J. Luque, and M. Orozco. Frontiers in Molecular Dynamics Simulations of DNA. *Acc. Chem. Res.*, 45(2):196–205, 2012.

[368] P. Várnai and K. Zakrzewska. DNA and its counterions: A molecular dynamics study. *Nucl. Acids Res.*, 32(14):4269–4280, 2004.

[369] C. Grindon, S. Harris, T. Evans, K. Novik, P. Coveney, and C. Laughton. Large-scale molecular dynamics simulation of DNA: Implementation and validation of the AMBER98 force field in LAMMPS. *Philos. T. Roy. Soc. A*, 362(1820):1373–1386, 2004.

[370] I. Ivani, P. D. Dans, A. Noy, A. Pérez, I. Faustino, A. Hospital, J. Walther, P. Andrio, R. Goñi, A. Balaceanu, G. Portella, F. Battistini, J. L. Gelpí, C. González, M. Vendruscolo, C. A. Laughton, S. A. Harris, D. A. Case, and M. Orozco. Parmbsc1: A refined force field for DNA simulations. *Nat. Meth.*, 13(1):55–58, 2016.

[371] Accelrys Software Inc.,. Accelrys Material Studio 8.0. *Accelrys Mater. Studio 80*, 2007.

[372] D. C. Rapaport. *The Art of Molecular Dynamics Simulation*. Cambridge University Press, 2004. ISBN 978-0-521-82568-9.

[373] J. M. Haile. *Molecular Dynamics Simulation: Elementary Methods*. Wiley, 1997. ISBN 978-0-471-18439-3.

[374] V. Brázdová and D. R. Bowler. *Atomistic Computer Simulations: A Practical Guide*. John Wiley & Sons, 2013. ISBN 978-3-527-67183-0.

[375] D. A. McQuarrie and J. D. Simon. *Physical Chemistry: A Molecular Approach*. University Science Books, 1997. ISBN 978-0-935702-99-6.

[376] B. M. Lowe, Y. Maekawa, Y. Shibuta, T. Sakata, C.-K. Skylaris, and N. G. Green. Dynamic behaviour of the silica-water-bio electrical double layer in the presence of a divalent electrolyte. *Phys. Chem. Chem. Phys.*, 2016.

[377] O. Stern. The theory of the electrolytic double-layer. *Z. Elektrochem Angew. P.*, 30:508–16, 1924.

[378] H. Helmholtz. Ueber einige Gesetze der Vertheilung elektrischer Ströme in körperlichen Leitern mit Anwendung auf die thierisch-elektrischen Versuche. *Ann. Phys.*, 165(6):211–233, 1853.

[379] G. Gouy. Constitution of the Electric Charge at the Surface of an Electrolyte. *J. Phys.*, 9:457–67, 1910.

[380] D. L. Chapman. LI. A contribution to the theory of electrocapillarity. *Philos. Mag. Series 6*, 25(148):475–481, 1913.

[381] S. Rumyantsev, G. Liu, M. S. Shur, R. A. Potyrailo, and A. A. Balandin. Selective Gas Sensing with a Single Pristine Graphene Transistor. *Nano Lett.*, 12(5):2294–2298, 2012.

[382] I. Jokić, M. Frantlović, Z. Djurić, K. Radulović, and Z. Jokić. Adsorption–desorption noise in microfluidic biosensors operating in multianalyte environments. *Microelectron. Eng.*, 144:32–36, 2015.

[383] I.-Y. Chung, J. Lee, M. Seo, and C. H. Park. Particle simulation of electrolytic ion motions for noise in electrolyte–insulator–semiconductor field-effect transistors. *Jpn. J. Appl. Phys.*, 55(12):127001, 2016.

[384] Y. Maekawa, Y. Shibuta, and T. Sakata. Elucidation of Semiconductor/Bio-Interface Structure with Massive Classical Molecular Dynamics Simulation. *J. Surf. Finish. Soc. Jpn.*, 65(6):251–256, 2014.

[385] Y. Maekawa, Y. Shibuta, and T. Sakata. Effect of double-stranded DNA on electrical double layer structure at oxide/electrolyte interface in classical molecular dynamics simulation. *Chem. Phys. Lett.*, 619:152–157, 2015.

[386] F. S. Emami, V. Puddu, R. J. Berry, V. Varshney, S. V. Patwardhan, C. C. Perry, and H. Heinz. Force Field and a Surface Model Database for Silica to Simulate Interfacial Properties in Atomic Resolution. *Chem. Mater.*, 26(8):2647–2658, 2014.

[387] F. S. Emami, V. Puddu, R. J. Berry, V. Varshney, S. V. Patwardhan, C. C. Perry, and H. Heinz. Prediction of Specific Biomolecule Adsorption on Silica Surfaces as a Function of pH and Particle Size. *Chem. Mater.*, 26(19):5725–5734, 2014.

[388] H. Zhang, A. A. Hassanali, Y. K. Shin, C. Knight, and S. J. Singer. The water–amorphous silica interface: Analysis of the Stern layer and surface conduction. *J. Chem. Phys.*, 134(2):024705, 2011.

[389] Á. Cimas, F. Tielens, M. Sulpizi, M.-P. Gaigeot, and D. Costa. The amorphous silica-liquid water interface studied by ab initio molecular dynamics (AIMD): Local organization in global disorder. *J. Phys.: Condens. Matter*, 26(24):244106, 2014.

[390] W. Li, L. Nordenskiöld, and Y. Mu. Sequence-Specific Mg2+–DNA Interactions: A Molecular Dynamics Simulation Study. *J. Phys. Chem. B*, 115(49):14713–14720, 2011.

[391] B. Luan and A. Aksimentiev. DNA Attraction in Monovalent and Divalent Electrolytes. *J. Am. Chem. Soc.*, 130(47):15754–15755, 2008.

[392] E. Wernersson, R. Kjellander, and J. Lyklema. Charge Inversion and Ion-Ion Correlation Effects at the Mercury/Aqueous MgSO4 Interface: Toward the Solution of a Long-Standing Issue. *J. Phys. Chem. C*, 114(4):1849–1866, 2010.

[393] A. Y. Grosberg, T. T. Nguyen, and B. I. Shklovskii. Colloquium: The physics of charge inversion in chemical and biological systems. *Rev. Mod. Phys.*, 74(2):329–345, 2002.

[394] K. Besteman, M. A. G. Zevenbergen, H. A. Heering, and S. G. Lemay. Direct Observation of Charge Inversion by Multivalent Ions as a Universal Electrostatic Phenomenon. *Phys. Rev. Lett.*, 93(17):170802, 2004.

[395] J. B. Edel and A. de Mello. Nanofluidics: Nanoscience and Nanotechnology. In *Nanofluidics: Nanoscience and Nanotechnology*, page 7. Royal Society of Chemistry, 2009. ISBN 978-0-85404-147-3.

[396] B. Luan and A. Aksimentiev. Electric and electrophoretic inversion of the DNA charge in multivalent electrolytes. *Soft Matter*, 6(2):243–246, 2010.

[397] S. P. Das. *Statistical Physics of Liquids at Freezing and Beyond*. Cambridge University Press, 2011. ISBN 978-1-139-50067-8.

[398] R. W. Impey, P. A. Madden, and I. R. McDonald. Hydration and mobility of ions in solution. *J. Phys. Chem.*, 87(25):5071–5083, 1983.

[399] F. Bruni, S. Imberti, R. Mancinelli, and M. A. Ricci. Aqueous solutions of divalent chlorides: Ions hydration shell and water structure. *J. Chem. Phys.*, 136(6):064520, 2012.

[400] N. T. Skipper and G. W. Neilson. X-ray and neutron diffraction studies on concentrated aqueous solutions of sodium nitrate and silver nitrate. *J. Phys.: Condens. Matter*, 1(26):4141, 1989.

[401] S. B. Rempe and L. R. Pratt. The hydration number of Na+ in liquid water. *Fluid Phase Equilibr.*, 183–184:121–132, 2001.

[402] N. Korolev, A. P. Lyubartsev, A. Laaksonen, and L. Nordenskiöld. A molecular dynamics simulation study of oriented DNA with polyamine and sodium counterions: Diffusion and averaged binding of water and cations. *Nucleic Acids Res.*, 31(20):5971–5981, 2003.

[403] E. L. Cussler. Diffusion of Interacting Species. In *Diffusion: Mass Transfer in Fluid Systems*, page 162. Cambridge University Press, 2009. ISBN 978-0-521-87121-1.

[404] S. E. Ingebritsen and W. E. Sanford. *Groundwater in Geologic Processes*. Cambridge University Press, 1999. ISBN 978-0-521-66400-4.

[405] A. Chatterjee, M. K. Dixit, and B. L. Tembe. Solvation Structures and Dynamics of the Magnesium Chloride (Mg2+–Cl–) Ion Pair in Water–Ethanol Mixtures. *J. Phys. Chem. A*, 117(36):8703–8709, 2013.

[406] K. Krynicki, C. D. Green, and D. W. Sawyer. Pressure and temperature dependence of self-diffusion in water. *Faraday Discuss. Chem. Soc.*, 66:199, 1978.

[407] D. van der Spoel, P. J. van Maaren, and H. J. C. Berendsen. A systematic study of water models for molecular simulation: Derivation of water models optimized for use with a reaction field. *J. Chem. Phys.*, 108(24):10220–10230, 1998.

[408] I. Waluyo, C. Huang, D. Nordlund, U. Bergmann, T. M. Weiss, L. G. M. Pettersson, and A. Nilsson. The structure of water in the hydration shell of cations from x-ray Raman and small angle x-ray scattering measurements. *J. Chem. Phys.*, 134(6):064513, 2011.

[409] M. Sotomayor, V. Vásquez, E. Perozo, and K. Schulten. Ion Conduction through MscS as Determined by Electrophysiology and Simulation. *Biophys. J.*, 92(3):886–902, 2007.

[410] A. Bleuzen, P.-A. Pittet, L. Helm, and A. E. Merbach. Water exchange on magnesium(II) in aqueous solution: A variable temperature and pressure 17O NMR study. *Magn. Reson. Chem.*, 35(11):765–773, 1997.

[411] D. J. Wesolowski, M. L. Machesky, M. K. Ridley, D. A. Palmer, Z. Zhang, P. A. Fenter, M. Predota, and P. T. Cummings. Ion Adsorption on Metal Oxide Surfaces to Hydrothermal Conditions. *ECS Trans.*, 11(27):167–180, 2008.

[412] R. Jolsterå, L. Gunneriusson, and A. Holmgren. Surface complexation modeling of Fe3O4–H+ and Mg(II) sorption onto maghemite and magnetite. *J. Colloid Interf. Sci.*, 386(1):260–267, 2012.

[413] J.-B. d'Espinose de la Caillerie, M. Kermarec, and O. Clause. 29Si NMR Observation of an Amorphous Magnesium Silicate Formed during Impregnation of Silica with Mg(II) in Aqueous Solution. *J. Phys. Chem.*, 99(47):17273–17281, 1995.

[414] M. S. Kilic, M. Z. Bazant, and A. Ajdari. Steric effects in the dynamics of electrolytes at large applied voltages. I. Double-layer charging. *Phys. Rev. E*, 75(2):021502, 2007.

[415] O. Stern. Zur Theorie Der Elektrolytischen Doppelschicht. *Z. Elktrochem. Angew. P.*, 30(21-22):508–516, 1924.

[416] M. A. Brown, Z. Abbas, A. Kleibert, R. G. Green, A. Goel, S. May, and T. M. Squires. Determination of Surface Potential and Electrical Double-Layer Structure at the Aqueous Electrolyte-Nanoparticle Interface. *Phys. Rev. X*, 6(1):011007, 2016.

[417] M. A. Brown, G. V. Bossa, and S. May. Emergence of a Stern Layer from the Incorporation of Hydration Interactions into the Gouy-Chapman Model of the Electrical Double Layer. *Langmuir*, 31(42):11477–11483, 2015.

[418] G. S. Manning. The molecular theory of polyelectrolyte solutions with applications to the electrostatic properties of polynucleotides. *Q. Rev. Biophys.*, 11(02):179, 1978.

[419] J. N. Glosli and M. R. Philpott. Molecular dynamics study of interfacial electric fields. *Electrochim. Acta*, 41(14):2145–2158, 1996.

[420] T. Baimpos, B. R. Shrestha, S. Raman, and M. Valtiner. Effect of Interfacial Ion Structuring on Range and Magnitude of Electric Double Layer, Hydration, and Adhesive Interactions between Mica Surfaces in 0.05–3 M Li+ and Cs+ Electrolyte Solutions. *Langmuir*, 30(15):4322–4332, 2014.

[421] M. Kosmulski. Electric Charge Density of Silica, Alumina and Related Surfaces. In *Encyclopedia of Surface and Colloid Science*, volume 3, page 1863. CRC Press, second edition edition, 2006. ISBN 978-0-8493-9606-9.

[422] S. Y. Ponomarev, K. M. Thayer, and D. L. Beveridge. Ion motions in molecular dynamics simulations on DNA. *Proc. Natl. Acad. Sci. USA*, 101(41):14771–14775, 2004.

[423] M. Rueda, E. Cubero, C. A. Laughton, and M. Orozco. Exploring the Counterion Atmosphere around DNA: What Can Be Learned from Molecular Dynamics Simulations? *Biophys. J.*, 87(2):800–811, 2004.

[424] G. S. Manning. Counterion binding in polyelectrolyte theory. *Acc. Chem. Res.*, 12(12):443–449, 1979.

[425] C. F. Anderson, M. T. Record Jr., and P. A. Hart. Sodium-23 NMR studies of cation-DNA interactions. *Biophys. Chem.*, 7(4):301–316, 1978.

[426] J. Skerjanc and U. P. Strauss. Interactions of polyelectrolytes with simple electrolytes. III. The binding of magnesium ion by deoxyribonucleic acid. *J. Am. Chem. Soc.*, 90(12):3081–3085, 1968.

[427] K. R. Bhat. *Physiochemical Investigations of Magnesium-DNA-Proflavine System.* Ph.D. thesis, Rutgers University, 1974.

[428] P. Spegt and G. Weill. Magnetic resonance distinction between site bound and atmospherically bound paramagnetic counterions in polyelectrolyte solutions. *Biophys. Chem.*, 4(2):143–149, 1976.

[429] W. H. Braunlin, C. F. Anderson, and M. T. Record. 23Na-nmr investigations of counterion exchange reactions of helical DNA. *Biopolymers*, 25(1):205–214, 1986.

[430] G. S. Manning and J. Ray. Counterion Condensation Revisited. *J. Biomol. Struct. Dyn.*, 16(2):461–476, 1998.

[431] M. A. Young, B. Jayaram, and D. L. Beveridge. Intrusion of Counterions into the Spine of Hydration in the Minor Groove of B-DNA: Fractional Occupancy of Electronegative Pockets. *J. Am. Chem. Soc.*, 119(1):59–69, 1997.

[432] B. I. Shklovskii. Screening of a macroion by multivalent ions: Correlation-induced inversion of charge. *Phys. Rev. E*, 60(5):5802–5811, 1999.

[433] F. Patolsky, G. Zheng, O. Hayden, M. Lakadamyali, X. Zhuang, and C. M. Lieber. Electrical detection of single viruses. *PNAS*, 101(39):14017–14022, 2004.

[434] E. Souteyrand, J. P. Cloarec, J. R. Martin, C. Wilson, I. Lawrence, S. Mikkelsen, and M. F. Lawrence. Direct Detection of the Hybridization of Synthetic Homo-Oligomer DNA Sequences by Field Effect. *J. Phys. Chem. B*, 101(15):2980–2985, 1997.

[435] M. O. Noor and U. J. Krull. Silicon nanowires as field-effect transducers for biosensor development: A review. *Anal. Chim. Acta.*, 825:1–25, 2014.

[436] D. Passeri, A. Morozzi, K. Kanxheri, and A. Scorzoni. Numerical simulation of ISFET structures for biosensing devices with TCAD tools. *Biomed. Eng. Online*, 14:S3, 2015.

[437] D. E. Draper, D. Grilley, and A. M. Soto. Ions and RNA Folding. *Annu. Rev. Bioph. Biom.*, 34(1):221–243, 2005.

[438] N. Elfström. *Silicon Nanowires for Biomolecule Detection*. Ph.D. thesis, Royal Institute of Technology, Stockholm, Sweden, 2008.

[439] R. J. Chen, H. C. Choi, S. Bangsaruntip, E. Yenilmez, X. Tang, Q. Wang, Y.-L. Chang, and H. Dai. An Investigation of the Mechanisms of Electronic Sensing of Protein Adsorption on Carbon Nanotube Devices. *J. Am. Chem. Soc.*, 126(5):1563–1568, 2004.

[440] H. R. Byon and H. C. Choi. Network Single-Walled Carbon Nanotube-Field Effect Transistors (SWNT-FETs) with Increased Schottky Contact Area for Highly Sensitive Biosensor Applications. *J. Am. Chem. Soc.*, 128(7):2188–2189, 2006.

[441] X. P. A. Gao, G. Zheng, and C. M. Lieber. Subthreshold Regime has the Optimal Sensitivity for Nanowire FET Biosensors. *Nano Lett.*, 10(2):547–552, 2010.

[442] N. K. Rajan, X. Duan, and M. A. Reed. Performance limitations for nanowire/nanoribbon biosensors. *WIREs Nanomed. Nanobiotechnol.*, 5(6):629–645, 2013.

[443] S. M. Sze. *Semiconductor Devices: Physics and Technology*. John Wiley & Sons, Inc., Hoboken, N.J, 2nd edition edition, 1985. ISBN 0-471-33372-7.

[444] A. Tarasov, W. Fu, O. Knopfmacher, J. Brunner, M. Calame, and C. Schönenberger. Signal-to-noise ratio in dual-gated silicon nanoribbon field-effect sensors. *Appl. Phys. Lett.*, 98(1):012114, 2011.

[445] N. K. Rajan, D. A. Routenberg, and M. A. Reed. Optimal signal-to-noise ratio for silicon nanowire biochemical sensors. *Appl. Phys. Lett.*, 98(26):264107, 2011.

[446] N. K. Rajan, D. A. Routenberg, J. Chen, and M. A. Reed. Temperature dependence of 1/f noise mechanisms in silicon nanowire biochemical field effect transistors. *Appl. Phys. Lett.*, 97(24):243501, 2010.

[447] N. D. Arora. Piecewise Drain-Current Model for Enhancement Devices. In *MOSFET Models for VLSI Circuit Simulation: Theory and Practice*, page 265. Springer Science & Business Media, 2012. ISBN 978-3-7091-9247-4.

[448] M. Nič, J. Jirát, B. Košata, A. Jenkins, and A. McNaught, editors. *IUPAC Compendium of Chemical Terminology: Gold Book*. IUPAC, Research Triagle Park, NC, 2.1.0 edition, 2009. ISBN 978-0-9678550-9-7.

[449] D. Sarkar, W. Liu, X. Xie, A. C. Anselmo, S. Mitragotri, and K. Banerjee. MoS2 Field-Effect Transistor for Next-Generation Label-Free Biosensors. *ACS Nano*, 8(4):3992–4003, 2014.

[450] N. K. Rajan, X. Duan, and M. A. Reed. Performance limitations for nanowire/nanoribbon biosensors: Performance limitations for nanowire/nanoribbon biosensors. *WIREs Nanomed. Nanobiotechnol.*, 5(6):629–645, 2013.

[451] B. N. Dominy, D. Perl, F. X. Schmid, and C. L. Brooks III. The Effects of Ionic Strength on Protein Stability: The Cold Shock Protein Family. *J. Mol. Biol.*, 319(2):541–554, 2002.

[452] S. K. Milonjić. Determination of surface ionization and complexation constants at colloidal silica/electrolyte interface. *Colloids Surface.*, 23(4):301–312, 1987.

[453] M. Kosmulski. pH-dependent surface charging and points of zero charge. IV. Update and new approach. *J. Colloid Interf. Sci.*, 337(2):439–448, 2009.

[454] A. Tarasov, M. Wipf, R. L. Stoop, K. Bedner, W. Fu, V. A. Guzenko, O. Knopfmacher, M. Calame, and C. Schönenberger. Understanding the Electrolyte Background for Biochemical Sensing with Ion-Sensitive Field-Effect Transistors. *ACS Nano*, 6(10):9291–9298, 2012.

[455] S. Chen, J. G. Bomer, E. T. Carlen, and A. van den Berg. Al2O3/silicon nanoISFET with near ideal nernstian response. *Nano Lett.*, 11(6):2334–2341, 2011.

[456] L. J. Criscenti, R. T. Cygan, A. S. Kooser, and H. K. Moffat. Water and Halide Adsorption to Corrosion Surfaces: Molecular Simulations of Atmospheric Interactions with Aluminum Oxyhydroxide and Gold. *Chem. Mater.*, 20(14):4682–4693, 2008.

[457] R. Schasfoort, R. Kooyman, P. Bergveld, and J. Greve. A new approach to immunoFET operation. *Biosens. Bioelectron.*, 5(2):103–124, 1990.

[458] S. Chen, J. W. van Nieuwkasteele, A. van den Berg, and J. C. T. Eijkel. Ion-Step Method for Surface Potential Sensing of Silicon Nanowires. *Anal. Chem.*, 88(16):7890–7893, 2016.

[459] D. Clark-Carter. Geometric Mean. In *Encyclopedia of Statistics in Behavioral Science*. John Wiley & Sons, Ltd, 2005. ISBN 978-0-470-01319-9.

[460] H. H. Liu, T. H. Lin, and J.-T. Sheu. Enhancement of detection by selective modification of silicon nanobelt field-effect transistors via localized Joule heating. *Sens. Actuat. B-Chem.*, 192:111–116, 2014.

[461] K. Sun and I. Zeimpekis. Personal Communication, 2016.

[462] E. Buitrago. *High Performance, Vertically Stacked SiNW/Fin Based 3D FETs for Biosensing Applications*. Ph.D. thesis, École Polytechnique Fédérale de Lausanne, 2014.

[463] S. Kim, T. Rim, K. Kim, U. Lee, E. Baek, H. Lee, C.-K. Baek, M. Meyyappan, M. J. Deen, and J.-S. Lee. Silicon nanowire ion sensitive field effect transistor with integrated Ag/AgCl electrode: pH sensing and noise characteristics. *Analyst*, 136(23):5012–5016, 2011.

[464] X. T. Vu, R. Stockmann, B. Wolfrum, A. Offenhäusser, and S. Ingebrandt. Fabrication and application of a microfluidic-embedded silicon nanowire biosensor chip. *phys. stat. sol. (a)*, 207(4):850–857, 2010.

[465] C.-E. Lue, T.-C. Yu, C.-M. Yang, D. G. Pijanowska, and C.-S. Lai. Optimization of Urea-EnFET Based on Ta2O5 Layer with Post Annealing. *Sensors*, 11(12):4562–4571, 2011.

[466] A. Tarasov, N. de Rooij, C. Schönenberger, and L. Linnros. *Silicon Nanowire Field-Effect Transistors for Sensing Applications*. Ph.D. thesis, University of Basel, 2012.

[467] S. Zafar, C. D'Emic, A. Afzali, B. Fletcher, Y. Zhu, and T. Ning. Optimization of pH sensing using silicon nanowire field effect transistors with HfO $_2$ as the sensing surface. *Nanotechnology*, 22(40):405501, 2011.

[468] K. Bedner, V. A. Guzenko, A. Tarasov, M. Wipf, R. L. Stoop, D. Just, S. Rigante, W. Fu, R. A. Minamisawa, C. David, and others. pH response of silicon nanowire sensors: Impact of nanowire width and gate oxide. *Sens. Mater.*, 25(8):567–576, 2013.

[469] S. Rigante, M. Wipf, A. Bazigos, K. Bedner, D. Bouvet, and A. M. Ionescu. FinFET with fully pH-responsive HfO2 as highly stable biochemical sensor. pages 1063–1066. IEEE, San Francisco, CA, USA, 2014. ISBN 978-1-4799-3509-3.

[470] P. Bergveld. The future of biosensors. *Sens. Actuators Phys.*, 56(1):65–73, 1996.

[471] H. H. Lee, M. Bae, S.-H. Jo, J.-K. Shin, D. H. Son, C.-H. Won, and J.-H. Lee. Fabrication and Characterization of an Extended-Gate AlGaN/GaN-Based Heterostructure Field-Effect Transistor-Type Biosensor for Detecting Immobilized Streptavidin-Biotin Protein Complexes. *Sens. Mater.*, 2015.

[472] P. Casal, X. Wen, S. Gupta, T. Nicholson, Y. Wang, A. Theiss, B. Bhushan, L. Brillson, W. Lu, and S. C. Lee. ImmunoFET feasibility in physiological salt environments. *Phil. Trans. R. Soc. A*, 370(1967):2474–2488, 2012.

[473] D. E. Yates, S. Levine, and T. W. Healy. Site-binding model of the electrical double layer at the oxide/water interface. *J. Chem. Soc., Faraday Trans. 1*, 70(0):1807–1818, 1974.

[474] T. W. Healy and L. R. White. Ionizable surface group models of aqueous interfaces. *Adv. Colloid Interfac.*, 9(4):303–345, 1978.

[475] T. Akiyama, Y. Ujihira, Y. Okabe, T. Sugano, and E. Niki. Ion-sensitive field-effect transistors with inorganic gate oxide for pH sensing. *IEEE Trans. Electron Devices*, 29(12):1936–1941, 1982.

[476] Meng-Nian Niu, Xin-Fang Ding, and Qin-Yi Tong. Effect of two types of surface sites on the characteristics of Si/sub 3/N/sub 4/-gate pH-ISFET's. pages 189–193. IEEE, Penang, Malaysia, 1996. ISBN 978-0-7803-3388-8.

[477] P. Schuck and H. Zhao. The Role of Mass Transport Limitation and Surface Heterogeneity in the Biophysical Characterization of Macromolecular Binding Processes by SPR Biosensing. *Methods Mol. Biol.*, 627:15–54, 2010.

[478] P. E. Sheehan and L. J. Whitman. Detection limits for nanoscale biosensors. *Nano Lett.*, 5(4):803–807, 2005.

[479] B. S. Kang, F. Ren, L. Wang, C. Lofton, W. W. Tan, S. J. Pearton, A. Dabiran, A. Osinsky, and P. P. Chow. Electrical detection of immobilized proteins with ungated AlGaN/GaN high-electron-mobility Transistors. *Appl. Phys. Lett.*, 87(2):023508, 2005.

[480] X. Wen, S. Gupta, T. R. Nicholson, S. C. Lee, and W. Lu. AlGaN/GaN HFET biosensors working at subthreshold regime for sensitivity enhancement. *Phys. Status Solidi C*, 8(7-8):2489–2491, 2011.

[481] K. Shoorideh and C. O. Chui. Optimization of the Sensitivity of FET-Based Biosensors via Biasing and Surface Charge Engineering. *IEEE Trans. Electron Devices*, 59(11):3104–3110, 2012.

[482] R. L. Rich and D. G. Myszka. Survey of the year 2005 commercial optical biosensor literature. *J. Mol. Recognit.*, 19(6):478–534, 2006.

[483] R. B. M. Schasfoort and A. J. Tudos. *Handbook of Surface Plasmon Resonance*. Royal Society of Chemistry, 2008. ISBN 978-0-85404-267-8.

[484] P. Politzer, P. R. Laurence, and K. Jayasuriya. Molecular electrostatic potentials: An effective tool for the elucidation of biochemical phenomena. *Environ. Health Perspect.*, 61:191–202, 1985.

[485] S. Srebrenik, H. Weinstein, and R. Pauncz. Analytical calculation of atomic and molecular electrostatic potentials from the Poisson equation. *Chem. Phys. Lett.*, 20(5):419–423, 1973.

[486] H. Rangwalla and A. Dhinojwala. Probing Hidden Polymeric Interfaces Using IR–Visible Sum-Frequency Generation Spectroscopy. *J. Adhes.*, 80(1-2):37–59, 2004.

[487] F. Li, L. Wang, J. Zhao, J. R.-H. Xie, K. E. Riley, and Z. Chen. What is the best density functional to describe water clusters: Evaluation of widely used density functionals with various basis sets for (H2O)n (n = 1-10). *Theor. Chem. Acc.*, 130(2-3):341–352, 2011.

[488] M. Chaplin. 6-31G** RHF calculations using Hyperchem 8 Software. `http://www1.lsbu.ac.uk/water/index2.html`, 5th February 2014.

[489] F. Franks. *Water. 1. The Physics and Physical Chemistry of Water*. Plenum Press, 1972. ISBN 978-0-306-37181-3.

[490] J. M. Hermida-Ramòn and G. Karlström. Study of the hydronium ion in water. A combined quantum chemical and statistical mechanical treatment. *J. Mol. Struct-theochem*, 712(1-3):167–173, 2004.

[491] F. F. Muguet. MCSCF vibrational spectra of the symmetric and asymmetric dihydronium cations. *J. Mol. Struct-theochem*, 368:173–196, 1996.

[492] E. G. Diken, J. M. Headrick, J. R. Roscioli, J. C. Bopp, M. A. Johnson, and A. B. McCoy. Fundamental Excitations of the Shared Proton in the $H_3O_2^-$ and $H_5O_2^+$ Complexes. *J. Phys. Chem. A*, 109(8):1487–1490, 2005.

[493] D. T. Puerta and S. M. Cohen. [(TpMe,Ph)2Zn2(H3O2)]ClO4: A new H3O2 species relevant to zinc proteinases. *Inorg. Chim. Acta.*, 337:459–462, 2002.

[494] J. J. Novoa, F. Mota, C. Perez del Valle, and M. Planas. Structure of the First Solvation Shell of the Hydroxide Anion. A Model Study Using OH-(H2O)n (n = 4, 5, 6, 7, 11, 17) Clusters. *J. Phys. Chem. A*, 101(42):7842–7853, 1997.

[495] M. Löbbus, W. Vogelsberger, J. Sonnefeld, and A. Seidel. Current Considerations for the Dissolution Kinetics of Solid Oxides with Silica. *Langmuir*, 14(16):4386–4396, 1998.

[496] M. Kosmulski. Adsorption of Methanol and Supporting Electrolyte on Silica and Alumina in Mixed Solvent Systems. *J. Colloid Interf. Sci.*, 156(2):305–310, 1993.

[497] COMSOL Multiphysics® v. 5.2. Diffuse Double Layer - Application ID: 21981. Technical report, COMSOL AB, Stockholm, Sweden, 2016.

[498] J. Linnros. Personal Communication, 8th September 2016.

[499] G. Shalev, A. Cohen, A. Doron, A. Machauf, M. Horesh, U. Virobnik, D. Ullien, and I. Levy. Standard CMOS Fabrication of a Sensitive Fully Depleted Electrolyte-Insulator-Semiconductor Field Effect Transistor for Biosensor Applications. *Sensors*, 9(6):4366–4379, 2009.

Part I.

Appendices

A. Appendix: Terminology - Electrostatic Potential

The term 'electrostatic potential', a concept related to the electric potential difference, has become popular within the field of computational chemistry. A summary of the meaning and use of electrostatic potential in biochemical molecular modelling has been published by Politzer et al. [484], for which Politzer states that the electrostatic potential $V(\mathbf{r})$ at any point $\mathbf{r}$ can be rigorously defined by considering a static nuclear environment whereby nuclei, A, of charge Z_A are located at positions $\mathbf{R}$, with electrons at positions r and an electronic density function $\rho(\boldsymbol{r})$:

$$V(\mathbf{r}) = \sum_{A} \frac{Z_A}{|\mathbf{R_A} - \mathbf{r}|} - \int \frac{\rho(\mathbf{r}')}{|\mathbf{r}' - \mathbf{r}|} d\mathbf{r}'. \tag{A.1}$$

In this expression, the first term represents the contribution of the nuclei and can be evaluated exactly. The second term represents the contribution of the electrons, and can only be approximated. It can be determined either experimentally by diffraction methods [101] or using quantum mechanical calculations [484]. $V(\boldsymbol{r})$ is exactly equal to the Coulombic interaction energy between the unperturbed charge distribution of the system and a positive unit charge at $\mathbf{r}$ [101].

Other methods of calculating the electrostatic potential exist, such as substituting $\rho(\mathbf{r})$ into the Poisson equation (Equation 3.1) and evaluating the resulting integrals either approximately or exactly [485]:

Politzer describes the electrostatic potential as [484]:

> ...a real physical property, as evidenced by the fact that it can be determined experimentally. It is rigorously and unambiguously defined by Equation A.1 and has a clear physical meaning: it expresses the net electrical effect of the electrons and nuclei of a system in the surrounding space.

A useful derived quantity can be formed by taking the gradient of the electrostatic potential; the resulting vector field, referred within this report as the 'electrostatic field', is a specific case of the electric field, $\mathbf{E}$, relevant to atomic systems which represents the force per unit charge at all points in space due to Coulombic interactions with the nuclei and electrons.

B. Appendix: Sum Frequency Generation and Second Harmonic Generation Background

The dielectric silica layer on the surface of many BioFETs has an unusual acid-base behaviour. Some of the most compelling experimental evidence towards silica surface acidity and the structure of the silica-water interface originated from sum frequency generation and second harmonic generation measurements.

Second harmonic generation is a non-linear optical process which can be used to study interfaces. In second harmonic generation measurements, two input high intensity lasers are focused such that they overlap at the surface. The input photons annihilate each other and result in a generated output beam with a frequency ω_3 which is the sum of the two input lasers with frequencies ω_1 and ω_2 (Equation B.1).

$$\hbar\omega_3 = \hbar\omega_2 + \hbar\omega_1 \tag{B.1}$$

In sum frequency generation spectroscopy, one of the input lasers is held at a constant visible wavelength whilst the other is varied through the infrared range, and the output beam is measured with a detector. This facilitates measurement of the vibrational spectra at the interface. Second harmonic generation is a special case of sum frequency generation measurement whereby $\omega_1 = \omega_2 = \frac{\omega_3}{2}$, and is easier to perform experimentally as only one input laser is required.

The input beam induces polarisation at the interface $P_{2\omega}$ which leads to a coherant surface response $E_{2\omega}$. Importantly, the measured intensity is a function of the incident electric field E_ω and the second-order susceptibility of the surface $\chi^{(2)}$, which is itself related to the interfacial molecular composition and orientation of the target system. Under the electric-dipole approximation (ignoring multipoles and magnetic moments) $\chi^{(2)}$ is only non-zero in non-centrosymmetric media, meaning this technique selectively measures interfacial regions. Increasing intensity of the measured response suggests an increasingly net polar orientation of molecules at the surface [486]. The intensity is also modulated by a third order susceptibility $\chi^{(3)}$ due to the electric field from charged sites at the surface. Taking this into consideration the intensity can be expressed as:

$$E_{2\omega} \propto P_{2\omega} = \chi^{(2)} E_{\omega_1} E_{\omega_2} + \chi^{(3)} E_{\omega_1} E_{\omega_2} E_0 + ..., \tag{B.2}$$

where E_0 is the static electric field in the interfacial region. A key limitation of this technique is that the region defined as the interface is not always clear, and so it not trivial to map response onto its chemical origin using this technique alone.

In main text (Section 3.3.2.2), the work of Ong et al. is referred to [145], in which they measured the second harmonic generation response of silica over a range of pH values. By varying temperature and electrolyte concentration, Ong et al. showed that the observed signal cannot be explained using simply the $\chi^{(2)}$ term, and showed a good theoretical fit to a model incorporating the $\chi^{(3)}$ term due to surface charge-induced polarisation effects. This result therefore provides evidence for polarisation of water at the interface [145]. More explicitly, in order to calculate $P_{2\omega}$, they removed the significant contribution of the $\chi^{(2)}$ term by subtracting the signal from the neutral surface (pH 2) from the fully charged surface (pH 13), leaving only the contribution from $\chi^{(3)}$ and higher order terms. They then fitted a 'Constant Capacitance Model' to the data, in which the data could best be fitted by introducing two distinct pK_a values at the surface as discussed in the main text (Section 3.3.2.2). Ong et al. also argued that second harmonic generation can be used to directly measure the surface potential [145].

C. Appendix: Introduction to Density Functional Theory

The following report was prepared solely by myself as part of an MSc-level component to my 4-year integrated PhD programme. It provides an introduction to DFT and electronic structure theory to the non-specialist. The full report, including a subsequent DFT study of the silica-biomolecule interface is available online at the University of Southampton repository: `http://eprints.soton.ac.uk/401427/`

COMP6055 - Complex Systems Independent Research Project

Benjamin Lowe

bml1g12@soton.ac.uk

Institute for Complex Systems Simulation

I. Notes

This research report is split into two sections. The first section is that of an overview of the theory that I have learned as a crucial part of this IRP, as my knowledge of Quantum Chemistry in Simulation work was poor beforehand. The second section focuses on some work I have performed in replicating a paper which investigates the properties of the Amino Acids/Silica surface interface. This system was chosen to be simple so as to ensure I am familiar with the principles, and gain some experience with simulation in this area. This work could lay a foundation for further work on more Complex Systems, whereby the interactions of many components are investigated, for example, studying the properties of entire proteins on surfaces, or incorporating the interaction of networks of water molecules on the system. The interface between biological molecules and inorganic surfaces is currently poorly understood, and of great importance in areas such as Bionanotechnology (e.g. biosensors [1], [2] and drug-delivery [3]). Furthermore, it is believed the first organic molecules may have been catalyzed by inorganic surfaces, and therefore understanding this interface has relevance to understanding the mechanism behind the formation of primordial life [4].

II. Quantum Mechanics

Throughout the 20th Century it became evident that a new theory was required which would reconcile the differences between classical models and experiments in the microscopic world. Experiments such as the famous Young's interference experiment lead to the discovery that matter could no longer considered as simply particles or waves, but rather must be considered as wave-particles at very small length scales. As a result, new discipline, Quantum Mechanics was required. Quantum Mechanics is a branch of physics that describes the phenomena observed at microscopic scales. From Quantum Mechanics we can obtain the fundamental laws of Chemistry, and thereby an understanding of the properties of materials and biological molecules. For example, Quantum Mechanics can be used to aid *in silico* predictions of drug-affinity for proteins; and therefore has important applications in the Pharmaceutical industry.

In Classical Mechanics, the state of a particle's characteristics, such as position and energy can be measured precisely and deterministically. In Quantum Mechanics this is no longer the case, and the only deterministic factor is the probability distribution of an observable. A wavefunction can describe a chemical system (several molecules), a single molecule or a single wave-particle (e.g. an electron, or photon). According to the correspondence principle, the laws of Classical Mechanics are simply the result of a statistical average over the quantum properties of a large number of particles [5].

The material discussed throughout the theory section of this report can be found within most textbooks in the area of Quantum Chemistry, of which the works of Atkins and Friedman [6] is particularly good, and also that of Szabo and Ostlund [7].

Quantum Mechanics describes the state of a system not through its position and energy, but through an abstract property called the 'Wavefunction',φ. An axiom of Quantum Mechanics states that the wavefunction fully characterises *all* properties of a chemical system and, once φ is known, we can determine any property of interest by applying the appropriate operator $\hat{O}$:

$$< \hat{O} >= \int \varphi^* \hat{O} \varphi \, \mathrm{d}x. \tag{1}$$

The wavefunction has no direct physical interpretation, however the probability of finding a chemical system is the integral of $|\varphi^* \varphi|$ over all space, or simply the integral of $|\varphi|^2$ for real wavefunctions.

III. Schrödinger Equation

Once the wavefunction of a molecule is known, any observable property of interest can be calculated *ab initio*, which means 'from first principles' based on the axions of quantum mechanics, without fitting to experimental data. The wavefunction can be determined from the (non-relativistic) time-independent Schrödinger equation:

$$\hat{H}\varphi = E\varphi, \tag{2}$$

This seemingly simple but powerful equation states that by applying an the Hamiltonian operator to the wavefunction, the resulting eigenvalues are the total energy of the system described by the wavefunction. In order to find other properties, such as the dipole moment or kinetic energy, different operators are used. The Hamiltonian operator is an important operator, and is a sum of contributions from the inter electronic repulsion, internuclear repulsion, electronic and nuclear kinetic energies and the electron-nucleus attraction.

Except in the simplest of cases (e.g. atomic hydrogen), the time-independent Schrödinger equation cannot be solved analytically, and as such normally only an approximate solution can be obtained using numerical computations. Furthermore various approximations must be utilised in order to make these computations feasible. In order to solve Equation 2 for many electron problems, an important assumption that is made is the Born-Oppenheimer approximation; because the electrons move much faster than the nuclei, is often a very good approximation to assume that the nuclear kinetic energy can be dealt with separately to the electronic energy, and added as a classical term at the end of the calculation. As such we are concerned with solving the electronic time-independent Schrödinger:

$$\hat{H}_{elec}\varphi_{elec} = E_{elec}\varphi_{elec}, \tag{3}$$

for each set of fixed nuclear coordinates. In order to consider this problem mathematically, Figure 1 demonstrates the relevant vectors describing the coordinate system.

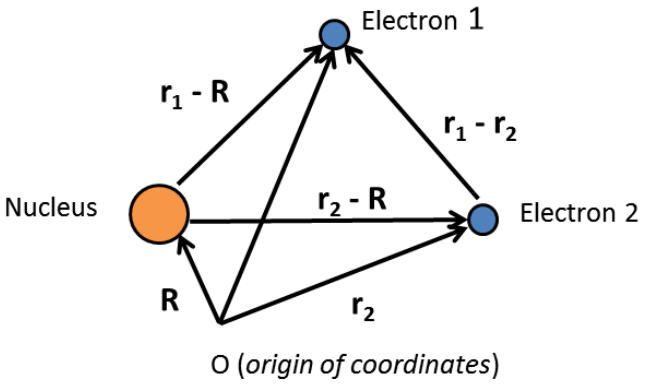

Figure 1. Schematic of the Electronic Problem for a Helium atom showing the various coordinate vectors relevant to electronic calculations.

The total electronic energy Hamiltonian operator $\hat{H}_{elec}$ can be written in Atomic Units as:

$$\hat{H}_{elec} = -\sum_{i=1}^{N_{elec}} \frac{1}{2}\nabla^2_{\mathbf{r_i}} - \sum_{i=1}^{N_{elec}}\sum_{A=1}^{M_{nuc}} \frac{Z_A}{|\mathbf{r_i}-\mathbf{R_A}|} + \sum_{i=1}^{N_{elec}}\sum_{j=i}^{N_{elec}} \frac{1}{|\mathbf{r_i}-\mathbf{r_j}|}, \tag{4}$$

where the first is the electron kinetic energy operator, the second term is the electron-nuclear attraction (where Z is the atomic number of the nucleus A) operator, and is the electron-electron repulsion operator.

In summary, the Schrödinger equation can be numerically solved to provide an approximation to the molecular electronic wavefunction by solving Equation 3 and the resulting wavefunction can be used to determine determine electronic properties of the system. These methods are often based on 'Hartree-Fock' theory (Section IV-C). Remarkably, this approach can be performed almost[1] entirely from first principles ('*ab initio*') whereby only the atomic numbers and initial coordinates of the nuclei are provided. In an attempt to provide reduced computational cost at the expense of accuracy, another common approach ('Semi-Empirical') to is to replace the electronic Hamiltonian (Equation 4) with a highly parametrized empirical expression. In both cases, it is a challenging task to compute chemically accurate energies to within about 5 kJmol^{-1} [6]. Finally, Density Function Theory (DFT) is a popular branch of quantum chemistry which approaches the problem of calculating molecular properties from an entirely different perspective. In DFT properties are calculated as functional of the electronic density. Figure 5 summarises the various methodologies. This report will outline Hartree-Fock methods and briefly introduce DFT.

IV. Hartree-Fock Molecular Orbital Theory

A. Representing the Wavefunction

The aim of this section is the present the notation used to approximate a molecular wavefunction. We can describe a single electron through via its spatial coordinates ($\mathbf{r} = x, y, z$) and its spin ω, we denote these four coordinates as **x.** The wavefunction for a single electron can therefore be expressed as a spin orbital,$\chi(\mathbf{x})$, which is a product of the spatial wavefunction $\psi(\mathbf{r})$ and a spin function $\alpha(\omega)$ or $\beta(\omega)$ to represent spin up and spin down respectively.

$$\chi(\mathbf{x}) = \begin{cases} \psi(\mathbf{r})\alpha(\omega) \\ or \\ \psi(\mathbf{r})\beta(\omega) \end{cases}. \tag{5}$$

The mathematical function expressing a spin orbital is not known, however the properties of them are known. Figure 2 summaries the notation for one electron wavefunctions. The mathematical function for a spatial orbital is typically a basis set expansion of any arbitrary function ϕ; most often Gaussian or Slater type functions, as further discussed in Appendix and shown in Equation 6.

$$\psi(\mathbf{r}) = \sum_{\mu=1}^{M} C_{\mu i}\phi_\mu(\mathbf{r}). \tag{6}$$

We have shown that the molecular wavefunctions $\varphi(\mathbf{x})$, can be numerically approximated as functions of spin orbitals (Equation 7).

$$\varphi(\mathbf{x}) \approx \Psi\left(\chi(\mathbf{x})\right) \tag{7}$$

The exact wavefunction φ we desire could be approximated (Ψ) in several ways. For example, it could represented as a simple product of one electron wavefunctions ('Hartree-Product'), e.g. for two electrons :

$$\Psi(\mathbf{x_1}, \mathbf{x_2}) = \chi_i(\mathbf{x_1})\chi_j(\mathbf{x_2}). \tag{8}$$

[1] often with a small empirical correction to increase accuracy

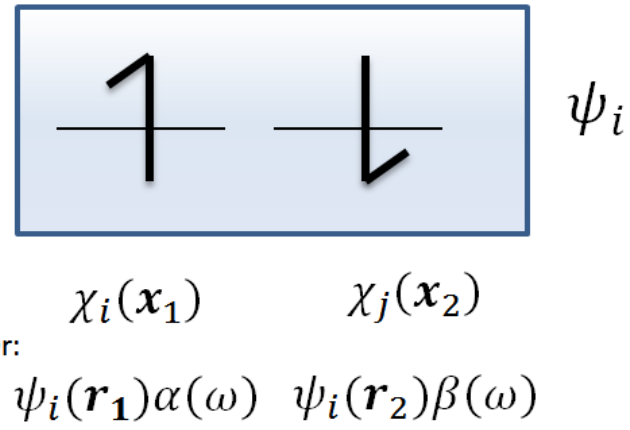

Figure 2. Each electron can be described via its spin orbital (χ_i). For restricted closed shell configurations, the spatial function is considered the same for both electrons, and the only difference between the two spin orbitals is the spin function. This is as shown above ('Restricted Hartree-Fock'). For open shell configurations, separate spatial functions are used ('open-shell Hartree-Fock'), this can be for just the the open-shell orbitals (restricted) or for all orbitals ('unrestricted').

However such a representation has various issues. Firstly a wavefunction should not distinguish between electrons (in the Hartree-Product, $\mathbf{x}_1$is always associated with χ_i) and secondly it does not satisfy the *antisymmetry principle* (Equation 9). An antisymmetric wavefunction is one where the interchange of the coordinate $\mathbf{x}$ (both space and spin) of any two electrons results in a change in the sign of the wavefunction:

$$\Psi(\mathbf{x_1}, \mathbf{x_2}) = -\Psi(\mathbf{x_2}, \mathbf{x_1}). \tag{9}$$

These principles can be incorporated into the expression for Ψ with the use of Slater Determinants, e.g. for the two electron case above:

$$\begin{aligned}\Psi(\mathbf{x_1}, \mathbf{x_2}) &= \frac{1}{\sqrt{2}} \begin{vmatrix} \chi_i(\mathbf{x_1}) & \chi_j(\mathbf{x_1}) \\ \chi_i(\mathbf{x_2}) & \chi_j(\mathbf{x_2}) \end{vmatrix} \\ &= \frac{1}{\sqrt{2}} \Big(\chi_i(\mathbf{x_1})\chi_j(\mathbf{x_2}) - \chi_i(\mathbf{x_1})\chi_j(\mathbf{x_2}) \Big), \end{aligned} \tag{10}$$

It can be seen that this obeys the antisymmetry principle because exchanging the positions of electrons (interchanging two rows of the determinant) changes the sign of the determinant. The spin orbitals no longer distinguish between electrons. Furthermore, the antisymmetry principle also leads to the concept of the Pauli Exclusion principle, because two electrons cannot occupy the same spin orbital, as the determinant becomes zero. In general, the Slater determinant has N electrons occupying N spin orbitals:

$$\Psi(\mathbf{x_1}, \mathbf{x_2} ... \mathbf{x_N}) = A \begin{vmatrix} \chi_i(\mathbf{x_1}) & \chi_i(\mathbf{x_1}) & \dots & \chi_k(\mathbf{x_1}) \\ \chi_i(\mathbf{x_2}) & \chi_j(\mathbf{x_2}) & \dots & \chi_k(\mathbf{x_2}) \\ \vdots & \vdots & \ddots & \vdots \\ \chi_i(\mathbf{x_N}) & \chi_j(\mathbf{x_N}) & \dots & \chi_k(\mathbf{x_N}) \end{vmatrix}, \tag{11}$$

where $A = \frac{1}{\sqrt{N}}$.Note also there is one other important difference from the Hartree-product. In the Hartree-product, electrons are uncorrelated i.e. the probability of finding electron-one in $\mathrm{d}x_1$at $\mathbf{x}_1$and electron-two in $\mathrm{d}x_2$at $\mathbf{x}_2$ is was just the average of the product of the probabilities. This is unphysical, and the well known Van der Waal forces are an effect of this correlation. For the Slater Determinant, because the antisymmetry principle must be satisfied if the position of two electrons are exchanged, the motion of parallel spins must be correlated; the Slater Determinant introduces 'exchange correlation' for parallel spins. A limitation of the Slater determinant is that it completely neglects description of any electron correlation of unparalleled spins. The simplest (and consequently least accurate) antisymmetric wavefunction which can be used to describe the ground state of an N-electron system is a single Slater determinant.

B. The Variational Principle

An important principle in all quantum chemistry calculations is the Variational Principle. This principle states that the total energy of *any* well-behaved, normalised wave function will *always* be higher than the ground state of the system. As a result, the Hamiltonian of a single Slater determinant approximation of the wavefunction Ψ_{SD} will always be above the ground state of the system:

$$\epsilon = \Big\langle \Psi | \hat{H} | \Psi \Big\rangle \geq \epsilon_0 \tag{12}$$

Therefore, by varying $\Psi(\mathbf{x})$, we know that any reduction in total energy corresponds to a better approximation of the true ground state wavefunction of the system.

C. Hartree-Fock Self-Consistent Field method (SCF)

We are seen that we are interested in determining the approximate wavefunction for the system Ψ, which can be expressed, in the simplest case, as a single determinant. From the Variational Principle (Section IV-B), we know that the best wave function of this form can be obtained by varying the choice of spin orbitals in the Slater determinant in order to minimise the energy. This optimal configuration of spin orbitals can be obtained by applying solving the Hartree-Fock equations for each spin orbital (χ_i):

$$f(i)\chi(\mathbf{x}_i) = \epsilon\chi(\mathbf{x}_i), \tag{13}$$

where f is the 'Fock-Operator' :

$$\begin{aligned} f(i) &= \hat{h} + v^{HF}(i) \\ &= -\frac{1}{2}\nabla^2_{\mathbf{r_i}} - \sum_{A=1}^{M_{nuc}} \frac{Z_A}{|\mathbf{r_i} - \mathbf{R_A}|} + v^{HF}(i) \end{aligned} \tag{14}$$

The first term is the kinetic energy of each electron, the second term is the Coulomb attraction of the electron to the nucleus and the final term is *average* potential experienced by the *i*th electron, as a result of interactions with other electrons. Electron-electron interactions are key to accurate descriptions of wavefunctions. The Hartee-Fock assumption deals with electron-electron interaction by accounting for them in an 'average' way, and an unfortunate consequence of this assumption is that does not entirely account for electron

correlation. v^{HF} comprises of a Coulomb operator, which pseudo-classically can be seen to represent electron-electron repulsion, and an exchange operator which is a purely quantum effect which is a consequence of the antisymmetry principle (equation 9).

The set of M simultaneous Hartree-Fock equations which must be solved are known as the 'Roothaan equations'. As each 'field' seen by an electron depends on every other electron, the equation must be solved iteratively using a procedure called Self-Consistent Field (SCF) method.The principle is simple; an initial guess of the spin orbitals is made, and from this the average field is calculated (v^{HF}). This is then used to solve the eigenvalue equation 13 and obtain new spin orbitals from which the procedure can be repeated until convergence of energy is reached. For an N-electron system, the N lowest energy spin orbitals are then used to construct a single Slater determinant wavefunction for the system as shown in Equation 11. This lowest energy configuration is the Hartree-Fock approximation Ψ_0^{HF} of the true wavefunction ground state. Figure 3 depicts an overview of the process.

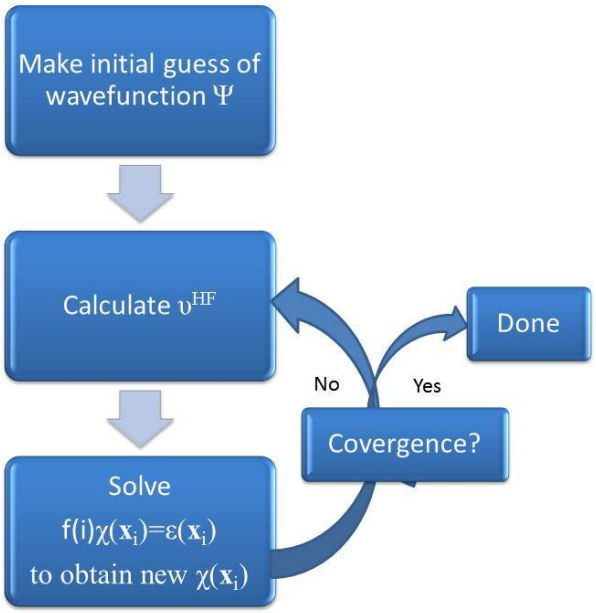

Figure 3. Flowchart summarising the Hartree-Fock Self-Consistant Field Procedure.

D. Accuracy of the Hartree-Fock method and Post-Hartree-Fock methods

As with any *ab initio* method for determining a many-electron wavefunction, the resulting wavefunction Ψ_0^{HF} is the result of several approximations, and therefore in any practical implementation will not be exact. Approximations include the Born-Oppenheimer Approximation and the neglect of relativistic effects, and neglect of of electron correlation for electrons of opposite spin. The accuracy of the wavefunction, and therefore Energy may be improved by increasing the number of basis functions, with diminishing returns up until the 'Hartree-Fock limit'.

Many improvements have been made to the Hartree-Fock method since its conception, and these improved methods often collectively referred to as 'Post-Hartree Fock' methods. These methods incorporate the effect of electron correlation for electrons of opposite spin. A popular post-Hartree-Fock methodology is called 'full Configurational Interaction' (full CI). This method considers the excited states of the molecules in order to better represent the wavefunction of the system.In short, the an exact wavefunction φ can be expressed as a linear combination of all the infinite symmetry adapted Slater determinants. Therefore to reach the exact solution (up to the Born-Oppenheimer approximation), an infinite number of basis sets would be needed and an infinite number of Slater determinants, as shown in Figure 4, and a compromise between accuracy and efficiency must be made. Another widely used post-Hartree-Fock methodology is that of Møller–Plesset perturbation theory, which treats electron correlation as a perturbation of the Fock operator [8].

Although Hartree-Fock and Post-Hartree-Fock methods are still widely used today, they require the computation of many two-electron integrals, which leads to poor scaling in time with the number (N) of basis sets (HF methods scale at around N^4 or higher). As an increased number of basis sets is needed to describe an increased number of atoms, this means that systems of many atoms are highly intensive, and computations beyond several hundred atoms are likely infeasible.

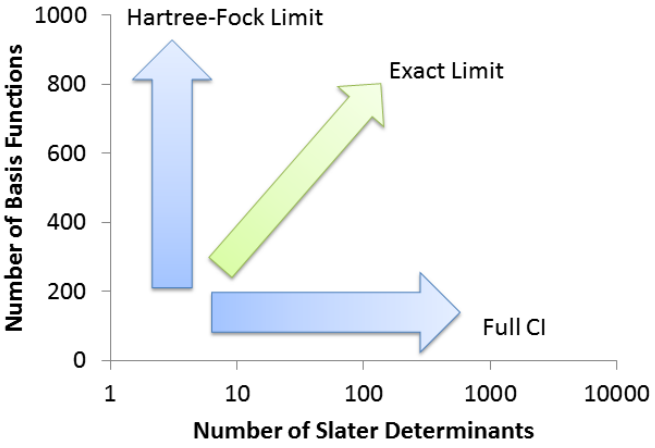

Figure 4. Graph showing how accuracy of Hartree-Fock methods increases with either increasing Slater Determinants or increased number of Basis Functions. When the number of basis functions is complete in describing the system, and all states have been considered as Slater Determinants, the exact solution (up to the Born Oppenheimer Approximation) will be attained.

E. Calculating Molecular and Electronic Properties from the Wavefunction

Once the wavefunction for the system has been determined, the electronic properties (e.g. dipole moment, charge density etc.) can be obtained trivially by applying the correct operator as shown in Equation 1. In order to obtain molecular geometries, thermodynamics properties (e.g. Gibbs Free energy,

entropy) and predict spectroscopic properties (bond vibration frequencies, chemical shifts etc.) a Potential Energy Surface (PES) must be constructed, which describes how the energy of the system as a function of the atomic positions. A PES is generated by combining information from the electronic wavefunction with the nuclear wavefunction using the Born-Oppenheimer Approximation. Figure 5 depicts this schematically. Further information on PES can be found within many Quantum Chemistry textbooks [6], [7], [9].

V. Density Functional Theory

Density Functional Theory (DFT) represents a very different approach to obtaining molecular and electronic properties which is not based on the concept of first finding spin orbitals χ as in Hartree-Fock calculations. DFT uses the concept of electronic probability density, as shown in Equation as its fundamental unit, not the wavefunction - which brings several advantages, such as being more experimentally relevant. Furthermore, whilst the wavefunction of an N-electron system depends on 4N variables (x,y,z,ω for each of N electrons), the density just depends on 3 variables (x,y,z) and therefore does not increase in complexity for larger systems.The popularity of DFT can be explained in part because it can include electron correlation, as in Post-Hartree-Fock methods, whilst being less computationally demanding (scaling as N^3 to the number of basis sets, compared to N^4 for Hartree-Fock methods). The electron density $n(\mathbf{r})$ can be thought of as the probability of finding any of the N electrons at a particular point in space, $\mathbf{r}$:

$$n(\mathbf{r}) = N_{el} \int \cdots \int |\varphi(\mathbf{x}_1, \mathbf{x}_2 ... \mathbf{x}_{N_{el}})|^2 \, \mathrm{d}\mathbf{x}_1 \mathrm{d}\mathbf{x}_2 ... \mathrm{d}\mathbf{x}_{N_{el}}. \tag{15}$$

Although DFT has existed since the 1920's, it was not until the 1960's, whereby a formal proof Hohenberg and Kohn, showed that for a single ground state probability density, all corresponding ground-state electronic properties can be uniquely determined, for example; for a given density, there is a corresponding electronic energy; it is said that the electronic energy is a *functional*[2] of density *[10].* This remarkable proof is considered one of the most significant developments in quantum theory since the development of Schrodinger Equation in 1926 as it allows us to tackle the Electronic Problem from a difference angle. Unfortunately the Hohenberg-Kohn theorem does not tell us the *form* of the functional; originally there was a focus on 'pure' or 'orbital-free' DFT, which attempts to compute the energy of *interacting* electrons as a functional of density. However, pure DFT is limited by the poor quality of these approximations, in particular for the kinetic energy functional.

In 1965, Kohn and Sham developed a novel DFT method which solved this issue, by utilising fictitious *non-interacting* one-electron spatial orbitals as a tool to approximate the kinetic energy functional [11]. A detailed discussion of DFT is beyond the scope of this report, however the reader can find an excellent introduction by Atkins and Friedman [6]. In short, Kohn-Sham DFT has become an important part of many DFT calculations. Using this principle, the electron density of an N electron system can be obtained as simply a sum of spatial orbitals squared:

$$n(\mathbf{r}) = \sum_{i=1}^{N} |\psi_i(\mathbf{r})|^2, \tag{16}$$

The spatial orbitals required to construct the density can be determined as follows. Firstly, the expression for the total energy function for the system is formulated, comprising of functionals for the non-interacting Kohn-Sham Kinetic Energy and the other energy components (Coulombic, Nuclear-Electron and Exchange-Correlation). Secondly, this functional is minimised analytically resulting in the following expression :

$$(-\frac{1}{2}\nabla^2 + V_{KS})\psi_j(\mathbf{r}) = \epsilon_j \psi_j(\mathbf{r}) \tag{17}$$

Finally, equation 17 is solved an Self-Consistent Field approach, similar to that described in Figure 3, which yields the KS-orbitals. The density can the then be obtained using equation 16. V_{KS} is an "effective potential" which allows us to generate a density equal to the real system from the fictions system of non-interacting electrons. It is composed of a set of known functionals representing the the nucleus-electron attraction and electron-electron repulsion. An exact expression for the exchange-correlation potential is unknown, and an approximation for the exchange-correlation potential is therefore used. Many functionals have been proposed in the literature, each with different advantages and disadvantageous, and it is therefore important that a suitable functional is chosen to suit the properties of the system. Once the density is known, electronic properties of the system can be calculated provided an appropriate functional of the density is known.

A. Linear-Scaling DFT

Considering one of the limiting factors in the progress of Quantum Chemistry has long since been its high computational expense, much work has gone into finding methods which scale better with the number of basis sets (and thereby atoms), whilst retaining accuracy. Whilst conventional cubic scaling DFT has been traditionally limited to systems of less than around 100 atoms (and similarly for *ab initio* Hartree-Fock methods), various linear scaling algorithms have recently been developed. One such example is the ONETEP (Order-N Electronic Total Energy Package) program, which scales linearly with both the number of atoms and processors [12]. Linear scaling methods often gain this increases in scaling by exploiting the fact that systems with a distinct band-gap show electronic localization due to exponential decay of electron density as the distance from the atom increases.

B. Accuracy and Limitations of DFT

Despite many improvements, a common limitation of DFT when used alone is that it cannot accurately describe Van der Waals dispersion forces, as these require accurate modelling

[2]A functional takes a function as input and outputs a number

of electron correlation. As a result, systems where dispersion forces are important often require additional corrections. Furthermore, as described earlier, DFT requires an approximation (e.g. Local Density Approximation or Generalised Gradient Approximation) for the exchange-correlation functional, which is often a significant source of error. In general, DFT calculations can perform at similar or better accuracy when compared to Post-Hartree-Fock methods, however for all *ab initio* calculations it remains a challenge to compute chemically accurate energies to within about 5 kJmol^{-1} [6].

VI. Summary

This report has considered some of the most widely used methods of calculating properties of chemical systems from first principle: Hartree-Fock, Post-Hartree Fock and Density Functional Theory. The flowchart in Figure 5 summarises the commonly used methodologies for determining first principles properties of chemical systems. In order to make significant progress on this problem for many-electron systems we must adopt the Born-Oppenheimer approximation, which treats the electronic and nuclear wavefunction as separable. Hartree-Fock methods attempt to numerically approximate the electronic wavefunction, from which electronic properties can be derived by applying the appropriate quantum mechanical operator. The Hartree-Fock method neglects important electron correlation and so Post-Hartree-Fock methods attempt to incorporate electron correlation with the cost of increased computational expense.

In contrast, DFT methods utilise the the electron density as the fundamental quantity, from which electronic properties can be derived by evaluating an appropriate functional of the density. DFT methods incorporate an approximation for the electron correlation via a exchange-correlation functional. Once electronic properties have been obtained from either DFT or Hartree-Fock methods, information from the nuclear wavefunction can be used to calculate a large range of structural (e.g. geometry optimisation) and thermodynamic properties (e.g. entropy). These properties can be used to support experimental evidence, and to provide information which is difficult or impossible to obtain experimentally.

As computer become more powerful, and advances in quantum chemistry techniques improve, more accurate calculations can be obtained and larger systems can be studied. While traditionally *ab initio* calculations have been limited to small numbers of atoms, advances such as Linear Scaling DFT have facilitated the study of entire materials and macromolecules such as proteins. Many systems on the interface between biomolecules and inorganic materials demonstrate complex interactions which are currently poorly understood despite numerous experimental studies; *ab initio* calculations may be used to provide improved understanding of these systems, as further discussed in the second part of this report.

VII. Appendices

1) Basis Sets: As we are interested in computing numerical approximations to the spatial orbital $\psi(\mathbf{r})$, a method of discretising the system is required. This is achieved via a basis set expansion, whereby each spatial orbital is represented as a linear combination of M basis functions:

$$\psi(\mathbf{r}) = \sum_{\mu=1}^{M} C_{\mu i}\phi_{\mu}(\mathbf{r}).$$

We are free to choose any basis set. Ideally they should be complete, meaning that they can represent any molecular orbital. Increasing the number of basis functions increases the accuracy of the spatial orbital (with diminishing returns), however a small number is usually possible due to the computation required for large basis sets. The choice of basis functions is often done using a Linear Combination of Atomic Orbitals (LCAO); the mathematical functions of each atomic orbital (ϕ_{μ}) are known within the literature, and the correct linear combination (i.e. the values of $C_{\mu i}$) can be determined by solving the Hartree-Fock equations (Section IV-C) or, in the very simplest of cases, by symmetry alone. These principles are exemplified in Appendix VII-A.

A. Appendix 1 - Example of possible choice of spatial orbitals for a H_2 Molecule

We could choose the basis sets (ϕ) from the atomic orbitals of each Hydrogen. For H_2 a linear combination of the two atomic orbitals $\phi_1(\mathbf{r})$ and $\phi_2(\mathbf{r})$ will form a gerade ψ_1 and ungerade ψ_2:

$$\psi_1 = [2(1+S_{12})]^{-1/2}(\phi_1+\phi_2)$$

$$\psi_2 = [2(1+S_{12})]^{-1/2}(\phi_1+\phi_2),$$

where S_{12} is the overlap integral which describes the extent to which the two wavefunctions overlap, and is equal to δ_{ij} if the basis sets are orthogonal:

$$S_{12} \quad = \quad \int \phi_1^*\phi_2 \, d\mathbf{r}, \tag{18}$$

and the basis functions are known:

$$\phi_1(\mathbf{r}) = \sqrt{\frac{1}{\pi}}e^{-|\mathbf{r}-\mathbf{R_1}|}, \; \phi_2(\mathbf{r}) = \sqrt{\frac{1}{\pi}}e^{-|\mathbf{r}-\mathbf{R_2}|}.$$

In this example we need not apply Hartree-Fock to determine the coefficients $C_{\mu i}$ as symmetry has been used to determine them as $[2(1+S_{12})]^{-1/2}$.

References

[1] S. H. Lim, J. Wei, J. Lin, Q. Li, and J. KuaYou, "A glucose biosensor based on electrodeposition of palladium nanoparticles and glucose oxidase onto nafion-solubilized carbon nanotube electrode," *Biosensors and Bioelectronics*, vol. 20, no. 11, pp. 2341–2346, May 2005.

[2] S.-J. Bao, C. M. Li, J.-F. Zang, X.-Q. Cui, Y. Qiao, and J. Guo, "New nanostructured TiO2 for direct electrochemistry and glucose sensor applications," vol. 18, no. 4, p. 591âĂŞ599, 2008.

[3] C. BarbÃl', J. Bartlett, L. Kong, K. Finnie, H. Q. Lin, M. Larkin, S. Calleja, A. Bush, and G. Calleja, "Silica particles: A novel drug-delivery system," vol. 16, no. 21, p. 1959âĂŞ1966, 2004.

[4] R. M. Hazen, "Mineral surfaces and the prebiotic selection and organization of biomolecules," vol. 91, no. 11/12, p. 1715, 2006.

[5] A. Bokulich, "BohrÅŻ correspondence principle," in *The Stanford Encyclopedia of Philosophy*, winter 2010 ed., E. N. Zalta, Ed., 2010.
[6] P. W. Atkins and R. S. Friedman, *Molecular Quantum Mechanics*, 5th ed. OUP Oxford, Nov. 2010.
[7] A. Szabo and N. S. Ostlund, *Modern Quantum Chemistry: Introduction to Advanced Electronic Structure Theory*, new edition ed. Dover Publications Inc., Jan. 1996.
[8] P. W. Atkins and R. S. Friedman, "Time-independent perturbation theory," in *Molecular Quantum Mechanics*, 5th ed. OUP Oxford, Nov. 2010, pp. 168–182.
[9] F. Jensen, *Introduction to Computational Chemistry*, 2nd ed. Wiley, Nov. 2006.
[10] P. Hohenberg and W. Kohn, "Imhomogeneous electron gas," no. 136, pp. B864–B871, 1964.
[11] W. Kohn and L. Sham, "Self-consistent equations including exchange and correlation effects," no. 140, pp. A1133–1140, 1965.
[12] C. K. Skylaris, P. D. Haynes, A. A. Mostofi, and M. C. Payne, "Introducing ONETEP: linear-scaling density functional simulations on parallel computers," vol. 122, p. 084119, 2005.

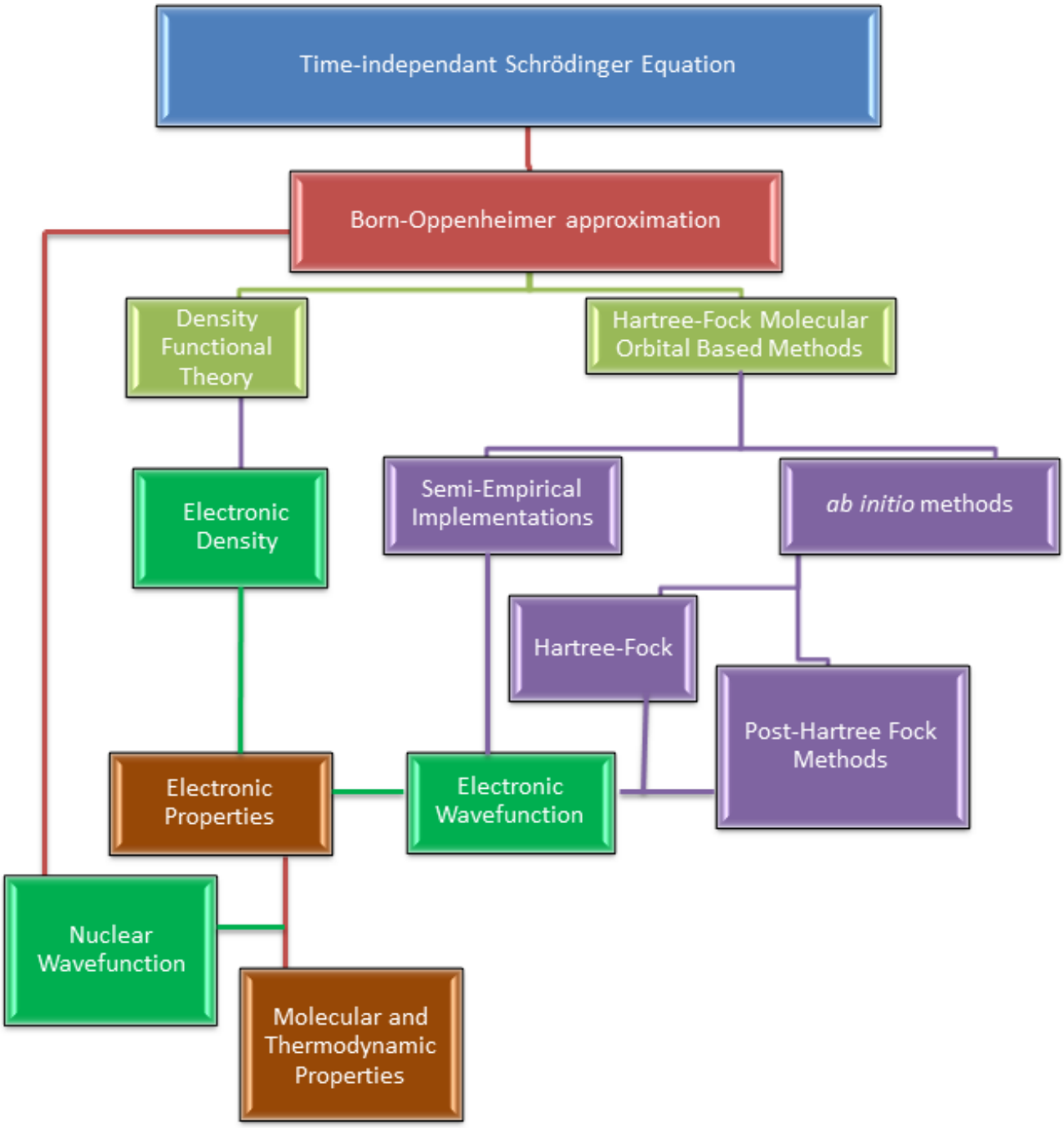

Figure 5. Flowchart summary of widely used quantum chemistry methodologies for first principles calculations of the properties of chemical systems.

D. Appendix: Density Functional Theory Parameters

D.1. ONETEP parameters

Unless otherwise specified, all ONETEP calculations were performed using the PBE-GGA functional [245] using 'fine_bl' settings and an effective kinetic energy cutoff of approximately 800 eV.

```
//'fine_bl' settings:
NGWF_THRESHOLD_ORIG 0.0000018375
ELEC_ENERGY_TOL 0.001 eV
MAXIT_NGWF_CG 100
MINIT_LNV 10
MAXIT_LNV 10
MAXIT_PEN 3
PEN_PARAM 4
MAXIT_HOTELLING 100
SPINPOLARIZED FALSE

GEOM_METHOD CARTESIAN
GEOM_MAX_ITER 100
GEOM_ENERGY_TOL 0.0000100000 eV
GEOM_FORCE_TOL 0.0300000000 "eV/ang"
GEOM_DISP_TOL 0.0010000000 ang
DO_PROPERTIES TRUE

//NGWF Parameters:
//NGWF per atom: default
//NGWF Radius of approximately 9
```

In the final publication simulations were run using a new parameter set, which is the similar to the above except that the NGWF per Si atom was increased to 9 and the NGWF radius was taken as exactly 9.0.

D.2. NWChem parameters

Unless otherwise specified, all NWChem calculations were performed using these settings:

```
basis "ao basis" cartesian print
  * library aug-cc-pvtz
END

dft
 direct
 tolerances accCoul 10
 tolerances tol_rho 1e-12
 tolerances radius 35.0
 tolerances tight
 grid xfine
 convergence energy 1e-8
 mult 1
 XC xpbe96 cpbe96
```

```
 mulliken
 decomp
 print geometry
end
driver
  default
  maxiter 100
end

task dft optimize
```

E. Appendix: ONETEPConv Documentation

The following documentation is for the ONETEPConv software, an open-source utility which is freely available online (doi:10.6084/m9.figshare.4001049.v1).

Benjamin Lowe

University of Southampton

10/03/15

E.1. What is ONETEPConv?

ONETEPConv a set of scripts, written in the Bash scripting language, aimed to make the calculation of Energy and Force convergence data more automated.

To have confidence in any DFT calculation it is important that the calculation is run with sufficient accuracy for the purpose required. At the most basic level, this can be done via comparing the convergence of properties such as the Total System Energy or Forces with respect to varying the resolution of the basis set.

By providing ONETEPConv with an example .dat file, ONETEPConv will generate duplicates of this input .dat file, each time varying one parameter of the basis set to form a 'convergence sweep'. ONETEPConv has the following features:

- .dat file generation:
  - Varying equivalent Kinetic Energy Cutoff (Parameter: 'CUTOFF_ENERGY')
  - Varying Radius of the NGWFs per species (Parameter in: %block_species section)
  - Varying Number of NGWFs per species (Parameter in: %block_species section)
- To speed up sweeps, ONETEPConv supports resuming calculations (reuse_calculations T) from the result of previous calculations (reading .dkn and .tighbox_ngwfs)
- Results analysis:
  - Collates the resulting data into sorted .csv files ready for analysis

E.2. Usage

1. Place a template .dat file into /input/
   a) Ensure the .dat contains a geometry which is not fully geometry optimised because non-zero forces are required to investigate force convergence
   b) Ensure the .dat file is a Single Point Energy calculation with 'WRITE_FORCES T'
   c) Ensure the .dat file has 'WRITE_DENSITY_PLOT F' as writing these files required unnecessary computation and space requirements.
   d) Do not use a high quality basis set in the template, as it will be used for all calculations. It is sufficient to use a low quality basis set and observe the effect of increasing each parameter (kinetic energy cutoff, ngwf radius, number of ngwfs) respectively.
2. Place the .recpots norm-conserving pseudopotentials that you would like to use into the /recpots/ folder

3. Configure ONETEPConv by editing ./input/settings.conv
4. Run ONETEPConv from the root directory:

   ```
   ./conv_generate.sh
   ```

   a) This will generate .dat files in the ./cutoff, ./num_ngwfs and ./ngwf_radius folders respectively
5. Within each subdirectory, run ONETEP manually. You may wish to use a script similar to the provided 'run_jobs.sh'.
6. Extract the results of ONETEPConv into sorted CSV files by running:

   ```
   ./extract_to_csv.sh
   ```

   a) This will generate .csv files in the ./cutoff, ./num_ngwfs and ./ngwf_radius folders respectively, containing both energies (Ha) and forces (Ha/Bohr) for each result.

E.3. ONETEPConv Settings

These can be edited within ./input/settings.conv

- `clean: T/F`

  Remove all input files in subfolders generated from previous runs
- `reuse_calculations: T/F`

  Reuse a density kernel and NGWFs found in ./input/. This will copy these files into the respective folders, and ensure they are read in by the .dat file. Speeds up the calculations in principle. Note that for this to be enabled, you must have already performed a Single Point Energy calculation and placed the .dkn and .tighbox_ngwfs into ./input. If this is set to T, ensure you set READ_TIGHTBOX_NGWFS T and READ_DENSKERN T in your initial .dat file. If this is set to, ensure that this is not the case.

Kinetic Energy Cutoff Sweep Settings

- `min_cutoff: x.`
  `[float] [units=eV]`

  For the Kinetic Energy Cutoff scan, this is the starting (minimum) value of the Kinetic Energy Cutoff
- `cutoff_spacing: x.`
  `[float] [units=eV]`

  This is the spacing between each Single Point Energy calculation for the Kinetic Energy Cutoff sweep.
- `cutoff_number_of_SPE: x`
  `[integer]`

  This is how many Single Point Energy calculations will be performed, starting from $min_cutoff defined above
  - i.e. max_cutoff=($min_cutoff)+ ($cutoff_spacing*$cutoff_number_of_SPE)

NGWF Radius Sweep Settings

- `min_NGWF_radius: x.`
  `[float] [units=Bohr]`

  Starting NGWF radius for the sweep

- NGWF_radius_spacing: x.
  [float] [units=Bohr]

  Spacing between each Single Point Energy calculation

- NGWF_radius_number_of_SPE: x
  [integer]

  This is how many Single Point Energy calculations will be performed, starting from $min_NGWF_radius defined above.

  - i.e. max_NGWF_radius=($min_NGWF_radius)+ ($NGWF_radius_spacing*$NGWF_radius_number_of_SPE)

NGWF Quantity Sweep Settings

- increased_ngwfs: x
  [integer]

  The NGWFs quantity sweep will begin with the number defined in the initial.dat file. Each additional Single Point Energy calculation will increase the number of NGWFs by 1.

- per_element: T/F

  Setting this to True will mean that the '%block_species' parameters (NGWF radius/quantity) will be varied on a per_species basis. This is the default behavior. Setting this to False will vary all species parameters simultaneously, which could be useful for quickly investigating what range of parameters may be required.

E.4. Setting up ONETEP Calculations

- See http://www2.tcm.phy.cam.ac.uk/onetep/Main/Utilities for a variety of useful scripts.
  - For example, 'dat2bounds' calculates the width of your system including NGWF radii, and based on this provides a suggestion as to what a sensible box size might be for either a periodic vacuum padded cell or an open boundary condition simulation (e.g. Implicit Solvent).
- Along with Cutoff Energy, and NGWF parameters, you must also ensure that the SCF convergence is small enough for the calculation accuracy required (NGWF_THRESHOLD_ORIG)
- For calculations involving a periodic slab (x,y direction) which is vacuum separated (z direction), it is important to test the convergence of the slab thickness with respect to your properties of interest.
- If SCF Convergence is taking many iterations, one option is to try a smaller kinetic energy preconditioning parameter 'K_ZERO' (e.g. setting it to 2.5 a_0^{-1}), however it is important to ensure that the accuracy of your calculations is still maintained.
- As a rule of thumb for new users of ONETEP, the following parameters usually fall in the below range, depending on the required accuracy of the calculation:
  - NGWF radius: 7 Bohr to 10 Bohr
  - Cutoff energy: 700 eV to 1200 eV
  - Usually this would match the valence chemistry e.g. 1 for Hydrogen or 4 for Oxygen. You may need to increase this in some cases, e.g. Silicon crystal required 9 NGWFs for an accurate description (see doi:10.1063/1.2796168).

F. Appendix: Density Functional Theory Slab Thickness Validation

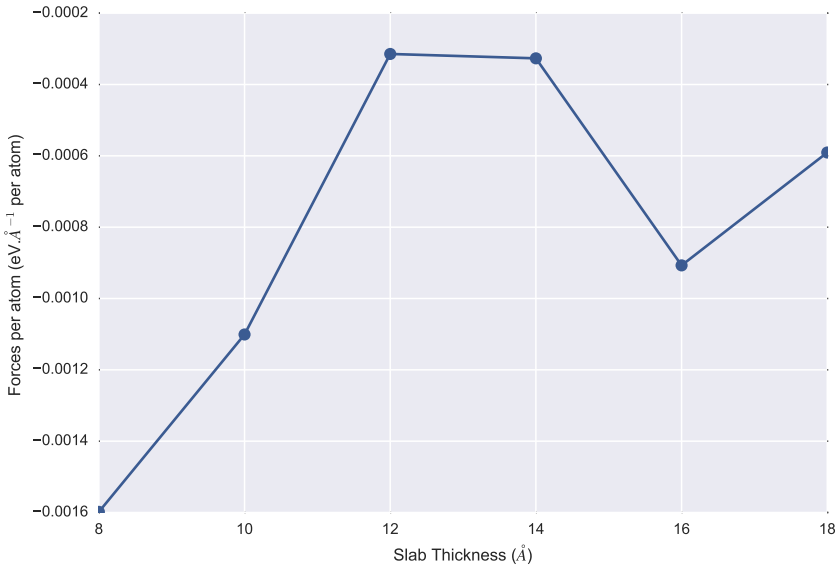

Figure F.1.: Convergence study investigating the choice of 'slab' thickness in the silica model. Slab Thickness is plotted against the Forces per atom, showing a minima at 14 Å. This thickness was utilised in subsequent calculations. The forces per atom were calculated using an example oxygen atom. The properties were calculated using a single point energy calculation using 'fine_bl' ONETEP parameters.

G. Appendix: Paper 1 Supplementary Information

Supplementary Information for 'Publication Acid-Base Dissociation Mechanisms and Energetics at the Silica-Water Interface: An Activationless Process'

Throughout the main text joules were used to express energy and angstroms to express lengths, however in Computational Methods Section, the units of Bohr (a_0), hartree (E_h) and electron volts (eV) were given for input parameters to the simulation software which operate under these units systems.

$1\,a_0 = 0.529\,177\,211\,\text{Å}$

$1\,\text{eV} = 1.602\,177 \times 10^{-19}\,\text{J}$

$1\,E_\mathrm{h} = 4.359\,744 \times 10^{-18}\,\text{J}$

Videos of the *ab initio* molecular dynamic simulations can be found at doi:10.5258/SOTON/401050.

G.1. Input Files

Please find data such as compiler versions, software versions, and example input files at the following link: doi:10.5258/SOTON/401050.

G.2. Optimisation of Water Clusters

A 50 Å periodic box was used to optimise water clusters using the ONETEP software with an approximately 800 eV cutoff and the PBE-GGA functional. Consistent with the literature, it was found that the PBE-GGA functional provided a reasonable description of simple water molecule geometries, as shown in Table G.1. For example, it has been shown that on 9 different small water clusters, that average RMSD with regard to MP2 calculations was 0.032 Å for the average O-O distance [487]. The PBE functional is however well known to systematically over-structure liquid water (see main text, Computational Methods Section).

System (system charge)	O-H bond length	H-O-H angle
hydroxide (-1)	0.97 Å (0.958 Å simulation gas [488])	-
water (0)	0.97 Å (0.96 Å[489] expt. gas)	104.0° (104.5°[489] expt. gas)
hydronium (+1)	0.99 Å (1.00 Å expt. aq. [490] or 0.961 Å simulation gas. [488])	111.7° (106.7° expt. aq. [490] or 114.7° simulation gas [488])

Table G.1.: Calculated geometric parameters for an isolated hydroxide ion, water and hydronium ion in vacuum. Literature values shown in brackets. expt.= experiment. gas=gas phase. aq.=aqueous phase

The images in Figure G.1 show the optimised structures of solvated hydronium ions. Similarly the images in Figure G.2 show the optimised structured of solvated hydroxide ions.

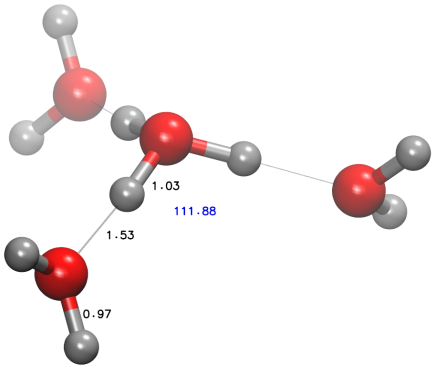

Eigen cation ($H_9O_4^+$). The hydronium O-H length is 1.03 Å (0.98 Å 6-31G** RHF [488]) and the H-bond distance is 1.53 Å (1.61 Å 6-31G** RHF [488]) with a 111.9° H-O-H angle (106.7° aq. expt. [490])

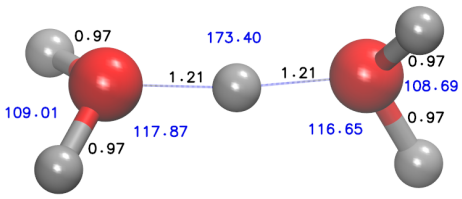

Zundel cation ($H_5O_2^+$). The hydrogen in the middle is separated by 1.21 Å symmetrically, and the remaining H-O lengths are 0.97 Å . This shows excellent agreement with the high level multi-configurational SCF calculations of Muguet who showed lengths of 1.18 Å and 0.95 Å respectively [491].

Figure G.1.: Optimised solvated hydronium clusters. H-O-H Angles shown in blue, O-H bond lengths shown in black.

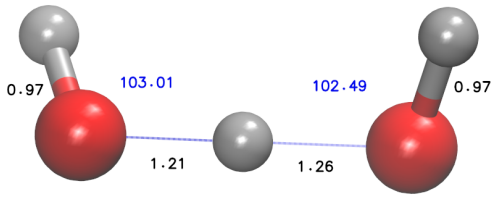

Optimised $H_3O_2^-$ anion. The hydrogen in the middle is located asymmetrically between two oxygen atoms at a distance of 1.21 Å from the leftmost oxygen and 1.26 Å from the rightmost oxygen. The H-O-H angles are 103° and 102° from left to right. This gives a relatively poor agreement with calculations at the MP2/aug-cc-pVDZ level which show a greater asymmetry of 1.42 Å and 1.09 Å from left to right [492] however it is thought that, similarly to the Zundel cation, the proton resonates between the two oxygen atoms. X-Ray crystallography has resolved the proton as symmetrically located between the oxygens [493].

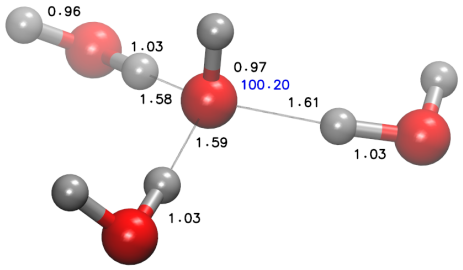

$H_7O_4^-$ anion. The hydrogen bond length is 1.58 to 1.61 Å. This structure is consistent with calculations at the B3LYP/6-31+G(2d,2p) level [494].

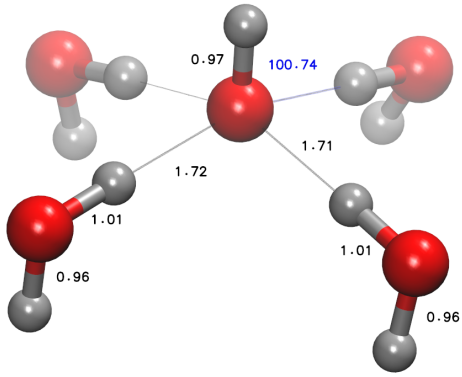

$H_9O_5^-$ anion. This structure is consistent with calculations at the B3LYP/6-31+G(2d,2p) level [494].

Figure G.2.: Optimised Solvated Hydroxide clusters. H-O-H Angles shown in blue, O...H distances shown in black. The lengthening of the hydrogen bonds to the OH^- with increasing solvation is consistent with the B3LYP/6-31+G(2d,2p) calculations of Novoa et al. [494].

G.3. Optimised Water/Surface Model Systems

This section shows the initial and optimised structures of various water-silica model systems.

G.3.1. Cluster Models

Geometry optimisations using DFT (PBE-GGA) and MP2-level calculations in NWChem were compared for a simple silanol monomer system reacting with OH^-/H_3O^+ , as shown in Figures Figure G.3 and Figure G.4.

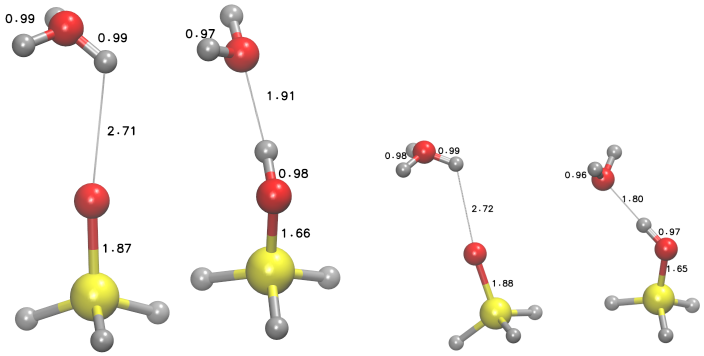

(a) NWChem (PBE) **(b)** NWChem (MP2)

Figure G.3.: Geometry optimisation of a $SiH_3OH \cdot\cdot H_3O^+$ using NWChem. Each left hand image shows the initial structure, with the optimised structure on the right. The captions shows which software and functional in used brackets. Activationless protonation of the silanolate was observed, with the MP2 geometry in good agreement with the PBE geometry, but with slightly shorter (0.11 Å) hydrogen bond lengths than the PBE simulation.

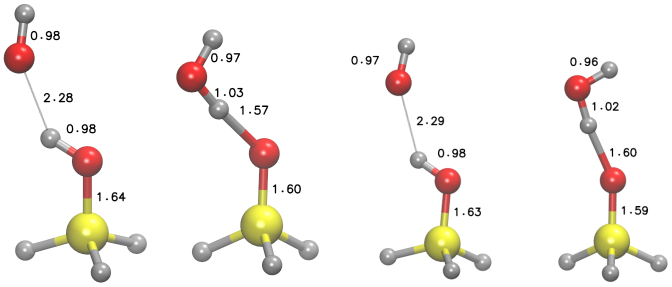

(a) NWChem (PBE) **(b)** NWChem (MP2)

Figure G.4.: Geometry Optimisation of $SiH_3OH \cdot\cdot OH^-$ using NWChem. Each left hand image shows the initial structure, with the optimised structure on the right. The captions shows which software and functional the simulation was run using. Activationless deprotonation of the silanol was observed, with the MP2 geometry in good agreement with the PBE geometry, but with slightly longer (0.03 Å) hydrogen bond lengths than the PBE simulation.

The implicit solvent model of ONETEP was used to study these proton transfers for the model silanol system, as shown in Figures Figure G.5 and Figure G.6.

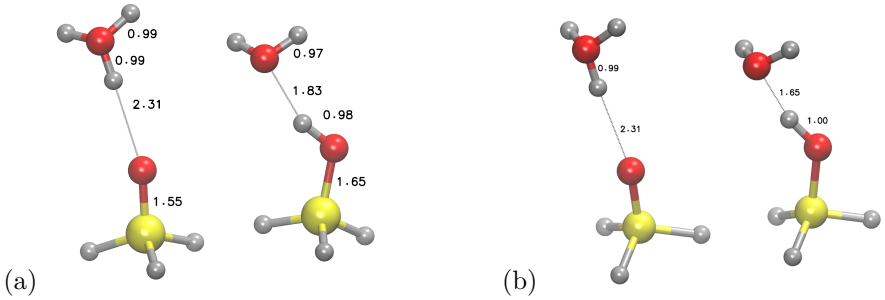

(a) ONETEP (vacuum, PBE) **(b)** ONETEP (implicit solvent, PBE)

Figure G.5.: Geometry optimisation of a $SiH_3OH \cdot\cdot H_3O^+$ using ONETEP in vacuum, shown in (a) and in implicit solvent, shown in (b). The addition of implicit solvation had little affect on the geometry beside a slight shortening of the hydrogen bond by 0.2 Å. Activationless protonation of the silanolate was observed.

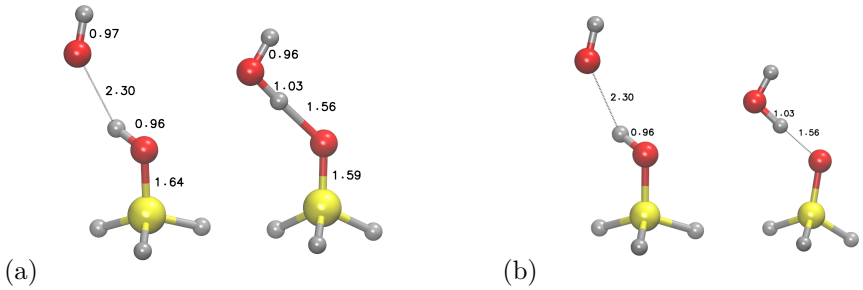

(a) **(a)** ONETEP (vacuum, PBE) (b) **(b)** ONETEP (implicit solvent, PBE)

Figure G.6.: Geometry Optimisation of $SiH_3OH \cdot .. OH^-$ using ONETEP using in vacuum, shown in (a) and in implicit solvent, shown in (b). The addition of implicit solvation had no significant affect on the geometry. Activationless deprotonation of the silanol was observed.

Whereas isolated silanols are the focus of this study, vicinal and geminal silanols were briefly examined, as shown in Figures Figure G.7 and Figure G.8.

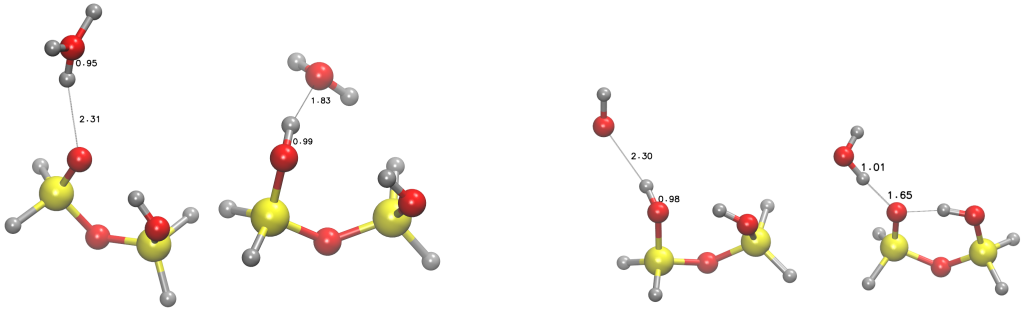

(a) $(SiH_3OH)O(SiH_3O^-) \cdot .. H_3O^+$ **(b)** $(SiH_3OH)O(SiH_3OH) \cdot .. OH^-$

Figure G.7.: Geometry optimisation of a water ion (OH^- or H_3O^+) encounter-paired with a minimal silanol dimer model of a vicinal silanol. Activationless proton transfer is observed, similar to the case of isolated silanols. Calculation performed in NWChem/PBE-GGA.

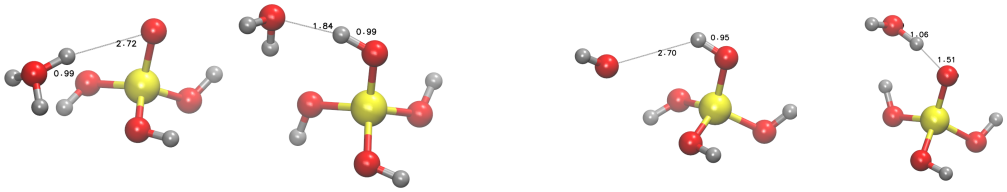

(a) Geometry optimisation of $Si(OH)_3O^- \cdot .. H_3O^+$ **(b)** Geometry optimisation $Si(OH)_4 \cdot .. OH^-$

Figure G.8.: Geometry optimisation of a water ion (OH^- or H_3O^+) encounter-paired with a minimal silicic acid monomer model of a geminal silanol. Activationless proton transfer is observed, similar to the case of isolated silanols. Calculation performed in NWChem/PBE-GGA.

G.3.2. Hydroxide Ion Above Neutral Surface

Geometry optimisation of the stable $H_9O_5^-$ cluster at the silica surface did not show proton transfer, as discussed in the main text and shown in Figure G.9.

(a) **(b)**

Figure G.9.: Geometry optimisation of $H_9O_5^-$ above silanol group at the silica surface using the ONETEP software. Initial structure show in (a), and optimised structure in (b). Deprotonation of the silanol did not occur as a due to the well-known high stability of the $H_9O_5^-$ ion. The silanol OH is stretched from 0.96 Å to 1.01 Å, and there is an assymetry intoduced into the hydrogen bonding pattern of the $H_9O_5^-$ square-pyramidal structure.

G.4. Natural Population Analysis showing Natural Charges

In the main text, a silanolate group on the silica surface is protonated by the solvated hydronium during a geometry optimisation. The natural population analysis of the geometry optimised (after proton transfer) structures is shown here in Figure G.10. Prior to optimisation, the silanolate group surface-terminal oxygen had a Natural Charge of -1.17 and all other surface-terminal oxygens showed a Natural Charge of -1.04 ± 0.01. After optimisation all surface-terminal oxygens showed a Natural Charge of -1.04 ± 0.01, which indicates that the silanolate had been neutralised.

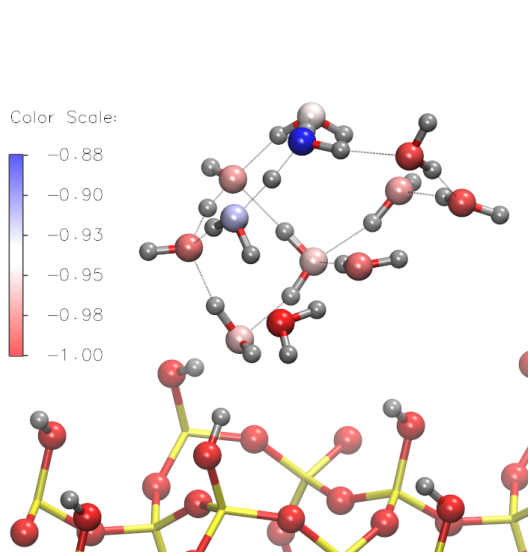

(a) $H_3O^+(H_2O)_{11}$.

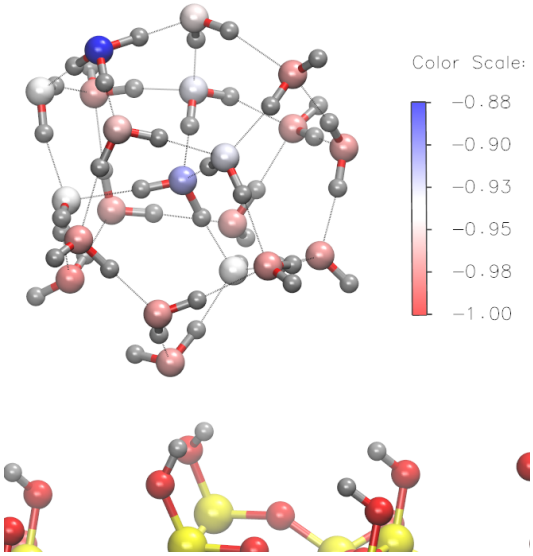

(b) $H_3O^+(H_2O)_{20}$ Conformation A

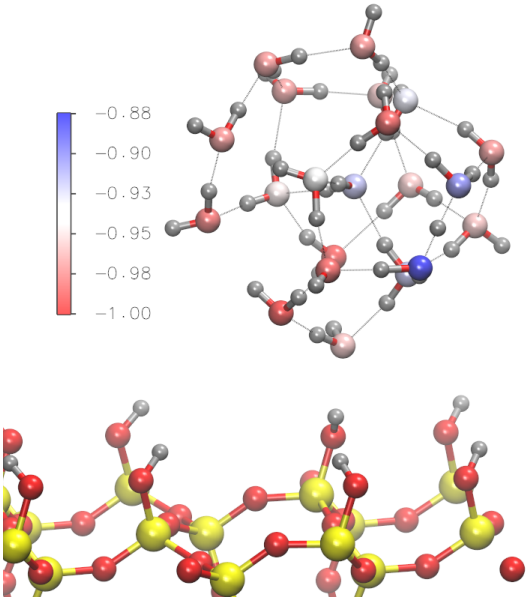

(c) $H_3O^+(H_2O)_{20}$ Conformation B

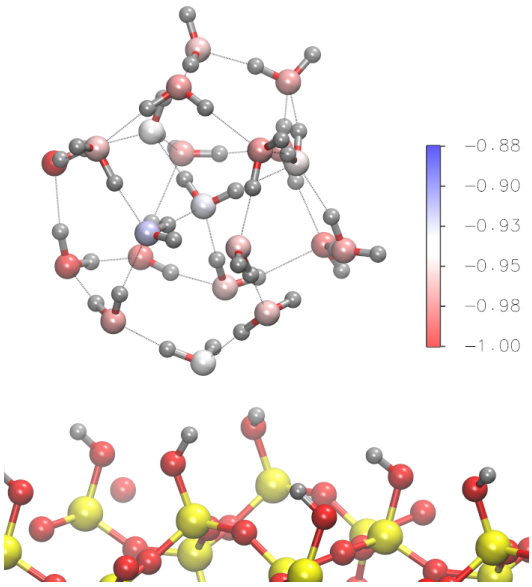

(d) $H_3O^+(H_2O)_{20}$ Conformation C

Figure G.10.: Natural Population Analysis showing the Natural Charge of the oxygen atoms of the water molecules above the silica surface. Each structure is taken from the optimised structure shown in the main text. Oxygen atoms are colored according to their Natural Charge on a linear red, white, blue color scale between -1.00 and below (red) to -0.88 and above (blue). Silicon atoms are shown as yellow and hydrogen atoms as grey.

G.5. Reaction Energies

In order to obtain an estimate of the reaction energies for Equation 1 and Equation 3 from the main text, three reaction schemes were considered for each reaction upon a model orthosilicic acid system [$Si(OH)_4$] and silanol system [SiH_3OH], these reaction schemes are shown in Figure G.11. The first reaction scheme considers products which involve single water molecule physisorption to the surface, the second reaction considers the case of no water physisorption to the surface, and the third reaction considers both molecules being physisorbed (one to the surface, and one to the other water molecule). The results are presented in Figure G.12, and it can be seen that all these reactions are highly exothermic, with the SiR_3O^- protonation reactions in the presence of hydronium being significantly more exothermic than the SiROH deprotonation reaction in the presence of hydroxide (R=OH, H). All-electron (PBE/aug-cc-pvtz) calculations were performed in NWChem, and reaction energies were found to underestimate the reaction energies as calculated by Leung et al. (CCSD(T)/aug-cc-pVDZ corrected for basis set incompleteness) by approximately 12 kJ/mol.

Hydronium/SiR_3O^- (Equation 1 in main text):

$$SiR_3O^- + H_2O \cdot\cdot H_3O^+ \longrightarrow SiR_3OH \cdot\cdot H_2O + H_2O \tag{G.1}$$

$$SiR_3O^- + H_2O \cdot\cdot H_3O^+ \longrightarrow SiR_3OH + H_2O \cdot\cdot H_2O \tag{G.2}$$

$$SiR_3O^- + H_2O \cdot\cdot H_3O^+ \longrightarrow SiR_3OH \cdot\cdot H_2O \cdot\cdot H_2O \tag{G.3}$$

Hydroxide/SiR_3OH - (Equation 3 in main text):

$$SiR_3OH + H_2O \cdot\cdot OH^- \longrightarrow SiR_3O^- \cdots H_2O + H_2O \tag{G.4}$$

$$SiR_3OH + H_2O \cdot\cdot OH^- \longrightarrow SiR_3O^- + H_2O \cdot\cdot H_2O \tag{G.5}$$

$$SiR_3OH + H_2O \cdot\cdot OH^- \longrightarrow SiR_3O^- \cdots H_2O \cdots H_2O \tag{G.6}$$

Figure G.11.: List of Reaction Schemes considered for each of the surface charging and neutralisation reactions described in the main text.

Reaction	R	Uncorrected Reaction Energy	BSSE Correction + ZPE Correction
Equation G.1	OH	-653.5	-650.9
Equation G.1	H	-661.6	-660.7
Equation G.2	OH	-638.9	-637.2
Equation G.2	H	-656.5 (-650.3)	-654.8
Equation G.3	OH	-693.8	-682.1
Equation G.3	H	-707.3	-693.2
Equation G.4	OH	-114.5 [-127.7]	-104.9 [-118.3]
Equation G.4	H	-95.91	-88.30
Equation G.5	OH	-53.41 [-64.89]	-43.49 [-56.15]
Equation G.5	H	-35.78 (-36.30)	-25.91
Equation G.6	OH	-172.3	-153.3
Equation G.6	H	-159.2	-141.8

Figure G.12.: Table of Reaction Energies (kJ/mol) calculated using the PBE-GGA functional and aug-cc-pvtz basis set in NWChem. The uncorrected energy is the calculated using electronic energy of each system, and the correct energy is calculated using Basis Set Superposition Error (BSSE) calculated using the counter-poise method, combined with Zero Point Energy (ZPE) correction. Energies in round brackets indicate those calculated by Leung et al. [144] using CCSD(T)/aug-cc-pVDZ energies corrected for basis set incompleteness. Energies in square brackets are those calculated using ONETEP using the settings described in the main text (PBE functional), using a cubic cell with spherical truncation of the coulomb potential to remove periodic interactions between images. The reactions are highly exothermic, by comparison k_bT at 298 K is ~2.48 kJ/mol.

H. Appendix: Paper 2 Supplementary Information

Supplementary Information for 'Dynamic Behaviour of the Silica-Water-Bio Electrical Double Layer in the Presence of a Divalent Electrolyte'

Authors: B. M. Lowe, Y. Maekawa, Y. Shibuta, T. Sakata, C-K. Skylaris, and N. G. Green,

In the interest of reproducibility, the molecular dynamics trajectories (.xyz files), videos of the trajectories, analysis code and analysis data are openly available from the University of Southampton repository at: http://dx.doi.org/10.5258/SOTON/401018

H.1. Surface Charge Density

The surface charge density used in these simulations of $0.2\,\mathrm{Cm}^{-2}$ corresponds to pH 5.5 according to the XPS experiments of Duval et al. on Quartz [154]. However, accurate quantification of silica surface charge is complicated by the strong ionic strength dependency and variability depending on silica surface preparation. For example, some studies correlate this surface charge density to pH 8.5-9.5 based on 0.1 M ionic strength [495, 496]. Emami et al. [386] estimates at 0.1-0.3 M this surface charge density would correspond to silica at pH greater than 9 or quartz at pH between 7 and 9. This work utilised a (100) alpha-quartz (SiO_2) surface.

H.2. Electric Field Calculation Methodology

For electric field calculations within the main text, post-processing of the trajectory was performed to calculate the electric field at the position of a test charge. Two methods were utilised, each with advantages and disadvantages.

H.2.1. Coulomb Summation

In the Coulomb Summation method (e.g. Figure 12, main text) a non-periodic super-cell was extracted containing the unit cell and its 9 closest neighbours in the x-y plane. A finite-coulomb sum over all atoms to a $-1\,e$ test charge was used to obtain the electrostatic force and thereby the electric field at the test charge coordinates. This method allows neglect of the field introduced by periodic images in the z-axis and is computationally cheap for calculating the electric field across a plane.

Figure H.1 shows the electric field on a test charge centered 1 Å below the silica slab using the Coulomb Summation method.

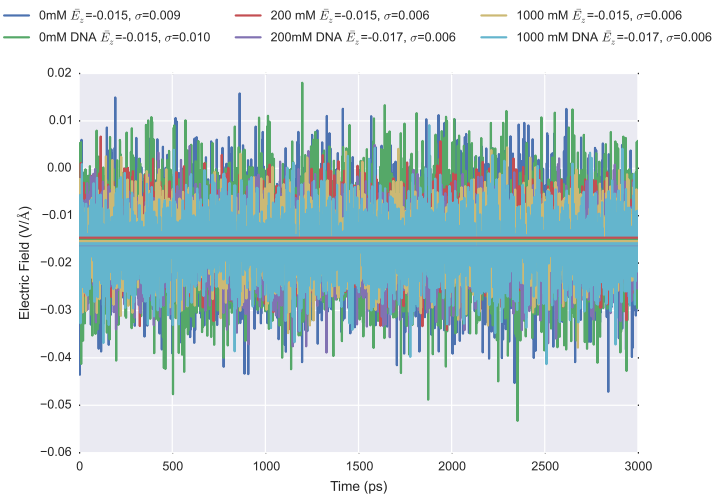

Figure H.1.: Electric Field of mixed valency systems from this work, calculated via finite-coulomb summation for a test charge centered 1 Å below the slab, included in the calculation are the 9 adjecent periodic xy images.

H.2.2. Ewald Summation

The other method utilised was an Ewald sum (e.g. Figure 11 , main text), which provides accurate treatment of periodic electrostatic interactions, but suffers from high computational expense and error introduced by the non-uniform compensating background charge introduced with the test charge for orthorhombic systems [252]. A test charge near the base of the cell will experience electrostatic forces dominated by the periodic image in the z-direction, therefore, for these calculations, an extra unit cell of vacuum padding was introduced to reduce this contribution. The Ewald sum was implemented using the open source software Pysic 0.6 (https://github.com/thynnine/pysic/) and the following parameters:

```
real_cutoff=10
k_cutoff=0.8999999999999999
sigma=3.3333333333333335
epsilon=0.00552635
```

Where epsilon is in units of $\frac{e^2}{eVA}$.

Figure H.2 shows the electric field on a test charge centered 1 Å below the silica slab using the Ewald Summation method.

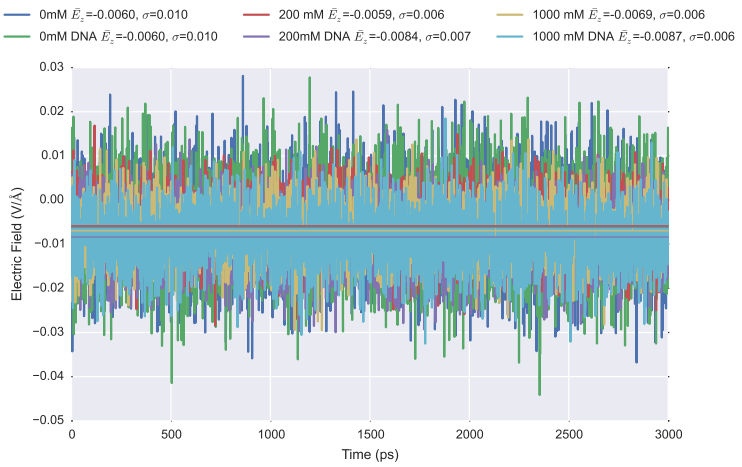

Figure H.2.: Electric Field of mixed valency systems from this work, calculated via Ewald summation for a test charge centered 1 Å below the periodic slab.

H.3. Silanolate coordination numbers

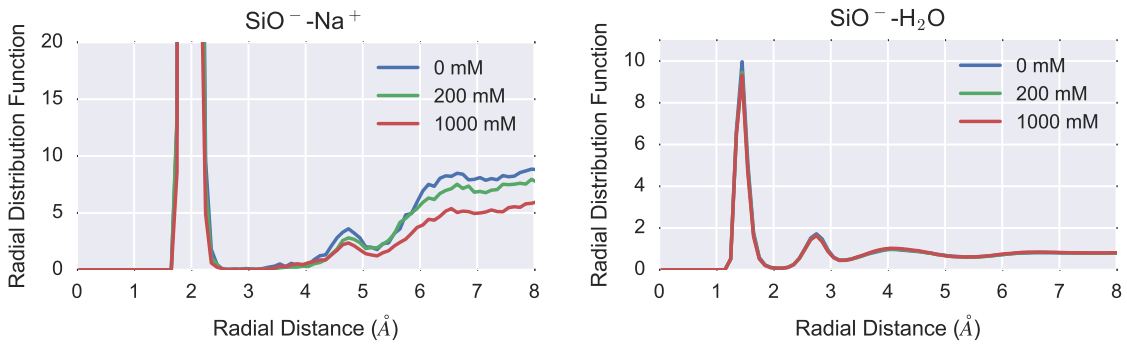

Figure H.3.: Silanolate-[atom] Radial Distribution function (RDF) as a function of 0 mM, 200 mM and 1000 mM ionic strength for silica-water systems. (a) Silanolate-Na^+ RDF, each silanolate showed an average of 1.6-2.3 Å O$\cdot\cdot$Na ion-pair distance (b) Silanolate-Water (H) RDF, each silanolate showed an average of 1.25-2.0 Å O$\cdot\cdot$H hydrogen bond length. These figures were integrated and scaled appropriately to obtain the coordination numbers displayed in the main text Figure 5. Increasing ionic strength resulted in an increase in sodium ion coordination to silanolate ions and corresponding decrease in water coordination.

H.4. Residence Times of $Si{-}O^- \cdot\cdot H_2O$

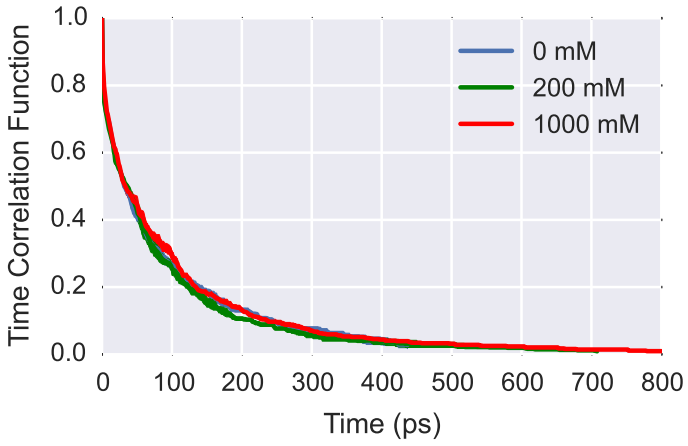

Figure H.4.: Residence time of water to silanolate groups at the silica surface as a function of ionic strength. The coloured region around each line represents the standard deviation of the mean based on three separate samplings 100 ps apart, starting at 2 ns. No significant effect on the residence time is observed due to changes in ionic strength, with a fixed residence time (1/e) of approximately 80 ps. The residence time of water molecules around a silanolate ion was calculated from the Time Correlation Function calculated as per the definition of Impey et al. [398] with a $t_{absence}$=0 and the solvation sphere defined based on the second RDF peak shown in Figure 5, i.e. hydrogen atoms within 3.5 Å.

H.5. Diffusion Coefficient of Dissociating Na^+

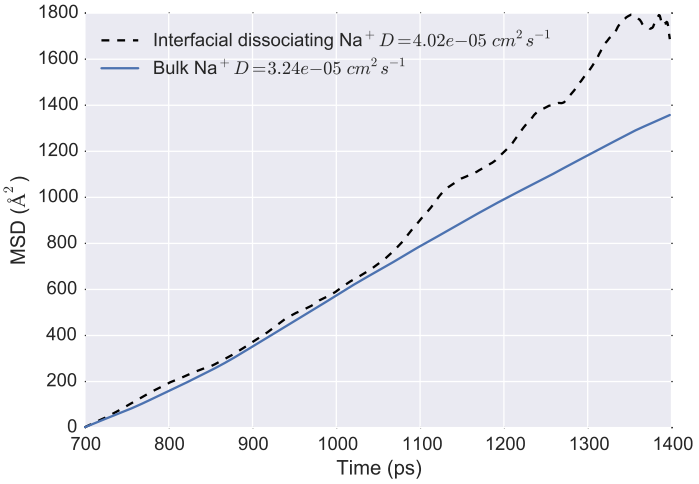

Figure H.5.: Plot of the Mean Squared Displacement (MSD) as a function of time for Na^+ in a simple interfacial system (0 mM system), shown as a dashed line, compared to bulk water shown as a solid line. Both systems show a roughly linear increase in MSD which is characteristic of a freely diffusing system. The diffusion coefficients were calculated (Equation 1, main text) from the MSD as $4.02 \times 10^{-5}\,\mathrm{cm^2 s^{-1}}$ and $3.24 \times 10^{-5}\,\mathrm{cm^2 s^{-1}}$ for the interfacial dissociating ion and bulk systems respectively. A 1 ps interval was used for the MSD calculation. Bulk water simulation performed using 20 Å cubed simulation cell.

H.6. Residence time of $Na^+ \cdot .. H_2O$

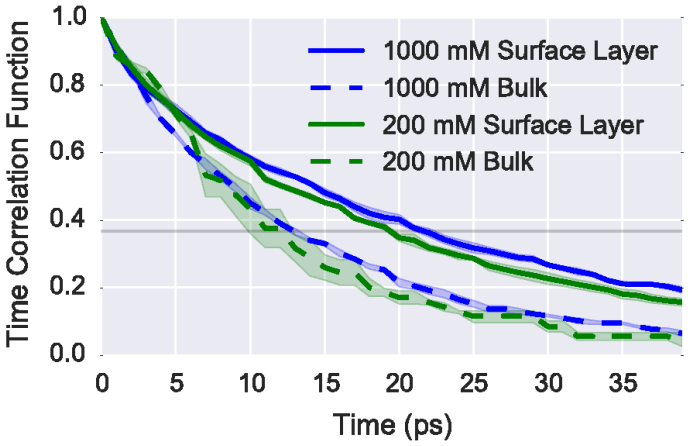

Figure H.6.: The residence time of water molecules around sodium ions as a function of ionic strength for the interfacial systems. The system is divided into two regions, the surface being z < 22 Å, i.e. within ~5 Å of the surface, and the bulk being the rest of the system. Calculated from the Time Correlation Function calculated as per the definition of Impey et al. [398] with a $t_{absence}$=0 and the solvation sphere defined based on the second RDF peak shown in Figure 5 (main text) i.e. hydrogen atoms within 3.5 Å. The time correlation function represents the average number of water molecules which haven't been exchanged with the bulk solvent, i.e. 1 represents the initial state and 0 represents all ions completely exchanging their initial solvation sphere. The coloured region around each line shows the standard deviation of the mean based on three separate samplings 100 ps apart, starting at 2 ns. The residence time (1/e) can be seen to be approximately 20 ps at the surface and approximately 11 ps in the bulk, with a slight dependence on ionic strength. The demonstrated increase in residence time at the surface suggests a more kinetically stable solvation sphere for surface coordinated ions, and is likely a result of the structuring of water and ions found at the interface.

H.7. Poisson-Nernst-Planck Theory

The PNP model utilised in this work is an extension of the 1D model provided by COMSOL Multiphysics® for diffuse double layers, modified to incorporate Mg^{2+} mixed electrolyte [497]. The fluxes ($\mathbf{N}_i$) of the ions are obtained by solving the Nernst-Plank equation:

$$\mathbf{N}_i = -D_i \nabla c_i - u_m i z_i F c_i \nabla \phi,$$

where the concentrations c_i where i =$\mathrm{Na_C l_M g}$ with respective charges z_i of +1, -1 and +2. D_i is the diffusion coefficient, $u_{m,i}$ the mobility (s.mol/kg), F the Faraday constant and ϕ the electric potential in the electrolyte phase.

From conservation of mass:

$$\nabla \cdot \mathbf{N_i} = 0.$$

For the potential, Poisson equation states:

$$\nabla \cdot (-\epsilon \nabla \phi) = \rho,$$

where ϵ is the permittivity, which is the vacuum permittivity multiplied by the relative permittivity of the medium ($\varepsilon_0 \varepsilon_r$) and ρ is the charge density, which depends upon the ion concentration according to:

$$\rho = F(z_{\mathrm{Na}} c_{\mathrm{Na}} + z_{\mathrm{Mg}} c_{\mathrm{Mg}} - z_{\mathrm{Cl}} c_{\mathrm{Cl}}).$$

With regard to boundary conditions, the bulk is grounded (ϕ(bulk) = 0) and at the bulk position, the ion concentrations are set to their bulk values, whereby the positive and negative ions have equal concentration. At the surface, a Stern layer is incorporated, which extends to λ_S. The numerical simulation 1D domain spans from λ_S to x = bulk, therefore $x = 0$ represents the outer Helmholtz plane (OHP), for which the following boundary condition is satisfied:

$$\mathbf{n} \cdot (-\epsilon \nabla \phi) = -\frac{\epsilon(\phi_M - \phi)}{\lambda_S}$$

Where ϕ_M is the electrode/surface potential, ϕ is the electrolyte potential at $x = 0$ and $\mathbf{n}$ is the vector normal to the surface (i.e. x-direction in this 1D model).

Therefore surface charge density σ is obtained over the Stern layer as (simple capacitor):

$$\sigma = \frac{\varepsilon(\phi_M - \phi)}{\lambda_S}$$

The parameters used in these simulations can be found in Table H.1.

The effect of ionic strength at 190 mV surface potential can be found in Figure H.7, independent of ionic strength, the bulk concentration is reached within ~1 nm.

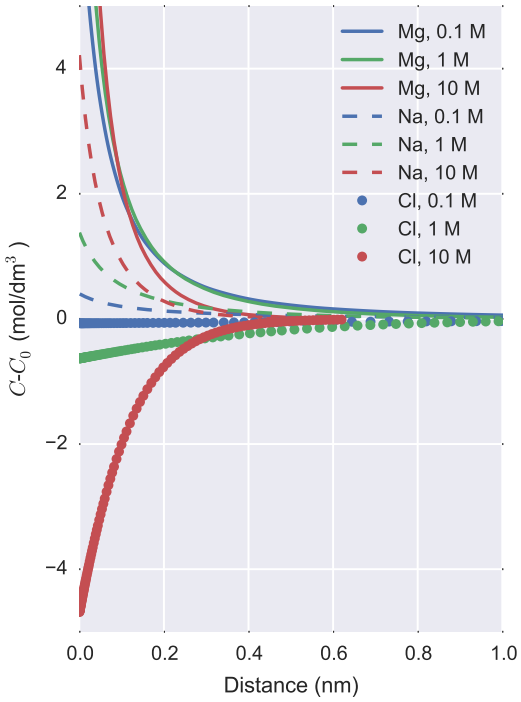

Figure H.7.: GCS model, calculated concentration profile of ions relative to bulk concentration ($C - C_0$), as a function of distance from the surface at a surface potential of 190 mV. Bulk ionic strengths of 0.1 M, 1 M and 10 M are shown. Calculated using parameters in Table H.1 . Independent of ionic strength, the bulk concentration is reached within ~1 nm.

Parameter	Value	Units
$Cl_{bulk}{}^{-}$(Bulk Cl^- concentration)	0.745251724	mol/dm^3
$Mg_{bulk}{}^{2+}$(Bulk Mg^{2+} Cation concentration)	0.248417241	mol/dm^3
$Na_{bulk}{}^{+}$(Bulk Na^+ concentration)	0.248417241	mol/dm^3
I_{bulk}(Ionic Strength of Bulk)	$0.5(4Mg_{bulk}{}^{2+}+Na_{bulk}{}^{+}+Cl_{bulk}{}^{-})$	-
D_{Cl}(Diffusion Coefficient)	2×10^{-9}	m^2/s
D_{Mg}(Diffusion Coefficient)	0.71×10^{-9}	m^2/s
D_{Na}(Diffusion Coefficient)	1.3×10^{-9}	m^2/s
Relative permittivity of water (ε_r)	78.5	1
Maximum mesh element size: bulk	(Cell length)/20	m
Maximum mesh element size: electrode	(Debye Length)/100	m
Cell length	(Debye Length)*10	m
φ_M	-0.19	V
T_0(Temperature)	298.15	K
V_{therm}(Thermal voltage)	RT_0/F	V
Debye length	sqrt($\varepsilon_0 \epsilon_{h_2o}$*$V_{therm}$/(2F*$I_{bulk}$))	-
Stern layer thickness	0.5×10^{-9}	m

Table H.1.: Parameters used in GCS calculations. The mobility constants were calculated via the Einstein relation.

H.8. Average Charge Distribution and Electric field

In this paper, the average charge distribution as a function of distance from the silica surface was calculated, as shown Figure H.8. The cumulative sum of this curve is plotted in the main paper Figure 9. In order to calculate the potential, the 1D Poisson Equation was solved using the average charge distribution, and the electric field was calculated as the gradient of this curve, both of which can also be found in Figure H.8.

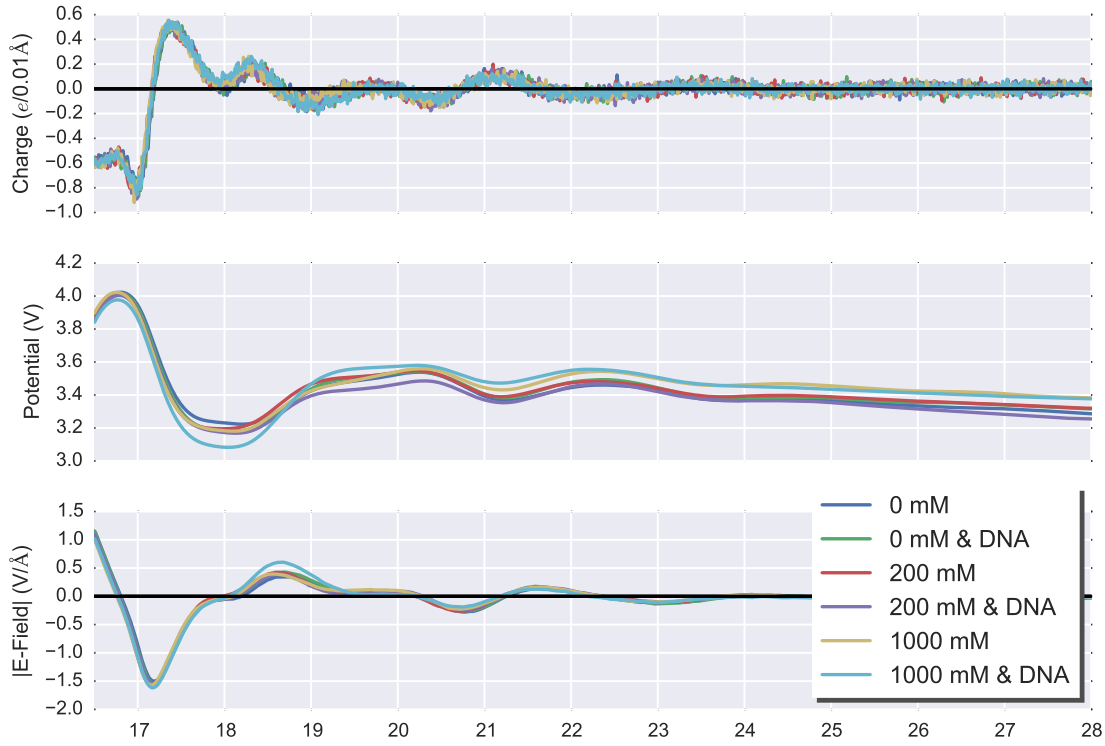

Figure H.8.: The mean charge density as a function of distance normal to the silica surface, note that Figure 9 (main text) is the cumulative sum of this curve. Potential calculated by solving the Poisson equation using the charge density in the top figure. The Gauss–Seidel method was used with Neumann boundary conditions at the base of the silica (z_{base}=0 Å) and at z_{bulk}=80 Å, which was considered the bulk, thereby providing a relative potential within the system. The solution was converged such that successive iterations of the surface potential ($\psi(z_{\text{bulk}})$-$\psi(z = 16.86)$) were within a tolerance of 1e-6 V. An additional constraint required convergence of the each point with its previous iteration to be within 1e-5 V for the entire system and remain so for over 5000 iterations. The potential shown was then referenced to the minimum potential in the system due to a layer of atoms in the fixed silica substrate, which offers a consistent reference potential between all the simulations. The electric field is calculated as a the gradient of the potential. Calculated based on the mean charges in 0.01 Å thick slabs parallel to the xy plane.

H.9. Effect of DNA on Water Orientation

The negative charge on the DNA phosphate groups is expected to orientate the water in its environment, much like the silica surface charge. A plot of the water orientation with respect to the silica surface is shown in Figure H.9, the DNA significantly affects the water orientation at the surface. For the 200 mM/1000 mM systems, the DNA linker was more extended and the perturbation due to the DNA can therefore be seen at a greater distance from the surface than for the 0 mM system.

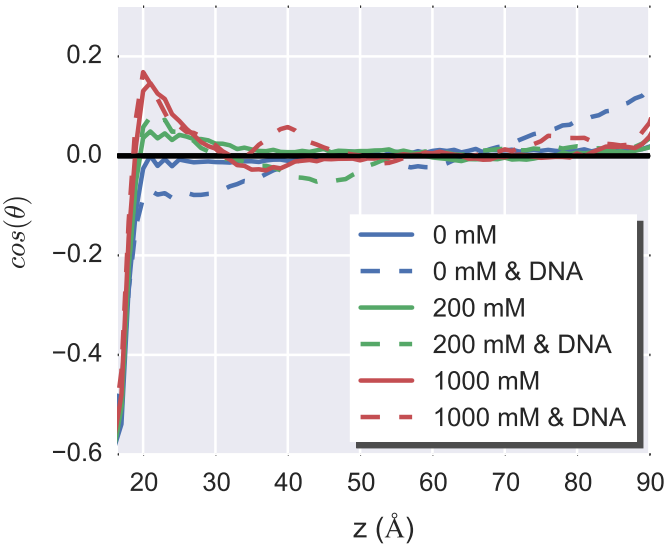

Figure H.9.: The mean orientation of water dipoles ($cos(\theta)$) relative to the silica surface normal, as a function of the z-distance from the surface, using 1 Å bins. Increased ionic strength led to a layer of water at 20 Å which oriented towards the chloride ions, as discussed in Figure 9(C) (main text) and the work of Maekawa et al. [264]. Dashed lines show the corresponding system incorporating DNA; it can seen that DNA is disrupting the orientation of water across the system, particularly in the case of low ionic strength. The standard error of the mean was negligible near the surface due to the strongly oriented water but 0.05 ± 0.01 for all $\cos(\theta)$ past 20 Å.

H.10. Electric Field in NaCl

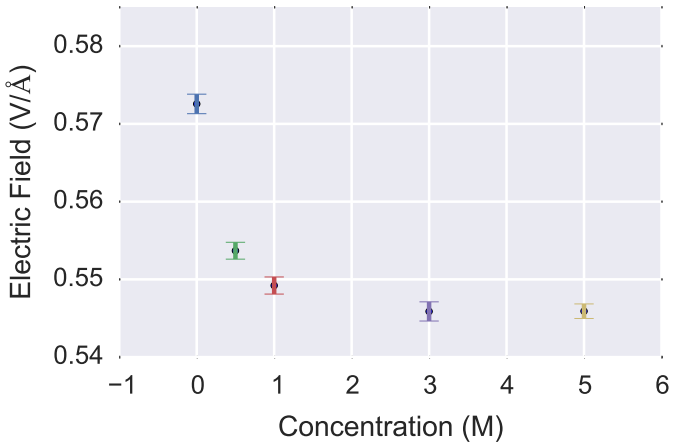

Figure H.10.: Electric Field of monovalent interfacial silica-water systems from Maekawa et al. as a function of ionic strength[264]. Calculated via Ewald summation for a test charge 1 Å below the periodic slab. Error bars show the standard error of the mean.

I. Appendix: Meta-analysis of FET-sensors

I.1. Paper-specific Details

This meta-analysis involved extraction of data for many literature sources. Some of the papers reported their data with some ambiguity, and therefore in this appendix paper-specific notes are provided which explain any assumptions made and any notes regarding uncertainty of the literature data.

Stern et al.

Two data points were shown for the streptavidin sensing result of Stern et al. [61]; these are not two separate experiments but one experiment. In their work, the biosensing current response was normalised by 'pre-addition average current', but it is ambiguous whether this was done after each addition, or normalised to the original addition and therefore two possible (unbounded) Sensitivity values were calculated 59% and 33%; only one of which is correct.

The SS for these data points is also uncertain because the SS for the device used for biosensing was not reported. Current-Potential curve in the paper was at a different back-gate voltage to the biosensing experiments, with the unfunctionalised pH sensing data at V_{bg}=-33 V, which, based on the IV graph, corresponds to the onset of the linear region, and V_{bg} =-20 V for the biosensing experiments. As the pH sensing is the linear regime, it cannot be used to infer the SS, and as the I-V characteristics of the functionalised device are not provided, the SS cannot be accurately obtained. The SS of the dry unfunctionalised device was available (1.21 V/dec).

Buitrago et al.

Buitrago et al. [19] did not allow the system to fully equilibrate as their system was immediately washed with buffer[462], so their Sensitivity is underestimated.

Elfström et al.

For the work of Elfström, the concentration of 1×10^8 M measurement was excluded as the sensor response was deemed to have saturated, showing a less than a 1% increase in sensitivity with a 10-fold increase in sensitivity.

The region of operation was not specified for the work of Elfström et al. [59] however personal communication received suggested that it was in the subthreshold region [498]. Furthermore, their device was operated without a reference electrode, which is generally believed to be required for a well-defined signal.

Wen et al.

For the work of Wen et al. [70], the SS was obtained from their Figure 2 of 0.19 V/dec has an error of +/- 0.1 V/dec due to the curvature of their I-V characteristic, whilst they report 3.208 dec/V (0.3117 V/dec).

It is unclear whether the I_0 used in their sensitivity values is from before any streptavidin was added or after the previous addition of streptavidin, however if it was the former then the linear sensitivity values would increase monotonically therefore it was assumed that it is the latter.

It is unclear whether their sensitivities calculated in their work are I^+_{norm} I^-_{norm}. In their Figure 4 they give negative values suggesting I^-_{norm} but in their table they give positive values. In this work it was assumed they were all calculated as $\mid I^-_{\mathrm{norm}}$ and so their values were converted to I^+_{norm} for comparison in the graphs presented in the thesis.

Dual et al.

The work of Duan et al. [72] is assumed to be in the linear region given the perfectly linear current-voltage characteristic in their Figure 2a and their discussion of the linear region in the supplementary information. As only subthreshold region data is presented in the thesis, the data of Duan et al. is not included.

Sarkar et al.

Within the work of Sarkar et al. [449], it is unclear what precise conditions are used in their Figure 4 subfigures. In Figure 4a, the results were likely obtained at ~pH 7.4 because PBS was used, but the device was operated in the linear region so not included in the work presented in this thesis. They show data in highly acidic conditions in a different subfigure. The data in their Figure 4f was obtained in the subthreshold region, however their work does not specify the pH at which this was operated. As a result, the pH may be significantly different and thereby the charge on streptavidin different to other work performed at ~pH 7.4. Because of these limitations, their data was not included in the analysis presented within the thesis.

Shalev et al.

For the work of Shalev et al. [499], the current response was provided in their Figure 11 as a function of drain-source voltage (V_{ds}) and the calculated I^{+}_{norm} varied between ~50-170% depending on the choice of V_{ds}. The highest value of 170% (at the lowest drain-source) voltage, was presented in the main text.

The buffer was '50 mM phosphate buffer': it is ambiguous whether this is PBS or sodium phosphate. For the work presented in the thesis, it was taken as equivalent to ~0.3X PBS (where 1X PBS has an ionic strength of 162.7 mM [87]).

I.2. Graphs with linear x-axis

This appendix presents the same graphs shown in the main text but with linear x-axis.

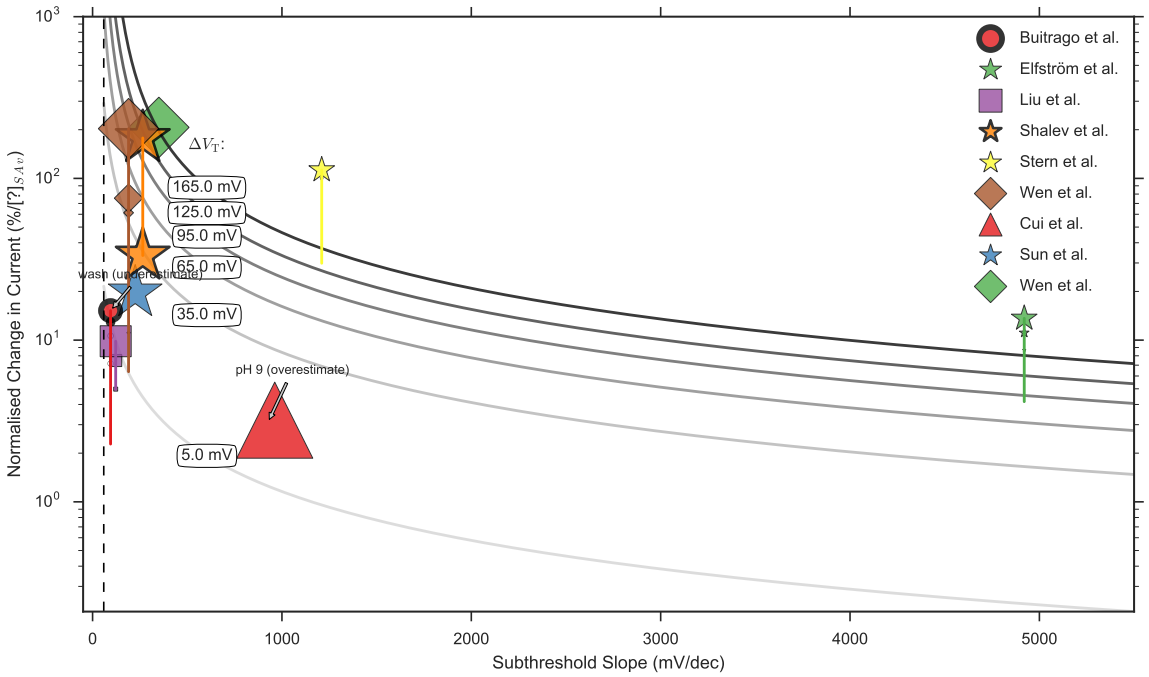

Figure I.1.: Same as Figure 8.3 in main text, but with a linear x-axis as opposed to logarithmic shown in the main text.

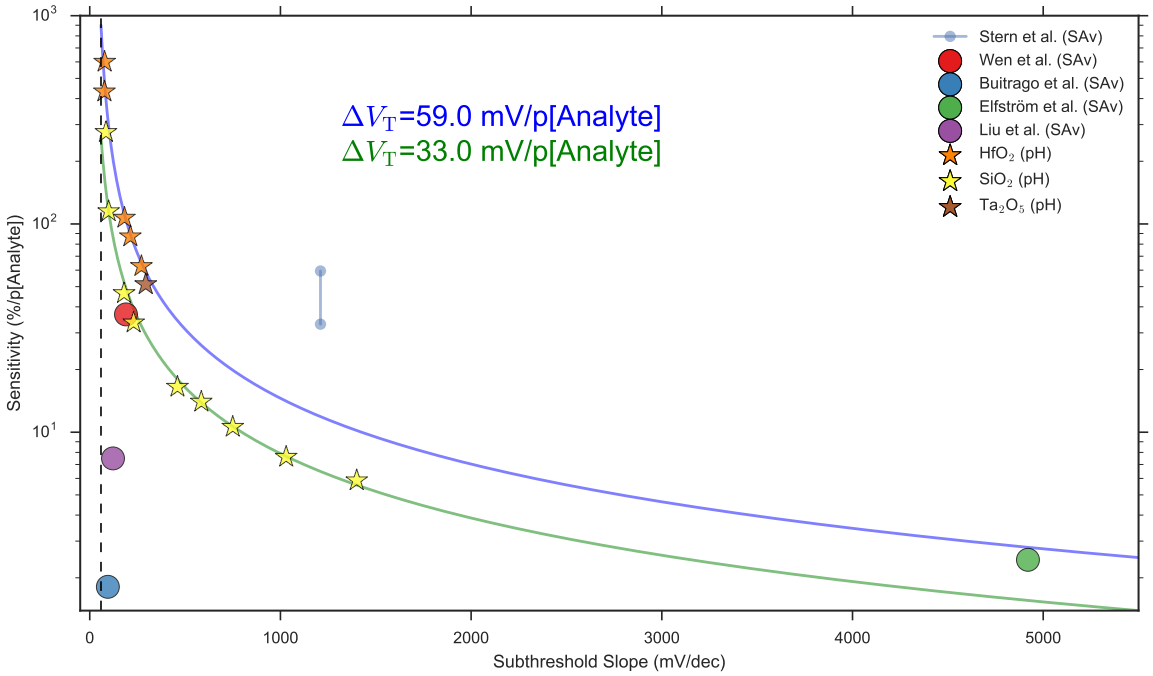

Figure I.2.: Same as in Figure 8.4 main text, but with a linear x-axis as opposed to logarithmic shown in the main text.

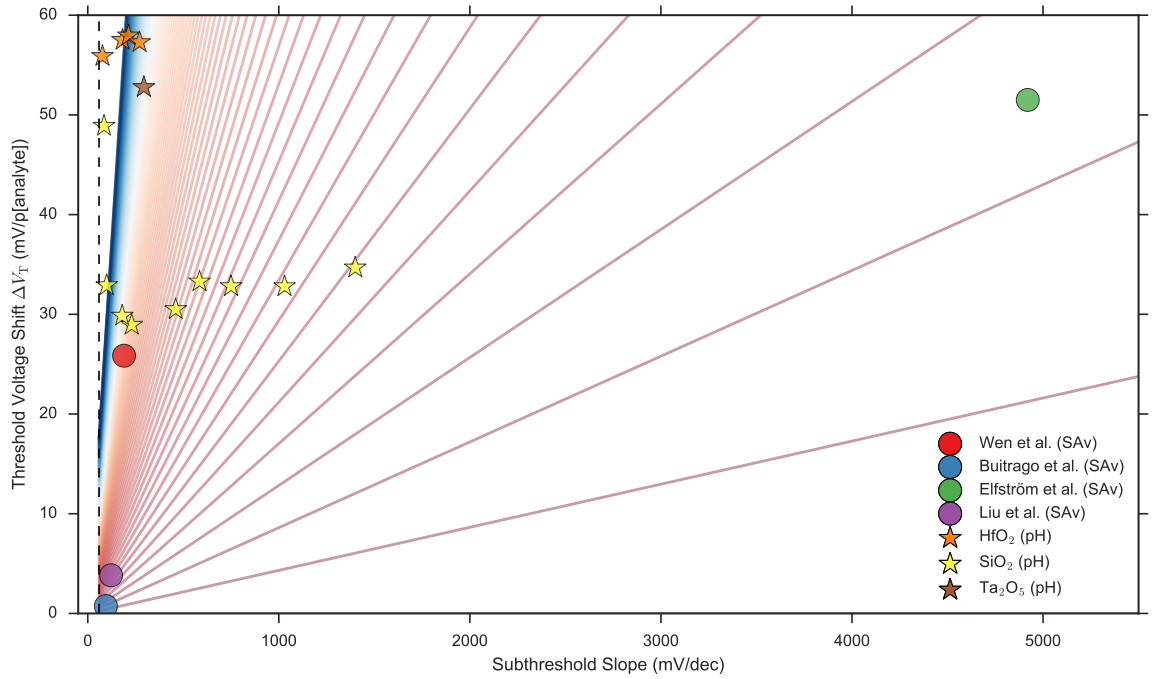

Figure I.3.: Same as Figure 8.5 in main text, but with a linear x-axis as opposed to logarithmic shown in the main text.

I.3. Notes on Figure 8.3 within the Main Text

For Figure 8.3, the ionic strength of each paper was shown by the marker outline thickness. If this was PBS, the dilution was noted (e.g. 1X = 1, 0.1X =0.1). If the buffer was not PBS, the dilution factor for a PBS solution with equivalent ionic strength was used. Finally, each data point was assigned one bin based on its dilution value using the following intervals: [0,0.2500001, 0.50001,1.00001, infinity], resulting in each measurement being assigned a bin from low to high ionic strength. The marker width was chosen such that the thickest was the highest ionic strength.

J. Appendix: Summary Table of Streptavidin-Sensing BioFET Literature

Author	*Semiconductor Material (Device Behaviour)*	*Semiconductor Surface Functionalisation*	*Device Geometry*	*Buffer*	*SAv Conc. (nM)*	*SAv Vendor*	*Electrode (pseudo or conventional)*	*Mode of Operation for Biosensing*
Sun	Si (n-type)	APTES	Nanoribbon	0.01X PBS equiv. (HEPES)	20	?	Ag/AgCl (custom, pseudo)	Subthreshold
Cui[i]	Si (p-type)	APTES	Nanowire	1 mM NaP_i (pH 9) with 10 mM NaCl.	250	"Sigma"	No liquid electrode, read via back-gate	?
Stern[2]	SOI (p-type)	dec-9-enyl-carbamic acid tert-butyl ester	Nanoribbon	0.1X PBS	0.01	AlexFluor 655-linked (Molecular Probes) for imaging but ? for the sensing	No liquid electrode, read via back-gate	Subthreshold (Onset of linear for pH sensing)
Shalev[3]	SOI (n-type)	APTMS	Nanoribbon	50mM "phosphate buffer" NaP_i?/PBS?	20	?	Ag/AgCl (custom, pseudo)	Subthreshold
Wen[4-6]	AlGaN/GaN (n-type)	APTES	Planar	0.25X PBS	(0.00047, 4.73, 5 log intervals[4])	?	Pt	Linear and Subthreshold
Sarkar[7]	MoS_2 (n-type)	HfO_2-APTES	Nanocrystals	0.01X PBS	0.00010 and 10000	?	Ag/AgCl (pseudo?)	Linear, Subthreshold and Saturation
Buitrago[8-10]	Si (n-type)	APTES	3D Nanowire Array	1X PBS‡	0.42	?	Ag/AgCl (conventional commercial, ALS RE-1S)	Subthreshold
Liu[11]	∝-Si SOI (n-type)	Si_3N_4-APTMS	Nanobelt (flow)	0.001X PBS	(0.015, 1.5, 3 log intervals)	Alexa Fluor® 488 Streptavidin (Invitrogen) with 0.1% TWeen20	Ag/AgCl (pseudo?)	Subthreshold
Cheng[12]	SnO_2 (n-type)	APTES	Nanobelt (flow)	1X PBS	0.037	Alexa Fluor® 488 conjugate (Invitrogen)	No liquid electrode. Read out via back-gate	Linear
Ishikawa[13]	intrinsic In_2O_3 (n-type)	Phosphonic acid-based	Nanowire	0.0001X, 0.01X and 1X PBS	100	?	Ag/AgCl (conventional[14])	Linear
Elfström[15-17]	Si SOI (n-type)	APTES	Nanoribbon	0.1X PBS	(0.001, 1, 4 log intervals)[15]	Pierce	No liquid electrode, constant back-gate voltage	Subthreshold[18]
Lee[19]	AlGAN/GaN (n-type)	†Au/Ni-SAM-SAv (no biotin)	Planar EG-FET	1X PBS	0.996	Sigma Aldrich	Ag/AgCl (conventional, commercial RE-5B BASi)	Linear
Martínez[20]	SW-CNT (Ambipolar)	None. SAv adsorb directly	CNT	2X PBS	?	Aldrich S4762	No liquid electrode, read out via back-gate	Linear
Duan (2015)[21]	SOI (p-type)	APTES	Nanowire	~0.01X PBS equiv. (1 mM HEPES)	10	Rockland Immunochemical	? material, commercial Harvard Apparatus "Miniature Reference"	Linear
Duan (2012)[22]	SOI (p-type)	Biotinylated polyelectrolyte (PLL) monolayer	Nanoribbon	~0.01X PBS equiv. (1 mM HEPES)	(0.02, 2, 3 log intervals)	Rockland Immunochemical	Pt top-gate. Read out via back-gate ₸	Linear ₸
Upadhyay[23]	Intrinsic InAs (n-type)	Oxide-BSA-biotin-SAv	Nanowire	0.03X, 0.3X, 3X ‡ NaP_i	100	?	Ag/AgCl (conventional)	Linear
Gupta[24]	AlGaN/GaN (n-type)	APTES	Planar	Dulbecco's PBS	~16000 #	Alexa Fluor 488 is fromInvitrogen Inc. (Carlsbad, CA)	?	?
Star[25]	Carbon nanotube (p-type)	PEI/PEG passivation and biotin functionalisation	CNT	~0.1X PBS (0.01 M PBS)	2500	Streptavidin (from Streptomyces avidinii, Sigma Chemicals) with/without Gold label	No liquid electrode, read out via back-gate	?
Bradley[26]	carbon nanotube (p-type IV behaviour at negative V_g)	None	CNT	15 mM NaP_i (~1X NaP_i)	40	?	"silver" electrode (pseudo?) top-gate. Pt back-gate.	?
Kang[27]	AlGaN/GaN (n-type)	APTES	Planar	? mM NaP_i	~94,000#	?	?	?

Summary Table of Streptavidin BioFET literature with quantitative response data available. The device behaviour refers to the $I_{ds}V_g$ response in the region used for sensing i.e. n-type means decrease in current with decrease (negative change) in gate voltage. For the Streptavidin Concentration (SAv), the data is sometimes presented as (initial, final, n) where n represents the number of intermediate concentrations separated by log intervals. "No liquid electrode" is used to refer to devices with no electrode in the liquid. SOI= Silicon on Insulator, NaP_i = Phosphate Buffer. PBS = Phosphate Buffered Saline. EG-FET = Extended-Gate FET, CNT=Carbon Nanotube. * shows characteristics of a Schottky barrier, metal oxide semiconductor field effect transistor. † On the EG ‡ Reported as 30 mM sodium phosphate buffer as 1 X, whereas by convention this would be 3 X. ǂ Not reported in paper, but in thesis[28]. ∓ Linear region of operation inferred from constant slope of I_{ds}-V_g with linear y-axis. Read out via backgate inferred from statement that top gate was fixed for sensing measurements, and sensing measurement shows sweep of "V_g". # Assuming 53 kDa molecular weight of streptavidin

References for Summary Table of Streptavidin BioFET Literature:

1. Cui, Y., Wei, Q., Park, H. & Lieber, C. M. Nanowire Nanosensors for Highly Sensitive and Selective Detection of Biological and Chemical Species. *Science* **293,** 1289–1292 (2001).
2. Stern, E. *et al.* Label-free immunodetection with CMOS-compatible semiconducting nanowires. *Nature* **445,** 519–522 (2007).
3. Shalev, G. *et al.* Standard CMOS Fabrication of a Sensitive Fully Depleted Electrolyte-Insulator-Semiconductor Field Effect Transistor for Biosensor Applications. *Sensors* **9,** 4366–4379 (2009).
4. Wen, X. *et al.* High sensitivity AlGaN/GaN field effect transistor protein sensors operated in the subthreshold regime by a control gate electrode. *Appl. Phys. Lett.* **99,** 043701 (2011).
5. Wen, X., Gupta, S., Nicholson, T. R., Lee, S. C. & Lu, W. AlGaN/GaN HFET biosensors working at subthreshold regime for sensitivity enhancement. *Phys. Status Solidi C* **8,** 2489–2491 (2011).
6. Wen, X. *et al.* Improved Sensitivity of AlGaN/GaN Field Effect Transistor Biosensors by Optimized Surface Functionalization. *IEEE Sens. J.* **11,** 1726–1735 (2011).
7. Sarkar, D. *et al.* MoS2 Field-Effect Transistor for Next-Generation Label-Free Biosensors. *ACS Nano* **8,** 3992–4003 (2014).
8. Buitrago, E. *et al.* Electrical characterization of high performance, liquid gated vertically stacked SiNW-based 3D FET biosensors. *Sens. Actuators B Chem.* **199,** 291–300 (2014).
9. Buitrago, E. *et al.* Attomolar streptavidin and pH, low power sensor based on 3D vertically stacked SiNW FETs. in *Proceedings of Technical Program - 2014 International Symposium on VLSI Technology, Systems and Application (VLSI-TSA)* 1–2 (2014). doi:10.1109/VLSI-TSA.2014.6839691
10. Buitrago, E. *et al.* Functionalized 3D 7 #x00D7;20-array of vertically stacked SiNW FET for streptavidin sensing. in *Device Research Conference (DRC), 2013 71st Annual* **Supplement,** 1–2 (2013).
11. Liu, H. H., Lin, T. H. & Sheu, J.-T. Enhancement of detection by selective modification of silicon nanobelt field-effect transistors via localized Joule heating. *Sens. Actuators B Chem.* **192,** 111–116 (2014).
12. Cheng, Y. *et al.* Functionalized SnO2 nanobelt field-effect transistor sensors for label-free detection of cardiac troponin. *Biosens. Bioelectron.* **26,** 4538–4544 (2011).
13. Ishikawa, F. N. *et al.* A Calibration Method for Nanowire Biosensors to Suppress Device-to-Device Variation. *ACS Nano* **3,** 3969–3976 (2009).
14. Ishikawa, F. Applications of one-dimensional structured nanomaterials as biosensors and transparent electronics. (University of Southern California, 2009).
15. Elfström, N., Karlström, A. E. & Linnros, J. Silicon Nanoribbons for Electrical Detection of Biomolecules. *Nano Lett.* **8,** 945–949 (2008).
16. Elfström, N. & Linnros, J. Biomolecule detection using a silicon nanoribbon: accumulation mode versus inversion mode. *Nanotechnology* **19,** 235201 (2008).
17. Elfström, N. Silicon Nanowires for Biomolecule Detection. (Royal Institute of Technology, 2008).
18. Linnros, J. Personal Communication. (2016).
19. Lee, H. H. *et al.* Fabrication and Characterization of an Extended-Gate AlGaN/GaN-Based Heterostructure Field-Effect Transistor-Type Biosensor for Detecting Immobilized Streptavidin-Biotin Protein Complexes. *Sens. Mater.* (2015). doi:10.18494/SAM.2015.1092
20. Martínez, M. T., Tseng, Y.-C., González, M. & Bokor, J. Streptavidin as CNTs and DNA Linker for the Specific Electronic and Optical Detection of DNA Hybridization. *J. Phys. Chem. C* **116,** 22579–22586 (2012).
21. Duan, X. *et al.* Functionalized Polyelectrolytes Assembling on Nano-BioFETs for Biosensing Applications. *Adv. Funct. Mater.* **25,** 2279–2286 (2015).
22. Duan, X. *et al.* Quantification of the affinities and kinetics of protein interactions using silicon nanowire biosensors. *Nat. Nanotechnol.* **7,** 401–407 (2012).
23. Upadhyay, S. *et al.* Indium arsenide nanowire field-effect transistors for pH and biological sensing. *Appl. Phys. Lett.* **104,** 203504 (2014).
24. Gupta, S. *et al.* Detection of clinically relevant levels of protein analyte under physiologic buffer using planar field effect transistors. *Biosens. Bioelectron.* **24,** 505–511 (2008).
25. Star, A., Gabriel, J.-C. P., Bradley, K. & Grüner, G. Electronic Detection of Specific Protein Binding Using Nanotube FET Devices. *Nano Lett.* **3,** 459–463 (2003).
26. Bradley, K., Briman, M., Star, A. & Grüner, G. Charge Transfer from Adsorbed Proteins. *Nano Lett.* **4,** 253–256 (2004).
27. Kang, B. S. *et al.* Electrical detection of immobilized proteins with ungated AlGaN/GaN high-electron-mobility Transistors. *Appl. Phys. Lett.* **87,** 023508 (2005).
28. Buitrago, E. High Performance, Vertically Stacked SiNW/Fin Based 3D FETs for Biosensing Applications. (École Polytechnique Fédérale de Lausanne, 2014).

Nomenclature

AIMD	*ab initio* Molecular Dynamics
C-USP	Civeralli and Harrison Ultrasoft Pseudopotentials designed for Generalised Gradient Approximation functionals.
DFT	Density Functional Theory
FET	Field Effect Transistor
FET-sensor	Field Effect Transistor-based Sensor - This term includes all types of FET-based sensors such as BioFETs and IS-FETs
FTIR	Fourier Transform Infrared
H-Bond	Hydrogen Bond
IS-FET	Ion-Sensitive Field Effect Transistor Sensor
KMC	Kinetic Monte Carlo
M-P	Norm conserving psuedopotential which are included with Acclerys Material Studio 6.0.0.
M-USP	Ultrasoft Pseudopotentials which are included with Acclerys Material Studio 6.0.0 designed for the PBE functional.
NGWFs	Nonorthogonal Generalized Wannier Functions - The basis set in ONETEP is composed of these Functions, expanded as a set of periodic cardinal sine functions
NMR	Nuclear Magnetic Resonance
pK_a	Acid- Base Dissociation Equilibrium Constant
PZC	Point of Zero Charge
SFG	Sum Frequency Generation
SHG	Sum Harmonic Generation
SS	Subthreshold Slope - Parameter quantifying the ability of a Field Effect Transistor to transduce a change in gate voltage to a change in drain current
USP	Ultrasoft Pseudopotentials
I	Drain Current (Current from the source to the drain)
V_{ds}	Drain Voltage (i.e. voltage between drain and source)
V_g	Gate Voltage (either of a MOSFET gate electrode, or from a Reference Electrode in a FET-sensor)
MOSFET	Metal-oxide-semiconductor field-effect transistor
MD	Classical molecular dynamics simulations
V_T	Threshold Voltage